MATHEMATICAL INVESTIGATION INTO NANOFLUIDS FLOW AND HEAT TRANSFER IN MICROCHANNELS FILLED WITH POROUS MEDIA

Ebba Hindebu Rikitu

A Dissertation Submitted to the Department of Applied Mathematics,
School of Applied Natural Science

Presented in Partial Fulfillment of the Requirements for the Degree of Doctor of Philosophy
in Applied Mathematics

Office of Graduate Studies
Adama Science and Technology University

February, 2022

Adama, Ethiopia

MATHEMATICAL INVESTIGATION INTO NANOFLUIDS FLOW AND HEAT TRANSFER IN MICROCHANNELS FILLED WITH POROUS MEDIA

Ebba Hindebu Rikitu

Main Supervisor: Professor Oluwole Daniel Makinde, Stellenbosch University, South Africa

Co-Supervisor: Dr. Lemi Guta Enyadene (Associate Professor, ASTU)

A Dissertation Submitted to the Department of Applied Mathematics,
School of Applied Natural Science

Presented in Partial Fulfillment of the Requirements for the Degree of Doctor of Philosophy in Applied Mathematics (Specialization in Computational Fluid Dynamics)

Office of Graduate Studies
Adama Science and Technology University

February, 2022

Adama, Ethiopia

Declaration

I hereby declare that this dissertation entitled "**Mathematical Investigation into Nanofluids Flow and Heat Transfer in Microchannels Filled with Porous Media**" is my original work. That is, it has not been submitted for the award of any academic degree, diploma or certificate in any other university. All sources of materials used for this dissertation have been duly acknowledged through appropriate citations.

Ebba Hindebu Rikitu	____________________	____________________
Name of Student	Signature	Date

Recommendation

We, the supervisors of this dissertation, hereby certify that we have read and revised the dissertation entitled "**Mathematical Investigation into Nanofluids Flow and Heat Transfer in Microchannels Filled with Porous Media**" prepared under our guidance by Ebba Hindebu Rikitu submitted in partial fulfillment of the requirements for the degree of Doctor of Philosophy in Applied Mathematics. Therefore, we recommend the submission of the dissertation to the department for further review and defense.

Professor Oluwole Daniel Makinde	______________	______________
Main Supervisor	Signature	Date
Dr. Lemi Guta Enyadene	______________	______________
Co-Supervisor	Signature	Date

Approval page

We hereby certify that the recommendations and suggestions made by the board of examiners are appropriately incorporated into the final version of the dissertation entitled "**Mathematical Investigation into Nanofluids Flow and Heat Transfer in Microchannels Filled with Porous Media**" by Ebba Hindebu Rikitu.

Professor Oluwole Daniel Makinde	____________	____________
Main Supervisor	Signature	Date
Dr. Lemi Guta Enyadene	____________	____________
Co-Spervisor	Signature	Date

We, the undersigned, members of the Board of Examiners of the dissertation open defense by Ebba Hindebu Rikitu have read and evaluated the dissertation entitled "**Mathematical Investigation into Nanofluids Flow and Heat Transfer in Microchannels Filled with Porous Media**" and examined the candidate during open defense. This is, therefore, to certify that the dissertation is accepted for partial fulfillment of the requirement of the degree of Doctor of Philosophy in Applied Mathematics.

____________________________	____________	____________
Chairperson	Signature	Date
____________________________	____________	____________
Internal Examiner 1	Signature	Date
____________________________	____________	____________
Internal Examiner 2	Signature	Date
____________________________	____________	____________
External Examiner 1	Signature	Date
____________________________	____________	____________
External Examiner 2	Signature	Date

Finally, approval and acceptance of the dissertation is contingent upon submission of its final copy to the Office of Postgraduate Studies (OPGS) through the candidate's Department Graduate Council (DGC) and School Graduate Committee (SGC).

____________________________	____________	____________
Department Head	Signature	Date
____________________________	____________	____________
School Dean	Signature	Date
____________________________	____________	____________
Office of Postgraduate Studies, Dean	Signature	Date

ACKNOWLEDGMENTS

First and foremost I would like to express my deep sense of appreciation to my main supervisor professor Oluwole Daniel Makinde, for his guidance, extraordinary interest, inspiring suggestions and tremendous support that was crucial for the success of this dissertation. Indeed, I am lucky to have the opportunity to interact with professor Oluwole Daniel Makinde, world class senior distinguished professor of applied mathematics and computations, who is enthusiastic, faith, energetic and benevolent in his tutelage during his stay at Adama Science and Technology University lecturing various courses. On top of these, thank you professor also for introducing me the concept of fluid flow in microchannels.

I would also like to express my heartiest gratitude and appreciation to my co-supervisor associate professor Dr. Lemi Guta Enyadene for his willingness to give his precious time, being Adama Science and Technology University president, and advising, encouraging and suggesting constructive comments in this dissertation. More importantly, I want to thank Dr. Lemi Guta on the be half of myself and fellow students for his very considerate and working tirelessly to help us from the day of our registration for PhD in coordinating the academics as well as in bringing professors from overseas and other in-country universities so that our course work as well as dissertation projects moved along in a timely manner.

Furthermore, I would like to express my sincere thanks to my wife Seble Melkamu, my daughter Nany Ebba and my son Benol Ebba for their moral support and unconditional love.

I am also grateful to the financial support of Adama Science and Technology University (Grant No. ASTU/SP–R/073/20) as well as sponsoring my PhD study.

Finally, I would like to express my sincere appreciation to my fellow students, instructors of applied mathematics department for all their support and smooth learning atmosphere.

Dedication

This dissertation is dedicate to all my family members.

Abstract

In the contemporary world, the demand for electronic devices that are smaller in size and owning fast performing capability is increasing at a tremendous pace. However, under operating conditions the lessening of size accompanied with high heat flux generation and hence sometimes these devices fail and damage due to overheating. As a consequence, numerous efforts have been undertaken by the thermofluidic industries in establishing the thermal management systems. Therefore, nowadays the demand for novel technologies concerning cooling mechanisms for thermal management in several electronic industries is increasing. Among such novel technological revolutions, microchannels are the most essential one to transport fluids in the miniaturization systems. Despite of their high heat transfer capabilities, microchannel flows require a greater pumping power and hence nanofluids were invented to overcome such a challenging problem in microchannels. Nanofluids flow and heat transfer in microchannels have a wide range of attributes in industrial process as well as engineering and biomedical applications. Further augmentation of heat transfer rates in microchannels as well as in heat exchangers can be achieved by the syndication of nanofluids with porous media. Due to the aforementioned reasons, the hydrodynamic and thermal behaviours of nanofluids flow in microchannels filled with porous media were studied in this dissertation. Flows induced due to the pressure gradient, suction/injection and buoyancy forces were given attention and the Darcy-Forchheimer model was considered to examine the nanofluds and porous media interaction. Specific problems were mathematically modeled and studied under various scenarios including variable transport properties, thermal radiation, chemical reaction, no slip and convective boundary conditions. Therefore, mixed convection flows of variable transport properties nanofluids without as well as with thermal radiation and chemical reaction were investigated. The Buongiorno nanofluids flow model was used to analyze the effects of the Brownian diffusion and thermophoresis of nanoparticles. Moreover, the hydrodynamic and thermal behaviors of ferrofluid ($Fe_3O_4 - H_2O$) *using the Tiwari and Das nanofluids flow model was examined. Hence, the highly non-linear partial differential equations that govern the flow problems were formulated, transformed into ordinary differential equations using the semi-discretization finite difference method and solved numerically via the fourth order Runge-Kutta integration scheme. Consequently, the wall heat transfer rate for the variable viscosity nanofluid indicated an increasing pattern with increasing values of the pressure gradient parameter, variable viscosity parameter, thermal Grashof number, Schmidt number and Prandtl number. Similarly, the heat transfer rate for the ferrofluid revealed a rising behaviour with rising values of variable viscosity parameter, Darcy number, Eckert number and Prandtl number. Furthermore, the radiation parameter indicated a retarding effect on the temperature profiles of the radiating and reacting nanofluid and hence, radiation quite effectively controls the microchannel temperature distribution and flow transport which plays a significant role in cooling the system. The results were also compared with that of the existing related literature where a very sound agreement has been attained. Finally, summary and conclusions as well as recommendation and suggestions for future research were given based on the findings.*

Keywords: Microchannels; Nanofluids; Porous media; Suction/injection; Variable viscosity; Thermal radiation; Chemical reaction.

List of Published Papers

This PhD dissertation contributed the following original papers which were published in peer reviewed journals and indexed in Scopus to the scientific community in the field of applied mathematics.

Paper1) Hindebu, B., Makinde, O.D., Guta, L. (2021). Unsteady mixed convection flow of variable viscosity nanofluid in a microchannel filled with a porous medium. Indian Journal of Physics, 95 (5), pp. 1–18, Springer Nature.
https://doi.org/10.1007/s12648-021-02116-y

Paper2) Hindebu, B., Makinde, O.D., Guta, L. (2021). Modeling heat transfer enhancement of ferrofluid ($Fe_3O_4 - H_2O$) flow in a Microchannel filled with a porous medium. Journal of nanofluids, Vol. 10, No. 1, pp. 31–44, American Scientific Publishers.
https://doi.org/10.1166/jon.2021.1764

Paper3) Hindebu, B., Makinde, O.D., Guta, L. (2021). Unsteady mixed convection of a radiating and reacting nanofluid with variable properties in a porous medium microchannel. Archieve of Appllied Mechanics, 91 (10), pp. 1–21, Springer Nature.
https://doi.org/10.1007/s00419-021-02043-8

TABLE OF CONTENTS

LIST OF TABLES

LIST OF FIGURES

List of Symbols

Symbols

a	Microchannel width
A	Dimensionless nanofluid pressure
b	Porous inertial resistance coefficient
Bi	Biot number
C	Chemical species concentration
C_f	Coefficient of skin friction
C_p	Specific heat at constant pressure
Da	Darcy number
D_b	Brownian diffusion coefficient
D_T	Thermal diffusion coefficient
Ec	Eckert number
F	Forchheimer number
g	Gravitational acceleration
G	Dimensionless ferrofluid pressure
Gc	Solutal Grashof number
Gt	Thermal Grashof number
h_f	Convective heat transfer coefficient
$\vec{j}$	Mass diffusion flux
j_w	Wall mass flux
K	Permeability parameter
k^*	Rosseland mean absorption coefficient
k(T)	Temperature dependent thermal conductivity
k_0	Initial thermal conductivity
Nb	Brownian motion parameter
Nt	Thermophoresis parameter
Nu	Nusselt number
P	Nanofluid pressure
Pr	Prandtl number
q_r	Thermal radiative heat flux
q_w	Wall heat flux
R	Dimensionless radiation parameter
Re	Injection/suction Reynolds number
S	Porous medium shape parameter
Sc	Schmidt number
Sh	Sherwood number
t	Time
T	Temperature of nanofluid
T_0	Cold wall temperature
T_w	Hot wall temperature
(u,v)	Velocity components
V_0	Wall suction/injection velocity
W	Dimensionless axial velocity
X	Dimensionless axial axis
(x,y)	Cartesian coordinates

Greek Symbols

α	Chemical reaction parameter
β_1	Thermal expansion coefficient
β_2	Concentration expansion coefficient
Γ	Heat capacity ratio
γ	Dimensionless variable viscosity parameter
γ_1	Viscosity variation parameter
γ_2	Thermal conductivity variation parameter
ε	Reaction rate
η	Dimensionless normal axis
θ	Dimensionless temperature
λ	Dimensionless variable thermal conductivity
μ_0	Initial nanofluid dynamic viscosity
$\mu(T)$	Temperature dependent dynamic viscosity
τ	Dimensionless time
τ_w	Wall shear stress
ρ	Nanofluid density
σ^*	Stefan Boltzmann constant
ϕ	Dimensionless nanoparticles concentration
φ	Ferrofluid volume fraction

Subscripts

∞	Ambient
0	Initial
w	Wall
nf	Nanofluid
f	Base fluid
s	Solid nanoparticles
p	At constant pressure

CHAPTER 1

INTRODUCTION

1.1 Background of the Study

1.1.1 Heat Transfer and Its Applications

The dynamics of heat transfer phenomenon is commonly encountered in our daily life activities as well as in engineering and industrial processes. Some common examples of heat transfer in our daily life include boiling of water, heating and cooling of room and heat from sun or light bulb. Heat, also known as thermal energy is a form of energy which transfers from one physical system to another as a result of temperature difference (Bergman et al., 2011). Thermodynamics is a branch of physics that deals with the amount of heat transfer as a system undergoes a process from one equilibrium state to another. More importantly, heat transfer is a branch of engineering science that deals with the determination of the rates of such energy transfers as well as variation of temperature and thus it is the main quantity of interest in the design and evaluation of heat transfer devices (Holman, 2010). Consequently, there are three fundamental mechanisms of heat transfer namely conduction, convection and radiation.

Thermal conduction is the direct body contact or microscopic exchange of kinetic energy of particles through the boundary between two systems. The Fourier's law of heat conduction states that the time rate of heat transfer through a material is proportional to the negative gradient of temperature and to the area at right angles through which the heat flows. In mathematical form:

$$\vec{q}_{cond} = -k\nabla T \tag{1.1}$$

where $\vec{q}_{cond}$ is the thermal conduction heat flux vector, T is temperature and $k > 0$ stands for thermal conductivity of the medium.

Convection heat transfer is the mechanism of heat transfer process between the layers of a fluid, when the fluid is in motion or between a fluid in motion and a boundary surface in contact with it when they are at different temperatures. That is, thermal convection involves the combined processes of conduction (heat diffusion) and advection (heat transfer by bulk fluid flow). In the absence of any bulk fluid motion, heat transfer between a solid surface and the adjacent fluid is by pure conduction. The Newton's law of cooling states that the rate of convective heat transfer by a body is proportional to the difference in temperatures between the body and its surroundings.

$$\vec{q}_{conv} = h(T_s - T_\infty) \tag{1.2}$$

where $\vec{q}_{conv}$ is the thermal convection heat flux vector, h is the convection heat transfer coefficient, T_s is the surface temperature, and T_∞ is the temperature of the fluid sufficiently far from the surface. The convection heat transfer coefficient h is not a property of the fluid but it is an experimentally determined parameter whose value depends on all the variables influencing convection such as the surface geometry, the nature of fluid motion, the properties of the fluid, and the bulk fluid velocity.

Depending on the driving forces of fluid motion, convective heat transfer is classified as free or natural convection, forced convection and mixed convection. In free or natural convection, the fluid motion is induced by density differences from natural means such as gravitational field or by buoyancy force due to temperature variations in the fluid. On the other hand, in forced convection the fluid motion is induced by pressure differences from external forces like a fan, a pump, a blower, and a suction device other than temperature differences. Forced convection is typically used to increase the rate of heat exchange. Many types of mixing also utilize forced convection to distribute one substance within another. The mechanism of mixed convection occurs when forced convection and natural convection act simultaneously to transfer heat. In other words, the interaction of both pressure and buoyant forces is also called mixed convection.

The convection heat transfer, the heat transport through the bulk motion of fluids is found to be a very efficient source to analyze the rate of heat removal or addition. Therefore, the convection heat transfer occurs in a broad range of applications in engineering and industrial heating and cooling process such as cooling of microelectronics, nuclear reactor cooling, cooling/heating systems in buildings, vehicles, heaters, furnaces, refrigerators, textile industry, food plants, chemical industry, space cooling, power generation, energy production, manufacture and extraction of polymer and rubber sheets, paper production, wire drawing and glass fiber production, air conditioning in aerodynamics and biomedical applications such as laser surgery, magnetic drug targeting and heat conduction in tissues and many others (Mohsan et al., 2019; Khan et al., 2019). Because of such wider range of applications, a great number of researchers studied natural, forced or mixed convection flows of fluids under various situations. For-instances, Delisle et al. (2019) presented an experimental and numerical study of forced convection flow of nanofluid in microporous channel. It was found that the pressure drop can be considered negligible. A negligible pressure drop means that operating costs are minimal. Another observation was that the temperature distribution has optimal results when nanofluid with 0.6% alumina is used. Moreover, the experimental and numerical studies are in good agreement with an average relative error of 3.3%, which is determined by analyzing the temperature distribution.

Meanwhile, Anwar et al. (2020) investigated a comprehensive analysis of time-dependent free convection electrically and thermally conducted water-based nanofluid flow containing Copper and Titanium oxide past a moving porous vertical plate. A uniform transverse magnetic field is imposed perpendicular to the flow direction. Thermal radiation and heat sink terms are included in the energy equation. According to their findings, fluid accelerates with increasing Grashof number and porosity parameter while increasing values of heat sink parameter and Prandtl number drop the thermal profile.

Vaidya et al. (2021) focused on the heat and mass transfer characteristics of a mixed convective flow of an electrically conducting nanofluid past a slender Riga plate in the presence of viscous dissipation and chemical reaction. The thermophoresis and Brownian motion aspects for nanoliquid were proposed using Buongiorno's relations. The similarity transformation were utilized to obtain dimensionless forms of flow field equations and then solved via optimal homotopy analysis method (OHAM). One of important observations of their study was that for higher values of modified Hartmann number the velocity profile increased and temperature profile suppressed.

Thermal radiation is a process of heat transfer in a vacuum or media (most gases and some liquids or solids) via electromagnetic waves. Unlike conduction and convection, the transfer of heat by radiation does not require the presence of an intervening medium but depends on the factors like temperature, solid geometric arrangement, surface properties of the material that are emitting or absorbing heat. Since all matters emit and absorb electromagnetic radiation therefore radiation heat transfer is everywhere. It is quite clear that when temperature difference is high/low, the radiation transmission between two bodies is intensified/declined. The Stefan-Boltzmann law states that the time rate of heat transfer by radiation per unit surface area of a material is directly proportional to the fourth power of the material thermodynamic temperature T and given as:

$$\vec{q}_r = \varepsilon\sigma^* T^4 \tag{1.3}$$

where $\vec{q}_r$, is the thermal radiation heat flux vector, σ^* is the constant of proportionality called the Stefan-Boltzmann constant, ε is emissivity of the surface $(0 \leq \varepsilon \leq 1)$ which measures how closely a surface approximates a black-body for which $\varepsilon = 1$ and T is the surface temperature. Black-body radiation represents the maximum amount of radiation that can be emitted from a surface at a specified temperature. Absorptivity (ξ) is the fraction of the radiation energy incident on a surface that is absorbed by the surface, $0 \leq \xi \leq 1$. A black-body absorbs the entire radiation incident on it $(\xi = 1)$. Kirchhoff's law states that the emissivity and the absorptivity of a surface at a given temperature and wavelength are equal. Of-course, in heat transfer studies we are interested in thermal radiation, which is the form of radiation emitted or absorbed by bodies because of their temperature.

In moving fluids, the effect of radiation also plays a significant role in several industrial and engineering application areas such as in aerospace, chemical, environmental, solar power technology, space technology, nuclear power plants, atomic reactor, glass generation as turbines, glass production and furnace design, cosmic flight aero dynamics rocket, propulsion systems for aircraft, missiles, satellites, and space vehicles (Sujatha et al., 2019; Suresh et al., 2018). Due to these diverse applications, the study of fluids flow with heat and mass transfer in the presence of radiation has attracted the attention of many researchers. For example, Matao et al. (2020) presented the numerical investigation of unsteady magnetohydrodynamics (MHD) mixed convection flow of radiating and chemically reacting fluid past an impulsively started oscillating vertical plate with variable temperature and constant mass diffusion. The transport model employed includes the hall current and a uniform magnetic field. The Rosseland approximation was used to describe the radiation heat flux in the energy equation. The dimensionless governing system of partial differential equations of the flow was solved numerically by employing the finite element method.

Later on the study of laminar, viscous, incompressible nanofluid flow in a microchannel with thermal radiation was given by Sindhu and Gireesha (2021). They considered heat source, thermal heat flux, convective boundary, thermal radiation and shape effect. The non-dimensional equations were computed by using Runge-Kutta-Fehlberg method. Effects of heat source, buoyancy force, radiation parameter and convective boundary condition on the thermal system were demonstrated.

1.1.2 Applications of Microchannels

Nowadays, with increasing energy prices and a demand for energy efficiency, many efforts were made for energy saving and reduction of production costs and hence heat enhancement and heat storage are becoming important engineering topics related to renewable energy (Ganji and Malvandi, 2016). As a result, for the last four to five decades, many techniques have been presented to improve the efficiency in industrial equipment, especially in different heat conversion devices or heat exchangers. This technological revolution ensured the strong industrial productivity growth which in turn has brought an improved societal quality of life world-wide. In general, the goal is improving heat transfer performance of the heat exchangers which is referred to as enhancement in heat transfer rate that improve the overall performance of the industrial system including reducing the initial and capital costs of the heat transfer devices or heat exchangers in addition to increasing heat transfer rate.

According to Kandlikar et al. (2006), for the convection flow in a channel, heat transfer enhancement methods can be classified into two main groups known as passive and active techniques. Passive techniques are those which do not require direct application of external power, while active techniques require external power. In the case of active techniques, the addition of external power essentially facilitates the desired flow modification and the concomitant improvement in the rate of heat transfer. On the other hand, the passive techniques improve the heat transfer coefficients by disturbing or altering the existing flow behavior which is usually accompanied by a rise in the pressure drop. Active techniques commonly present higher augmentation though they need additional power that increases the initial capital and operational costs of the system. The common active techniques are mechanical aids (stirring the fluid by mechanical equipment), surface vibration, fluid vibration, electrostatic/magnetic fields and suction/injection.

The passive methods do not need external power and usually utilize flow channel geometry refinement and fluid additives. As far as refining the flow channel geometry is concerned, there have been countless efforts undertaken by the research community for the last four to five decades in the fields of device miniaturization. Among the refined channel flow geometries, microchannels have been identified as the most essential one to transport fluids within a miniaturization systems. The convective thermal transport from a channel surface to a fluid in motion, the dimensionless heat transfer rate which is also known as Nussselt number Nu is given by

$$Nu = \frac{hD}{k} \tag{1.4}$$

where h is the convective heat transfer coefficient, k is the fluid thermal conductivity and D is the channel diameter. Then from equation (1.4) the convective heat transfer coefficient is given by

$$h = \frac{kNu}{D} \tag{1.5}$$

Hence, from (1.5) it can be seen that, as the channel diameter D reduces to micron or nano-size, the heat transfer coefficient h can increase to thousand or million times the original value in order to maintain a constant value of the Nusselt number Nu. Therefore, microchannels enhance the heat transfer rates for convection flows.

A microchannel is a medium through which fluid is used to dissipate heat from a hot surface by forcing the fluid through a passage of hydraulic diameter ranges from 1μm-100μm (Mehendale et al., 2000). The concept of the microchannel was demonstrated for the first time by Tuckerman and Pease (1981) in 1981 who came out with a ground breaking idea of generating high heat transfer coefficients within heat exchangers in the Stanford Electronics Laboratories. They achieved high heat flux removal capacity of about 800 W/cm^2 by utilizing a channel with hydraulic diameter of 100μm. They noted that as the hydraulic diameter of the channel decreases, the convection heat transfer coefficient increases. Microchannel has higher heat transfer surface area to fluid volume ratio and hence it provides high heat transfer coefficient for convective heat transfer. Furthermore, microchannels as heat exchangers have numerous attributes including high thermal effectiveness, small size, low weight, low fluid inventory, and design flexibility, lower materials and manufacturing costs and light weight because of extreme compactness when compared to conventional channels and thus brought about an attractive advantage that would draw the interest of many manufacturers.

As a result, microchannels are increasingly used in a wide range of industrial and engineering applications including electronic cooling, cooling of computer chips, chemical engineering, automotive heat exchangers, laser equipment, aerospace technology, cooling of microchips, heat sinks of micro-electro-mechanical systems (MEMS) based devices, drug delivery applications, DNA hybridization, chemical processing, environmental control, and energy conversion technologies, biochemical and pharmaceutical applications, bio-technologies, sensing technologies so and so on (Rai et al., 2018; Jahangiri et al., 2018; Saleel et al., 2019). Therefore, in recent years a number of researchers have reported the analysis of fluid flow and heat transfer phenomena in microchannels. To mention some, Prameela et al. (2019) examined the steady fully developed hydromagnetic natural convection flow in a vertical microchannel under the influence of heat generation and viscous dissipation. The exact analytical solutions for energy and momentum equations were obtained using perturbation method. Accordingly, increasing the value of heat generation parameter enhances the microchannel slip velocity and temperature. It was also noticed that the skin friction coefficient increases at the cold wall and decreases at the hot wall whereas the heat transfer coefficient decreases at the cold wall and increases at the hot wall with an increase in the heat generation parameter.

Furthermore, Moon et al. (2019) performed numerical investigations into three-dimensional heat transfer enhancement in multi-harmonic wavy microchannels. The solutions by the finite element method illustrated that as wave amplitude and Reynolds number increase the effectiveness of the device also increases and that the selection of specific material highly impacts the diffusion of heat in the solid but it is negligible on the Nusselt number for the fluid.

1.1.3 Nanofluids and Their Applications

Regarding to the passive heat transfer enhancement technique through fluid additives for convection flows in channels, the most successful one is the inclusion of nanometer-sized solid particles into the common base fluids, such as water, oil, and ethylene-glycol. The motivation was to improve the thermal conductivity of a mixture with a solid particle which has a higher thermal conductivity. These nanoparticles are fairly close in size to the molecules of the base fluid and thus can enable extremely stable suspensions with only slight gravitational settling over long periods. To this end, Choi (1995) was the first scientist in pioneering the term nanofluid at Argonne National Laboratory of USA to indicate that nanofluids are engineered suspensions or dispersions of nanometer-sized (1nm–100nm) particles in conventional fluids (base fluids) such as water, ethylene glycol or oils to enhance thermal conductivity.

The nanoparticles $(1nm = 1 \times 10^{-9}m)$ used in nanofluids are typically made of metals (Al, Cu, Ag, Au, Fe, Ti), carbides (SiC), nitrides (AlN, SiN), nonmetals (graphite, carbon nanotubes) or oxides $(Al_2O_3, CUO, TiO_2, SiO_2, Fe_3O_4)$ (Anwar et al., 2019). Nanofluids have higher thermal conductivity, better absorption capacity and wonderful stability (Sheikholeslami et al., 2020). Thus, nanofluids became a most promising way of fluid additives for improving the convective heat transfer rate. The working together of two things to produce an effect greater than the sum of their individual effects is the key to success of nanofluids.

Nanofluids are also important remediation in overcoming the drawback of microchannels flow. Despite of their high heat transfer capabilities, a challenging problem in microchannels is that the higher heat transfer coefficient comes at the cost of greater pressure drop per unit length and hence greater requirement of pumping power in the the microchannel flow geometries (the resistance is increased due to the reduced radius of the channel). That is, high frictional resistance of the coolants due to its compactness and rapid transformation of kinetic energy of the flow to internal energy, leading to high temperature being generated within the fluid (Dewan and Srivastava, 2015). Furthermore, convectional heat transfer fluids such as water, air, oils and ethylene are poor in heat transfer capabilities due to their low thermal conductivity (Kumar et al., 2014). Therefore, with continued miniaturization and increasing heat dissipation in new generations of products, there is a need for intensification of cooling issues in many industries like electronics, transportation, energy supply, defense and medicine.

Nanofluids are being developed in response to these pressing needs for more efficient heat transfer fluids in microchannels in many industries (Das et al., 2008). Such fluids anticipated to have improved heat conduction, diminish the particles settling, therefore, creating nanofluids further secure chill microchannels without blockage owing to their miniature size and diminish the probabilities of surface attrition (zero pressure drop).

According to Dogonchi et al. (2020), apart from higher thermal conductivity, the addition of nano-sized particles over micro-sized particles into conventional base fluid was preferred due to several valid scientific reasons such as longer suspension time (more stable), larger surface area/volume ratio (1000 times, larger), lower erosion and clogging, lower demand for pumping power, reduction in inventory of heat transfer fluid and significant energy saving.

Several authors have attempted to develop convective transport models for nanofluids, among which the Buongiorno's non-homogeneous (two-phase) model and Tiwari and Das homogeneous (single-phase) model are very popular. Buongiorno (2006) developed a complete model of convective heat transport in nanofluids by considering a nanoparticle-fluid relative velocity. Although compared to other solid-liquid mixtures with particles larger than micrometers and millimeters, nanofluids behave more like a fluid, they are essentially two-phase fluids and contain some common characteristics of solid-liquids. The nanoparticles are capable of flowing effortlessly without making any blockage to themselves as they are tiny enough to act likewise to liquid molecules. The nanoparticles absolute velocity can be viewed as the sum of the base fluid velocity and a relative (slip) velocity.

Buongiorno proposed seven slip mechanisms that can produce a relative velocity between the nanoparticles and the base fluid. These are inertia, Brownian diffusion, thermophoresis, diffusiophoresis, Magnus effect, fluid drainage, and gravity. Owing to the small size of nanoparticles, Buongiorno identified that only Brownian diffusion and thermophoresis are the dominant slip mechanisms in nanofluids. Brownian diffusion is the random motion of particles within the base fluid that occurs from the continuous collisions of particles and molecules of base fluid. Thermophoresis is the diffusion of particles from hotter region to colder region under the effect of temperature gradient. It is not a result of thermal convection currents but is due entirely to the presence of a temperature gradient. Based on the experimental results, Buongiorno developed four equations for non-homogeneous (two-phase) model that includes two continuity equations for mass conservation, momentum, and heat energy transport in nanofluids. The momentum equation for nanofluid under boundary layer approximations remained the same as that of base fluid. Only due to the presence of nanoparticles, the Brownian motion and thermophoresis effects were exhibited through the energy and the species concentration equations. The conservation equations for nanofluids with no body forces are given as follows:

Continuity equation for the nanofluid is given by

$$\nabla \cdot U = 0 \tag{1.6}$$

where U is the nanofluid velocity. Equation (1.6) is identical to the continuity equation for a pure incompressible fluid.

The continuity equation for the nanoparticles is given by

$$\frac{\partial \phi}{\partial t} + (U \cdot \nabla)\phi = \frac{-1}{\rho_p} \nabla \cdot J_p \tag{1.7}$$

where t is time, ϕ is nanoparticle volumetric fraction and J_p is the diffusion mass flux for the nanoparticles and represents the nanoparticle flux relative to the nanofluid velocity U. J_p can be written as the sum of only two diffusion terms namely, Brownian diffusion and thermophoresis.

$$J_p = J_{p,B} + J_{p,T} = -\rho_p D_B \nabla \phi - \rho_p \frac{D_T}{T_0} \nabla T \tag{1.8}$$

where D_B and D_T are Brownian diffusion coefficient and thermal diffusion coefficient respectively and T is the nanofluid temperature

Now substituting (1.8) into (1.7), the continuity equation for the nanoparticles becomes

$$\frac{\partial \phi}{\partial t} + (U \cdot \nabla)\phi = \nabla \cdot (D_B \nabla \phi + \frac{D_T}{T_0} \nabla T) \tag{1.9}$$

Equation (1.9) states that the nanoparticles can move homogeneously with the fluid (second term of the left-hand side), and they also possess a slip velocity relatively to the fluid (right-hand side), which is due to Brownian diffusion and thermophoresis.

The momentum equation for the nanofluid with negligible external body forces is given by

$$\rho \left(\frac{\partial U}{\partial t} + (U \cdot \nabla) U \right) = \nabla \cdot \tau_{ij} \tag{1.10}$$

Note that (1.10) is identical to the momentum equation for a pure fluid. The stress tensor,τ_{ij} can be expanded as follows by assuming Newtonian behavior and incompressible flow.

$$\tau_{ij} = -PI + \mu[\nabla \cdot U + (\nabla \cdot U)^{\mathtt{t}}] \tag{1.11}$$

where P is pressure, I is the identity matrix and the superscript $\mathtt{t}$ indicates the transpose of $\nabla \cdot U$. If the dynamic viscosity μ is constant, equation (1.10) becomes the usual Navier-Stokes equations given as follows.

$$\rho\left(\frac{\partial U}{\partial t} + (U \cdot \nabla)U\right) = -\nabla P + \mu \nabla[\nabla \cdot U + (\nabla \cdot U)^{\mathtt{t}}] \tag{1.12}$$

Similarly, the energy equation for nanofluid is given by

$$(\rho C)_{nf}\left(\frac{\partial T}{\partial t} + (U \cdot \nabla)T\right) = \nabla \cdot k\nabla T + (\rho C)_p\left(D_B \nabla\phi \cdot \nabla T + \frac{D_T}{T_0}\nabla T \cdot \nabla T\right) \tag{1.13}$$

where C_{nf} and C_p are the nanofluid specific heat, and the nanoparticle specific heat respectively and k is thermal conductivity of the nanofluid. Equation (1.13) states that heat can be transported in a nanofluid by convection (second term on the left-hand side), by conduction (first term on the right-hand side), and also by virtue of nanoparticle diffusion (second and third terms on the right-hand side). It is important to emphasize that $(\rho C)_{nf}$ is the heat capacity of the nanofluid, and thus already accounts for the sensible heat of the nanoparticles as they move homogeneously with the fluid. Therefore, the last two terms on the right-hand side truly account for the additional contribution associated with the nanoparticle motion relative to the fluid.

Later on, Tiwari and Das (2007) studied the mixed convection of nanofluids in a cavity with moving side walls by neglecting the effect of Brownian motion and thermophoresis instead of the Buongiorno's model. They assumed that the nanofluid flow is single phase and nanoparticles have been dispersed in the base fluid as homogenous. Consequently, the nanofluid may be considered as a conventional homogeneous single-phase fluid with effective physical properties being function of the properties of both constituents and their respective concentrations. An interesting result from such an assumption resides in the fact that an extension from a conventional fluid to a nanofluid appears feasible, and one may expect that the classical theory as developed for conventional single-phase fluids can be then applied to nanofluids as well. Thus, all the equations of conservation (mass, momentum and energy) as well known for single-phase fluids can be directly extended and employed for nanofluids. In the present dissertation, in conjunction with the aforementioned arguments, both the two-phase and the single-phase nanofluid models approaches have been adopted to study the hydrodynamic and thermal behaviors of nanofluids in microchannels.

1.1.4 Mass Transfer and Chemical Reactions

Many convective heat transfer processes often occur in coupling with mass diffusion or mass transfer. Mass transfer is the transport of chemical species in fluids under the influence of concentration gradient. That is, mass transfer is an irreversible process by which an individual chemical species travels from a region where it has high concentration to a region where it has low concentration. From this perspective, mass transfer is analogous to heat transfer as thermal energy diffuses from a region of high temperature to a region of low temperature. Analogously, therefore the diffusional mass flux of a species is directly proportional to its concentration gradient which is known as Fick's law of mass diffusion. The Fick's law states that the time rate of mass transfer per unit area is proportional to concentration gradient of the chemical species. Mathematically,

$$\vec{J} = -D\nabla C \tag{1.14}$$

where $\vec{J}$ is the mass diffusion flux vector, C is the concentration of chemical species and D denotes the proportionality constant known as the diffusion coefficient/convective mass transfer coefficient.

Chemical reaction is a process that leads the conversion of one set of chemical substances to another. The reaction rate or rate of reaction is the time rate at which a chemical reaction takes place, defined as proportional to the increase in the concentration of a product per unit time and to the decrease in the concentration of a reactant per unit time. Chemical reactions are always coupled with mass transfer since the reactants have to travel to the location where the conversion takes place (sink for the reactants) while the products have to travel away (source for the products).

When some external mass is available in the fluid, then the chemical reaction takes place in the flow system which can be of two types: homogeneous and heterogeneous. The former occurs consistently in case of single phase of material such as gas, solid or liquid while the latter takes place when we have two or more than two phases such as liquid and solid or gas and solid. According to Chaudhary and Merkin (1995), homogeneous (bulk) reaction occurs as single phase volume reaction while heterogeneous (surface) reaction occurs at the boundary surface. Common real life applications of homogeneous reaction are the reaction between household gas and oxygen to get the flame.

Chaudhary and Merkin (1995) initially studied simple mathematical model for homogeneous-heterogeneous reactions in boundary layer flow near a stagnation point. They gave the formulation of homogeneous (bulk) reaction by isothermal cubic kinetics and the heterogeneous (surface) reaction by considering the first-order kinetics. Kinetics is a mathematical expression of the correlation between rates and reactant or product concentration.

The isothermal homogeneous reaction is defined as:

$$D + 2E \rightarrow 3E, \ \ \text{rate} = k_1 d e^2 \tag{1.15}$$

while on the catalyst surface we have the single, isothermal, first order reaction:

$$D \rightarrow E, \ \ \text{rate} = k_s d \tag{1.16}$$

where d and e are the concentrations of the species D and E, respectively, and k_1 and k_s are the rate constants.

Recent investigations indicated that industrial fluids may be chemically reactive and chemical reaction may alter diffusion rates. As a consequence, diffusion of species involving chemical reaction finds widespread applications in engineering and industry. Such application areas include pollution studies, oxidation and synthesis of materials, fibrous insulation, processing of food, cooling towers, formation and dispersion of fog, moisture and temperature distributions over agricultural fields (Nayak et al., 2018; Mabood et al., 2018). Therefore, heat and mass transfer problems with a chemical reaction have received a considerable amount of attention in recent years. Fore example, a theoretical study of the combined effects of activation energy and binary chemical reaction in an unsteady mixed convective nanofluid flow with convective boundary conditions was given by Dhlamini et al. (2019). Their study incorporated the influence of the Brownian motion, thermophoresis and viscous dissipation on the velocity of the fluid, temperature of the fluid and concentration of chemical species. The model equations were solved numerically to a high degree of accuracy using the spectral quasilinearization method. Brownian motion was noted as the main process by which the mass was transported out of the boundary layer.

1.1.5 Porous Media and Their Applications

Further augmentation of heat transfer rates in microchannels as well as in heat exchangers can be achieved by the syndication of nanofluids with porous media. According to Mahmoudi et al. (2020) a porous medium is defined as a solid matrix which is characterized by the presence of void spaces called pores which are interconnected by a network of channels where a fluid can move. Usually both the solid matrix and the fluid are assumed to be continuous. Typical examples of natural porous media are rocks, sands, soils, biological tissues like bones, lungs and kidneys. On the other hand, man made materials such as bread, sponges, cements, rubber, foams and ceramics can be considered as porous media (Mahmoudi et al., 2020). Porous media increase the contact surface area between liquid and solid surface so that the fluid flow interruptions are increasing, and therefore, the effective heat transfer rate is enhancing.

The first description of transport phenomena in a porous medium was proposed by Henry

Darcy in 1856 (Whitaker, 1986). He formulated the basic law known as Darcy's law that governs the flow of fluids through porous media on the basis of experimental results on the flow of water through beds of sand. The Darcy law also formed the scientific basis of fluid permeability used in the earth sciences, particularly in hydro-geology. It is analogous to the Fourier's law in the field of heat conduction, Ohm's law in the field of electrical networks and Fick's law in diffusion theory. One application of Darcy's law is to analyze water flow through an aquifer. Darcy's law is also used to describe oil, water, and gas flows through petroleum reservoirs. Darcy studied water flow in the soil environment and found a linear relationship between the macroscopic flow velocity, U and the fluid pressure gradient (resistance produced by solid-fluid interaction) across the medium. Darcy's law is valid to describe flow in saturated porous media at low flow rates ($Re \ll 1$), when the flow rate and the pressure gradient have a linear relationship. This law assumes that viscous forces dominate over inertial forces in porous media and hence, inertial forces can be neglected. Thus, for steady state flow of an incompressible Newtonian fluid through a porous medium, the Darcy's law is given by

$$\nabla P = -\frac{\mu}{K} U \tag{1.17}$$

where U is Darcy velocity, ∇P is the pressure gradient in the direction of flow, K is material conductivity also called Darcy permeability or specific (intrinsic) permeability of the porous medium and μ is dynamic viscosity (Kasaeian et al., 2017; Menni et al., 2018).

Despite these, the Darcy model has got limitations. Among these limitations, the main is that the Darcy model takes into account the frictional force which is offered due to the presence of solid particles to the fluid rather than the boundary and internal effects. That is, the Darcy law neglects inertia and boundary viscous effects which are not significant for a low permeability and when the flow velocity is low. Therefore, the Darcy law does not hold well for high velocity and high permeability flows and hence to overcome these shortcomings of the Darcy law, notable equations have been developed by modifying the Darcy equation which include Forchheimer-Darcy, Brinkman-Darcy, and Darcy-Brinkman-Forchheimer (Amhalhel and Furmanski, 1997). The Brinkman-Darcy model includes the viscous stresses (forces) introduced by solid boundary. The Forchheimer-Darcy model considers nonlinear drag effect (quadratic velocity term) due to interaction of the fluid and the solid matrix, which should be considered when the Reynolds number or permeability is large. In addition, by adjoining the Brinkman-Darcy and the Forchheimer-Darcy models, a generalized Darcy-Brinkman-Forchheimer flow model has been developed.

The Darcy-Brinkman model is given by:

$$\nabla P = -\frac{\mu}{K} U - \mu \nabla^2 U \tag{1.18}$$

The Darcy-Forchheimer model is given by:

$$\nabla P = -\frac{\mu}{K}U - \frac{\rho b}{\sqrt{K}}U^2 \tag{1.19}$$

where ρ is fluid density and b is dimensionless Forchheimer inertial resistance coefficient.

Fluid flows and heat transfers in channels filled with porous media occur in numerous application areas. Such application areas include transpiration cooling, separation processes in chemical industries, filtration, transport processes in aquifers, geothermal extraction, and fiber insulation, crude oil extraction, thermal energy storage, heating and cooling in buildings, underground heat pump systems and solar energy, cooling turbine blades, cooling electronic equipment and combustion systems, heating and drying process, waste treatment, radioactive nuclear waste, solar energy, float glass production, ground water movement, petroleum engineering, geology and geophysics, biomedical sciences and so on (Vafai, 2005; Al-Rashed et al., 2020; Muthamilselvan and Ureshkumar, 2018; Menni et al., 2018; Chamkha et al., 2020).

The major drawback in using microchannels is the dramatic increase of pressure drop which is inversely proportional to the cross-sectional length scale (Pence, 2010). The alleviation for this problem is combining microchannels with porous media to develop a novel design. Similar to microchannels, highly porous structures (sufficiently large pore spaces) feature low-weight, high surface-to volume ratios, and high heat transfer coefficients (Tadrist et al., 2004). Therefore, it is expected that microchannels filled with porous media (micro-porous channels) have thermal properties similar to that of regular microchannels while the pressure drop is lower. Micro-porous channels also have potential applications in filtration, detection of particles, cooling electronic equipment, insulation of buildings, heat and fluid exchange inside human and animal organs (tissue engineering), drying of food, etc (Waghmare et al., 2008). Moreover, such structures have been used in biological and life sciences for analyzing biological materials such as proteins, DNA, cells, embryos, and chemical reagents (Tamayol et al., 2010).

Consequently, the study of fluid flow and heat transfer in microchannels filled with porous media has been receiving prodigious interest by many researchers nowadays. To mention few, Venkateswarlu et al. (2019) examined the influence of thermal radiation and heat generation on steady fully developed hydromagnetic mixed convection flow in a vertical micro-porous-channel with Darcy's law in the presence of the suction/injection. The influence of thermal radiation and heat generation are taken into account. Incorporating the non-dimensional variables, exact analytical solutions for the energy and momentum equations in the presence of velocity slip and temperature jump are obtained. The permeability parameter reduced the fluid velocity at the microchannel walls and enhances the fluid velocity in the central region of the microchannel in presence of suction/injection.

In summary, from the above literature reviews and discussions, it can be ascertained that the analysis of fluids flow and heat transfer phenomena in microchannels, either due to free, forced or mixed convection has been presented. However, limited studies on flows of nanofluids in microchannels have been carried out. Such studies are even scarce in the presence of porous media. Therefore, this dissertation mainly focused on the mathematical investigations of nanofluids flow and heat transfer enhancements due to mixed convection in microchannels filled with porous media.

1.2 Statement of the Problem

The analysis of nanofluids flow and heat transfer either due to free, forced or mixed convection in microchannels have been presented by a significant number of scholars. Fore example very recently, Nayak et al. (2019) presented the investigation of heat transfer and buoyancy-driven convective magnetohydrodynamics (MHD) flow of nanofluids past over a thin needle moving in a parallel stream. The Buongiorno's nanofluid flow model was implemented to study the effects of the Brownian motion and thermophoresis. They considered a transverse magnetic field, variable viscosity, buoyancy, viscous dissipation, Joule heating, heat generation and convective boundary condition. Similarly, Nwaigwe et al. (2019) investigated the heat and mass transfer in a variable viscosity channel flow simultaneously accounting for viscous dissipation, external pollutant injection and Soret-Dufour effects. By adopting the Boussinesq approximation and assuming a fully developed uni-direction flow, they formulated a set of governing equations. Furthermore, Eegunjobi and Makinde (2019) presented the irreversibility analysis and heat transfer in a buoyancy-driven variable viscosity liquid along an inclined heated wall with convective cooling. They assumed that the free surface exchange heat with the environment and nanofluid viscosity is exponentially dependent on temperature.

Prameela et al. (2019) examined steady fully developed hydromagnetic natural convection flow in a vertical microchannel under the influence of heat generation and viscous dissipation. The influence of velocity slip and temperature jump was taken into account. Moreover, Venkateswarlu et al. (2019) presented the study of steady fully developed hydromagnetic mixed convection flow in a vertical micro-porous-channel in presence of suction/injection. The influence of velocity slip, temperature jump, thermal radiation and heat generation was taken into account.

However, limited studies on unsteady, two-phase flows and heat transfer of nanofluids with injection/suction in microchannels. Such studies are even scarce in the presence of porous media with Darcy-Forchheimer model. Therefore, this dissertation mainly focused on the mathematical investigations of the hydrodynamic and thermal behaviours of unsteady mixed convection flows of nanofluids in microchannels filled with porous media.

For fluid flow in microchannels, there always exists high frictional resistance of the coolants leading to generation of high temperature within the fluid and thus, the viscosity of the fluid is assumed to be erratic with temperature (Makinde, 2018). Consequently, temperature dependent variable viscosity was also considered in this study. More specifically, the flow dynamics of nanofluids in microchannels filled with porous media that were investigated in this dissertation include:

1. Unsteady Mixed Convection flow of Variable Viscosity Nanofluid in a Microchannel filled with Porous Medium
2. Modeling Heat Transfer Enhancement of Ferrofluid (Fe_3O_4-H_2O) Flow in a Microchannel filled with a Porous Medium.
3. Unsteady Mixed Convection of a Radiating and Reacting Nanofluid with Variable Properties in a Porous Medium Microchannel.

1.3 Objectives of the Study

1.3.1 General Objective of the Study

The general objective of this study was to present the mathematical investigation of nanofluids flow and heat transfer in microchannels filled with porous media.

1.3.2 Specific Objectives of the Study

The specific objectives of this study were to

1. formulate a mathematical model for unsteady mixed convection flow of variable viscosity nanofluid in a microchannel filled with a porous medium.
2. develop a mathematical model of heat transfer enhancement of ferrofluid (Fe_2O_3-H_2O) flow in a microchannel filled with a porous medium.
3. Formulate a mathematical model of unsteady mixed convection of a radiating and reacting nanofluid with variable properties in a porous medium microchannel.
4. determine the pertinent flow parameters and their effects on the velocity, temperature and concentration profiles as well as on the skin friction coefficient, the wall heat transfer rate and the wall mass transfer rate.

1.4 Significance of the Study

The mathematical modeling and investigations of unsteady nanofluids flow and heat transfer in microchannels filled with porous media have a wide range of attributes in engineering, bio-medicine, industries and applied sciences. Therefore, the following are among the significance of this dissertation.

- The combination of porous media and nanofluids which have high thermal conductivity may result in efficient designs for equipment in the thermal management systems in industries. Therefore, the results obtained in this dissertation can provide insights into designs of small heat exchangers with high efficiency and low cost.
- The study can also serve as a useful tool for heat transfer rate prediction.
- The results that are obtained in this dissertation can fill knowledge gaps in the study of nanofluids flow and heat transfer in microchannels.
- This dissertation can serve as a reference for researchers and other interested people working on nanofluids flow and heat transfer in microchannels filled with porous media.
- This dissertation can be used as a base of ideas that can be extended to different related flow problems. That is, opportunity of extending the study.

1.5 Organization of the Dissertation

This dissertation is divided into seven chapters which were organized as follows:
Chapter 1 provides a general overview of the research context with the descriptions of the background of the study, statement of the problem, objectives of the study, significance of the study, and organization of the dissertation.
Chapter 2 presents review of literature related to the concepts of the dissertation title including heat transfer due to convection, heat transfer due to radiation, flows in microchannels, nanofluids, flows with chemical reactions and flows trough porous media.
Chapter 3 comprises research methodology with the description of formulation of the mathematical models, procedures of numerical solutions and method of result analysis.
Chapter 4 is about an investigation of unsteady mixed convection flow of variable viscosity nanofluid in a microchannel filled with a porous medium. The model takes into consideration the effect of Brownian motion and thermophoresis of the nanoparticles. The nanofluid thermophysical properties are modeled using the Buongiorno's (two-phase) nanofluid models. In addition, the chapter presents the results graphically for velocity, temperature and concentration fields as well as for the skin friction coefficient, local Nusselt number and local Sherwood number of the flow system.
Chapter 5 deals with modeling heat transfer enhancement of ferrofluid ($Fe_3O_4 - H_2O$) in a microchannel filled with a porous medium. The hydrodynamic and thermal behaviors of ferrofluid ($Fe_3O_4 - H_2O$) was investigated using the Tiwari and Das (single-phase) nanofluids

flow model. Discussions for the numerical results were given in detail.
Chapter 6 presents the study of unsteady mixed convection of a radiating and reacting nanofluid with variable properties in a porous medium microchannel. The Buongiorno (two-phase) nanofluids flow model was used to study the effects of the Brownian motion and the thermophoresis of the nanoparticles. Moreover, in this chapter temperature dependent thermal conductivity were considered and convective boundary condition was also taken into account. The numerical results were displayed via graphs for the embedded governing flow parameters. Finally, chapter 7 comprises summary, conclusions, recommendation and suggestions for future researches on the topic.

CHAPTER 2

REVIEW OF RELATED LITERATURE

2.1 Heat Transfer due to Convection

Convection heat transfer is the study of the mechanism of heat transfer process between the layers of a fluid, when the fluid is in motion or between a fluid in motion and a boundary surface in contact with it when they are at different temperatures (Holman, 2010). Moreover, the convective mode of heat transfer is generally divided into two basic processes. If the motion of the fluid arises from external agents such as flows maintained mechanically by pressure drop, mixer, agitator, fan blowing, wind or the motion of heated object itself, then the process is termed as forced convection. On the other hand, if there is no provision of such externally induced force and the flow arises naturally from the effect of a density difference, resulting from a temperature or concentration difference in a body force field such as the gravitation field, then the process is termed as natural or free convection. The density difference gives rise to buoyancy force to which flow is generated.

Mohsan et al. (2019) examined the effects of natural convection flow of viscoelastic polydimethylsiloxane non-Newtonian nanofluid under the impact of nanoparticles of different materials past a vertical cone. Their result indicated that the temperature profile and the rate of heat transfer behave as an increasing function of nanoparticles. It is found that tiny size particles are more efficacious as compared to large particles on the rate of heat transfer and fluid motion.

computational study on a rectangular microchannels heat sink using nanofluids flow for forced convection cooling of electronics device under uniform heat flux condition was carried out by Patel et al. (2019). In their investigation water, ethylene glycol and a mixture of ethylene glycol and water were considered as base fluids with varying concentration of five different nanoparticles including Al_2O_3, TiO_2, CuO, SiO_2 and ZnO. It was noted that with addition of nanoparticles, there is sharp increment in local heat transfer coefficient and decrements in local thermal resistance compared to base fluid but at same time viscosity of fluid increases that provide more drag or pressure drop which ultimately increases the pumping power. $CuO-$Water nanofluid of concentration 1% and 4% give large improvement in heat transfer parameters. Besides, at the same time there was little enhancement in pressure losses or pumping power and also it has less cost and more stability in base fluid as compared to other nanofluids.

In higher-power output devices, the forced convection alone is not sufficient in order to dissipate all the heat and thus combining natural and forced convection (mixed) will usually give desired results (Mahdy and Hoshoudy, 2019). Mixed convection is that type of heat transfer in which there is a noteworthy interaction between free and forced convection with comparable order. Such processes occur when the effects of buoyancy force in forced convection or the effects of forced flow in free convection become significant. The buoyancy forces may aid (aiding or assisting mixed convection) or oppose (opposing mixed convection) the forced flow, causing an increase or decrease in heat transfer rates. The occurrence of mixed convection flow requires the engagement of free and forced convection flows, where either the buoyancy force effect in forced convection or the forced flow effect in free convection happens to be substantial. Commonly, the flow impact of free convection to that of forced convection is measured by buoyancy parameter. The forced convection is dominant when buoyancy parameter declines to zero while free convection is dominant when buoyancy parameter gets larger (Okari et al., 2018).

The phenomenon of mixed convection occurs in several industrial and engineering applications such as cooling of electric devices, heating and cooling of buildings, nuclear reactors cooled during an emergency shutdown, a heat exchanger placed in a low velocity environment, solar collectors, manufacture and extraction of polymer and rubber sheets, paper production, wire drawing and glass fiber production, melt spinning, continuous casting and so on (Jothimani and Vidhya, 2015; El-dawy and Gorla, 2019).

Several authors have studied the problem of mixed convection about different surface geometries. To name some, Maghsoudi and Siavashi (2018) examined the mixed convection heat transfer of $Cu-$water nanofluid inside a two-sided lid-driven cavity saturated with heterogeneous porous media. The two-phase mixture model and Darcy-Brinkman-Forchheimer relation were employed for simulation of nanofluid and fluid flow through porous region, respectively. This examination revealed that the heterogeneity of the porous medium was optimized to reach the maximum heat transfer rate. Besides, Henniche and Ziane (2018) studied mixed convection heat transfer enhancement of laminar unsteady flow in a baffled and asymmetrically heated vertical channel. The numerical solution was done trough finite volume method. They showed that the ratios of mean Nusselt number and friction factor increase with increasing Reynolds number and decrease with increasing Grashof number.

Alkasasbeh et al. (2019) examined the micro-rotation and micro-inertia characteristics of nanofluids over a solid sphere under mixed convection effect. The problem was solved numerically using an implicit finite difference scheme known as Keller box method and consequently, the result indicated that the mixed convection parameter led to an increase of both the local Nusselt number and the local skin friction coefficient. Moreover, Alzgool et al. (2019) conducted a study to develop a numerical solution of heat transfer in magneto-hydrodynamic mixed convection flow of micropolar Casson fluid with thermal radiation about solid sphere. The numerical solution of the finite difference scheme known as the Keller-box method indicated that values of temperature profiles decrease when Casson parameter and mixed convection parameter increase.

Jamaludin et al. (2020) investigated the MHD stagnation point mixed convection flow of Fe_3O_4-water (ferrofluid) over a nonlinearly moving surface. A collocation method, namely the bvp4c function in the MATLAB software used to solve the problem numerically. As a result, the temperature profiles of the ferrofluid decreased with an increase in magnetic parameter, however, they increased with increasing the radiation parameter. Consequently, the rate of convective heat transfer increases as the magnetic parameter increases.

Furthermore, Roy et al. (2020) investigated the influence of the angle of inclination on mixed convection heat transfer from rectangular plate fine array computationally. Their findings showed that an increase in clearance from 0.01 to 0.25 results in an increase of local Nusselt number by as high as 15% near the exit. Increase in Grashoff number by 1.37 times results in enhancement of Nusselt number by a maximum of 25-30%. Around 10% increase in overall value of Nusselt number was observed with an increase in inclination from 30^0 to 60^0.

2.2 Heat Transfer due to Radiation

Due to the diverse applications of heat transfer as a result of radiation, the study of fluids flow with heat and mass transfer in the presence of radiation has attracted the attention of many researchers. For example, Sajid et al. (2018) applied the Darcy-Forchheimer medium model to study the flow of Maxwell nanofluid over a linearly stretching surface. The governing nonlinear partial differential equations (PDEs) with convective boundary conditions were first converted into the nonlinear ordinary differential equations (ODEs) with the help of similarity transformation and then solved with the help of bvp4c. The effects of the independent variables such as variable thermal conductivity, activation energy, nonlinear thermal radiative heat flux, Brownian motion parameter, thermophoresis parameter, Reynolds number, magnetic parameter, Prandtl number, Lewis number, reaction rate constant and Biot number on Nusselt number, velocity, temperature and concentration profile were discussed. Accordingly, the temperature profile has indicated an increasing trend with the thermophoresis parameter, the radiation parameter, the thermal conductivity, porosity parameter and Deborah number. Besides, rising the value of the Biot number resulted in an enhancement in both the velocity and the concentration profiles. It was also seen that both thermophoresis parameter and activation energy parameter has shown an ascending effect on the concentration profile. Moreover, the heat transfer rate has shown a decreasing behavior with an increasing values of the thermal radiation parameter, the variable thermal conductivity parameter and the thermophoresis parameter.

Nilankush (2019) simulated the influence of radiative solar energy on the revolving hybrid nanoliquid flow inside a microchannel. Here, alumina and copper were dispersed into water to frame hybrid nanoliquid where copper was utilized for the usual nanofluid. The nonlinear governing partial differential equations were translated to nonlinear ordinary differential equations and solved via Runge-Kutta fourth order with shooting technique. The outcomes revealed that the solar radiation fosters the heat transport in suction. Hybrid solution exhibited impressive increment in suction even though injection reduced the effect.

Later on, the study of laminar, viscous and incompressible nanofluid flow in a microchannel was given by Sindhu and Gireesha (2021). They considered heat source, thermal heat flux, convective boundary condition and shape effect. The non-dimensional equations were computed by using Runge-Kutta-Fehlberg method. It was obtained that aluminum foam has shown higher thermal field as compared to Al_2O_3 and it was also explored that the entropy generation has been reduced by lowering Eckert number and Grashof number. Furthermore, the results indicated that the temperature distribution was declined with increased values of Biot number. This is because, increment in Biot number results in enhanced convective heat transport and as a result lowering of thermal field take place. In addition to this, it was attained that lowering of Grashof number and Eckert number reduced the entropy of the thermal system.

Matao et al. (2020) also presented the numerical investigation of unsteady MHD mixed convection flow of radiating and chemically reacting fluid past an impulsively started oscillating vertical plate with variable temperature and constant mass diffusion. The transport model employed includes the Hall current and a uniform magnetic field. The Rosseland approximation was used to describe the radiation heat flux in the energy equation. The dimensionless governing system of partial differential equations of the flow has been solved numerically by employing the finite element method. Consequently, it has been found that thermal and mass buoyancy force, Hall parameter, radiation parameter and time tends to accelerate both primary and secondary velocities whereas an increase in Prandtl number, Schmidt number, and chemical reaction parameter tend to decelerate both primary and secondary velocities. These parameters have shown a similar effect on both primary and secondary skin frictions. The fluid temperature was enhanced with increment in radiation parameter and time whereas a reverse trend was noticed with Prandtl number. The fluid concentration was declined with increment in Schmidt number and chemical reaction parameter whereas opposite trend was observed with progression of time.

Madhura et al. (2020) reported the numerical study of the thermal performance of the straight porous fin with temperature-dependent thermal conductivity, radiation, and magnetic field effects. The heat transfer model comprised the Darcy's law for simulating flow with solid-fluid interactions in porous medium, Rosseland approximation for heat transfer through radiation, Maxwell equations for magnetic field effect and linearly varying temperature dependent thermal conductivity. The governing equations were solved numerically by using a finite difference scheme. Thus, the findings pointed out that higher values of the Hartmann number lead to a decrease in the temperature field. In addition, the fin thermal performance was reduced with increasing values of thermophoresis parameter, radiation parameter and Rayleigh number. More importantly, from their experimental analysis, it was clearly noted that due to the presence of a porous medium, fin exhibits 16.95% less heat transfer rate.

Furthermore, a Sisko fluid model with non-uniform sink/source for curved surface was considered by Ali et al. (2020). The chemical processes, radiation and thermophoresis diffusion aspects were also under consideration. Bvp4c scheme was employed for solving the model equations. It was found that radius of curvature and temperature dependent heat sink/source were significantly affected heat and mass transport mechanisms for the curved surface. Brownian motion parameter was served to deteriorate concentration distribution but it was intensified via thermophoresis parameter.

The comprehensive analysis of time-dependent free convection electrically and thermally conducting water-based nanofluid flow containing Copper and Titanium oxide past a moving porous vertical plate was given by Anwar et al. (2020). A uniform transverse magnetic field was imposed perpendicular to the flow direction. Thermal radiation and heat sink terms were included in the energy equation. The Laplace transformation technique was applied to the non-dimensional equations to get the closed form exact solutions. Accordingly, the nanofluid was accelerating with increasing Grashof number and porosity parameter while increasing values of heat sink parameter and Prandtl number dropped the temperature profile.

Yashkun et al. (2020) presented the investigation of heat transfer characteristic of the magnetohydrodynamic (MHD) hybrid nanofluid over the linearly stretching and shrinking surface in the presence of suction and thermal radiation effects. The governing mathematical equations for a single-phase nanofluid model were transformed into pairs of self-similar equations using similarity transformation. Boundary value problem solver (bvp4c) in MATLAB was adopted to solve the system of reduced similarity equations. From their analysis, it was noticed that the efficiency of heat transfer of hybrid nanofluid ($Cu-Al_2O_3/H_2O$) was greater than the nanofluid (Cu/H_2O). Furthermore, it was also found that dual solutions exist for a specific range of the stretching/shrinking parameter with different values of suction and radiation parameters. The results also indicated that the skin friction coefficient and the local Nusselt number increase with suction effect.

Zigita (2020) focused on the theoretical analysis of blood flow in the presence of thermal radiation and chemical reaction under the influence of time dependent magnetic field intensity. The governing non linear partial differential equations of motion, energy and concentration were converted into ordinary differential equations using similarity transformations and then solved numerically by applying ode45. From the simulation, it was obtained that the velocity of blood flow was increased with the increment of both permeability and unsteadiness parameter. Moreover, the temperature of blood was increased at the vessel wall as the Prandtl number and Hartmann number increased. Concentration of blood was decreased as time dependent chemical reaction parameter and Schmidt number increased. The result of the simulation also revealed that as the thermal radiation parameter increased during blood flow in the vessel, there was a significant rise in the blood temperature.

2.3 Flows in Microchannels

For the last four to five decades, with increasing need of energy as well as energy prices, on the other hand, increasing demand for energy saving and reduction of production costs which is also called energy efficiency, many efforts were made by the research community for the improvement of thermal management systems. Accordingly, microchannels are among many alternative methods/techniques that have been recommended to improve the efficiency in industrial equipment, especially in different heat exchangers (Khodabandeh et al., 2018).

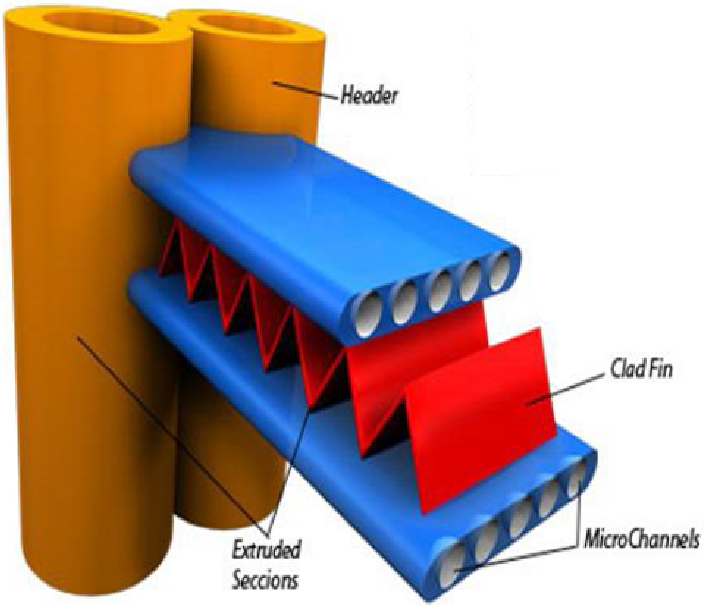

Figure 2.1: Model of a unique microchannel with a superior heat exchange surface (Risto and Zahid, 2009)

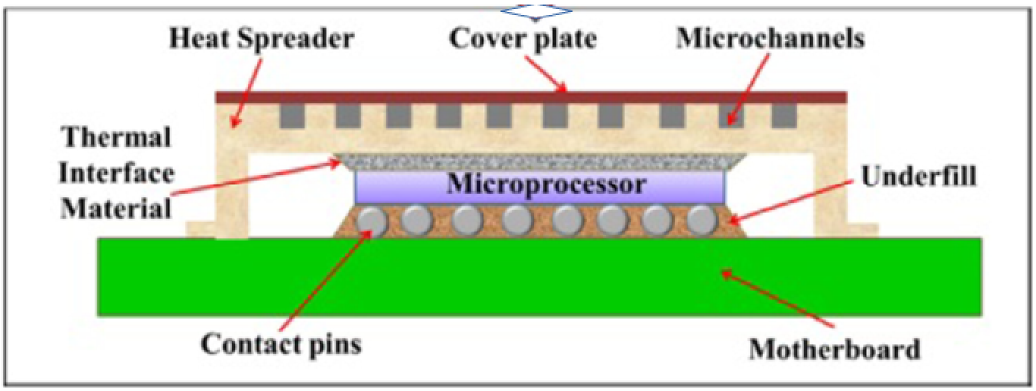

Figure 2.2: Model of a silicon microprocessor cooling system employing microchannels (Lakshmi et al., 2017)

Microchannels which are light in weight, smaller in size handle low amount of coolants and have higher surface area to fluid volume ratio which in turn increases the heat transfer

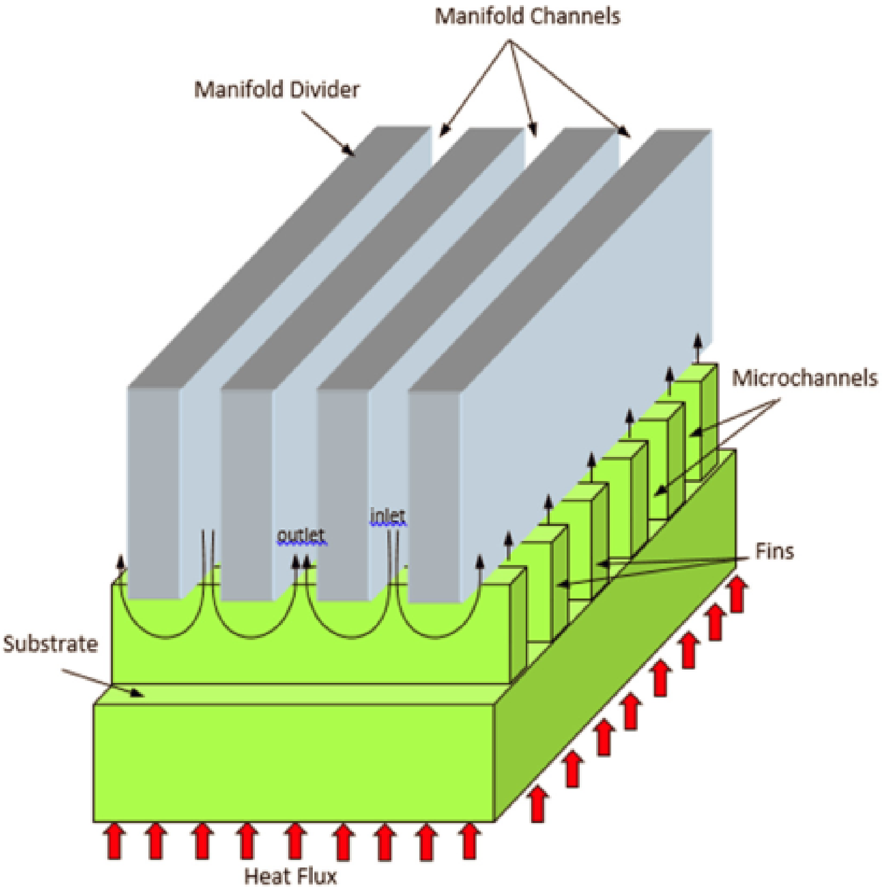

Figure 2.3: Model of manifold microchannel heat sink
(Farzad et al., 2019)

from various modern electronic systems (small electronic components) where higher heat fluxes are encountered. The microchannel has higher heat transfer surface area to fluid volume ratio which in turn increases the heat transfer from small electronic components. The pioneer work in the field of heat transfer using microchannel heat sink for electronic cooling was first time demonstrated by Tuckerman and Pease (1981) by achieving high heat flux removal capacity of up to 800W/cm^2 with microchannels in single-phase and two-phase flows. They noted that as the hydraulic diameter of the channel decreases, the heat transfer coefficient increases. This landmark work paved the door for further research in the area of microchannel heat transfer.

Thereafter, lot of literature have been communicated concerning fluid flow and heat transfer phenomena through microchannels. To mention some, Reddy et al. (2018) investigated the combined effects of wall slip, viscous dissipation, and Joule heating on magnetohydrodynamics (MHD) electro-osmotic peristaltic motion of Casson fluid with heat transfer through a rotating asymmetric microchannel. It is found that Casson fluid velocity, temperature, and heat transfer rate are enhanced with a boost in electro-osmotic force. Furthermore, Kmiotek and Kucab-Pietal (2018) used the finite element method to explain the influence of slim obstacle geometry on the flow and heat transfer in microchannels. The results indicated that microchannels with obstacles exhibit higher heat transfer than the smooth microchannels.

Moreover, the numerical investigation of the unsteady two-dimensional laminar flow of an incompressible, electrically and thermally conducting fluid across the space separated by two infinite rotating permeable walls was presented by Khan et al. (2018). The unsteady system of dimensionless PDEs were solved with the help of finite difference scheme. Later on, Sarkar et al. (2019) investigated the Dual-Phase-Lag and diffusion-thermo effects on time-dependent MHD second-grade double diffusive flow in a fully developed microchannel filled with porous material in the presence of chemical reaction. The governing partial differential equations were solved by using the Laplace transform method and the result indicated that increasing the Dufour number, permeability parameter, Knudsen number increase fluid velocity while magnetic parameter, second-grade parameter and chemical reaction parameter decrease fluid velocity.

Xu et al. (2019) studied the heat transfer of nanofluid flow driven by the movement of channel walls in a microchannel under the effects of the electrical double layer and slippery properties of channel walls using homotopy analysis method (HAM). Consequently, with the increase of the slip-length, the pressure constant of the nanofluid in the horizontal microchannel decreases. The local volumetric entropy generation rate at the upper wall is always higher than that of the lower region. Also, the larger the slip-length is, the lower the total cross-sectional entropy generation rate is when the thermal diffusion is moderate.

Noreen et al. (2019) scrutinized the investigation of the electroosmotic peristaltic pumping of MHD nanofluid in an asymmetric microfluidic channel with zeta potentials. They showed that the fluid velocity increases in the middle section of the channel, with a reduction in the vicinity due to electroosmotic parameter and mobility of the medium. Moreover, the magnitude of axial pressure gradient firstly decreases then increases with the increase of electroosmotic parameter, Hartmann number and mobility of the medium.

Ahadi et al. (2019) presented a detailed computational fluid dynamic evaluation of heat transfer enhancement due to unsteady natural convection in microchannel solar collectors coupled with alumina nanofluid using finite element method. Consequently, they established that the optimal heat removal is achieved at 2% nanoparticle concentration and they also observed that increasing the inclination angle of the microchannel solar collector from 0 to $\frac{\pi}{3}$ decreased the heat removal efficiency.

The experimental and numerical study of the heat transfer enhancement potential of micro-porous channels and nanofluid was given by Delisle et al. (2019). They considered the forced convection and Darcy-Brinkman nanofluid model and the numerical solution was given by the finite element method. It was found that the temperature distribution has optimal results when nanofluid with 0.6% alumina is used. They also showed that the experimental and numerical results were in good agreement with an average relative error of 3.3%, which was determined by analyzing the temperature distribution.

Sharaf et al. (2019) presented the numerical investigation of nanofluid particle migration and convective heat transfer in microchannels. A transient, two-way coupled hybrid Eulerian-Lagrangian model was used to characterize nanofluid flow, heat transfer and particle distribution in a microchannel. According to the results, an increase in Reynolds number Re resulted in a lower bulk fluid temperatures and a corresponding enhancement of convective heat transfer and Nusselt number from channel walls to the fluid due to the larger temperature gradient normal to the channel wall.

Meanwhile, Dong et al. (2020) presented the analysis of mixing enhancement of electroosmotic flow in microchannels via applying direct current and different wave forms of alternating current signal on the electrode plates. The simulation work was performed with finite element method. According to the findings, the vortices generated by the direct current or alternating current field improve significantly the mixing efficiency of different fluids concentration. It was also observed that the mixing efficiency rises with time and then reaches a stable periodic state for mixing efficiently.

Shahrestani et al. (2020) presented the numerical investigation of forced convective heat transfer and performance evaluation of Al_2O_3-water nanofluid flow inside an axisymmetric microchannel. From their results, it was noticed that the expense of increased pressure loss for the increment of the heat transfer coefficient. They also observed that an increase in inlet velocity leads to more viscous dissipation rates and the temperature of the wall grows more intensely compared with the bulk temperature of the fluid.

Convective heat transfer and pressure drop using alumina-water nanofluid under laminar and turbulent flow regimes using the viscous laminar model have been studied by Suniland and Kumar (2019). A circular microchannel heat exchanger (0.1m long and 0.5mm inner diameter) with constant wall temperatures, and 0 to 5% Al_2O_3-water nanofluid flowing inside and cold water flowing outside was used. This experiment showed that convection heat transfer increased remarkably with the increase of nanoparticle concentration under various values of Reynolds numbers. The heat transfer coefficient increased 15% compared to pure water under 5% volume concentration for the laminar regime and 12% for the turbulent zone (Nusselt number decreased about 2.5%).

2.4 Nanofluids

Conventional (common) heat transfer fluids also called base fluids or host fluids such as water, ethylene glycol and oils have limited heat transfer capabilities owing to their low thermal conductivity, whereas metals have much higher thermal conductivity than these fluids. Thus, it is naturally desirable to combine both metals and fluids to produce a medium for heat transfer that would behave like a fluid, but have the thermal conductivity of metals (Irfan et al., 2019). The term nanofluid was coined by Choi (1995) for the first time at Argonne national laboratory, United States of America, to represent an engineered stable colloidal suspension of a small amount usually comprise up to 5% of volume fraction of nanometer-sized particles

$(1-100nm)$ known as nanoparticles within host fluids for effectual heat transfer improvements. Contrary to the milli and micro-sized particle slurries, nanoparticles are relatively close in size to the molecules of the base fluid, and thus can realize very stable suspensions with little gravitational settling over long periods of time. The nanoparticles utilized in nanofluids are mostly formulated from oxides such as alumina, silica, titania and copper oxide, and metals such as copper, ferrous, diamond and gold. Carbides or carbon nanotubes have also been used to realize nanofluids.

Choi's pioneering experiment with nanofluids also showed that nanofluids have new thermal transport phenomena that display remarkable enhancement in thermal properties such as thermal conductivity, dynamic viscosity, convective heat transfer coefficients compared to that of base fluids. The working together of two things to produce an effect greater than the sum of their individual effects is the key to success of nanofluids. Nanofluids have a broad range of engineering applications and used to enhance the heat transfer and energy efficiency in various kinds of thermal systems.

Figure 2.4: Transparent dispersion of 30% alumina nanoparticles in water. Source: (https://www.nanoshel.in/dispersion.html)

Figure 2.5: Nanocopper powder dispersed in water. (Source: https://www.alibaba.com/product-detail/Nano-Copper-Colloidal-Price-5-10nm_62176204863.html)

Nanofluids have large scale utilization, particularly as coolants in industrial and technological processes such as electronic cooling, transportation (engine cooling/vehicle thermal management), space and nuclear system cooling, defense applications (cooling military devices and systems), cooling in chillers and refrigerators, biomedical applications (cancer

Figure 2.6: Ferrofluid/magnetic fluid interacting with a magnet. (Source: `https://www.aliexpress.com/item/4000251927626.html`)

therapy, drug delivery), air conditioning, CPU, micro-elecrto-mechanics (MEMS) etc (Jedi et al., 2020; Subramanian et al., 2020; Ahadi et al., 2019; Mondal et al., 2020).

Consequently, a number of literature has been communicated in line with nanofluid flow and heat transfer phenomena in microchannels. For instance, the influences of the thermophoresis and Brownian motion on magnetohydrodynamics (MHD) electro-osmotic Jeffrey nanofluid peristaltic flow in an asymmetric rotating microchannel was studied by (Reddy et al., 2019). It was observed that the skin friction coefficient and Sherwood number enhance with an increase in the electro-osmosis parameter and the magnetic parameter while opposite trend observed for the Nusselt number.

Moreover, Xu et al. (2019) used the Buongiorno's model to analyze the nanofluid flow in a horizontal microchannel under the effects of electrical double layer together with slip properties of the channel walls using homotopy analysis method (HAM). With the increase of the slip length, the pressure constant of the nanofluid in the horizontal microchannel decreases. Besides, Patel et al. (2019) carried out a computational study on a rectangular microchannels heat sink using nanofluids flow for cooling of electronics device under uniform heat flux condition. It was noted that with addition of nanoparticles there is sharp increment in local heat transfer coefficient and decrements in local thermal resistance compared to base fluid. CuO-Water nanofluid of concentration 1% and 4% give large improvement in heat transfer parameters and at the same time there is little enhancement in pressure losses or pumping power also has less cost and more stability in base fluid as compared to other nanofluids containg nanoparticles such as Al_2O_3, TiO_2, SiO_2 and ZnO.

Niazi and Xu (2020) studied a fully developed steady immiscible flow of nanofluid in a two-layer microchannel in the presence of electro-kinetic effects. The Buongiorno's model was employed for describing the behavior of nanofluids and the HAM was employed for the numerical computation. It was found that the Brownian diffusion, the thermophoresis diffusion, and the viscosity have significant effect on altering the flow behaviors.

Therefore, extensive analysis have been done by a number of researchers to investigate heat and mass transport phenomena accompanied by nanofluids. For example, Mahanthesh et al. (2019) scrutinized the boundary layer transient two-phase flow of dusty nanoliquid on an isothermal plate which is deforming with time-dependent velocity in the presence of exponential heat source. The problem was solved numerically by employing Runge-Kutta-Fehlberg method along with shooting technique. They found that a rise in the magnitude of magnetic parameter, both axial and transverse velocities are diminished while the temperature profiles are enhanced. Moreover, the temperature of nanofluid and dust phases increase with an increase in solid volume fraction of nanoparticle.

Anwar et al. (2019) studied Casson nanofluid boundary layer flow over an inclined extending surface with Soret and Dufour effects numerically by the Keller-Box Scheme. Consequently, the temperature profile increases as the radiations factor increases and the Dufour effect also causes the enhancement in the temperature profile. Besides, the thermophoresis factor increases the temperature profile and decreases the concentration profile. Moreover, Manjunatha et al. (2019) explored the way of heat transfer enhancement by variations in the basic properties of fluids in the presence of free convection and magnetic field with the aid of suspended hybrid nanofluids. The model equations were solved numerically by Runge-Kutta-Fehlberg method. According to the findings, the boundary layer thickness of both hybrid nanofluid and normal nanofluid diminishes due to decrease in variable viscosity. In addition, the fluid flow and temperature of the hybrid nanofluid and normal nanofluid increases as there is a rise in volume fraction.

Besides, Waqas et al. (2020) characterized the Powell-Eyring nanofluid over a stretching surface in the regime of magnetic dipole. The problem was solved numerically via Runge-Kutta with shooting scheme. According to the result, the concentration profile and its corresponding layer thickness enhance for larger thermophoresis parameter but decays for higher estimation of Brownian diffusion parameter.

Furthermore, Ilias et al. (2020) did a theoretical investigation on the unsteady aligned MHD boundary layer flow as well as magnetic nanofluid's heat transfer through an inclined plate with leading edge accretion. The Keller-Box method was used to solve model equations numerically. Their outcomes revealed that the temperature profile decreases with the increase in both magnetic parameter and free convection parameter but the reverse trend was observed for Nusselt number.

Ferrofluids or magnetic nanofluids are among the nanofluids which are usually stable liquids comprising dispersed colloidal magnetic nanoparticles in the carrier base fluids (Vinod et al., 2016). The magnetic nanoparticles in ferrofluids include ferromagnetic metals like Fe, Co, or ferrimagnetic metallic oxides, for example, magnetite (Fe_3O_4), cobalt ferrite $(CoFe_2O_4)$, maghemite (Fe_2O_4). Ferrofluids possess superior heat transfer properties and thus they have wider application areas in engineering and industries like micro-devices cooling, eliminating heat from the loudspeakers voice coil, cooling in aerospace, spinning machinery, generation of thermal power, nuclear reactors cooling, devices of storage, rotors of gas turbine, disk drives of high-speed computer, medical equipment, crystal growth process, and in biomedical applications such as a contrast agent for magnetic resonance imaging (MRI), magnetic drug targeting, and tumor cell hyperthermia (Joshi et al., 2018; Geridonmez, 2020; Ram et al., 2020).

There is a great deal of research studies on the flow of ferrofluids and heat transfer characteristics through different geometries for the last decades. For example, very lately, Dogonchi et al. (2020) presented the analysis of the ferrofluid $(Fe_3O_4 - H_2O)$ natural convection in a triangular annulus numerically by a robust numerical technique based on CVFEM. This numerical scheme is basically a combination of FVM and FEM. The outcomes further illustrate that average Nusselt number raises with rising in heat source/sink parameter, Rayleigh number, radiation parameter and nanoliquid volume fraction parameter and it reduces with magnetic parameter.

Similarly, the numerical investigation of the effect of partial slip on the mixed convection flow of magneto-ferrofluid inside the enclosure is given by Rashad et al. (2020). The numerical and analytical investigation of the flow of Fe_3O_4-water nanofluid through a porous movable surface in a parallel free stream is given by Rashad et al. (2019). Besides, Makinde (2018) studied temporal stability of the stagnation point flow of $Fe_3O_4 - H_2O$ past a permeable stretching/shrinking sheet which is heated convectively. The analysis of water-based ferrofluid $(Fe_3O_4 - H_2O)$ flow and heat transfer through a trapezoidal cavity filled with porous media was done by Khan et al. (2019). Similar studies can be obtained in references (Das et al., 2019; Ilias et al., 2020; Shaw et al., 2018).

2.5 Flows with Chemical Reactions

Heat and mass transfer problems with a chemical reaction have received a considerable amount of attention in recent years. Sujatha et al. (2019) developed a mathematical model to investigate the chemical reaction effects on electrically conducting magnetohydrodynamic (MHD) nanofluid flow over a cone and a wedge. They also considered a nonlinear thermal radiation, viscous dissipation, Joule heating with non-uniform heat source/sink. The transformed governing equations were solved by using shooting technique based on Runge-Kutta fourth order method. Thermal Grashof number and solutal Grashof number declined the temperature profile while radiation parameter, the temperature ratio parameter, heat generation parameter and magnetic parameter encouraged the temperature. It was also revealed that the concentration profile was decreased for larger values of chemical reaction parameter.

In another study, Dhlamini et al. (2019) presented a theoretical study of the combined effects of activation energy and binary chemical reaction in an unsteady mixed convective nanofluid flow with convective boundary conditions. Their study incorporated the influence of the Brownian motion, thermophoresis and viscous dissipation on the velocity of the nanofluid, temperature of the nanofluid and concentration of chemical species. The model equations were solved numerically using the spectral quasi-linearization method. Their investigation reported that unsteady parameter reduced the velocity and temperature of the nanofluid while it increased the concentration of the chemical species. The Eckert and the thermophoresis parameters were found to increase the temperature of the fluid. The activation energy and thermophoresis parameters increased the concentration of the chemical species in the boundary layer while the Brownian motion and the chemical reaction parameters reduced the concentration of the chemical species.

A mathematical model was developed and analyzed by Tarakaramu and Narayana (2019) to study the effect of chemical reaction on bio-convection nanofluid flow between two parallel plates in rotating system with variable viscosity. The governing system of non-linear PDEs was transformed into non-linear ODEs by using suitable similarity variables and then solved by using robust shooting method with the help of bvp4c in MATLAB. The result indicated that the concentration of bio-convection fluid flow was strictly increased with rising values of the chemical reaction parameter. They also found that the mass transfer rate has shown an opposite effect with the chemical reaction parameter and the Schmidt number. The study done by Rasool et al. (2019) was aimed to numerically investigate the Marangoni convective flow of nanoliquid initiated by surface tension and heading towards a radiative Riga surface. The influence of first order chemical reaction was involved in the system with sufficient boundary conditions. Set of governing non-linear PDEs was transformed into nonlinear ODEs using suitable transformations and solved by using the homotopy analysis method (HAM). Following their results, Prandtl number, radiation and thermophoresis parameters were increasing factors for temperature distribution. Moreover, a prominent decreasing behavior was witnessed with elevated values of chemical reaction parameter while the heat flux was enhanced with augmented values of thermophoresis parameter.

Bhandari (2019) examined two-dimensional incompressible magnetohydrodynamics (MHD) flow of a micropolar nanofluid over a stretching sheet in the presence of chemical reactions, radiation and viscous dissipation. A similarity approach was used to transform the original set of PDEs into a set of highly non-linear ODEs in dimensionless form and then solved numerically with the help of the finite element method. Their findings indicated that on increasing the Brownian motion parameter and the chemical reaction parameter, the fluid temperature became higher. Meanwhile, Ramzan et al. (2020) were envisioned a mathematical model that discussed the flow of nanofluid comprising Nickel-Zinc Ferrite-Ethylene glycol ($Ni-ZnFe_2O_4-C_2H_6O_2$) amalgamation past an elongated curved surface with chemical reaction. They considered the impacts of heat generation/absorption and thermal radiation on the flow model. They also considered the slip and the convective boundary conditions. The governing system was solved numerically by applying bvp4c solver that is MATLAB build-in function. Consequently, it was comprehended that the concentration field declined for both homogeneous and heterogeneous reaction parameters.

Zuhra et al. (2020) constructed a mathematical model to analyze the simultaneous flow and heat transfer of two nanoliquids (Casson and Williamson) in the presence of gyrotactic microorganisms and cubic autocatalysis chemical reaction through a porous medium under the potentiality of buoyancy forces. Heterogeneous reaction existing on the surface was described by isothermal cubic autocatalytic chemical reaction whereas homogeneous reaction was taking place at far field described by first-order kinetics. Similarity transformations were used to get ODEs from the governing PDEs which were solved via homotopy analysis method (HAM). The result revealed that the velocity increased with the Weissenberg parameter but decreased with the Casson nanofluid parameter in the presence of magnetic field and porous medium. The temperature profile decreased with high values of slip condition. Besides, the dual behavior of concentration profile for the strength of homogeneous reaction parameter was observed. Moreover, flow of microorganisms was decreased based on the parameters of porous medium, magnetic field, and heterogeneous reaction.

Very recently, Khan et al. (2021) investigated the distribution of heat transmission for chemically reactive nanofluid flow past a thin moving needle. The needle was placed horizontally in nanofluid with an application of hall current and viscous dissipation. The popular Buongiorno model was employed in order to explore the impact of Brownian and thermophoretic forces exerted by the fluid. The governing PDEs were converted into ODEs by using a suitable group of similarity variables and then solved by employing homotopy analysis method (HAM). The result established that the flow of nanoluid was reduced with growth in magnetic effects and volume fractions of nanoparticles. Thermal characteristics were increased with augmentation of Eckert number, magnetic field, volume fractions of nanoparticles, Brownian motion parameter but declined with increased values of Prandtl number. Moreover, concentration of nanoparticles was reduced with corresponding growth in Lewis number and thermophoresis and chemical reaction parameters while increased with growth in Brownian motion parameter.

Similarly, investigation of heat and mass transfer characteristics of mixed convective flow of an electrically conducting nanofluid past a slender riga plate in the presence of viscous dissipation and chemical reaction with convective boundary conditions was given by Vaidya et al. (2021). The thermophoretic and Brownian motion aspects for nanoliquid were proposed using Buongiorno's relations. The similarity quantities were utilized to obtain the dimensionless forms of flow field equations. The resulting coupled non-linear ODEs associated with the constituted boundary conditions were solved via optimal homotopy analysis method (OHAM). Their results pointed out that the enhancement of the concentration buoyancy parameter resulted in the reduced velocity profiles while temperature profiles enhanced for higher values of the viscous dissipation parameter. Temperature distribution showed an improvement for the Brownian motion and thermophoresis parameters whereas the concentration profile showed a decreasing pattern for higher values of chemical reaction parameter.

2.6 Flows Through Porous Media

Whitaker (1986) discovered that the area-averaged fluid velocity flowing through a column in porous material is proportional to the pressure and inversely proportional to the viscosity (μ) of the fluid seeping through the porous material, which is known as the Darcy's law. The convection of heat in porous materials have distinguished structural properties such as high thermal conductivity, low density and large contact surface area with fluid per unit volume which can enhance the heat transfer effect. The increased surface area and passage due to internal structure of the porous helps dynamic mixing of a moving fluid inside the porous which results in a significant increase in the loss of fluid pressure and fluid pumping power (Sharma et al., 2018). Therefore, convection heat transfer and fluid flow through porous media is a phenomenon of great interest from both theoretical and practical point of view because of its applications across a wide range of disciplines from mechanical, civil, environmental, chemical and petroleum engineering to agricultural, food, material and biomedical science.

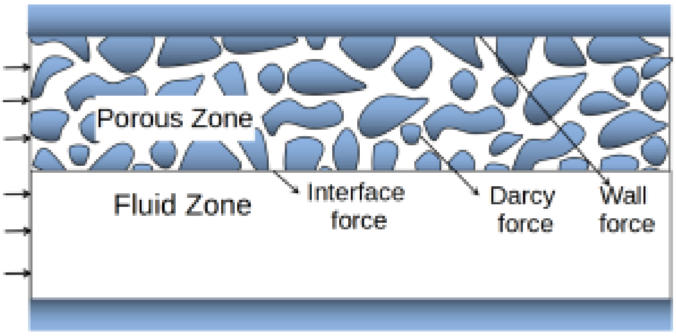

Figure 2.7: Illustration of forces of flow through porous media
(Li et al., 2020)

Owing to these stimulating benefits, a large number of researches in the scientific community are being carried out with the porous media. To list some, the slip flow in porous medium of micropolar fluid in a rectangular microchannel under the effect of a magnetic field was investigated by Agoor (2018). The system of differential equations were solved analytically by utilizing Fourier series. According to his findings, the velocity and microrotation were decreasing with the increase in the value of Hartman number while the volumetric flow rate was increasing with the increase in Hartman number. The increasing of porous parameter acted to increase the velocity but decreased the volumetric flow rate.

Similarly, Rashad et al. (2018) presented the investigation of partial slip and MHD combined convection flow of $Cu-$water nanofluid and heat transfer characteristics through a lid-driven porous enclosure. Moreover, the study of the stagnation point flow of nanofluid past a stretching sheet with a porous medium in the presence of heat generation is given by Sedighi et al. (2018). Later on, Nabway et al. (2019) studied mixed bioconvective flow of a nanofluid past over a wedge with a porous medium. Besides, Nwaigwe et al. (2019) investigated the heat and mass transfer in a variable viscosity channel flow simultaneously accounting for viscous dissipation, external pollutant injection and Soret-Dufour effects. Semi-implicit finite difference scheme was adopted for the numerical solution and they depicted that the velocity and temperature profiles decrease as the Darcy number increase.

Khan et al. (2019) investigated the thermal management and heat transfer augmentation of water based ferrofluid in an enclosed partially heated trapezoidal cavity filled with a porous medium. The numerical solutions are reported using finite element Galerkin method. It is demonstrated that the magnetic field, thermal buoyancy, porous medium permeability and the length of the heating element play a crucial role in the enhancement of dimensionless average heat transfer rate. Furthermore, the MHD peristaltic motion of Bingham fluid through a uniform channel under the influence of long wavelength and small Reynolds number was examined by Vaidya et al. (2020). They showed that magnetic parameter decreases velocity and temperature profiles but the temperature profile increases with an increase in the value of variable thermal conductivity.

Meanwhile, Yadav (2020) explored the combined effect of the internal heating and the variable gravity field on the beginning of buoyancy-driven convection in a nanofluid saturated an isotropic porous medium layer. The numerical solution of the governing equations was presented using higher order Galerkin method. The result indicated that the nanoparticle Rayleigh-Darcy number and the modified diffusivity ratio, and the modified nanofluid Lewis number were found to quick the onset of convection.

Akinshilo et al. (2020) investigated the effects of heat transfer and flow of electrically conducting magnetohydrodynamic nanofluid through a diverging or converging channel with porous medium considering internally generated heat. The homotopy perturbation method is utilized as a suitable numerical method of solution. It is seen that high Reynolds number enhances the fluid viscosity while decreases velocity. Similarly, heat transfer reduces at high Darcy's number owing to decreased flow consequently internal friction reduces. Moreover, Hayat and Alsaedi (2020) addressed the analysis of the mixed convective and flow of viscous fluids induced by a nonlinear inclined stretching surface. Heat and mass transfer phenomena were analyzed with additional effects of heat generation/absorption and activation energy. The nonlinear Darcy-Forchheimer relation was deliberated. The dimensionless problem was obtained through appropriate transformations and convergent series solutions were obtained by utilizing an optimal homotopic analysis method (OHAM). Enhancement in the velocity was observed through the local mixed convection parameter while an opposite trend of the concentration field was noted for the chemical reaction rate parameter. In addition, the Forchheimer number showed a retaerding effect on the velocity profile.

Rasool et al. (2020) investigated the consequences of binary chemical reaction, thermal radiation, and Soret-Dufour effects on a steady incompressible Darcy-Forchheimer flow of nanofluids. They considered the effects of Brownian motion and thermophoresis. The governing highly nonlinear system of equations which were advanced version of Navier-Stokes equations, were transformed into ordinary differential equations (ODEs) using appropriately adjusted transformations and then solved numerically using RK45 in connection with shooting technique. According to their findings, a rise of temperature field was observed with increasing values of thermal radiation parameter. Besides, a clear decline was noticed in velocity field for elevated values of Forchheimer number and porosity factor. The Dufour effect anticipated a rising factor for temperature distribution and the same was noticed for concentration distribution for increased values of Soret effect. The outcome also revealed that thermal radiation and binary chemical reaction had shown strong impact on heat transport rate.

Moreover, Yusuf et al. (2020) conducted a research to investigate the slip effect and to analyze entropy production in both hybrid nanofluids, and common nanofluids flow past a convectively heated three-dimensional stretching sheet placed in a porous medium. The slip flow was considered in a Darcy-Forchheimer's scheme by incorporating the nonlinear thermal radiation. Water was taken as base fluid, while Copper and Titanium dioxide nanoparticles were considered. The governing models were over-set into dimensionless variables using similarity transformation and then solved numerically. The results communicated that temperature was enhanced with porosity, whereas velocity was found to be decelerated. It was also seen that, Bejan number was decreasing with an increase in the nanoparticle volume fraction of nanoparticles. Furthermore, hybrid nanofluids generated less entropy than common nanofluids.

Roja et al. (2021) presented a numerical study on irreversibility investigation of Casson fluid flow in an inclined microchannel subject to a Darcy-Forchheimer porous medium. The governing partial differential equations were transformed into ordinary differential equations by using appropriate similarity transformat and then solved by the fourth-fifth order Runge-Kutta-Fehlberg method along with the shooting technique. From the perspective of numerical results, it was recognized that the production of entropy can be improved with the Joule heating, viscous dissipation, and convective heating aspects. It was concluded that the production of entropy was the maximum with increased values of the Casson parameter, the angle of inclination and the Hartmann number. Besides, both the Reynolds number and the radiation parameter caused the dual impact on entropy generation.

In addition, Aghamiri et al. (2021) investigated the forced convection of two-phase Ferronanofluid flow in a completely porous microchannel containing rotating cylinders. The results showed that increasing the Reynolds number and volume fraction of nanoparticles increased the heat transfer, pressure drop, and coefficient of friction. By comparing the porosity percentages with each other, it was also noticed that increasing the Reynolds number reduced the entropy generation due to heat transfer and increased the entropy generation due to friction. On the other hand, increasing the volume fraction of nanoparticles increasesd the entropy generations due to heat transfer and friction.

Raizah and Aly (2021) simulated natural convection flow resulting from heat partitions in an H-shaped enclosure filled with a nanofluid. The right area of the H-shaped enclosure was saturated with non-Darcy porous media. The center variable partitions of the H-shaped enclosure walls were kept at a high-temperature while the left and right walls of the H-shaped enclosure were positioned at a low temperature. The performed simulations proofed that the length of the heated partitions augments the velocity field and temperature distributions in an H-shaped enclosure. Rayleigh number raised the fluid velocity and heat transfer in an H-shaped enclosure. The porous layer on the right side of the H-shaped enclosure at a lower Darcy parameter caused a high resistance force for the fluid flow and heat transfer characteristic inside an H-shaped enclosure. Moreover, the added nanoparticles reduces the velocity field and enhances the heat transfer inside an H-shaped enclosure.

Similarly, Rundora and Makinde (2018) studied the unsteady reactive flow and heat transfer properties between two uniformly porous plates with suction/injection under the influence of constant pressure gradient, convective cooling, and buoyancy force. The coupled nonlinear partial differential equations for momentum and energy balance were numerically solved using a semi-discretization finite difference method coupled with a fourth order Runge-Kutta-Fehlberg integration scheme. From their results, it can be noticed that the skin friction is increased significantly by the variable viscosity parameter, buoyancy parameter, Eckert number, and suction/injection Reynolds number whereas the porous medium shape factor parameter reduces skin friction. Moreover, the buoyancy parameter, Eckert number and variable viscosity parameter were observed to increase the wall heat transfer rate.

Similarly, Endalew et al. (2018) investigated the dual phase lag heat transfer effect on MHD second grade fluid flow in fully developed microchannel filled with porous material. The governing equations of fluid velocity and temperature were solved using Laplace transform Method. The result indicated that as the second grade parameter increases, fluid velocity diminishes in the all fluid flow domain but it increases as the Darcy number increases. It is also noticed that for the smaller time, the fluid velocity and fluid temperature diminish as thermal relaxation time increases but for the larger time, the fluid velocity increases but fluid temperature attains steady state as thermal retardation time increases.

Furthermore, Shashikumar et al. (2018) considered the heat transfer and entropy generation in MHD flow of Casson fluid through a porous microchannel with thermal radiation and they investigated numerically by using fourth-fifth-order Runge-Kutta integration method along with shooting technique. Based on the numerical results, it was seen that the velocity profile increases for increasing values of slip parameter, Hartmann number and Casson parameter. The result also revealed that as the Casson fluid parameter, Eckert number and Prandtl number increase, the temperature within the microchannel increases.

Moreover, the analysis of entropy generation and heat transport of magnetohydrodynamics (MHD) Casson fluid flow with viscous and Joule heating in an inclined porous microchannel were presented by Gireesha et al. (2019). The numerical simulation for the model problem was given through Runge-Kutta-Felhberg with shooting technique. It was established that the greater values of Grashof number, heat source parameter, and Casson fluid parameter increase the velocity and temperature profiles. Velocity and temperature profiles decrease with increasing values of magnetic parameter,and permeability parameter in the microchannel.

Besides, the investigation of the fully developed laminar flow of a viscous incompressible and electrically conducting fluid in an inclined micro-porous-channel was given by Aina and Malgwi (2019). The governing equations were solved analytically and the injecting through the micro-porous channel thickens the thermal boundary layer, resulting to weakening the convective current and consequently decreasing the fluid velocity whereas suction weakens the thermal boundary layer yielding an increase in fluid velocity. It was also seen that injection thickens the thermal boundary layer, thereby weakening the convective current and consequently decreasing fluid velocity whereas suction weakens the thermal boundary layer yielding an increase in fluid velocity.

CHAPTER 3

RESEARCH METHODOLOGY

The study in this dissertation is an explanatory type of research and hence, devoted to the mathematical investigation of nanofluids flow and heat transfer in microchannels filled with porous media. Therefore, formulation of the mathematical models, procedures of the numerical solutions and method of sults reanalysis are discussed in detail as follows.

3.1 Formulation of the Mathematical Models

The continuum hypothesis was assumed in the formulation of the model problems. Moreover, the conservation law of mass/matter, conservation of momentum (Newton's second law of motion), conservation of energy (first law of thermodynamics) and the law of mass balance respectively were used in deriving the continuity, momentum, energy, and species concentration equations. These governing models equations were highly non-linear partial differential equations of initial boundary value problems (IBVPs). The initial and boundary conditions were also determined. Then the non-dimensional form of the governing models equations of initial boundary value problems (IBVPs) were formulated.

3.2 Procedures of the Numerical Solutions

The numerical approach namely the semi-discretization scheme also known as the method of lines was employed to transform the non-dimensionalized initial boundary value problems (IBVPs) into initial value problems (IVPs). Thereafter, the well known fourth order Runge-Kutta integration scheme (which is numerically stable and of fourth order accuracy) was utilized in solving the obtained initial value problems (IVPs). The computational algorithms were implemented in a computer using the MAPLE symbolic package. In the following subsections, brief explanations of these methods are given.

3.2.1 The Semi-Discretization Method (Method of Lines)

Partial differential equations (PDEs) arise in the mathematical modeling of chemical, biological, physical and engineering problems which include applications in chemical kinetics, heat and mass transfer in fluid dynamics, hydrology, electromagnetism, astrophysics and so on. This is due in large part to the three dimensional form of our physical world, and its variation with time. Thus, PDE models have at least four independent variables, that is, three spatial dimensions and time. Such PDE models are usually highly non-linear and therefore require numerical methods and computer based solution techniques (Schiesser, 2016).

To this end, several numerical methods have been developed and the choice of the method is dependent on the desired accuracy, as well as concerns about the stability and robustness of the system, while maintaining computational efficiency (Schiesser, 2017). A well known approach in the numerical solution of evolutionary problems in time dependent PDE models in fluid dynamics is the so called semi-discretization method also known as method of lines (MOL). The numerical method of lines (MOL) is a comprehensive approach to the solution of time dependent PDE models that basically proceeds in two steps namely the space discretization and the time integration. This version is also known as the vertical method of lines which is discrete in space and continuous in time. The basic idea behind MOL is to discretize along the spatial coordinates only and that is why the approximation is called semi-discretization.

Moreover, the convergence, stability and consistency of the MOL implemented in this dissertation for tackling parabolic PDEs are already published in the literature (Zafarullah, 1970; Verwer and Sanz-Serna, 1984). Discretizing the PDEs in space and leaving time continuous leads to a system of ordinary differential equations (ODEs). That is, in the space discretization, the spatial derivatives are first approximated using finite differences, finite elements, finite volumes, spectral techniques, or collocation method in such a way that the PDEs (IBVPs) are transformed into a system of ODEs (IVPs) corresponding to the solution at some grid points as a function of time (Hamdi and Griffiths, 2009). The time t is then the independent variable of the resulting semi-discrete system of ODEs. The assumption is that the ODEs are easier to analyze and solve as compared to the PDEs and indeed, one of the salient features of this method is the use of existing and generally well established numerical methods for ODEs (IVPs).

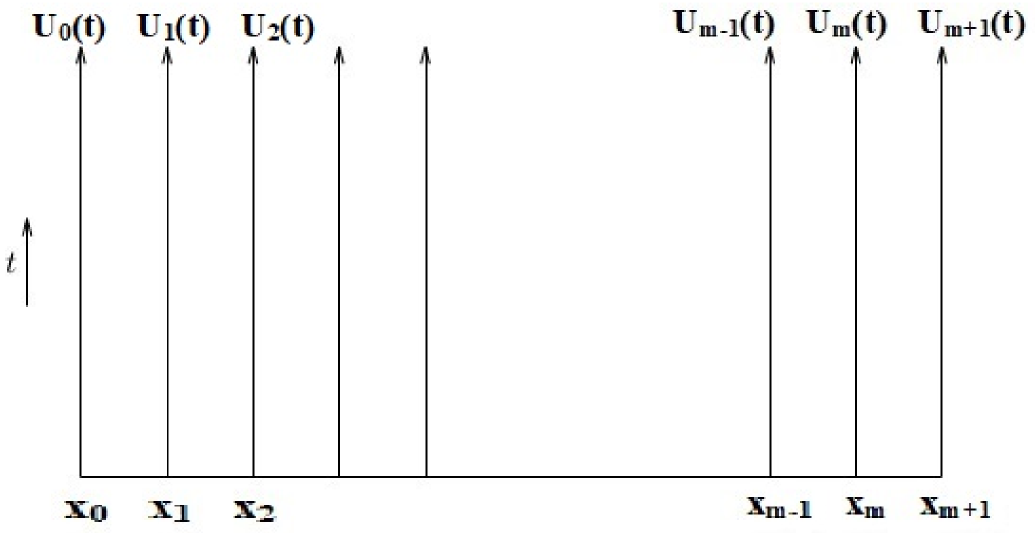

Figure 3.1: MOL: $U_i(t)$ is the solution along the line forward in time at the grid point x_i

A method of line obtained with finite differences is easiest to apply and hence it was used exclusively in this research study. Once the PDEs (IBVPs) are transformed into ODEs (IVPs), the spatial derivatives are no longer stated explicitly in terms of the spatial independent variables and thus in effect only the initial value variable time in a physical problem remains. In other words, with only one remaining independent variable time t, it is a system of ODEs (IVPs) that approximate the original PDEs (IBVPs). From the literature, the references (Roknujjaman and Asaduzzaman, 2018; Cortés-Molina et al., 2018; Rundora and Makinde, 2018; Makinde and Rundora, 2017; Ali, 2021) employed the MOL to study fluids flow and heat transfer characteristics.

To illustrate this method, consider the PDE of heat diffusion equation.

$$\frac{\partial u}{\partial t} = \frac{\partial^2 u}{\partial x^2} \tag{3.1}$$

with initial and boundary conditions

$$u(x,0) = f(x), u(0,t) = g_0(t), u(1,t) = g_1(t) \text{ for } t > 0 \text{ and } 0 \leq x \leq 1 \tag{3.2}$$

Now, divide the space variable x into m equal sub-intervals $[x_i, x_{i+1}]$ of mesh size h where $i = 0, 1, 2, ..., m$. Also, the function $U_i(t)$ is approximated as $U_i(t) \approx u(t, x_i)$. Then discretizing the heat diffusion equation (3.1) by using the second-order central differences in space at grid points x_i gives

$$\frac{d}{dt}U_i(t) = \frac{U_{i-1}(t) - 2U_i(t) + U_{i+1}(t)}{h^2}, \text{ for } i = 1, 2, ..., m \tag{3.3}$$

Expanding (3.3) for $i = 1, 2, ..., m$ yields the following system of equations.

$$\begin{aligned}
\frac{d}{dt}U_1(t) &= \frac{u_0(t) - 2U_1(t) + U_2(t)}{h^2}, \text{ for } i = 1 \\
\frac{d}{dt}U_2(t) &= \frac{U_1(t) - 2U_2(t) + U_3(t)}{h^2}, \text{ for } i = 2 \\
&\cdot \\
&\cdot \\
&\cdot \\
\frac{d}{dt}U_m(t) &= \frac{U_{m-1}(t) - 2U_m(t) + U_{m+1}(t)}{h^2}, \text{ for } i = m
\end{aligned} \tag{3.4}$$

Equation (3.4) is a coupled system of m ODEs for the variables $U_i(t)$, which vary continuously in time along the lines shown in figure 3.1 that can also be written in a matrix form as follows:

$$U_i'(t) = \mathbf{A}U_i(t) + g(t) \tag{3.5}$$

where **A** is a tridiagonal matrix and $g(t)$ includes the terms of the boundary conditions given as follows:

$$U_0(t) = g_0(t) \text{ and } U_{m+1}(t) = g_1(t) \tag{3.6}$$

$$\mathbf{A} = \frac{1}{h^2}\begin{bmatrix} -2 & 1 & 0 & & & \\ 1 & -2 & 1 & & & \\ & 1 & -2 & 1 & & \\ & & \ddots & \ddots & \ddots & \\ & & & 1 & -2 & 1 \\ & & & & 1 & -2 \end{bmatrix}, \quad g(t) = \frac{1}{h^2}\begin{bmatrix} g_0(t) \\ 0 \\ 0 \\ \vdots \\ 0 \\ g_1(t) \end{bmatrix} \tag{3.7}$$

Therefore, (3.5) is a semi-discretized form of equation (3.1) which can be solved using any standard method for solving IVPs. Indeed, in this dissertation the obtained IVPs were numerically solved by using the well known fourth order Runge-Kutta integration scheme.

3.2.2 Runge-Kutta Order Four Method

The most famous Runge-Kutta method which is widely used is that of forth order. That is, the local truncation error for this method is of order $O(h^4)$ provided that the solution has five continuous derivatives. The approximation to the solution of the IVP, (3.5) using the Runge-Kutta order four scheme is given as follows:

$$U_{i+1} = U_i + \frac{1}{6}\left(k_1 + 2k_2 + 2k_3 + k_4\right), \text{for } i = 0, 1..., m. \tag{3.8}$$

where

$$\left.\begin{aligned} k_1 &= hf(t_i, U_i) \\ k_2 &= hf(t_i + \tfrac{h}{2}, U_i + \tfrac{k_1}{2}) \\ k_3 &= hf(t_i + \tfrac{h}{2}, U_i + \tfrac{k_2}{2}) \\ k_4 &= hf(t_i + h, U_i + k_3) \end{aligned}\right\} \tag{3.9}$$

The Runge-Kutta order four scheme is based on finding the solutions in such a way that the value of U_{i+1} at the point x_{i+1} can be obtained from the known value of U_i at the point x_i. Here $h = x_{i+1} - x_i$ is the step size.

3.3 Method of Results Analysis

The entire computational algorithms evolved from this research works were implemented using MAPLE symbolic software. The quantitative analysis of this study was given in which the numerical solutions were displayed via graphs for each embedded parameters. Furthermore, the qualitative analysis for the physical meaning interpretation for each graph was established in detail. That is, reasons for the obtained numerical results in line with the effects of each embedded governing flow parameters on the velocity, temperature and concentration as well as on the physical quantities of engineering interests namely skin friction coefficient, local Nusselt number and local Sherwood number were justified in detail. The results were also compared with that of the existing literature.

CHAPTER 4

UNSTEADY MIXED CONVECTION FLOW OF VARIABLE VISCOSITY NANOFLUID IN A MICROCHANNEL FILLED WITH A POROUS MEDIUM

This chapter focuses on the mathematical investigation of unsteady flow of variable viscosity nanofluid through a microchannel filled with a saturated porous medium. The Buongiorno nanofluid flow model is used to study the Brownian diffusion and thermophoresis of nanoparticles.

4.1 Mathematical Model Formulation

Consider an unsteady mixed convective flow of Newtonian fluid in a microchannel filled with a saturated porous medium. The microchannel was assumed to have permeable walls placed at $y = 0$ and $y = a$ as shown in figure 4.1, where a denotes the distance between the two walls. It was also assumed that the flow is driven by the combined actions of axial pressure gradient together with fluid body forces due to solutal and thermal buoyancy variations. Furthermore, a nanofluid injection into the microchannel took place through the left wall ($y = 0$) while a nanofluid suction out of the microchannel occurs at the right wall ($y = a$).

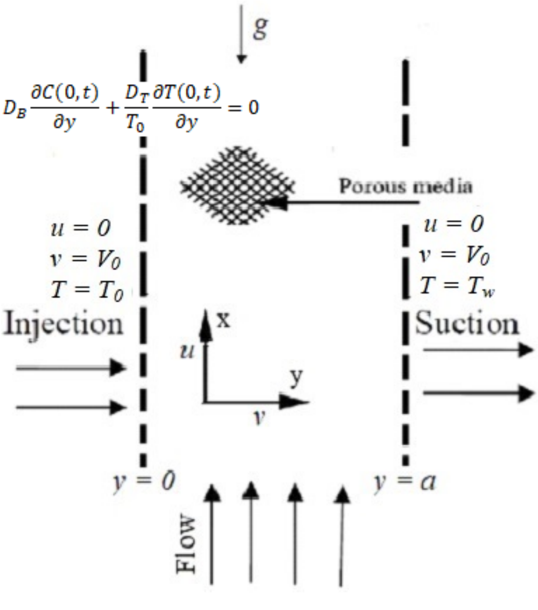

Figure 4.1: Physical flow model and coordinate system

At time $t = 0$, the fluid temperature was maintained at T_0 and the fluid was in the static position. For large time ($t > 0$), the flow occurred only when the nanofluid started to move with the time within the microchannel flow regime. Also no-slip conditions were imposed for axial velocity at the walls, and temperatures at the walls were taken to be non-uniform where the left microchannel wall was placed at temperature T_0 while the right wall was placed at temperature T_w such that $T_0 < T_w$. Both the temperature and concentration were initially zero within the fluid except at the walls where the constant values were maintained.

The nanofluid dynamic viscosity was assumed to be an exponential decreasing function of temperature and hence given as $\mu(T) = \mu_0 \, e^{-\gamma_1 (T - T_0)}$ where γ_1 is a viscosity variation parameter and μ_0 is the dynamic viscosity at the left wall of the microchannel. Moreover, the nanofluid was supposed to move through the control volume and across the control bounding surface. Besides, the governing partial differential equations for continuity, momentum, energy and chemical species concentration were formulated under the following assumptions.

(i) The microchannel was assumed to have permeable walls with non-uniform temperatures.

(ii) The porous media was assumed to be saturated, homogeneous and isotropic.

(iii) The nanofluid flow was a two-dimensional unsteady laminar flow, which satisfies the no-slip boundary condition.

(iv) The interaction between the porous medium and contacting fluid was formulated using the Darcy-Forchheimer model.

(v) The nanofluid dynamic viscosity was assumed to be temperature dependent.

(vi) The nanofluid injection/suction with constant velocity V_0 at the microchannel walls was also assumed.

4.1.1 Equation of Continuity: The Mass Conservation Law

To derive the governing equations, a finite control volume V of arbitrary shape of finite size was considered, which was fixed in space where there is no sources/sinks through which the fluid can enter or leave the control volume.

Let $\vec{n}$ be the unit vector normal to a surface element dS of S drawn outwards as indicated in figure 4.2. Let the velocity of the nanofluid be $U = (u, v, 0) = (u, V_0, 0)$, the y-component velocity is taken to be $v = V_0$ since it is assumed that the nanofluid injection/suction at the micro channel walls with constant velocity V_0. Let ρ be the density of the nanofluid contained in a control volume V. For small mass dm we have $dm = \rho dV$ since $m = \rho V$. So the total mass in the control volume V is given by

$$m = \int_V dm = \int_V \rho dV \tag{4.1}$$

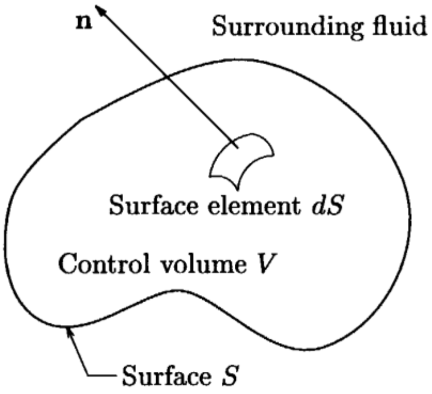

Figure 4.2: Finite control volume in a flow field.

From the conservation law of matter it is evident fact that the mass of a nanofluid in a volume containing the same particles all the time (no sources or sinks) is constant. That is, the time rate of change of mass of a nanofluid in a volume containing the same particles is zero. Thus,

$$\frac{dm}{dt} = \frac{d}{dt}\int_V \rho dV = 0 \tag{4.2}$$

But

$$\begin{aligned} \frac{d}{dt}\int_V \rho dV &= \int_V \frac{\partial \rho}{\partial t} dV + \int_S \rho(U\cdot\vec{n})dS, \text{ by the Reynolds transport theorem.} \\ &= \int_V \frac{\partial \rho}{\partial t} dV + \int_V \nabla\cdot(\rho U)dV, \text{ by the Gauss divergence theorem.} \\ &= \int_V \left(\frac{\partial \rho}{\partial t} + \nabla\cdot(\rho U)\right)dV \end{aligned}$$

Hence, (4.2) becomes

$$\int_V \left(\frac{\partial \rho}{\partial t} + \nabla\cdot(\rho U)\right)dV = 0 \tag{4.3}$$

Since the volume V is arbitrary, from (4.3) we write

$$\frac{\partial \rho}{\partial t} + \nabla\cdot(\rho U) = 0 \tag{4.4}$$

and thus, (4.4) is called continuity equation. But using the property of divergence $(\nabla\cdot)$ from vector calculus, we have

$$\nabla\cdot(\rho U) = \rho(\nabla\cdot U) + \nabla\rho\cdot U \tag{4.5}$$

Then, using (4.5), the equation of continuity (4.4) becomes

$$\frac{\partial \rho}{\partial t} + \rho(\nabla\cdot U) + \nabla\rho\cdot U = 0 \tag{4.6}$$

Since the fluid considered in the current problem is nanofluid, being liquid it is incompressible and consequently ρ is constant in space and time which leads to $\frac{\partial \rho}{\partial t} = 0$, $\nabla\rho = 0$. As a result, (4.6) reduces to

$$\nabla \cdot U = 0 \tag{4.7}$$

For microchannel nanofluid flow with velocity $U = (u, V_0, 0)$, (4.7) takes the form

$$\nabla \cdot U = (\frac{\partial}{\partial x}, \frac{\partial}{\partial y}, \frac{\partial}{\partial z}) \cdot (u, V_0, 0) = \frac{\partial u}{\partial x} = 0 \tag{4.8}$$

Therefore, the equation of continuity for the problem in consideration is given by

$$\frac{\partial u}{\partial x} = 0 \tag{4.9}$$

Physically, a continuity equation describes the movement of a fluid element.That is, when a nanofluid is in motion, it must move in such a way that its mass is conserved.

4.1.2 The Navier-Stokes Equations: The Conservation of Momentum

To derive the Navier-Stokes equations or the momentum equations also known as equations of motion, the Newton's second law of motion was applied which states that the total time rate of change of linear momentum is conserved. That is,

$$\left\{ \begin{array}{c} \text{Total time rate of change of momentum} \\ \text{of the fluid particle in the control volume} \\ \end{array} \right\} = \left\{ \begin{array}{c} \text{Sum of all forces acting on the fluid} \\ \text{particle in the control volume} \\ \end{array} \right\}$$

In this case we consider momentum per unit volume which is known as momentum flux, rather than the momentum itself. Thus, momentum of the fluid particle in the control volume is equal to ρU, since ρ is mass per unit volume. Hence,

$$\left\{ \begin{array}{c} \text{Total time rate of change of momentum} \\ \text{of the fluid particle in the control volume} \\ \end{array} \right\} = \frac{d}{dt}\int_V (\rho U) dV$$

Hence,

$$\frac{d}{dt}\int_V (\rho U) dV = F_t = F_s + F_b \tag{4.10}$$

where F_t is the total force which is the sum of is the total surface forces F_s and the total body forces F_b.

But

$$\begin{aligned}\frac{d}{dt}\int_V(\rho U)dV &= \int_V \frac{\partial(\rho U)}{\partial t}dV + \int_S(\rho U)(U\cdot\vec{n})dS, \text{ by the Reynolds transport theorem}\\ &= \int_V \frac{\partial(\rho U)}{\partial t}dV + \int_V \nabla\cdot(\rho U)U dV, \text{ by Gauss divergence theorem}\\ &= \int_V\left(\frac{\partial(\rho U)}{\partial t} + \nabla\cdot(\rho U)U\right)dV\end{aligned}$$

Thus, (4.10) becomes

$$\int_V\left(\frac{\partial(\rho U)}{\partial t} + \nabla\cdot(\rho U)U\right)dV = F_s + F_b \tag{4.11}$$

Then applying the identity in vector calculus, we have

$$\begin{aligned}\nabla\cdot(\rho U)U &= U\cdot\nabla(\rho U) + \rho U(\nabla\cdot U)\\ &= \rho(U\cdot\nabla)U + \rho U(\nabla\cdot U)\\ &= \rho(U\cdot\nabla)U, \text{ since } \nabla\cdot U = 0 \text{ from continity equation}\end{aligned}$$

Thus,

$$\nabla\cdot(\rho U)U = \rho(U\cdot\nabla)U \tag{4.12}$$

Now, substituting (4.12) into (4.11) yields

$$\int_V\left(\frac{\partial(\rho U)}{\partial t} + \rho(U\cdot\nabla)U\right)dV = \int_V\rho\left(\frac{\partial U}{\partial t} + (U\cdot\nabla)U\right)dV = F_s + F_b \tag{4.13}$$

The total surface force F_s which is force per unit surface area is given by

$$F_s = \int_S\Big((\tau_{ij} + P_{po})\cdot\vec{n}\Big)dS = \int_V \nabla\cdot(\tau_{ij+P_{po}})dV, \text{ by Gauss divergence theorem} \tag{4.14}$$

where τ_{ij} is force per unit surface area known as stress tensor and P_{po} is the drag resistance force (extra pressure stress) due to the perpendicular motion of the fluid particles towards pore spaces of the porous medium.

The total body force F_b is external force per unit volume. In this case the body force is due to buoyancy given by

$$F_b = \int_V \rho g dV \tag{4.15}$$

where g is the acceleration due to gravity. So, from (4.14) and (4.15) we have

$$F_s + F_b = \int_V\Big(\nabla\cdot(\tau_{ij} + P_{po}) + \rho g\Big)dV \tag{4.16}$$

Now, substituting (4.16) into (4.13) yields

$$\int_V \rho\left(\frac{\partial U}{\partial t}+(U\cdot\nabla)U\right)dV=\int_V\left(\nabla\cdot(\tau_{ij}+P_{po})+\rho g\right)dV \tag{4.17}$$

Since V is arbitrary, from (4.17) we have

$$\rho\left(\frac{\partial U}{\partial t}+(U\cdot\nabla)U\right)=\left(\nabla\cdot(\tau_{ij}+P_{po})+\rho g\right)=\nabla\cdot\tau_{ij}+\nabla P_{po}+\rho g \tag{4.18}$$

Thus, (4.18) is called the momentum equation which also known as the Navier-Stokes equations for incompressible fluid flow. For the incompressible Newtonian fluid flow, the stress tensor τ is given by

$$\tau_{ij}=-PI+\sigma_{ij} \tag{4.19}$$

where P is pressure also known as the normal stress tensor, I is the identity matrix tensor and σ_{ij} is the shearing stress tensor (Cauchy stress tensor). The Cauchy stress tensor σ_{ij} has nine components and described in matrix as

$$\sigma_{ij}=\begin{bmatrix}\sigma_{xx} & \sigma_{xy} & \sigma_{xz}\\ \sigma_{yx} & \sigma_{yy} & \sigma_{yz}\\ \sigma_{zx} & \sigma_{zy} & \sigma_{zz}\end{bmatrix} \tag{4.20}$$

The components of σ_{ij} in (4.20) are given as follows.

$$\begin{aligned}
\sigma_{xx}&=2\mu(T)\frac{\partial u}{\partial x},\ \ \sigma_{xy}=\mu(T)(\frac{\partial u}{\partial y}+\frac{\partial V_0}{\partial x})=\sigma_{yx}\\
\sigma_{yy}&=2\mu(T)\frac{\partial V_0}{\partial y},\ \ \sigma_{xz}=\mu(T)(\frac{\partial u}{\partial z}+\frac{\partial w}{\partial x})=\sigma_{zx}\\
\sigma_{zz}&=2\mu(T)\frac{\partial w}{\partial z},\ \ \sigma_{yz}=\mu(T)(\frac{\partial V_0}{\partial z}+\frac{\partial w}{\partial y})=\sigma_{zy}
\end{aligned} \tag{4.21}$$

Using the equation of continuity (4.9), expressions in (4.21) can be simplified as follows.

$$\begin{aligned}
&\sigma_{xx}=0,\ \ \sigma_{xy}=\mu(T)\frac{\partial u}{\partial y}=\sigma_{yx}\\
&\sigma_{yy}=0,\ \ \sigma_{xz}=0=\sigma_{zx}\\
&\sigma_{zz}=0,\ \ \sigma_{yz}=0=\sigma_{zy}
\end{aligned} \tag{4.22}$$

Therefore, (4.20) becomes

$$\sigma_{ij}=\begin{bmatrix}0 & \mu(T)\frac{\partial u}{\partial y} & 0\\ \mu(T)\frac{\partial u}{\partial y} & 0 & 0\\ 0 & 0 & 0\end{bmatrix} \tag{4.23}$$

where $\mu(T)$ is temperature dependent dynamic viscosity.

Now, let us determine the expression for the term $\nabla \cdot \tau_{ij}$ in (4.18). Then

$$\nabla \cdot \tau_{ij} = \nabla \cdot (-PI + \sigma_{ij}) = -\nabla \cdot (PI) + \nabla \cdot \sigma_{ij} \tag{4.24}$$

But

$$-\nabla \cdot (PI) = -\nabla \cdot \begin{bmatrix} P & 0 & 0 \\ 0 & P & 0 \\ 0 & 0 & P \end{bmatrix} = \begin{bmatrix} -\frac{\partial P}{\partial x} \\ -\frac{\partial P}{\partial y} \\ -\frac{\partial P}{\partial z} \end{bmatrix} \tag{4.25}$$

and

$$\nabla \cdot \sigma_{ij} = (\frac{\partial}{\partial x}, \frac{\partial}{\partial y}, \frac{\partial}{\partial z}) \cdot \begin{bmatrix} \sigma_{xx} & \sigma_{xy} & \sigma_{xz} \\ \sigma_{yx} & \sigma_{yy} & \sigma_{yz} \\ \sigma_{zx} & \sigma_{zy} & \sigma_{zz} \end{bmatrix} = \begin{bmatrix} \frac{\partial(\sigma_{xx})}{\partial x} + \frac{\partial(\sigma_{xy})}{\partial y} + \frac{\partial(\sigma_{xz})}{\partial z} \\ \frac{\partial(\sigma_{yx})}{\partial x} + \frac{\partial(\sigma_{yy})}{\partial y} + \frac{\partial(\sigma_{yz})}{\partial z} \\ \frac{\partial(\sigma_{zx})}{\partial x} + \frac{\partial(\sigma_{zy})}{\partial y} + \frac{\partial(\sigma_{zz})}{\partial z} \end{bmatrix} \tag{4.26}$$

Again, by using the values of the expressions in (4.22), the values for the expressions of the components in (4.26) can be determined as follows.

$$\frac{\partial(\sigma_{xx})}{\partial x} + \frac{\partial(\sigma_{xy})}{\partial y} + \frac{\partial(\sigma_{xz})}{\partial z} = \frac{\partial}{\partial x}(0) + \frac{\partial}{\partial y}\left[\mu(T)\frac{\partial u}{\partial y}\right] + \frac{\partial}{\partial z}(0) = \frac{\partial}{\partial y}\left[\mu\frac{\partial u}{\partial y}\right] \tag{4.27}$$

Similarly,

$$\frac{\partial(\sigma_{yx})}{\partial x} + \frac{\partial(\sigma_{yy})}{\partial y} + \frac{\partial(\sigma_{yz})}{\partial z} = 0, \frac{\partial(\sigma_{zx})}{\partial x} + \frac{\partial(\sigma_{zy})}{\partial y} + \frac{\partial(\sigma_{zz})}{\partial z} = 0 \tag{4.28}$$

Then using (4.27)and (4.28) into (4.26) gives

$$\nabla \cdot \sigma_{ij} = \begin{bmatrix} \frac{\partial}{\partial y}\left[\mu(T)\frac{\partial u}{\partial y}\right] \\ 0 \\ 0 \end{bmatrix} \tag{4.29}$$

Using (4.25) and (4.29), (4.24) reduces to

$$\nabla \cdot \tau_{ij} = \begin{bmatrix} -\frac{\partial P}{\partial x} \\ -\frac{\partial P}{\partial y} \\ -\frac{\partial P}{\partial z} \end{bmatrix} + \begin{bmatrix} \frac{\partial}{\partial y}\left[\mu(T)\frac{\partial u}{\partial y}\right] \\ 0 \\ 0 \end{bmatrix} = \begin{bmatrix} -\frac{\partial P}{\partial x} + \frac{\partial}{\partial y}\left[\mu(T)\frac{\partial u}{\partial y}\right] \\ -\frac{\partial P}{\partial y} \\ -\frac{\partial P}{\partial z} \end{bmatrix} \tag{4.30}$$

By using the Darcy-Forchheimer porous media flow model, the term ∇P_{po} in (4.18) is given by

$$\nabla P_{po} = -\frac{\mu(T)u}{K} - \frac{\rho b \cdot u^2}{\sqrt{K}} \tag{4.31}$$

The left hand side expression in the momentum equation (4.18) is

$$\begin{aligned}
\rho\left[\frac{\partial U}{\partial t}+(U\cdot\nabla)U\right] &= \rho\left[\frac{\partial(u,V_0,0)}{\partial t}+(u,V_0,0)\cdot(\frac{\partial}{\partial x},\frac{\partial}{\partial y},\frac{\partial}{\partial z})(u,V_0,0)\right]\\
&= \rho\left[\frac{\partial u}{\partial t}+(u\frac{\partial}{\partial x}+V_0\frac{\partial}{\partial y})(u,V_0,0)\right]\\
&= \rho\left[\frac{\partial u}{\partial t}+u\frac{\partial u}{\partial x}+V_0\frac{\partial u}{\partial y}\right]\\
&= \rho\left[\frac{\partial u}{\partial t}+V_0\frac{\partial u}{\partial y}\right]
\end{aligned}$$

Hence,

$$\rho\left[\frac{\partial U}{\partial t}+(U\cdot\nabla)U\right]=\rho\left[\frac{\partial u}{\partial t}+V_0\frac{\partial u}{\partial y}\right] \tag{4.32}$$

Therefore, by using (4.30), (4.31) and (4.32), the x-momentum equation becomes

$$\rho\left[\frac{\partial u}{\partial t}+V_0\frac{\partial u}{\partial y}\right]=-\frac{\partial P}{\partial x}+\frac{\partial}{\partial y}\left[\mu(T)\frac{\partial u}{\partial y}\right]-\frac{\mu(T)u}{K}-\frac{\rho b u^2}{\sqrt{K}}+\rho g \tag{4.33}$$

and the y-momentum becomes

$$\frac{\partial P}{\partial y}=0 \tag{4.34}$$

From (4.34) it can be seen that the pressure is as a function of x only. That is, $P(x,y)=P(x)$.

In buoyancy driven flows, a common approach is to consider constant thermophysical properties of the fluid with the exception of the density variations that are only taken into account in the buoyancy forces, that is, the so called Oberbeck-Boussinesq approximation. Now, applying the Boussinesq approximation on the equation of momentum (4.33), which states that density variation with temperature and concentration is important only for body force term but not for other terms. Hence, the body force term in (4.33) is given by $\rho g=\rho(T,C)g$. Using the Taylor series expansion for $\rho=\rho(T,C)$ about (T_0,C_0), yields the following where $\rho_0=\rho(T_0,C_0)$.

$$\rho=\rho_0+\frac{\partial\rho}{\partial T}(T-T_0)+\frac{\partial\rho}{\partial C}(C-C_0)+\frac{\partial^2\rho}{\partial T^2}\frac{(T-T_0)^2}{2!}+\frac{\partial^2\rho}{\partial C^2}\frac{(C-C_0)^2}{2!}+\cdots$$

Then, neglecting the second and higher order terms, we have

$$\rho-\rho_0=\frac{\partial\rho}{\partial T}(T-T_0)+\frac{\partial\rho}{\partial C}(C-C_0) \tag{4.35}$$

However, as $y\to 0, u=0, v=V_0$, then the momentum equation (4.33)) becomes

$$0=\rho_0 g \tag{4.36}$$

Subtracting (4.36) from (4.33) yields

$$\rho\left[\frac{\partial u}{\partial t}+V_0\frac{\partial u}{\partial y}\right]=-\frac{\partial P}{\partial x}+\frac{\partial}{\partial y}\left[\mu(T)\frac{\partial u}{\partial y}\right]-\frac{\mu(T)u}{K}-\frac{\rho bu^2}{\sqrt{K}}+(\rho-\rho_0)g \tag{4.37}$$

Substituting (4.35) into (4.37) gives

$$\rho\left[\frac{\partial u}{\partial t}+V_0\frac{\partial u}{\partial y}\right]=-\frac{\partial P}{\partial x}+\frac{\partial}{\partial y}\left[\mu(T)\frac{\partial u}{\partial y}\right]-\frac{\mu(T)u}{K}-\frac{\rho bu^2}{\sqrt{K}}+\left[\frac{\partial \rho}{\partial T}(T-T_0)+\frac{\partial \rho}{\partial C}(C-C_0)\right]g \tag{4.38}$$

Equivalently,

$$\frac{\partial u}{\partial t}+V_0\frac{\partial u}{\partial y}=-\frac{1}{\rho}\frac{\partial P}{\partial x}+\frac{1}{\rho}\frac{\partial}{\partial y}\left[\mu(T)\frac{\partial u}{\partial y}\right]-\frac{\mu(T)u}{\rho K}-\frac{bu^2}{\sqrt{K}}+\left[\frac{1}{\rho}\frac{\partial \rho}{\partial T}(T-T_0)+\frac{1}{\rho}\frac{\partial \rho}{\partial C}(C-C_0)\right]g \tag{4.39}$$

which implies that

$$\frac{\partial u}{\partial t}+V_0\frac{\partial u}{\partial y}=-\frac{1}{\rho}\frac{\partial P}{\partial x}+\frac{1}{\rho}\frac{\partial}{\partial y}\left[\mu(T)\frac{\partial u}{\partial y}\right]-\frac{\mu(T)u}{\rho K}-\frac{bu^2}{\sqrt{K}}+\beta_1 g(T-T_0)+\beta_2 g(C-C_0) \tag{4.40}$$

where $\beta_1=\frac{1}{\rho}\frac{\partial\rho}{\partial T}$ and $\beta_2=\frac{1}{\rho}\frac{\partial\rho}{\partial C}$ are the thermal expansion coefficient and the concentration expansion coefficient respectively. Therefore, (4.40) represents the equation of momentum.

The associated initial and boundary conditions (no slip conditions) are:

$$u(y,0)=0 \;\text{ and }\; \left.\begin{aligned} u(0,t)&=0\\ u(a,t)&=0\end{aligned}\right\}\text{for } t>0 \tag{4.41}$$

4.1.3 Energy Equation: The Conservation of Energy

To derive energy equation, the energy conservation principle known as the first law of thermodynamics was used. The first law of thermodynamics states that the time rate of change of energy within the volume element dV is equals to the sum of the rate that energy is received by heat (Q) and work done in the interaction process.

$$\frac{dE}{dt}=\frac{dQ}{dt}+\frac{dW}{dt} \tag{4.42}$$

where E is total energy, inclusive of internal energy and kinetic energy. The potential energy could have been included in E, but instead it will be absorbed into the work term W. Q is the amount of heat added or removed.

For a nanofluid within dV, the differential amount of total energy is give by

$$dE=\rho_{nf}edV+\frac{1}{2}\rho U^2dV=\rho dV(e+\frac{1}{2}U^2)=\rho_{nf}dV(e+\frac{1}{2}U^2) \tag{4.43}$$

where $\rho_{nf}dV$ represents mass, e is internal energy, ρ_{nf} designates density of nanofluid and $\frac{1}{2}U^2$ is kinetic energy.

Integrating (4.43) gives

$$E=\int_V \rho_{nf}(e+\frac{1}{2}U^2)dV. \text{ which implie that } \frac{dE}{dt}=\frac{d}{dt}\int_V \rho_{nf}(e+\frac{1}{2}U^2)dV.$$

$$\begin{aligned}\text{So, } \frac{dE}{dt}&=\frac{d}{dt}\int_V \rho_{nf}(e+\frac{1}{2}U^2)dV\\ &=\int_V \rho_{nf}(\frac{\partial e}{\partial t}+\frac{1}{2}\frac{\partial U^2}{\partial t})dV+\int_S \rho_{nf}(e+\frac{1}{2}U^2)(U.\vec{n})dS, \text{ by the Renolds transport theorem}\\ &=\int_V \rho_{nf}(\frac{\partial e}{\partial t}+\frac{1}{2}\frac{\partial U^2}{\partial t})dV+\int_V \nabla\cdot U\rho_{nf}(e+\frac{1}{2}U^2)dV, \text{ by the Gauss divergence theorem}\\ &=\int_V \rho_{nf}(\frac{\partial e}{\partial t}+\frac{1}{2}\frac{\partial U^2}{\partial t})dV+\int_V \rho_{nf}(\nabla\cdot Ue)dV+\int_V \frac{1}{2}\rho_{nf}(\nabla\cdot U(U^2))dV\\ &=\int_V \rho_{nf}(\frac{\partial e}{\partial t}+\nabla\cdot Ue)dV+\int_V \frac{1}{2}\rho_{nf}\Big(\frac{\partial U^2}{\partial t}+\nabla\cdot U(U^2)\Big)dV\end{aligned}$$

Therefore,

$$\frac{dE}{dt}=\int_V \rho_{nf}(\frac{\partial e}{\partial t}+\nabla\cdot Ue)dV+\int_V \frac{1}{2}\rho_{nf}\Big(\frac{\partial U^2}{\partial t}+\nabla\cdot U(U^2)\Big)dV \tag{4.44}$$

But $\nabla\cdot U(U^2)=U^2(\nabla\cdot U)+\nabla U^2\cdot U=\nabla U^2\cdot U$, since U^2 is scalar and $\nabla\cdot U=0$.

$$\begin{aligned}&=\nabla U^2\cdot U=(\frac{\partial U^2}{\partial x},\frac{\partial U^2}{\partial y},\frac{\partial U^2}{\partial z})\cdot(u,v,w)\\ &=2U(\frac{\partial U}{\partial x},\frac{\partial U}{\partial y},\frac{\partial U}{\partial z})\cdot(u,v,w)=2U(u\frac{\partial}{\partial x},v\frac{\partial}{\partial y},w\frac{\partial}{\partial z})U\\ &=2U(U\cdot\nabla)U\end{aligned}$$

Therefore, $\nabla\cdot U(U^2)=2U(U\cdot\nabla)U$ (4.45)

Again we have also $\frac{\partial U^2}{\partial t}=2U\frac{\partial U}{\partial t}$ (4.46)

Equations (4.45) and (4.46) gives

$$\int_V \frac{1}{2}\rho_{nf}\Big(\frac{\partial U^2}{\partial t}+\nabla\cdot U(U^2)\Big)dV=\int_V \rho_{nf}U\Big(\frac{\partial U}{\partial t}+(U\cdot\nabla)U\Big)dV \tag{4.47}$$

Since $e=(C_P)_{nf}T$, it yields

$$\frac{\partial e}{\partial t}=(C_P)_{nf}\frac{\partial T}{\partial t} \text{ and also } \nabla\cdot Ue=e(\nabla\cdot U)+U\cdot\nabla e=U\cdot\nabla e=(C_P)_{nf}(U\cdot\nabla)T \tag{4.48}$$

Similarly, (4.48) gives

$$\int_V \rho_{nf}(\frac{\partial e}{\partial t} + \nabla \cdot Ue)dV = \int_V (\rho C_P)_{nf}\left((\frac{\partial T}{\partial t} + (U \cdot \nabla)T\right)dV \tag{4.49}$$

Now using (4.47) and (4.49) into (4.44) yields

$$\frac{dE}{dt} = \int_V (\rho C_P)_{nf}\left((\frac{\partial T}{\partial t} + (U \cdot \nabla)T\right)dV + \int_V \rho_{nf} U\left(\frac{\partial U}{\partial t} + (U \cdot \nabla)U\right)dV \tag{4.50}$$

where $(C_P)_{nf}$ is specific heat of nanofluid at constant pressure.

For the work term we have the fact that work is done when a force acts through a distance, and a work rate arises when a force acts through a distance at a particular rate in time and hence velocity is involved. Thus, work done is the dot product (inner product) of the force vector $\vec{F}$ with the position vector $\vec{r}$. So

$$dW = d\vec{r} \cdot \vec{F}$$

This implies that work rate is

$$\frac{dW}{dt} = \frac{d\vec{r}}{dt} \cdot \vec{F} = U \cdot \vec{F} \tag{4.51}$$

Here the forces are the total surface force F_s and the total body force F_b.

$$F_s = \int_S \left((\tau_{ij} + P_{po}) \cdot \vec{n}\right)dS, \;\; F_b = \int_V \rho g dV \tag{4.52}$$

Hence, using (4.52) into (4.51) gives

$$\begin{aligned} \frac{dW}{dt} = \frac{d\vec{r}}{dt} \cdot \vec{F} = U \cdot \vec{F} = U \cdot (F_s + F_b) \\ = \int_S U\left((\tau_{ij} + P_{po}\right) \cdot \vec{n})dS + \int_V U(\rho g)dV \\ = \int_V \nabla \cdot \left(U(\tau_{ij} + P_{po})\right)dV + \int_V U(\rho g)dV \end{aligned} \tag{4.53}$$

However, $U \cdot P_{po} = 0$, since P_{po} is the drag resistance force (extra pressure stress) due to the perpendicular motion of the fluid particles towards pore spaces of the porous medium. Therefore, (4.53) is simplified as:

$$\frac{dW}{dt} = \int_V \nabla \cdot (U\tau_{ij})dV + \int_V U(\rho g)dV \tag{4.54}$$

But from vector calculus, it is true that

$$\nabla \cdot (U\tau_{ij}) = U(\nabla \cdot \tau_{ij}) + (\tau_{ij} \cdot \nabla)U$$

Therefore,

$$\begin{aligned}\frac{dW}{dt} &= \int_V \left[U(\nabla\cdot\tau_{ij}) + (\tau_{ij}\cdot\nabla)U + U(\rho g)\right]dV \\ &= \int_V \left[U(\nabla\cdot\tau_{ij}) + U(\nabla P_{po}) + U(\rho g) - U(\nabla P_{po}) + (\tau_{ij}\cdot\nabla)U\right]dV\end{aligned} \tag{4.55}$$

However, multiplying the equation of momentum (4.18) by U yields

$$\rho_{nf}U\left(\frac{\partial U}{\partial t} + (U\cdot\nabla)U\right) = U(\nabla\cdot\tau_{ij}) + U(\nabla P_{po}) + U(\rho g) \tag{4.56}$$

Using (4.56) into (4.55) yields

$$\frac{dW}{dt} = \int_V \left[\rho_{nf}U\left(\frac{\partial U}{\partial t} + (U\cdot\nabla)U\right) - U(\nabla P_{po}) + (\tau_{ij}\cdot\nabla)U\right]dV \tag{4.57}$$

The term $(\tau_{ij}\cdot\nabla)U$ in (4.57) is known as dissipation energy and it can be simplified as follows:

$$\begin{aligned}(\tau_{ij}\cdot\nabla)U &= (\mu(T)\frac{\partial u}{\partial y}, \mu(T)\frac{\partial u}{\partial y}, 0)\cdot(\frac{\partial}{\partial x}, \frac{\partial}{\partial y}, 0)U \\ &= \left[\mu(T)\frac{\partial u}{\partial y}\cdot\frac{\partial}{\partial x} + \mu(T)\frac{\partial u}{\partial y}\cdot\frac{\partial}{\partial y}\right](u, V_0, 0) \\ &= \mu(T)\frac{\partial u}{\partial y}\cdot\frac{\partial u}{\partial x} + \mu(T)\frac{\partial u}{\partial y}\cdot\frac{\partial u}{\partial y}, \text{ since } V_0 \text{ is constant} \\ &= \mu(T)\frac{\partial u}{\partial y}\cdot\frac{\partial u}{\partial y}, \text{ since } \frac{\partial u}{\partial x} = 0 \\ &= \mu(T)(\frac{\partial u}{\partial y})^2\end{aligned}$$

Hence,

$$(\tau_{ij}\cdot\nabla)U = \mu(T)(\frac{\partial u}{\partial y})^2 \tag{4.58}$$

Again using (4.31) gives

$$U\cdot(\nabla P_{po}) = (u, V_0, 0)\cdot\left(-\frac{\mu(T)u}{K} - \frac{\rho b u^2}{\sqrt{K}}, 0, 0\right) = -\frac{\mu(T)u^2}{K} - \frac{\rho b u^3}{\sqrt{K}} \tag{4.59}$$

Indeed, this is the case because ∇P_{po} is the pressure gradient in the direction of flow that is in the $x-$direction. So, $\nabla P_{po} = -\frac{\mu(T)U}{K} - \frac{\rho b U^2}{\sqrt{K}} = (-\frac{\mu(T)u}{K} - \frac{\rho b u^2}{\sqrt{K}}, 0, 0)$.

Now, substituting (4.58) and (4.59) into (4.57) gives

$$\frac{dW}{dt} = \int_V \left[\rho_{nf}U\left(\frac{\partial U}{\partial t} + (U\cdot\nabla)U\right) + \frac{\mu(T)u^2}{K} + \frac{\rho b u^3}{\sqrt{K}} + \mu(T)(\frac{\partial u}{\partial y})^2\right]dV \tag{4.60}$$

For the heat transfer term, define the heat flux vector $\vec{q}$ as the amount of heat energy per unit area and as a vector it points in the direction of thermal energy flow which has units of energy per area per time. Following Buongiorno (2006), the effects of Brownian and thermophoretic diffusions are considered to study heat transfer and thus according to Buongiorno, the Brownian and thermophoretic diffusions are the main slip mechanisms in nanofluids. That is, the thermophoretic and Brownian diffusions of the nanoparticles siginificantly contribute to the heat and mass transfer phenomena of the nanofluid. Brownian diffusion is due to random drifting of suspended nanoparticles in the base fluid which originates from continuous collisions among the nanoparticles and liquid molecules. Thermophoresis induces nanoparticle migration from warmer to colder region (in opposite direction of the temperature gradient), making a non-uniform nanoparticle volume fraction distribution.

The random motion of nanoparticles within the basefluid, which is due to the continuous collisions between the nanoparticles and the molecules of the basefluid, is called Brownian motion. The nanoparticle mass flux due to the Brownian diffusion is given by

$$\vec{J}_{p,B} = -\rho_p D_B \nabla C \tag{4.61}$$

where, $-\rho_p$ is density of the nanoparticle, D_B is Brownian diffusion coefficient and C is concentration of nanoparticle. Thermophoresis is a phenomenon, which causes the motion of small particles from a hot surface to cold one under the thermophoretic force that develops due to the temperature gradient. The nanoparticle mass flux due to the thermophoresis diffusion is given by

$$\vec{J}_{p,T} = -\rho_p \frac{D_T}{T_0} \nabla T \tag{4.62}$$

where, D_T is thermophoresis diffusion coefficient.

Therefore, the total nanoparticle mass flux is the sum of the nanoparticle mass fluxes due Brownian and thermophoresis diffusions, which is given by

$$\vec{J}_p = \vec{J}_{p,B} + \vec{J}_{p,T} = -\rho_p (D_B \nabla C + \frac{D_T}{T_0} \nabla T) \tag{4.63}$$

Thus, the net heat transfer rate through the surface S is given by

$$\frac{dQ}{dt} = -\int_S (\vec{q} - h_p \vec{J}_p) \cdot \vec{n} dS \tag{4.64}$$

The first term in (4.64) represents the contribution of heat conduction through base fluid and the second term represents the heat flux due to nanoparticle diffusion. The minus sign indicates that heat flux transfers from higher to lower direction.

$$\frac{dQ}{dt} = -\int_S (\vec{q} - h_p \vec{J}_p) \cdot \vec{n} dS = -\int_S \vec{q} \cdot \vec{n} dS + \int_S h_p \vec{J}_p \cdot \vec{n} dS \tag{4.65}$$

The specific enthalpy of the nanoparticle h_p is given by $h_p = (C_P)_p T$ and T is assumed to be constant over a given surface (isothermal wall). Hence,

$$\int_S h_p \vec{J}_p \cdot \vec{n} dS = h_p \int_S \vec{J}_p \cdot \vec{n} dS \tag{4.66}$$

Now, substituting (4.66) into (4.65) gives:

$$\frac{dQ}{dt} = -\int_S (\vec{q} - h_p \vec{J}_p) \cdot \vec{n} dS = -\int_S \vec{q} \cdot \vec{n} dS + h_p \int_S \vec{J}_p \cdot \vec{n} dS \tag{4.67}$$

Then by using the Gauss divergence theorem, (4.67) becomes,

$$\frac{dQ}{dt} = -\int_V \nabla \cdot \vec{q} dV + h_p \int_V \nabla \cdot \vec{J}_p dV = -\int_V (\nabla \cdot \vec{q} - h_p \nabla \cdot \vec{J}_p) dV \tag{4.68}$$

But the heat flux vector $\vec{q}$ can be calculated as the sum of the Fourier (conduction) heat flux and the heat flux due to nanoparticle diffusion.

$$\vec{q} = -k \nabla T + h_p \vec{J}_p \tag{4.69}$$

where k is the nanofluid thermal conductivity and T is the nanofluid temperature. Then operating both sides of (4.69) with divergence gives,

$$\nabla \cdot \vec{q} = -k \nabla^2 T + \nabla h_p \cdot \vec{J}_p + h_p \nabla \cdot \vec{J}_p \tag{4.70}$$

Now, substituting (4.70) into (4.68) gives,

$$\frac{dQ}{dt} = -\int_V (-k \nabla^2 T + \nabla h_p \cdot \vec{J}_p) dV \tag{4.71}$$

Then using (4.63) into (4.71) yields,

$$\frac{dQ}{dt} = -\int_V \left(-k \nabla^2 T + \nabla (C_P)_p T) \cdot \left[-\rho_p (D_B \nabla C + \frac{D_T}{T_0} \nabla T) \right] \right) dV$$

$$= \int_V \left(k \nabla^2 T + (\rho C_P)_p \left[D_B \nabla C \cdot \nabla T + \frac{D_T}{T_0} \nabla T \cdot \nabla T \right] \right) dV$$

Hence,

$$\frac{dQ}{dt} = \int_V \left(k \nabla^2 T + (\rho C_P)_p \left[D_B \nabla C \cdot \nabla T + \frac{D_T}{T_0} (\nabla T)^2 \right] \right) dV \tag{4.72}$$

Finally, substituting (4.50), (4.60) and (4.72) into (4.42) yields:

$$\int_V (\rho C_P)_{nf}\left(\frac{\partial T}{\partial t}+(U\cdot\nabla)T\right)dV+\int_V \rho_{nf}U\left(\frac{\partial U}{\partial t}+(U\cdot\nabla)U\right)dV$$

$$=\int_V\left[\rho_{nf}U\left(\frac{\partial U}{\partial t}+(U\cdot\nabla)U\right)+\frac{\mu(T)u^2}{K}+\frac{\rho bu^3}{\sqrt{K}}+\mu(T)(\frac{\partial u}{\partial y})^2\right]dV \tag{4.73}$$

$$+\int_V\left(k\nabla^2T+(\rho C_P)_p\left[D_B\nabla C\cdot\nabla T+\frac{D_T}{T_0}(\nabla T)^2\right)dV\right.$$

Since V is arbitrary, from (4.73) one can write

$$\begin{aligned}&(\rho C_P)_{nf}\left(\frac{\partial T}{\partial t}+(U\cdot\nabla)T\right)+\rho_{nf}U\left(\frac{\partial U}{\partial t}+(U\cdot\nabla)U\right)\\&=\rho_{nf}U\left(\frac{\partial U}{\partial t}+(U\cdot\nabla)U\right)+\frac{\mu(T)u^2}{K}+\frac{\rho bu^3}{\sqrt{K}}+\mu(T)(\frac{\partial u}{\partial y})^2\\&+k\nabla^2T+(\rho C_P)_p\left[D_B\nabla C\cdot\nabla T+\frac{D_T}{T_0}(\nabla T)^2\right]\end{aligned}$$

This implies that

$$\begin{aligned}(\rho C_P)_{nf}\left(\frac{\partial T}{\partial t}+(U\cdot\nabla)T\right)&=k\nabla^2T+(\rho C_P)_p\left[D_B\nabla C\cdot\nabla T+\frac{D_T}{T_0}(\nabla T)^2\right]\\&+\mu(T)(\frac{\partial u}{\partial y})^2+\frac{\mu(T)u^2}{K}+\frac{\rho bu^3}{\sqrt{K}}\end{aligned} \tag{4.74}$$

Rearranging and letting $\alpha_t=\frac{k}{(\rho C_P)_{nf}}$, $\Gamma=\frac{(\rho C_P)_p}{(\rho C_P)_{nf}}$ gives the thermal energy equation.

$$\begin{aligned}\frac{\partial T}{\partial t}+(U\cdot\nabla)T&=\alpha_t\nabla^2T+\Gamma\left[D_B\nabla C\cdot\nabla T+\frac{D_T}{T_0}(\nabla T)^2\right]\\&+\frac{\mu(T)}{(\rho C_P)_{nf}}(\frac{\partial u}{\partial y})^2+\frac{\mu(T)u^2}{(\rho C_P)_{nf}K}+\frac{\rho bu^3}{(\rho C_P)_{nf}\sqrt{K}}\end{aligned} \tag{4.75}$$

$$\begin{aligned}\Rightarrow\frac{\partial T}{\partial t}+u\frac{\partial T}{\partial x}+V_0\frac{\partial T}{\partial y}&=\alpha_t\left[\frac{\partial^2T}{\partial x^2}+\frac{\partial^2T}{\partial y^2}\right]+\frac{\mu(T)u^2}{(\rho C_P)_{nf}K}+\frac{\rho bu^3}{(\rho C_P)_{nf}\sqrt{K}}+\frac{\mu(T)}{(\rho C_P)_{nf}}(\frac{\partial u}{\partial y})^2\\&+\Gamma\left\{D_B\left[\frac{\partial C}{\partial x}\frac{\partial T}{\partial x}+\frac{\partial C}{\partial y}\frac{\partial T}{\partial y}\right]+\frac{D_T}{T_0}\left[(\frac{\partial T}{\partial x})^2+(\frac{\partial T}{\partial y})^2\right]\right\}\end{aligned} \tag{4.76}$$

Assuming $\frac{\partial T}{\partial x} \ll \frac{\partial T}{\partial y}$, $\frac{\partial C}{\partial x} \ll \frac{\partial C}{\partial y}$, gives

$$\begin{aligned}\frac{\partial T}{\partial t}+V_0\frac{\partial T}{\partial y} = \alpha_t(\frac{\partial^2 T}{\partial y^2})+\Gamma\left[D_B\frac{\partial C}{\partial y}\frac{\partial T}{\partial y}+\frac{D_T}{T_0}(\frac{\partial T}{\partial y})^2\right]+\frac{\mu(T)}{(\rho C_P)_{nf}}(\frac{\partial u}{\partial y})^2\\ +\frac{\mu(T)u^2}{(\rho C_P)_{nf}K}+\frac{\rho b u^3}{(\rho C_P)_{nf}\sqrt{K}}\end{aligned} \tag{4.77}$$

Thus, (4.77) is the governing equation of thermal energy for the nanofluid flow problem. The initial and boundary conditions are:

$$T(y,0)=T_0 \text{ and } \left.\begin{array}{l} T(0,t)=T_0, \\ D_B\frac{\partial C(0,t)}{\partial y}=\frac{-D_T}{T_0}\frac{\partial T(0,t)}{\partial y}, \\ T(a,t)=T_w \end{array}\right\} \text{for } t>0 \tag{4.78}$$

Here, the boundary condition $D_B\frac{\partial C(0,t)}{\partial y}=\frac{-D_T}{T_0}\frac{\partial T(0,t)}{\partial y}$ is due to the passive control of the nanoparticles.

4.1.4 Concentration Equation: The Law of Mass Balance

Let C be a concentration of the chemical species of the nanoparticles within a control volume V and let also C_0 and C_w be the concentration of the species at the cold wall and hot wall of the microchannel respectively. The law of mass balance was applied to derive the chemical species concentration equation. The law of mass balance, also called a material balance, is an application of conservation of mass to the analysis of physical systems and it is stated as follows:

$$\left\{\begin{array}{c}\text{Rate of change of mass of fluid}\\ \text{within the control volume}\end{array}\right\}=\left\{\begin{array}{c}\text{Net rate at which mass enters the control}\\ \text{volume through the control surface}\end{array}\right\}$$

Then the total rate of change of the chemical species concentration C within the control volume dV is given by

$$\frac{d}{dt}\int_V \rho_p C\, dV \tag{4.79}$$

and the net rate of entry of mass of the chemical species into the control volume through the area element dS is given by

$$-\int_S \vec{j}_p\cdot\vec{n}\, dS \tag{4.80}$$

Now equating (4.79) and (4.80) yields:

$$\frac{d}{dt}\int_V \rho_p C\, dV = -\int_S \vec{j}_p\cdot\vec{n}\, dS \tag{4.81}$$

where $\vec{j}_p$ is the mass flux of the chemical species due to the Brownian motion and thermophoresis diffusion given by $\vec{J}_p = -\rho_p(D_B\nabla C + \frac{D_T}{T_0}\nabla T)$ as described under the previous subsection. Then using the Reynolds transport theorem and the Gauss divergence theorem (4.79) becomes:

$$\frac{d}{dt}\int_V \rho_p C dV = \rho_p\left(\int_V \frac{\partial C}{\partial t}dV + \int_S C(U\cdot\vec{n})dS\right) = \rho_p\left(\int_V \frac{\partial C}{\partial t}dV + \int_V \nabla\cdot(CU)dV\right) \quad (4.82)$$

But $\nabla\cdot(CU) = C(\nabla\cdot U) + (U\cdot\nabla)C = (U\cdot\nabla)C$, since $\nabla\cdot U = 0$ from continuity equation. Thus

$$\frac{d}{dt}\int_V \rho_p C dV = \rho_p\left(\int_V \frac{\partial C}{\partial t}dV + \int_V (U\cdot\nabla)C dV\right) \quad (4.83)$$

Again by the Gauss divergence theorem, (4.80) becomes:

$$-\int_S \vec{j}_p\cdot\vec{n}\,dS = -\int_V \nabla\cdot\vec{j}_p dV \quad (4.84)$$

Now using (4.83) and (4.84), (4.81) reduces to

$$\rho_p\left(\int_V \frac{\partial C}{\partial t}dV + \int_V (U\cdot\nabla)C dV\right) = -\int_V \nabla\cdot\vec{j}_p dV \quad (4.85)$$

Since V is arbitrary from (4.85) gives

$$\rho_p\left(\frac{\partial C}{\partial t} + (U\cdot\nabla)C\right) = -\nabla\cdot\vec{j}_p \quad (4.86)$$

For two dimensional flow, (4.86) can be written as

$$\rho_p\left(\frac{\partial C}{\partial t} + u\frac{\partial C}{\partial x} + V_0\frac{\partial C}{\partial y}\right) = -\nabla\cdot\vec{j}_p = \nabla\cdot\left(\rho_p(D_B\nabla C + \frac{D_T}{T_0}\nabla T)\right) \quad (4.87)$$

Therefore,

$$\frac{\partial C}{\partial t} + V_0\frac{\partial C}{\partial y} = D_B\frac{\partial^2 C}{\partial y^2} + \frac{D_T}{T_0}\frac{\partial^2 T}{\partial y^2} \quad (4.88)$$

Thus, (4.88) is the governing equation for the chemical species concentration. The associated boundary conditions are:

$$C(y,0) = C_0 \;\text{ and }\; \left.\begin{array}{l} C(0,t) = C_0, \\ D_B\frac{\partial C(0,t)}{\partial y} = \frac{-D_T}{T_0}\frac{\partial T(0,t)}{\partial y}, \\ C(a,t) = C_w \end{array}\right\}\text{for } t > 0 \quad (4.89)$$

Therefore, the governing equations for the flow problem are summarized as follows:

$$\frac{\partial u}{\partial x} = 0 \quad (4.90)$$

$$\frac{\partial u}{\partial t}+V_0\frac{\partial u}{\partial y}=-\frac{1}{\rho}\frac{\partial P}{\partial x}+\frac{1}{\rho}\frac{\partial}{\partial y}\left[\mu(T)\frac{\partial u}{\partial y}\right]-\frac{\mu(T)u}{\rho K}-\frac{bu^2}{\sqrt{K}}+\beta_1 g(T-T_0)+\beta_2 g(C-C_0) \tag{4.91}$$

$$\frac{\partial T}{\partial t}+V_0\frac{\partial T}{\partial y}=\alpha_t\frac{\partial^2 T}{\partial y^2}+\Gamma\left[D_B\frac{\partial C}{\partial y}\frac{\partial T}{\partial y}+\frac{D_T}{T_0}(\frac{\partial T}{\partial y})^2\right]+\frac{\mu(T)}{\rho C_p}(\frac{\partial u}{\partial y})^2+\frac{\mu(T)u^2}{\rho C_p K}+\frac{bu^3}{C_p\sqrt{K}} \tag{4.92}$$

$$\frac{\partial C}{\partial t}+V_0\frac{\partial C}{\partial y}=D_B\frac{\partial^2 C}{\partial y^2}+\frac{D_T}{T_0}\frac{\partial^2 T}{\partial y^2} \tag{4.93}$$

with the initial and boundary conditions:

$$u(y,0)=0, T(y,0)=T_0, C(y,0)=C_0 \text{ and } \left.\begin{array}{l} u(0,t)=0, T(0,t)=T_0, C(0,t)=C_0 \\ D_B\frac{\partial C(0,t)}{\partial y}=\frac{-D_T}{T_0}\frac{\partial T(0,t)}{\partial y}, \\ u(a,t)=0, T(a,t)=T_w, \\ C(a,t)=C_1 \end{array}\right\} \text{for } t>0 \tag{4.94}$$

4.2 Non-Dimensional Formulation

In order to non-dimensionalize the above governing equations, the following dimensionless variables were introduced.

$$\eta=\frac{y}{a},\ X=\frac{x}{a},\ W=\frac{\rho a u}{\mu_0},\ \tau=\frac{\mu_0 t}{\rho a^2},\ \theta=\frac{T-T_0}{T_w-T_0},\ \phi=\frac{C-C_0}{C_1-C_0},\ P^*=\frac{\rho a^2 P}{\mu_0^2} \tag{4.95}$$

From these dimensionless variables defined in (4.95) and using the rules of partial differentiation, gives the following.

$$\frac{\partial u}{\partial t}=\frac{\partial u}{\partial \tau}\frac{\partial \tau}{\partial t}=\frac{\mu_0}{\rho a^2}\frac{\mu_0}{\rho a}\frac{\partial W}{\partial \tau}=(\frac{\mu_0}{\rho})^2\frac{1}{a^3}\frac{\partial W}{\partial \tau} \tag{4.96}$$

$$\frac{\partial u}{\partial x}=\frac{\partial u}{\partial X}\frac{\partial X}{\partial x}=\frac{1}{a}\frac{\partial u}{\partial X}=\frac{\mu_0}{\rho a^2}\frac{\partial W}{\partial X} \tag{4.97}$$

$$\frac{\partial u}{\partial y}=\frac{\partial u}{\partial \eta}\frac{\partial \eta}{\partial y}=\frac{1}{a}\frac{\partial u}{\partial \eta}=\frac{\mu_0}{\rho a^2}\frac{\partial W}{\partial \eta} \tag{4.98}$$

$$\frac{\partial^2 u}{\partial y^2}=\frac{\partial}{\partial y}(\frac{\partial u}{\partial y})=\frac{\partial}{\partial y}(\frac{\mu_0}{\rho a^2}\frac{\partial W}{\partial \eta})=\frac{\partial}{\partial \eta}(\frac{\partial W}{\partial y})\frac{\partial \eta}{\partial y}=\frac{\mu_0}{\rho a^3}\frac{\partial^2 W}{\partial \eta^2} \tag{4.99}$$

$$\frac{1}{\rho}\frac{\partial P}{\partial x}=\frac{1}{\rho}\frac{\partial P}{\partial X}\frac{\partial X}{\partial x}=\frac{1}{\rho a}\frac{\partial P}{\partial X}=(\frac{\mu_0}{\rho})^2\frac{1}{a^3}\frac{\partial P*}{\partial X} \tag{4.100}$$

$$\frac{\partial T}{\partial t}=\frac{\partial T}{\partial \tau}\frac{\partial \tau}{\partial t}=\frac{\mu_0}{\rho a^2}\frac{\partial T}{\partial \tau}=\frac{\mu_0}{\rho a^2}(T_w-T_0)\frac{\partial \theta}{\partial \tau} \tag{4.101}$$

$$\frac{\partial T}{\partial y}=\frac{\partial T}{\partial \eta}\frac{\partial \eta}{\partial y}=\frac{1}{a}\frac{\partial T}{\partial \eta}=\frac{(T_w-T_0)}{a}\frac{\partial \theta}{\partial \eta} \tag{4.102}$$

$$\frac{\partial^2 T}{\partial y^2} = \frac{\partial}{\partial y}(\frac{\partial T}{\partial y}) = \frac{\partial}{\partial y}\left(\frac{(T_w-T_0)}{a}\frac{\partial \theta}{\partial \eta}\right) = \frac{(T_w-T_0)}{a^2}\frac{\partial^2 \theta}{\partial \eta^2} \tag{4.103}$$

$$\frac{\partial C}{\partial t} = \frac{\partial C}{\partial \tau}\frac{\partial \tau}{\partial t} = \frac{\mu_0}{\rho a^2}\frac{\partial C}{\partial \tau} = \frac{\mu_0}{\rho a^2}(C_1-C_0)\frac{\partial \phi}{\partial \tau} \tag{4.104}$$

$$\frac{\partial C}{\partial y} = \frac{\partial C}{\partial \eta}\frac{\partial \eta}{\partial y} = \frac{1}{a}\frac{\partial C}{\partial \eta} = \frac{(C_1-C_0)}{a}\frac{\partial \phi}{\partial \eta} \tag{4.105}$$

$$\frac{\partial^2 C}{\partial y^2} = \frac{\partial}{\partial y}(\frac{\partial C}{\partial y}) = \frac{\partial}{\partial y}\left(\frac{(C_1-C_0)}{a}\frac{\partial \phi}{\partial \eta}\right) = \frac{(C_1-C_0)}{a^2}\frac{\partial^2 \phi}{\partial \eta^2} \tag{4.106}$$

$$\begin{aligned}
\frac{\partial}{\partial y}\left(\mu(T)\frac{\partial u}{\partial y}\right) &= \frac{\partial}{\partial y}(\mu(T))\frac{\partial u}{\partial y} + \mu(T)\frac{\partial^2 u}{\partial y^2} \\
&= \frac{\partial}{\partial \eta}(\mu(T))\frac{\partial \eta}{\partial y}\frac{\partial u}{\partial \eta}\frac{\partial \eta}{\partial y} + \mu(T)\frac{\partial^2 u}{\partial y^2} \\
&= \frac{1}{a^2}\frac{\partial}{\partial \eta}(\mu(T)\frac{\partial u}{\partial \eta} + \frac{(\mu_0)^2}{\rho a^3}e^{-\gamma_1\theta(T_w-T_0)}\frac{\partial^2 W}{\partial \eta^2} \\
&= \frac{\mu_0}{a^2}\frac{\partial}{\partial \eta}[e^{-\gamma_1\theta(T_w-T_0)}]\frac{\mu_0}{\rho a}\frac{\partial W}{\partial \eta} + \frac{(\mu_0)^2}{\rho a^3}e^{-\gamma_1\theta(T_w-T_0)}\frac{\partial^2 W}{\partial \eta^2} \\
&= \frac{(\mu_0)^2}{\rho a^3}\frac{\partial}{\partial \theta}(e^{-\gamma_1\theta(T_w-T_0)}\frac{\partial \theta}{\partial \eta}\frac{\partial W}{\eta} + \frac{(\mu_0)^2}{\rho a^3}e^{-\gamma_1\theta(T_w-T_0)}\frac{\partial^2 W}{\partial \eta^2} \\
&= \frac{-\gamma_1(T_w-T_0)(\mu_0)^2}{\rho a^3}e^{-\gamma_1\theta(T_w-T_0)}\frac{\partial \theta}{\partial \eta}\frac{\partial W}{\partial \eta} + \frac{(\mu_0)^2}{\rho a^3}e^{-\gamma_1\theta(T_w-T_0)}\frac{\partial^2 W}{\partial \eta^2} \\
&= \frac{(\mu_0)^2}{\rho a^3}e^{-\gamma_1\theta(T_w-T_0)}\left(\frac{\partial^2 W}{\partial \eta^2} - \gamma_1(T_w-T_0)\frac{\partial \theta}{\partial \eta}\frac{\partial W}{\partial \eta}\right)
\end{aligned}$$

Hence,

$$\frac{\partial}{\partial y}\left(\mu(T)\frac{\partial u}{\partial y}\right) = \frac{(\mu_0)^2}{\rho a^3}e^{-\gamma\theta}\left(\frac{\partial^2 W}{\partial \eta^2} - \gamma\frac{\partial \theta}{\partial \eta}\frac{\partial W}{\partial \eta}\right) \tag{4.107}$$

where $\gamma = \gamma_1(T_w-T_0)$.

By using (4.95)–(4.107), the dimensionless form of the governing equations (4.90)–(4.94) was derived as follows.

Continuity Equation

$\frac{\partial u}{\partial x} = 0$. But using (4.97) yields $\frac{\partial u}{\partial x} = \frac{\mu_0}{\rho a^2}\frac{\partial W}{\partial X}$. This implies that $\frac{\mu_0}{\rho a^2}\frac{\partial W}{\partial X} = 0$. Since $\frac{\mu_0}{\rho a^2} \neq 0$, we must have that $\frac{\partial W}{\partial X} = 0$.

Thus, the dimensionless equation of continuity takes the form:

$$\frac{\partial W}{\partial X} = 0 \tag{4.108}$$

Momentum Equation

$$\frac{\partial u}{\partial t}+V_0\frac{\partial u}{\partial y}=-\frac{1}{\rho}\frac{\partial P}{\partial x}+\frac{1}{\rho}\frac{\partial}{\partial y}\left[\mu(T)\frac{\partial u}{\partial y}\right]-\frac{\mu(T)u}{\rho K}-\frac{bu^2}{\sqrt{K}}+\beta_1 g(T-T_0)+\beta_2 g(C-C_0)$$

$$\begin{aligned}\Rightarrow (\frac{\mu_0}{\rho})^2\frac{1}{a^3}\frac{\partial W}{\partial \tau}+V_0\frac{\mu_0}{\rho a^2}\frac{\partial W}{\partial \eta}&=-\frac{\mu_0^2}{\rho^2 a^3}\frac{\partial P*}{\partial X}+\frac{\mu_0^2}{\rho^2 a^3}e^{-\gamma\theta}\left(\frac{\partial^2 W}{\partial \eta^2}-\gamma\frac{\partial \theta}{\partial \eta}\frac{\partial W}{\partial \eta}\right)\\ &\quad-\frac{\mu_0^2}{\rho^2 aK}e^{-\gamma\theta}W-\frac{b}{\sqrt{K}}\frac{\mu_0^2}{\rho^2 a^2}W^2+\beta_1 g(T_w-T_0)\theta+\beta_2 g(C_1-C_0)\phi\end{aligned}$$

$$\begin{aligned}\Rightarrow \frac{\partial W}{\partial \tau}+\frac{\rho V_0 a}{\mu_0}\frac{\partial W}{\partial \eta}&=-\frac{\partial P*}{\partial X}+e^{-\gamma\theta}\left(\frac{\partial^2 W}{\partial \eta^2}-\gamma\frac{\partial \theta}{\partial \eta}\frac{\partial W}{\partial \eta}\right)-\frac{a^2}{K}e^{-\gamma\theta}W-\frac{ba}{\sqrt{K}}W^2\\ &\quad+\frac{\beta_1 g\rho^2 a^3(T_w-T_0)}{\mu_0^2}\theta+\frac{\beta_2 g\rho^2 a^3(C_1-C_0)}{\mu_0^2}\phi\end{aligned}$$

$$\Rightarrow \frac{\partial W}{\partial \tau}+Re\frac{\partial W}{\partial \eta}=A+e^{-\gamma\theta}\left(\frac{\partial^2 W}{\partial \eta^2}-\gamma\frac{\partial \theta}{\partial \eta}\frac{\partial W}{\partial \eta}\right)-Se^{-\gamma\theta}W-FW^2+Gt\theta+Gc\phi$$

Hence, the dimensionless momentum equation takes the form:

$$\frac{\partial W}{\partial \tau}+Re\frac{\partial W}{\partial \eta}=A+e^{-\gamma\theta}\left(\frac{\partial^2 W}{\partial \eta^2}-\gamma\frac{\partial \theta}{\partial \eta}\frac{\partial W}{\partial \eta}\right)-Se^{-\gamma\theta}W-FW^2+Gt\theta+Gc\phi \qquad (4.109)$$

where $A=-\frac{\partial P^*}{\partial X}, Re=\frac{\rho V_0 a}{\mu_0}, S=\frac{a^2}{K}, F=\frac{ba}{\sqrt{K}}, Gt=\frac{\beta_1 g\rho^2 a^3(T_w-T_0)}{\mu_0^2}, Gc=\frac{\beta_2 g\rho^2 a^3(C_1-C_0)}{\mu_0^2}$.

Energy Equation

$$\frac{\partial T}{\partial t}+V_0\frac{\partial T}{\partial y}=\alpha_t\frac{\partial^2 T}{\partial y^2}+\Gamma\left[D_B\frac{\partial C}{\partial y}\frac{\partial T}{\partial y}+\frac{D_T}{T_0}(\frac{\partial T}{\partial y})^2\right]+\frac{\mu(T)}{\rho C_p}(\frac{\partial u}{\partial y})^2+\frac{\mu(T)u^2}{\rho C_p K}+\frac{bu^3}{C_p\sqrt{K}}$$

$$\begin{aligned}\Rightarrow \frac{\mu_0}{\rho a^2}(T_w-T_0)\frac{\partial \theta}{\partial \tau}+V_0\frac{(T_w-T_0)}{a}\frac{\partial \theta}{\partial \eta}&=\alpha_t\frac{(T_w-T_0)}{a^2}\frac{\partial^2 \theta}{\partial \eta^2}+\Gamma\Bigg[D_B\frac{(C_1-C_0)}{a}\frac{\partial \phi}{\partial \eta}\frac{(T_w-T_0)}{a}\frac{\partial \theta}{\partial \eta}\\ &\quad+\frac{D_T}{T_0}(\frac{(T_w-T_0)^2}{a^2}(\frac{\partial \theta}{\partial \eta})^2\Bigg]+\frac{\mu_0 e^{-\gamma\theta}}{\rho C_p}(\frac{\mu_0}{\rho a^2})^2(\frac{\partial W}{\partial \eta})^2\\ &\quad+(\frac{\mu_0}{\rho a})^2\frac{e^{-\gamma\theta}}{C_p K}W^2+(\frac{\mu_0}{\rho a})^3\frac{b}{C_p\sqrt{K}}W^3\end{aligned}$$

$$\begin{aligned}\Rightarrow \frac{\partial \theta}{\partial \tau}+\frac{a\rho V_0}{\mu_0}\frac{\partial \theta}{\partial \eta}&=\frac{\alpha_t\rho}{\mu_0}\frac{\partial^2 \theta}{\partial \eta^2}+\Gamma\Bigg[\frac{D_B(C_1-C_0)\rho}{\mu_0}\frac{\partial \phi}{\partial \eta}\frac{\partial \theta}{\partial \eta}+\frac{D_T}{T_0}(\frac{(T_w-T_0)\rho}{\mu_0}(\frac{\partial \theta}{\partial \eta})^2\Bigg]\\ &\quad+\left(\frac{\mu_0}{\rho a}\right)^2\frac{e^{-\gamma\theta}}{C_p(T_w-T_0)}(\frac{\partial W}{\partial \eta})^2+(\frac{\mu_0}{\rho a})^2\frac{e^{-\gamma\theta}}{C_p(T_w-T_0)}\frac{a^2}{K}W^2\\ &\quad+b\left(\frac{\mu_0}{\rho}\right)^2\frac{1}{a^2 C_p(T_w-T_0)}\frac{a}{\sqrt{K}}W^3\end{aligned}$$

$$\Rightarrow \frac{\partial \theta}{\partial \tau}+Re\frac{\partial \theta}{\partial \eta}=\frac{1}{Pr}\frac{\partial^2 \theta}{\partial \eta^2}+Nb\frac{\partial \phi}{\partial \eta}\frac{\partial \theta}{\partial \eta}+Nt(\frac{\partial \theta}{\partial \eta})^2+Ece^{-\gamma\theta}(\frac{\partial W}{\partial \eta})^2+EcSe^{-\gamma\theta}W^2+EcFW^3$$

Therefore, the dimensionless energy equation takes the following form.

$$\frac{\partial \theta}{\partial \tau}+Re\frac{\partial \theta}{\partial \eta}=\frac{1}{Pr}\frac{\partial^2 \theta}{\partial \eta^2}+Nb\frac{\partial \phi}{\partial \eta}\frac{\partial \theta}{\partial \eta}+Nt(\frac{\partial \theta}{\partial \eta})^2+Ece^{-\gamma\theta}(\frac{\partial W}{\partial \eta})^2+EcSe^{-\gamma\theta}W^2+EcFW^3 \tag{4.110}$$

where $Nt=\Gamma\frac{D_T}{T_0}(T_w-T_0)\frac{\rho}{\mu_0}, Nb=\Gamma D_B(C_1-C_0)\frac{\rho}{\mu_0}, Ec=\frac{\mu_0^2}{\rho^2 a^2 C_p(T_w-T_0)}, Pr=\frac{\mu_0}{\rho\alpha}$

Chemical Species Concentration Equation

$$\frac{\partial C}{\partial t}+V_0\frac{\partial C}{\partial y}=D_B\frac{\partial^2 C}{\partial y^2}+\frac{D_T}{T_0}\frac{\partial^2 T}{\partial y^2}$$

$$\Rightarrow \frac{\mu_0}{\rho a^2}(C_1-C_0)\frac{\partial \phi}{\partial \tau}+V_0\frac{(C_1-C_0)}{a}\frac{\partial \phi}{\partial \eta}=D_B\frac{(C_1-C_0)}{a^2}\frac{\partial^2 \phi}{\partial \eta^2}+\frac{D_T}{T_0}\frac{(T_w-T_0)}{a^2}\frac{\partial^2 \theta}{\partial \eta^2}$$

$$\Rightarrow \frac{\partial \phi}{\partial \tau}+\frac{\rho V_0 a}{\mu_0}\frac{\partial \phi}{\partial \eta}=D_B\frac{\rho}{\mu_0}\frac{\partial^2 \phi}{\partial \eta^2}+\frac{D_T}{T_0}\frac{\rho}{\mu_0}\frac{(T_w-T_0)}{(C_1-C_0)}\frac{\partial^2 \theta}{\partial \eta^2}$$

$$\Rightarrow \frac{\partial \phi}{\partial \tau}+\frac{\rho V_0 a}{\mu_0}\frac{\partial \phi}{\partial \eta}=D_B\frac{\rho}{\mu_0}\left[\frac{\partial^2 \phi}{\partial \eta^2}+\frac{D_T}{D_B T_0}\frac{(T_w-T_0)}{(C_1-C_0)}\frac{\partial^2 \theta}{\partial \eta^2}\right]$$

$$\Rightarrow \frac{\partial \phi}{\partial \tau}+Re\frac{\partial \phi}{\partial \eta}=\frac{1}{Sc}\left[\frac{\partial^2 \phi}{\partial \eta^2}+\frac{Nt}{Nb}\frac{\partial^2 \theta}{\partial \eta^2}\right]$$

Thus, the dimensionless form of the concentration equation is given by

$$\frac{\partial \phi}{\partial \tau}+Re\frac{\partial \phi}{\partial \eta}=\frac{1}{Sc}\left[\frac{\partial^2 \phi}{\partial \eta^2}+\frac{Nt}{Nb}\frac{\partial^2 \theta}{\partial \eta^2}\right] \tag{4.111}$$

where $Sc=\frac{\mu_0}{\rho D_B}$.

Initial and Boundary Conditions

$$u(y,0)=0 \text{ and } u(0,t)=0 \Rightarrow W(\eta,0)=0 \text{ and } W(0,\tau)=0$$

$$u(a,t)=0 \Rightarrow W(1,\tau)=0 \text{ since } y=a \text{ gives } \eta=1 \text{ because } \eta=\frac{y}{a}$$

$$T(y,0)=T_0 \Rightarrow \theta(\eta,0)(T_w-T_0)+T_0=T_0 \text{ since } \theta=\frac{T-T_w}{T_w-T_0}$$

$$\Rightarrow \theta(\eta,0)(T_w-T_0)=0$$

$$\Rightarrow \theta(\eta,0)=0$$

$$\begin{aligned}
\text{Similarly, } T(0,t) = T_0 &\Rightarrow \theta(0,\tau)(T_w - T_0) + T_0 = T_0 \\
&\Rightarrow \theta(0,\tau)(T_w - T_0) = 0 \\
&\Rightarrow \theta(0,\tau) = 0
\end{aligned}$$

$$\begin{aligned}
T(a,t) = T_w &\Rightarrow \theta(1,\tau)(T_w - T_0) + T_0 = T_w \\
&\Rightarrow \theta(1,\tau)(T_w - T_0) = T_w - T_0 \\
&\Rightarrow \theta(1,\tau) = \frac{T_w - T_0}{T_w - T_0} = 1
\end{aligned}$$

$$\begin{aligned}
C(y,0) = C_0 &\Rightarrow \phi(\eta,0)(C_1 - C_0) + C_0 = C_0 \text{ since } \phi = \frac{C - C_0}{C_1 - C_0} \\
&\Rightarrow \phi(\eta,0)(C_1 - C_0) = 0 \\
&\Rightarrow \phi(\eta,0) = 0
\end{aligned}$$

$$\begin{aligned}
C(a,t) = C_1 &\Rightarrow \phi(1,\tau)(C_1 - C_0) + C_0 = C_1 \\
&\Rightarrow \phi(1,\tau)(C_1 - C_0) = C_1 - C_0 \\
&\Rightarrow \phi(1,\tau) = \frac{C_1 - C_0}{C_1 - C_0} = 1
\end{aligned}$$

$$\begin{aligned}
D_B\frac{\partial C(0,t)}{\partial y} = \frac{-D_T}{T_0}\frac{\partial T(0,t)}{\partial y} &\Rightarrow D_B\frac{(C_1 - C_0)}{a}\frac{\partial \phi(0,\tau)}{\partial \eta} = -\frac{D_T}{T_0}\frac{(T_w - T_0)}{a}\frac{\partial \theta(0,\tau)}{\partial \eta} \\
&\Rightarrow \frac{\partial \phi(0,\tau)}{\partial \eta} = -\frac{D_T}{T_0 D_B}\frac{(T_w - T_0)}{(C_1 - C_0)}\frac{\partial \theta(0,\tau)}{\partial \eta} \\
&\Rightarrow \frac{\partial \phi(0,\tau)}{\partial \eta} = -\frac{Nt}{Nb}\frac{\partial \theta(0,\tau)}{\partial \eta} \\
&\Rightarrow Nb\frac{\partial \phi(0,\tau)}{\partial \eta} + Nt\frac{\partial \theta(0,\tau)}{\partial \eta} = 0
\end{aligned}$$

Therefore, the dimensionless initial and boundary conditions have the following form.

$$W(\eta,0) = 0, \theta(\eta,0) = 0, \phi(\eta,0) = 0 \text{ and } \left.\begin{array}{l} W(0,\tau) = 0, \theta(0,\tau) = 0, \\ Nb\frac{\partial \phi(0,\tau)}{\partial \eta} + Nt\frac{\partial \theta(0,\tau)}{\partial \eta} = 0, \\ W(1,\tau) = 0, \theta(1,\tau) = 1, \\ \phi(1,\tau) = 1 \end{array}\right\} \text{for } \tau > 0 \tag{4.112}$$

In general the non-dimensional form of the governing equations with the corresponding non-dimensional initial and boundary conditions are summarized as follows.

$$\frac{\partial W}{\partial X} = 0 \tag{4.113}$$

$$\frac{\partial W}{\partial \tau} + Re\frac{\partial W}{\partial \eta} = A + e^{-\lambda\theta}\left[\frac{\partial^2 W}{\partial \eta^2} - \lambda\frac{\partial \theta}{\partial \eta}\frac{\partial W}{\partial \eta}\right] - e^{-\lambda\theta}S^2W - FW^2 + Gt\theta + Gc\phi \tag{4.114}$$

$$\frac{\partial\theta}{\partial\tau}+Re\frac{\partial\theta}{\partial\eta}=\frac{1}{Pr}\frac{\partial^2\theta}{\partial\eta^2}+Nb\frac{\partial\phi}{\partial\eta}\frac{\partial\theta}{\partial\eta}+Nt(\frac{\partial\theta}{\partial\eta})^2+Ece^{-\lambda\theta}(\frac{\partial W}{\partial\eta})^2+S^2Ece^{-\lambda\theta}W^2+FEcW^3 \tag{4.115}$$

$$\frac{\partial\phi}{\partial\tau}+Re\frac{\partial\phi}{\partial\eta}=\frac{1}{Sc}\left[\frac{\partial^2\phi}{\partial\eta^2}+\frac{Nt}{Nb}\frac{\partial^2\theta}{\partial\eta^2}\right] \tag{4.116}$$

with the initial and boundary conditions:

$$W(\eta,0)=0,\theta(\eta,0)=0,\phi(\eta,0)=0 \text{ and } \left.\begin{array}{l} W(0,\tau)=0,\theta(0,\tau)=0,\\ Nb\frac{\partial\phi(0,\tau)}{\partial\eta}+Nt\frac{\partial\theta(0,\tau)}{\partial\eta}=0,\\ W(1,\tau)=0,\theta(1,\tau)=1,\\ \phi(1,\tau)=1 \end{array}\right\} \text{for } \tau>0 \tag{4.117}$$

where τ is dimensionless time, Re is the suction/injection Reynolds number, Gt is the Grashof number due to thermal buoyancy effect, Gc is the Grashof number due to solutal buoyancy effect, Ec is the Eckert number, Pr is the Prandtl number, A is dimensionless axial pressure gradient parameter, γ is the dimensionless viscosity variation parameter, S is the porous media shape factor parameter and F is the Forchheimer number also called the Forchheimer inertial resistance which is the second order porous media resistance parameter, Sc is the Schmidt number, Nb is the Brownian motion parameter and Nt is the thermophoresis parameter.

4.3 Physical Quantities of Engineering Interests

Other physical quantities of practical significance in this study are the wall shear stress (or skin friction coefficient C_f), the wall heat transfer rate (or local Nusselt number Nu) and the wall mass transfer rate (or local Sherwood number Sh). In the study of fluid flow and thermal systems, it is mandatory to examine the influences of the thermophysical parameters on C_f, Nu and Sh. This is because, the consequences of excessive heat generation is not only evaluated from the economy perspectives like the efficient operation of machinery, property destruction etc. but also it may jeopardizes the lives of machine operating personnel. Therefore, the dimensionless skin friction coefficient C_f, local Nusselt number Nu and local Sherwood number Sh at the microchannel walls are derived as follows.

The Wall Shear Stress: Skin Friction Coefficient (C_f)

$$C_f=\frac{\rho a^2\tau_w}{\mu_0^2},\ \text{where}\ \tau_w=\mu(T)\frac{\partial u}{\partial y}\bigg|_{y=0,a}=\mu_0e^{-\gamma\theta}\frac{\mu_0}{\rho a^2}\frac{\partial W}{\partial\eta}\bigg|_{\eta=0,1}$$

$$\Rightarrow C_f=\frac{\rho a^2}{\mu_0^2}\mu_0e^{-\gamma\theta}\frac{\mu_0}{\rho a^2}\frac{\partial W}{\partial\eta}\bigg|_{\eta=0,1}=e^{-\gamma\theta}\frac{\partial W}{\partial\eta}\bigg|_{\eta=0,1}$$

Hence, the dimensionless skin friction coefficient is given by:

$$C_f = e^{-\gamma\theta}\frac{\partial W}{\partial \eta}\bigg|_{\eta=0,1} \tag{4.118}$$

The Wall Heat Transfer Rate: Nusselt Number (*Nu*)

$$Nu = \frac{aq_w}{k(T_w - T_0)} \text{ where } q_w = -k\frac{\partial T}{\partial y}\bigg|_{y=0,a} = -\frac{k(T_w - T_0)}{a}\frac{\partial \theta}{\partial \eta}\bigg|_{\eta=0,1}$$
$$\Rightarrow Nu = \frac{aq_w}{k(T_w - T_0)} = \frac{-a}{k(T_w - T_0)}\frac{k(T_w - T_0)}{a}\frac{\partial \theta}{\partial \eta}\bigg|_{\eta=0,1} = -\frac{\partial \theta}{\partial \eta}\bigg|_{\eta=0,1}$$

Thus, the dimensionless Nusselt number is given by:

$$Nu = -\frac{\partial \theta}{\partial \eta}\bigg|_{\eta=0,1} \tag{4.119}$$

The Wall Mass Transfer Rate: Sherwood Number (*Sh*)

$$Sh = \frac{aj_w}{D_B(C_1 - C_0)} \text{ where } j_w = -D_B\frac{\partial C}{\partial y}\bigg|_{y=0,a} = -\frac{D_B(C_1 - C_0)}{a}\frac{\partial \phi}{\partial \eta}\bigg|_{\eta=0,1}$$
$$\Rightarrow Sh = \frac{aj_w}{D_B(C_1 - C_0)} = \frac{-a}{D_B(C_1 - C_0)}\frac{D_B(C_1 - C_0)}{a}\frac{\partial \phi}{\partial \eta}\bigg|_{\eta=0,1} = -\frac{\partial \phi}{\partial \eta}\bigg|_{\eta=0,1}$$

So, the dimensionless Sherwood number is given by:

$$Sh = -\frac{\partial \phi}{\partial \eta}\bigg|_{\eta=0,1} \tag{4.120}$$

4.4 Numerical Solutions

The semi-discretization finite difference scheme also known as the numerical method of lines (MOL) which is basically proceeds in two steps namely the space discretization and the time integration was applied to solve the governing equations (4.114)–(4.116) with initial and boundary conditions (4.117). This version is also known as the vertical method of lines which is discrete in space and continuous in time. In the space discretization, the spatial derivatives are first approximated using finite difference method in such a way that the partial differential equations (PDEs) are transformed into a system of ordinary differential equations (ODEs) corresponding to the solution at some grid points as a function of time.

The discretization of the governing equations is based on a linear cartesian mesh and uniform grid on which finite differences are taken. Both the second and first spatial derivatives are approximated by second-order central differences. The equations corresponding to the first and last grid points are modified to incorporate the boundary conditions. The resulting nonlinear system of the initial value problem (IVP) is then solved iteratively using the well known fourth order Runge-Kutta method in MAPLE software. Thus, the semi-discretization scheme for the velocity, temperature and concentration fields are recorded as follows.

$$\begin{aligned}\frac{dW_i}{d\tau} &= A - Re\frac{W_{i+1}-W_{i-1}}{2\Delta\eta} - e^{-\gamma\theta_i}S^2W_i - FW_i^2 + Gt\theta_i + Gc\phi_i \\ &+ e^{-\gamma\theta_i}\left[\frac{W_{i-1}-2W_i+W_{i+1}}{(\Delta\eta)^2} - \gamma\frac{\theta_{i+1}-\theta_{i-1}}{2\Delta\eta}\cdot\frac{W_{i+1}-W_{i-1}}{2\Delta\eta}\right]\end{aligned} \tag{4.121}$$

$$\begin{aligned}\frac{d\theta_i}{d\tau} &= -Re\frac{\theta_{i+1}-\theta_{i-1}}{2\Delta\eta} + \frac{1}{Pr}\frac{\theta_{i-1}-2\theta_i+\theta_{i+1}}{(\Delta\eta)^2} + Nb\frac{\phi_{i+1}-\phi_{i-1}}{2\Delta\eta}\cdot\frac{\theta_{i+1}-\theta_{i-1}}{2\Delta\eta} \\ &+ Nt\left[\frac{\theta_{i+1}-\theta_{i-1}}{2\Delta\eta}\right]^2 + Ece^{-\gamma\theta_i}\left[\frac{W_{i+1}-W_{i-1}}{2\Delta\eta}\right]^2 + S^2EcW_i^2 + S^2EcW_i^3\end{aligned} \tag{4.122}$$

$$\frac{d\phi_i}{d\tau} = -Re\frac{\phi_{i+1}-\phi_{i-1}}{2\Delta\eta} + \frac{1}{Sc}\left[\frac{\phi_{i-1}-2\phi_i+\phi_{i+1}}{(\Delta\eta)^2} + \frac{Nt}{Nb}\cdot\frac{\theta_{i-1}-2\theta_i+\theta_{i+1}}{(\Delta\eta)^2}\right] \tag{4.123}$$

with initial conditions

$$W_i(0) = 0, \ \ \theta_i(0) = 0, \ \ \phi_i(0) = 0 \tag{4.124}$$

where, $W_i(\tau) = W(\eta_i,\tau), \theta_i(\tau) = \theta(\eta_i,\tau), \phi_i(\tau) = \phi(\eta_i,\tau)$ and the spatial interval $[0,1]$ partitioned into N equal sub-intervals. The grid size and the grid points are defined as $\Delta\eta = \frac{1}{N}$ and $\eta_i = \frac{i-1}{\Delta\eta}$ for $1 \leq i \leq N+1$.

4.5 Results and Discussion

4.5.1 Transient and Steady State Profiles

The transient and steady state profiles for the velocity, temperature and concentration are portrayed in figures 4.3(a), 4.3(b) and 4.4 respectively. From these figures it can be observed that the velocity, temperature and concentration profiles show parabolic shapes with transient increase and reach the steady states at about $\tau \geq 0.9$. Besides, figure 4.3(a) indicates that the velocity profile attains its maximum value around the microchannel center line region and then reduces to zero because of the no-slip boundary conditions. Figure 4.3(b) demonstrates that the temperature profile attained its lowest value at the right wall and gradually increasing towards the left wall where it attained its pick value whereas figure 4.4 shows that the concentration profile attained its pick value at the right wall and starts decreasing gradually towards the left wall where it attains its lowest value.

4.5.2 Parameter Dependent Solutions

Figures 4.5(a), 4.5(b) and 4.6 are double graphs that portray the effects of *Re* and *A* on the fluid velocity, temperature and concentration profiles. In the current study, it was assumed

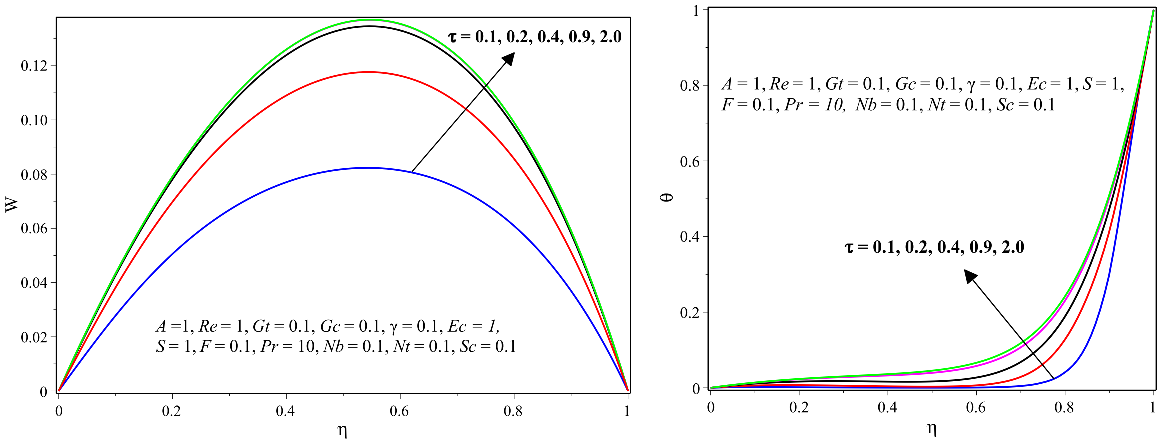

(a) **(b)**

Figure 4.3: **(a)** Velocity and **(b)** Temperature profiles with transient and steady state solutions

that there is a uniform fluid injection into the flow regime at the left permeable wall (vertical line $\eta = 0$) and suction out at the right wall (vertical line $\eta = 1$). Figures 4.5(a) and 4.5(b) portray that as the values of the suction/injection Reynolds number *Re* increases, both the velocity and temperature profiles tend to decline and also it can be seen that the velocity profile shows slightly skewing behavior towards the right wall of the microchannel. This result is similar to the one obtained by Rundora and Makinde (2018). Indeed, the argument for this result may be ascribed to the fact that as a fluid is sucked out of the right wall, the velocity towards the right wall is higher than elsewhere in the microchannel and this in turn increases the rate of convective heat transfer out of the right wall resulting in a significant drop in fluid temperature.

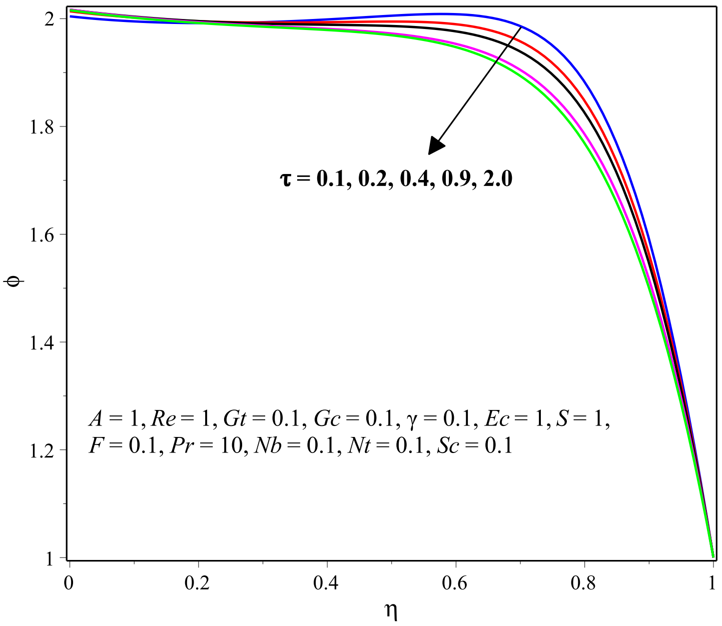

Figure 4.4: Transient and steady state solution of concentration profile

Figures 4.5(a) and 4.5(b) also reveal that both the fluid velocity and temperature profiles increase as the pressure gradient parameter A increases. This is the case because the fluid motion is due to the pressure gradient and hence as A increases the fluid moves faster which in turn increases the fluid velocity and temperature. Re and A have shown the opposite effects on the concentration profile as depicted in figure 4.6.

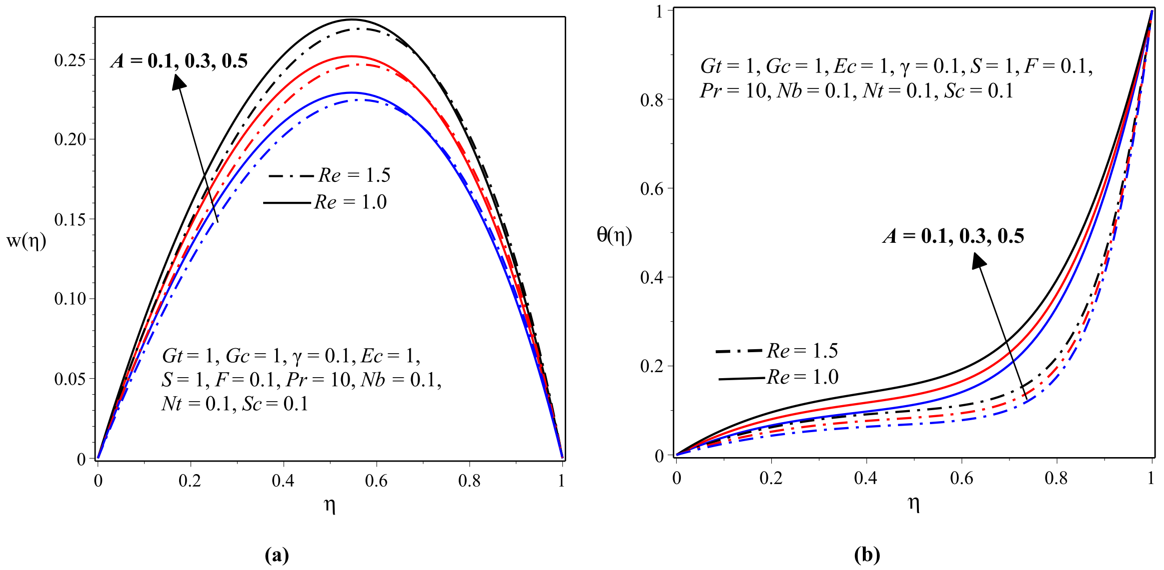

Figure 4.5: **(a)** Velocity and **(b)** Temperature profiles with varying A and Re

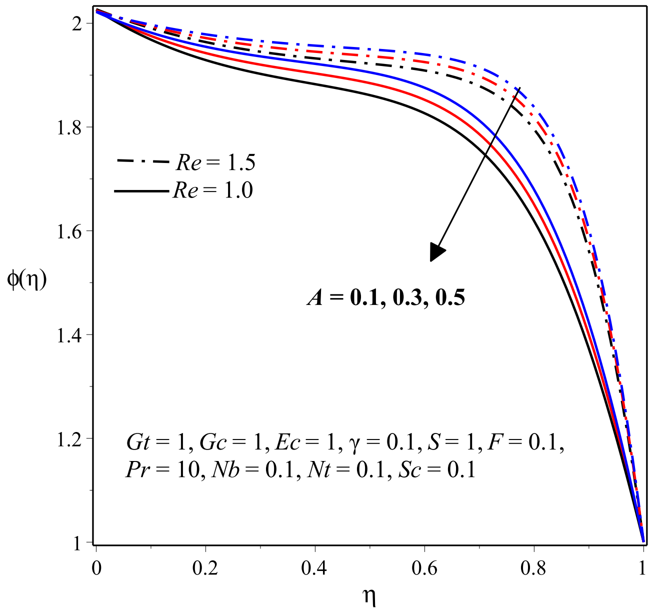

Figure 4.6: Effects of A and Re on concentration profile

Figures 4.7(a), 4.7(b) and 4.8 display the effects of the thermal Grashof number Gt and the solutal Grashof number Gc on velocity, temperature and concentration profiles. The velocity and temperature profiles increase with Gt and Gc as shown in figures 4.7(a) and 4.7(b).

This is the case because as the values of Gt and Gc enhanced, the body forces acting on the fluid (thermal and solutal buoyancy forces) also get enhanced which also enhance the velocity that in turn increase the viscous heating and hence increasing the fluid temperature. The opposite scenario is demonstrated in figure 4.8 for the concentration profile due to the fact that a small temperature increment will cause a very small decrement in the concentration which is also known as the cross-diffusion effect.

Figures 4.9(a) and 4.9(b) portray that as the dimensionless variable viscosity parameter γ increases a significant rise in the fluid velocity and temperature profiles is observed. This is the case because an increase in γ reduces the fluid viscosity since $\mu(T) = \mu_0 e^{-\gamma\theta}$. So, the fluid becomes less viscous and hence friction between fluid layers decrease due to which fluid velocity remains at higher levels for higher values of γ. Rundora and Makinde (2018) reported a similar result. However, increasing the values of γ decreases the concentration profile as indicated in figure 4.11(a).

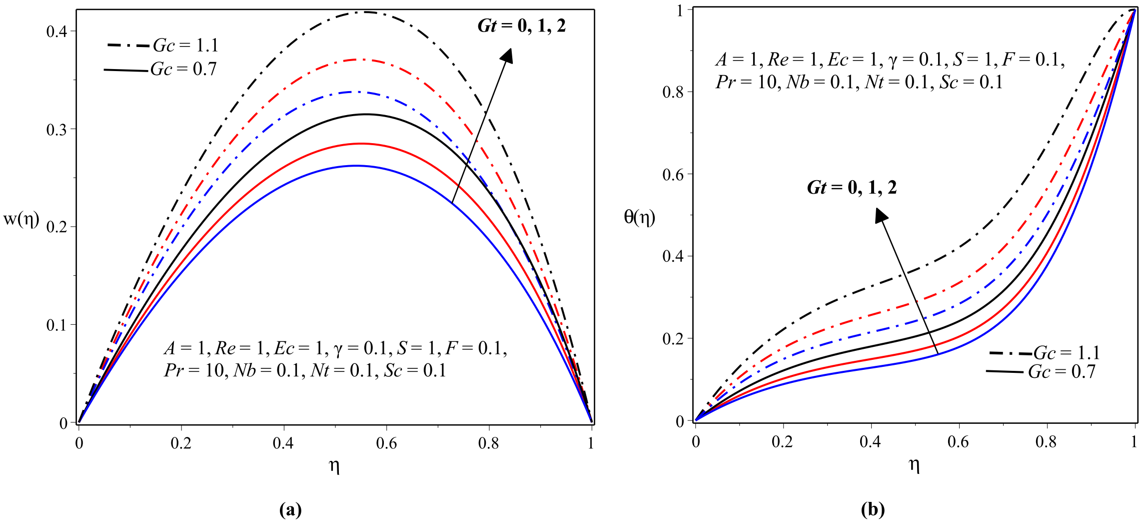

Figure 4.7: **(a)** Velocity and **(b)** Temperature profiles with varying Gt and Gc

The effects of the Eckert number Ec on the fluid velocity, temperature and concentration profiles are depicted in figures 4.10(a), 4.10(b) and 4.11(b) respectively. From figures 4.10(a) and 4.10(b), it is observed that as the magnitude of Ec increases, both the fluid velocity and temperature also increase. This result is similar to the one obtained in the papers (Rundora and Makinde, 2018) and (Makinde et al., 2019). Physically, the Eckert number Ec expresses the relationship between the flow boundary layer enthalpy difference and its kinetic energy which results in more heat to produce and hence Ec characterizes the viscous heating within the flow. Therefore, as the magnitude of Ec rises the viscous heating will be enhanced within the flow resulting in the fluid temperature increment which in turn increases the fluid velocity. Figure 4.11(b) displays the opposite phenomena for the concentration profile.

Figures 4.12(a)–4.14(b) depict the effects of the porous medium parameters S and F on the velocity, temperature and concentration profiles. Figures 4.12(a) and 4.12(b) portray that

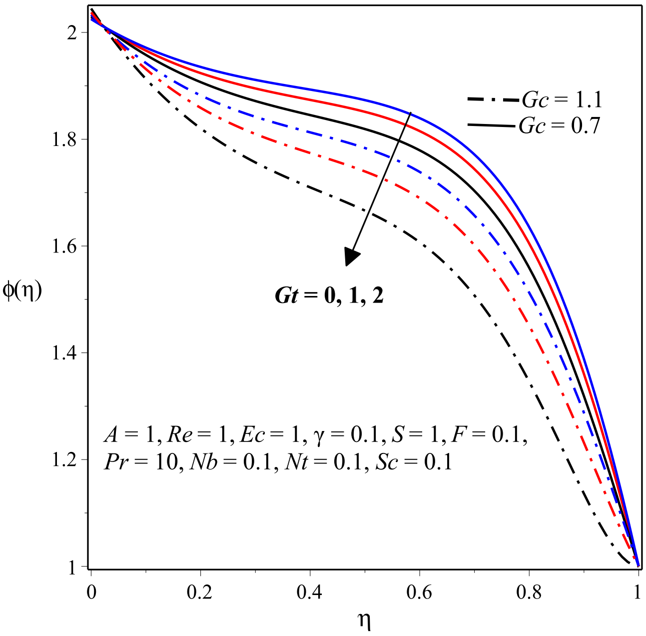

Figure 4.8: Effects of Gt and Gc on concentration profile

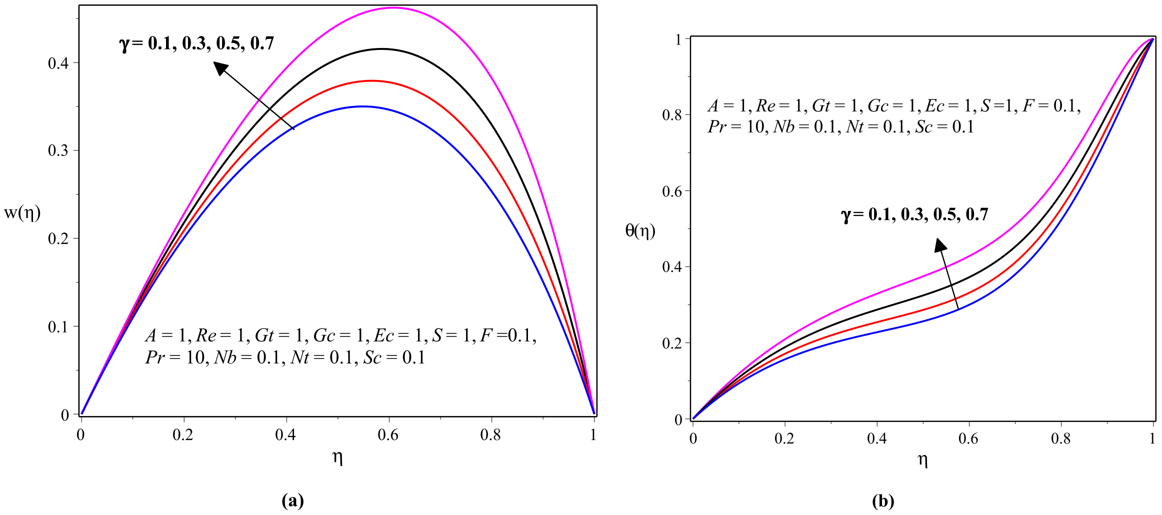

Figure 4.9: **(a)** Velocity and **(b)** Temperature profiles with varying γ

both the velocity and temperature profiles decrease significantly as the porous medium shape parameter S increases. From the literature, the studies in (Rundora and Makinde, 2018) and (Makinde and Rundora, 2018) reported similar results. The reason behind this result is the fact that as the value of S increases, the porous medium permeability decreases which should naturally dampens the fluid flow and thus the observed decline in the magnitude of fluid velocity which also results in the decrement of viscous heating which in turn decreases the magnitude of fluid temperature. On the contrary, figure 4.14(a) reveals that as the porous medium shape parameter S increases the concentration profile increases.

In figures 4.13(a) and 4.13(b), it is observed that the fluid velocity and temperature profiles decrease with increasing values of the Forchheimer number F which is also known as

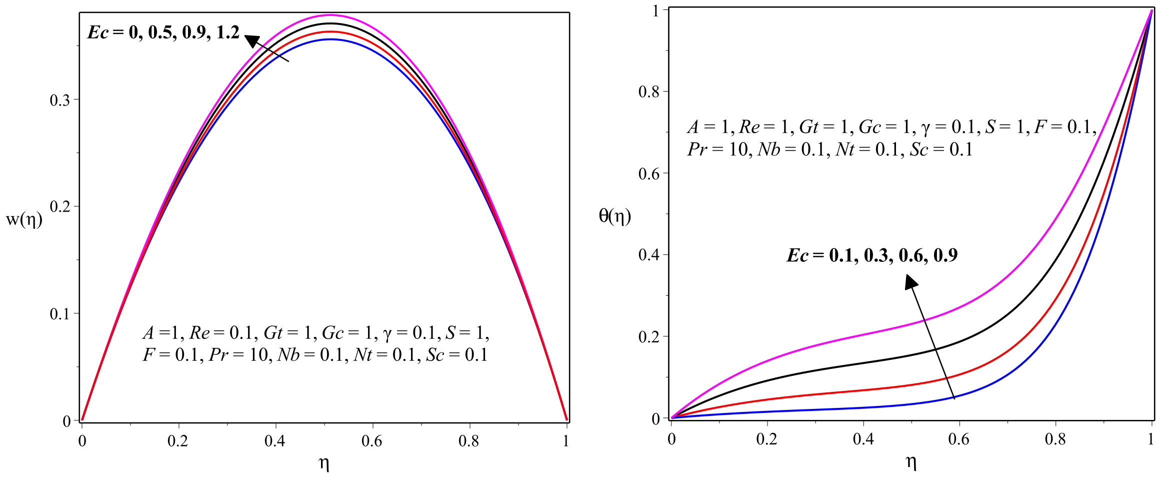

(a) **(b)**

Figure 4.10: **(a)** Velocity and **(b)** Temperature profiles with varying Ec

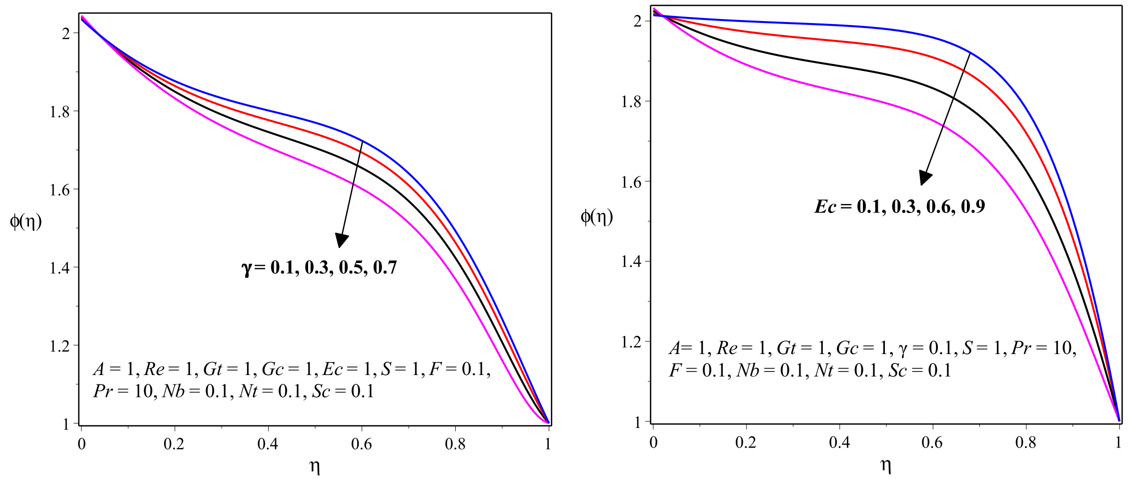

(a) **(b)**

Figure 4.11: **(a)** Effect of γ on concentration profile and **(b)** Effect of Ec on concentration profile

inertial resistance parameter. Physically, large values of F implies the stronger resistant inertial force in the direction normal to the fluid flow which is due to the intensive dimensionless drag force coefficient b since $F = \frac{ba}{\rho\sqrt{K}}$. For higher values of b stronger resistivity inertial force is effective within the fluid flow so that the velocity becomes lessen and consequently the fluid temperature decreases. From figure 4.14(b), we can see that the Forchheimer number F shows the opposite effect on the concentration profile.

Figures 4.15(a) and 4.15(b) are double graphs that display the effects of the Prandtl number Pr and the thermophoresis parameter Nt on the velocity and temperature profiles. Accordingly, the larger values of Pr leads to a significant decrease in the temperature profile since higher values of Pr corresponds to low thermal diffusivity of the fluid (Pr and thermal diffusivity have inverse relationship) which reduces the rate at which heat is transported from

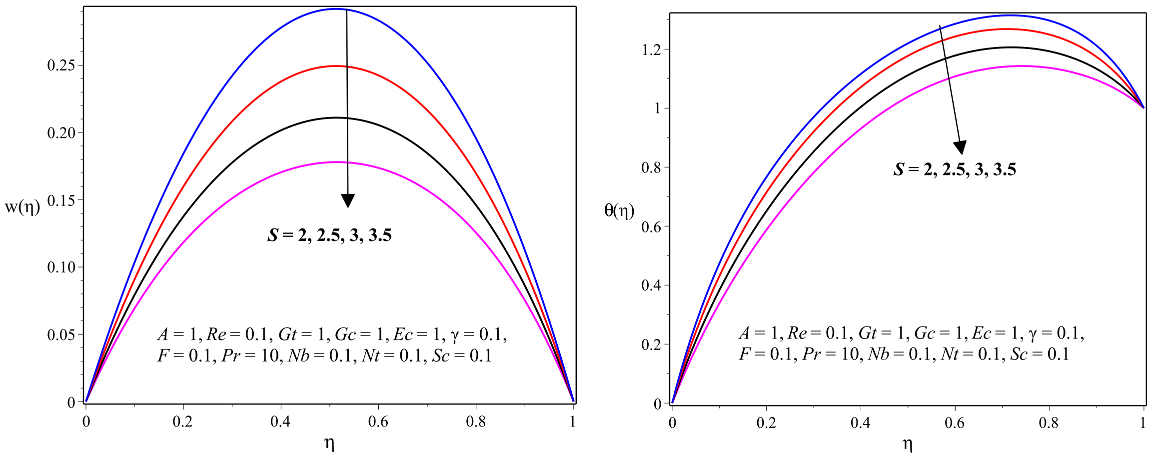

(a) **(b)**

Figure 4.12: **(a)** Velocity and **(b)** Temperature profiles with varying S

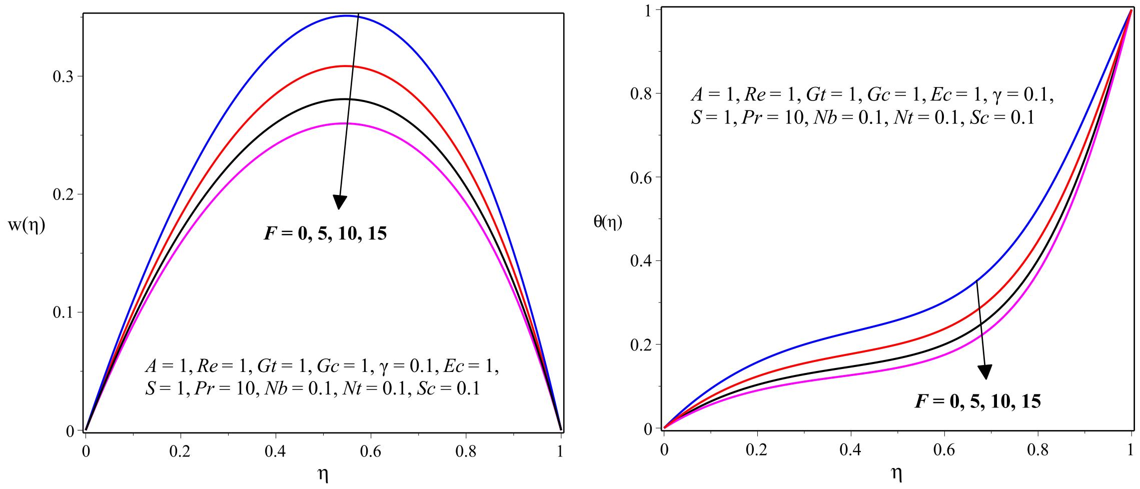

(a) **(b)**

Figure 4.13: **(a)** Velocity and **(b)** Temperature profiles with varying F

the heated microchannel walls into the fluid that was initially at zero temperature. Hence, as observed in figure 4.15(b) the fluid temperature decreases as the value of Pr increases which in turn decreases the fluid velocity profile as shown in figure 4.15(a). This result is similar to the one obtained by Makinde et al. (2019), Makinde and Rundora (2018) and Sarkar et al. (2019) but the opposite was observed in Rundora and Makinde (2018). On the other hand, thermophoresis is a mechanism in which small particles are pulled away from hot surface to cold one and thus, figures 4.15(a) and 4.15(b) declare that as the value of Nt enhances, both the velocity and temperature profiles also enhance. The reason behind this argument is that an enhancement in Nt yields a stronger thermophoretic force which allows deeper migration of nanoparticles from hot surface to cold fluid resulting in higher fluid temperature which in turn results in higher fluid velocity. Figure 4.16(a) shows that the concentration profile increases with both the Prandtl number Pr and the thermophoresis parameter Nt.

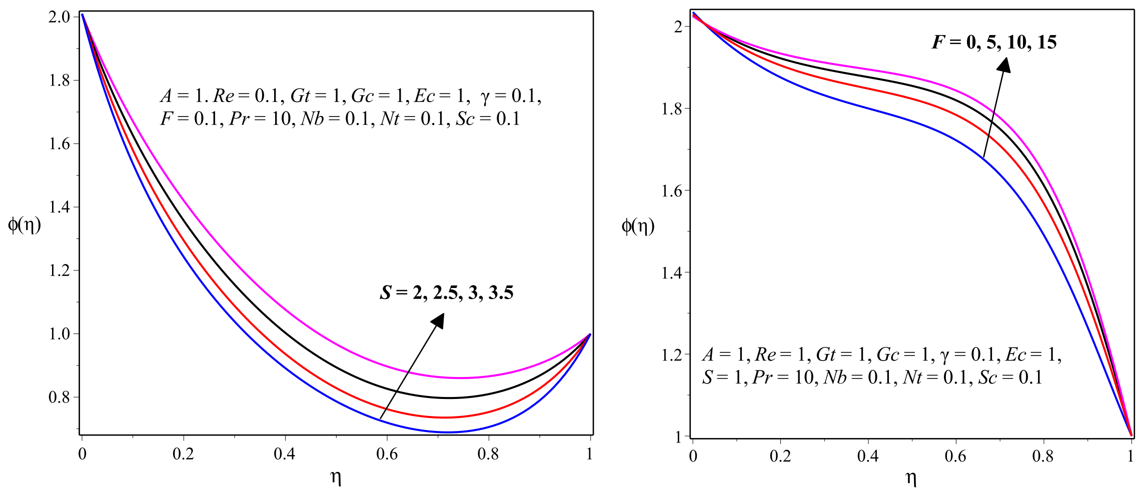

(a) **(b)**

Figure 4.14: **(a)** Effect of S on concentration profile and **(b)** Effect of F on concentration profile

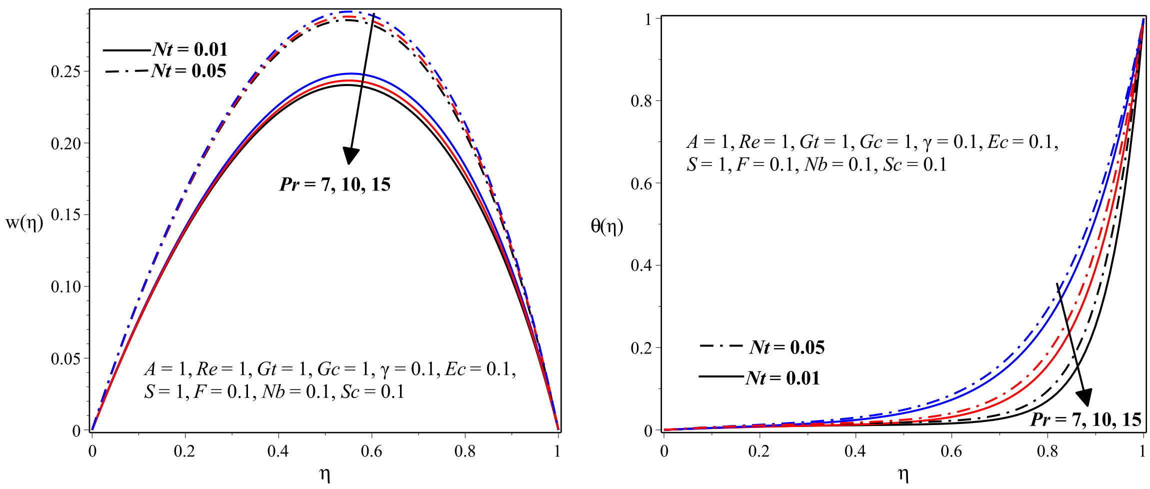

(a) **(b)**

Figure 4.15: **(a)** Velocity and **(b)** Temperature profiles with varying Pr and Nt

Figure 4.16(b) is also a double graph that displays the effects of Sc and Nb on the concentration profile. It shows that the concentration profile increases with the Schmidt number Sc. Physically, larger values of Schmidt number Sc indicate less mass diffusion which causes the concentration of nanoparticles to remain larger in the fluid. On the other hand, the Brownian motion is an arbitrary disorganized motion of nanoparticles dispersed in the base fluid resulting from their collision with moving molecules of the base fluid. Consequently, the concentration profile shows a decreasing behavior with increasing values of the Brownian diffusion parameter Nb as shown in figure 4.16(b). The argument behind this result is that when the magnitudes of Nb increases, the random motion and also collision of the nanoparticles in the fluid increase which reduce the concentration of the nanoparticles in the fluid. Similar results were observed for the nanofluid velocity and temperature as illustrated in

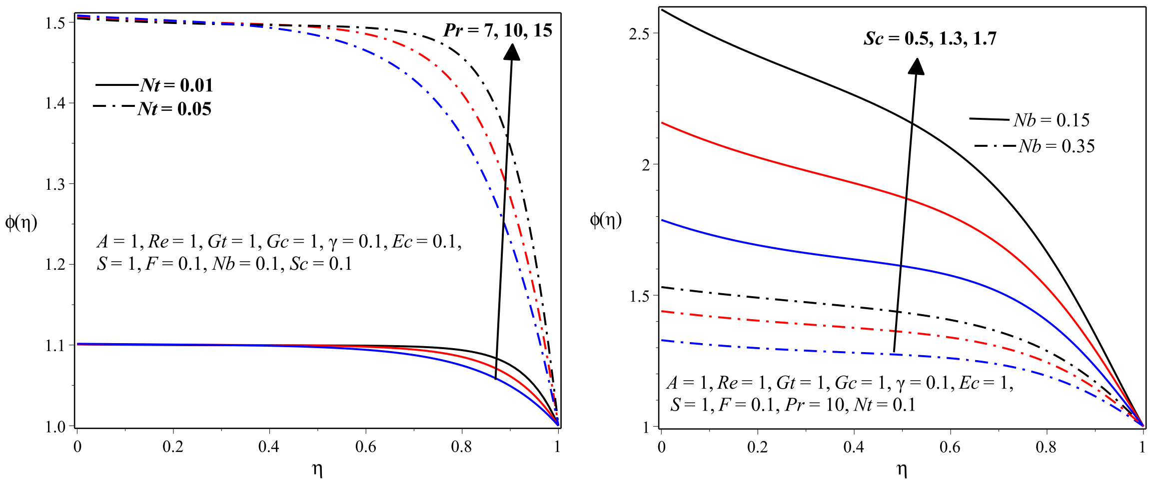

(a) **(b)**

Figure 4.16: **(a)** Effects of Pr and Nt on concentration profile and **(b)** Effects of Sc and Nb on concentration profile

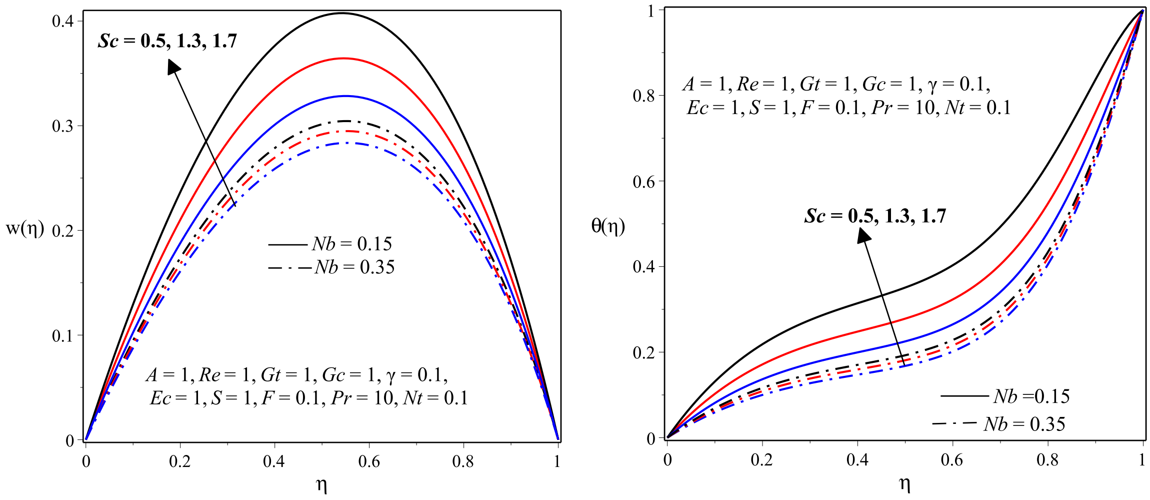

(a) **(b)**

Figure 4.17: **(a)** Velocity and **(b)** Temperature profiles with varying Sc and Nb

figures 4.17(a) and 4.17(b) respectively.

4.5.3 The Wall Shear Stress, Wall Heat and Mass Transfer Rates

This subsection comprises the effects of flow parameters on the wall shear stress, wall heat and mass transfer rates. Indeed, the graphical results that are illustrated in this subsection for the skin friction coefficient C_f, the Nusselt number Nu and the Sherwood number Sh are plotted for large time, say $\tau \geq 2$ (steady state) and thus the results obtained may not be affected by time increasing for all parameters values as a consequence of the results obtained in subsection 4.5.1.

The Wall Shear Stress: Skin Friction Coefficient

The effects of pertinent parameters on the wall shear stress at the left wall $\eta = 0$ and at the right wall $\eta = 1$ are illustrated in figures 4.18(a)-4.21(b). Consequently, from these graphs it can be observed that the wall shear stress, coefficient of skin friction C_f (at both left and right walls) shows an increasing behavior with increasing values of the Eckert number Ec and the thermal Grashof number Gt for varying scaled values of the suction/injection Reynolds number Re. The results in the works of Rundora and Makinde (2018) and Makinde et al. (2019) are similar with the outcomes of the present work. The pressure gradient parameter A, the Schmidt number Sc and the Prandtl number Pr also show an increasing effect on C_f (at both left and right walls) for varying scaled values of the suction/injection Reynolds number Re. However, the Forchheimer number F and the porous medium shape parameter S have a decreasing effect on C_f at both walls of the microchannel. In addition, C_f increases as the values of the variable viscosity parameter γ increases at the left wall of the microchannel $\eta = 0$ (see figure 4.21(a)) whereas C_f decreases with increasing values of the variable viscosity parameter γ at the right wall $\eta = 1$ (see figure 4.21(b)).

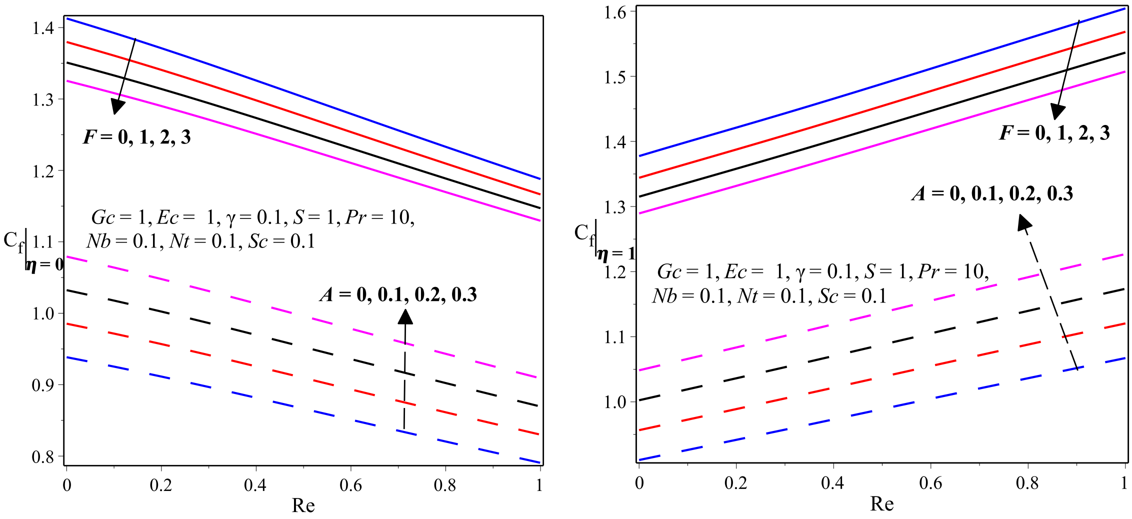

(a) **(b)**

Figure 4.18: **(a)** Skin friction at $\eta = 0$ and **(b)** Skin friction at $\eta = 1$ with varying A, F and Re

The Wall Heat Transfer Rate: Nusselt Number

The effects of prominent governing flow parameters on the wall heat transfer rate at the left wall $\eta = 0$ and at the right wall $\eta = 1$ are portrayed in figures 4.22(a)-4.25(b). Accordingly, from these graphs it can be seen that the wall heat transfer rate, the Nusselt number Nu at both left and right walls shows an increasing behavior with increasing values of the variable viscosity parameter γ and the thermal Grashof number Gt for varying scaled values of the suction/injection Reynolds number Re. This result is similar to the one obtained by Rundora

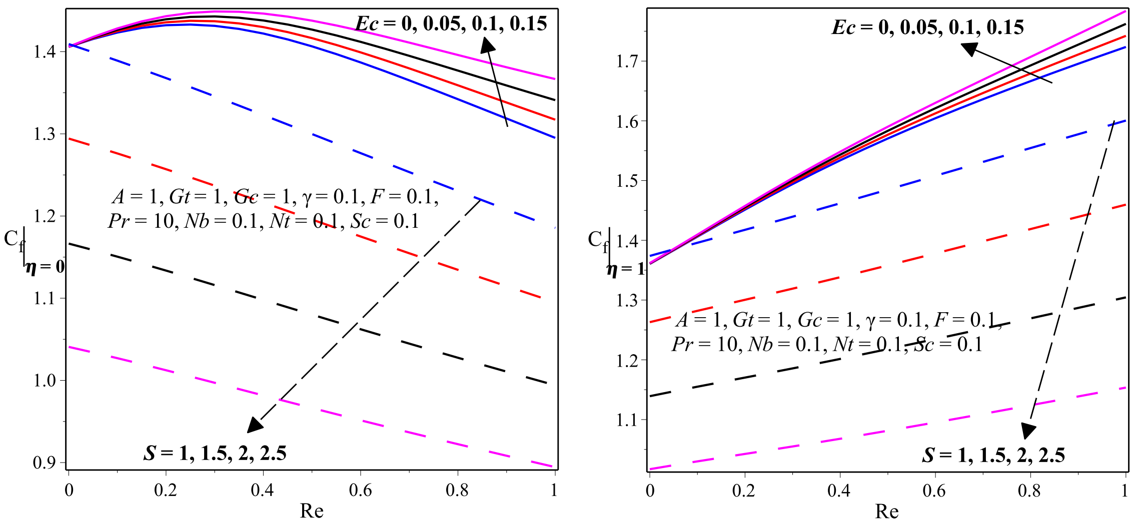

(a) **(b)**

Figure 4.19: **(a)** Skin friction at $\eta = 0$ and **(b)** Skin friction at $\eta = 1$ with varying S, Ec and Re

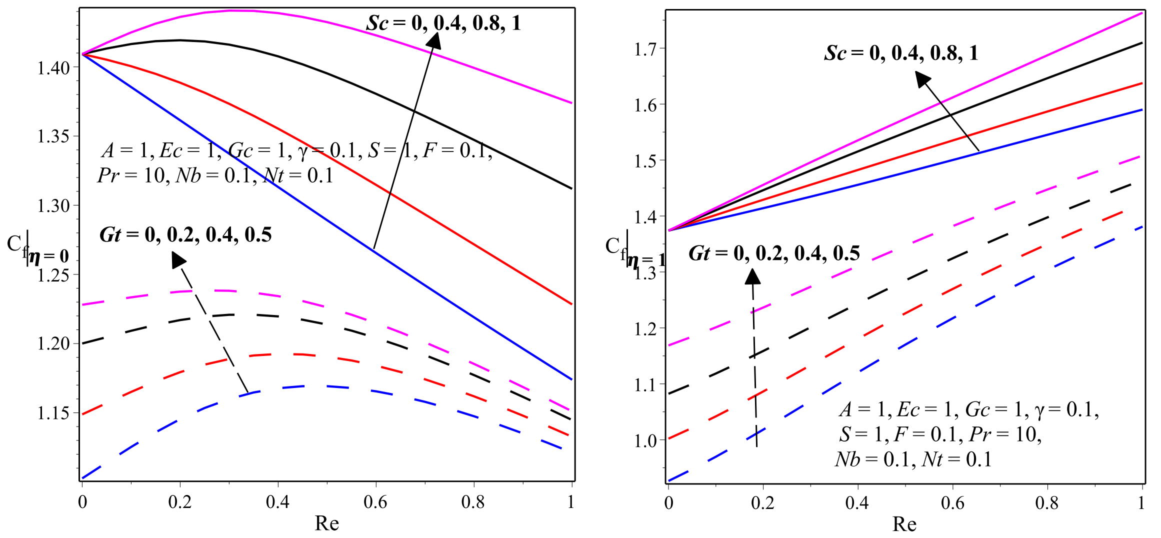

(a) **(b)**

Figure 4.20: **(a)** Skin friction at $\eta = 0$ and **(b)** Skin friction at $\eta = 1$ with varying Gt, Sc and Re

and Makinde (2018). Likewise, Nu at both left and right walls shows an increasing behavior with increasing values of the pressure gradient parameter A, the Schmidt number Sc and the Prandtl number Pr for varying scaled values of the suction/injection Reynolds number Re. Nevertheless, the Forchheimer number F and the porous medium shape parameter S have a decreasing effect on Nu at both walls of the microchannel. As presented in figure 4.23(a), the Nusselt number Nu increases as values of the Eckert number Ec increases at the left wall of the microchannel$\eta = 0$ but figure 4.23(a) revealed that Nu decreases with increasing values of the Eckert number Ec at the right wall $\eta = 1$.

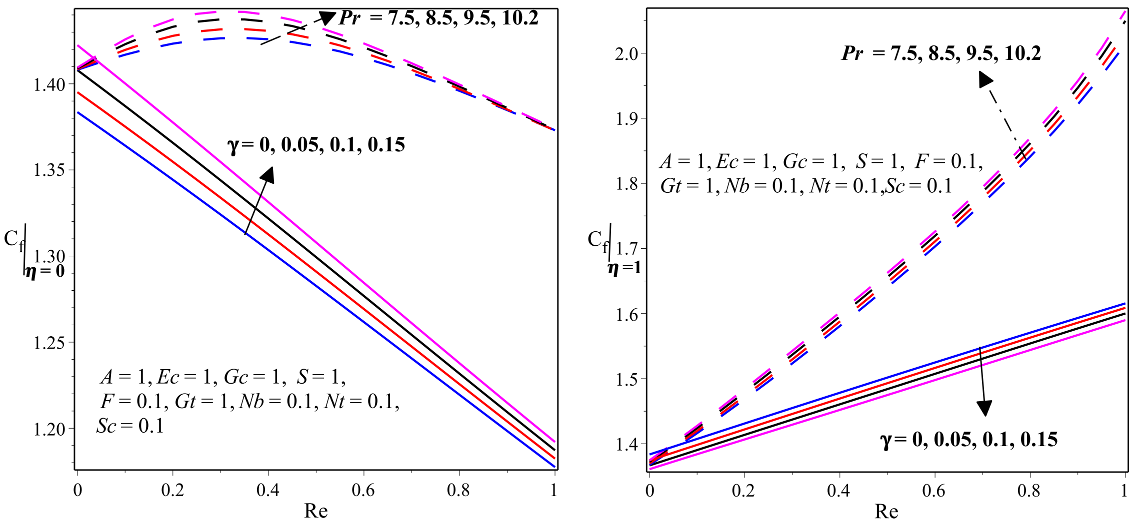

(a) **(b)**

Figure 4.21: **(a)** Skin friction at $\eta = 0$ and **(b)** Skin friction at $\eta = 1$ with varying γ, Pr and Re

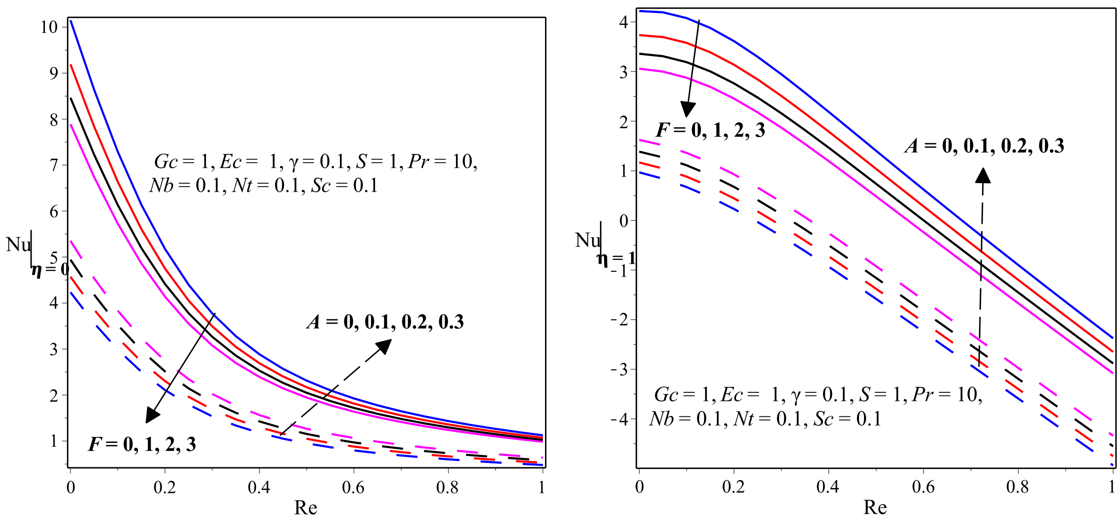

(a) **(b)**

Figure 4.22: **(a)** Nusselt number at $\eta = 0$ and **(b)** Nusselt number at $\eta = 1$ with varying A, F and Re

The Wall Mass Transfer Rate: Sherwood Number

The effects of the governing flow parameters on the wall mass transfer rate at the left wall $\eta = 0$ and at the right wall $\eta = 1$ are given in figures 4.26(a)-4.29(b). As a result, these graphs depict that the wall mass transfer rate, Sherwood number Sh at both left and right walls shows an increasing trend with increasing values of the pressure gradient parameter A, the variable viscosity parameter γ, the thermal Grashof number Gt, the Schmidt number Sc and the Prandtl number Pr for varying scaled values of the suction/injection Reynolds number Re. Nonetheless, the Forchheimer number F and the porous medium shape parameter S

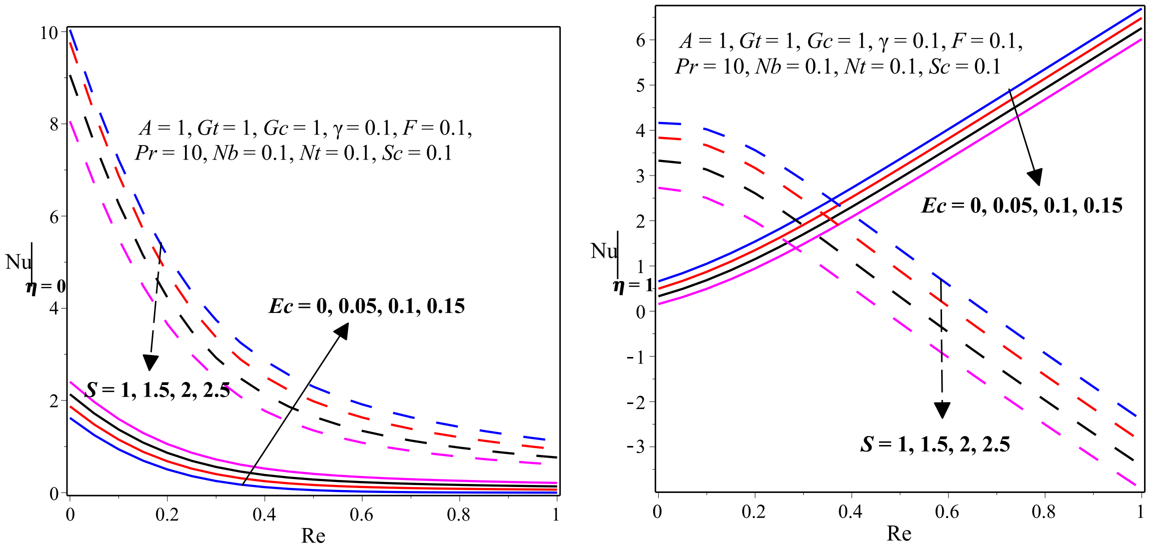

(a) **(b)**

Figure 4.23: **(a)** Nusselt number at $\eta = 0$ and **(b)** Nusselt number at $\eta = 1$ with varying S, Ec and Re

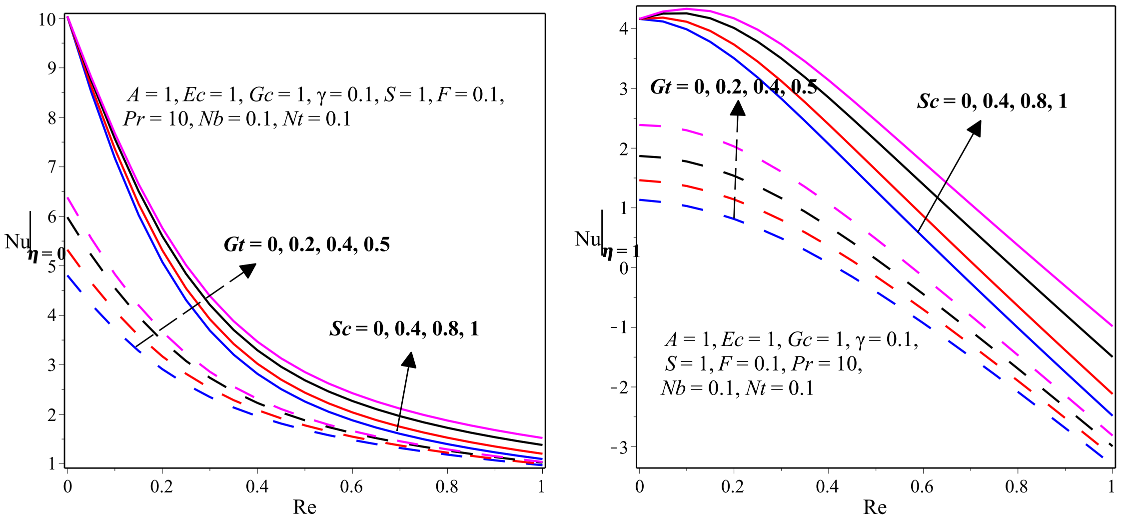

(a) **(b)**

Figure 4.24: **(a)** Nusselt number at $\eta = 0$ and **(b)** Nusselt number at $\eta = 1$ with varying Gt, Sc and Re

have a decreasing effect on Sh at both walls of the microchannel. From figure 4.27(a), it is noticed that Sh increases as values of the Eckert number Ec increases at the left wall of the microchannel$\eta = 0$ while figure 4.27(b) shows that Sh decreases with increasing values of the Eckert number Ec at the right wall $\eta = 1$.

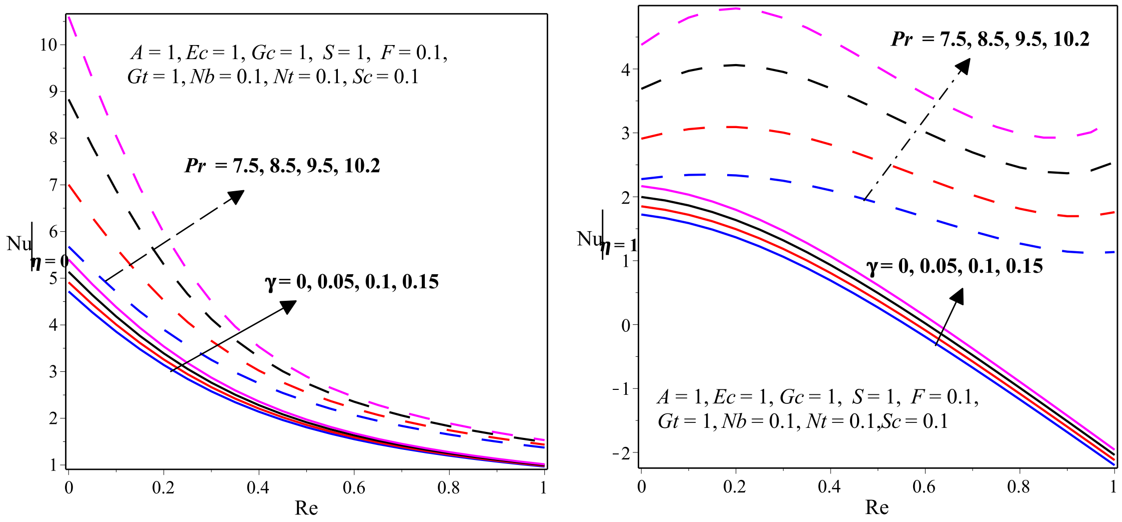

(a) **(b)**

Figure 4.25: **(a)** Nusselt number at $\eta = 0$ and **(b)** Nusselt number at $\eta = 1$ with varying γ, Pr and Re

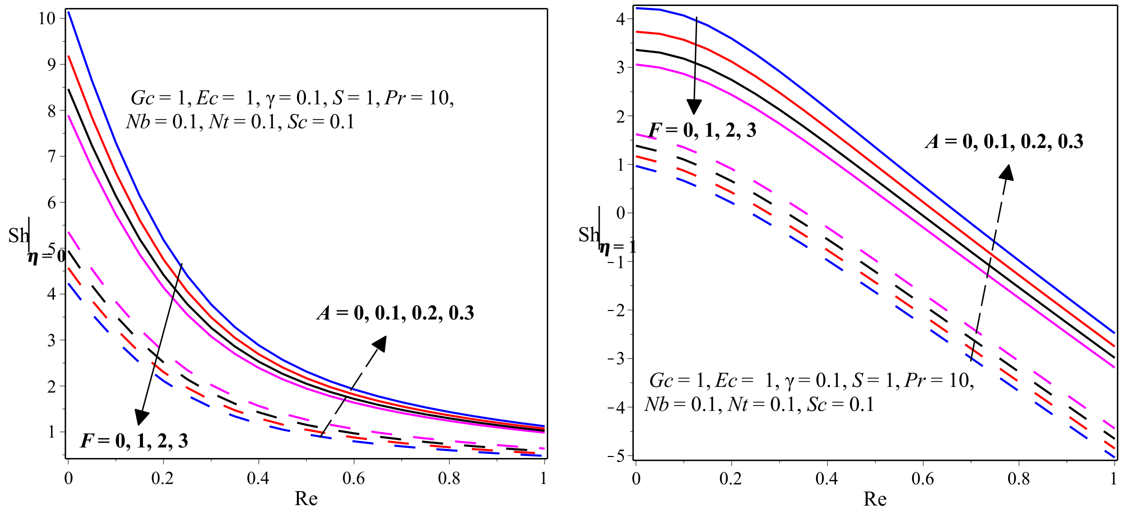

(a) **(b)**

Figure 4.26: **(a)** Sherwood number at $\eta = 0$ and **(b)** Sherwood number at $\eta = 1$ with varying A, F and Re

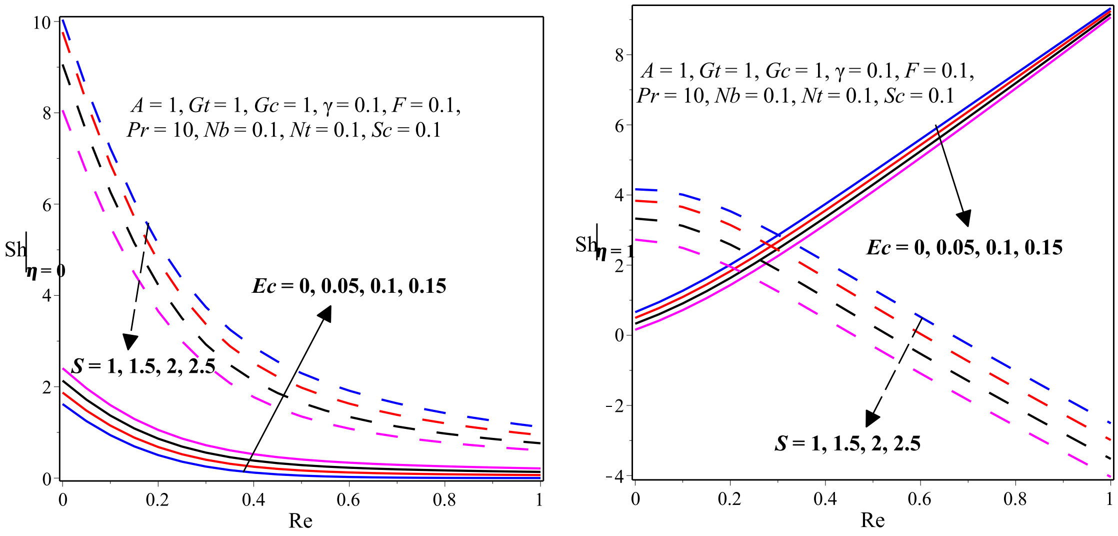

(a) **(b)**

Figure 4.27: **(a)** Sherwood number at $\eta = 0$ and **(b)** Sherwood number at $\eta = 1$ with varying S, Ec and Re

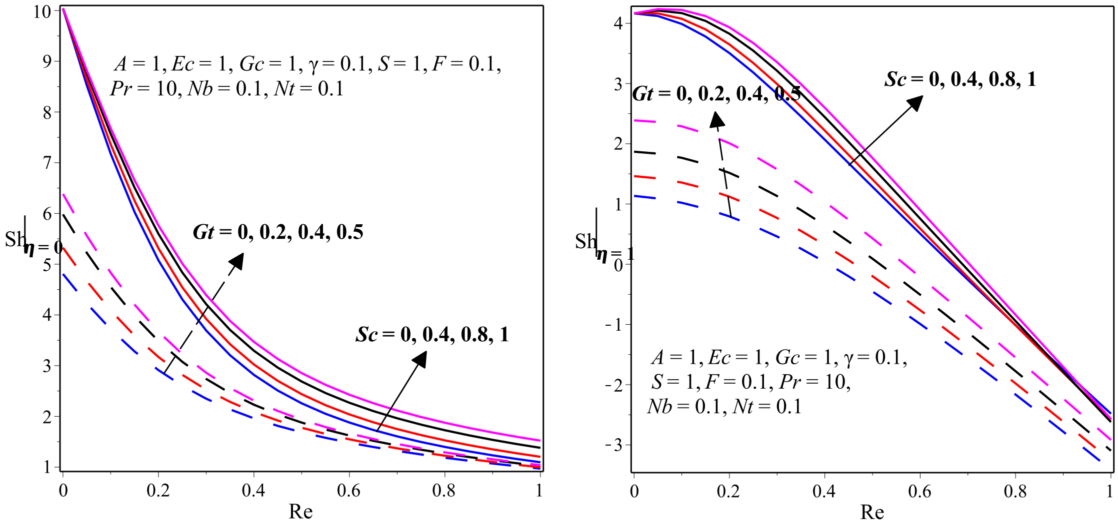

(a) **(b)**

Figure 4.28: **(a)** Sherwood number at $\eta = 0$ and **(b)** Sherwood number at $\eta = 1$ with varying Gt, Sc and Re

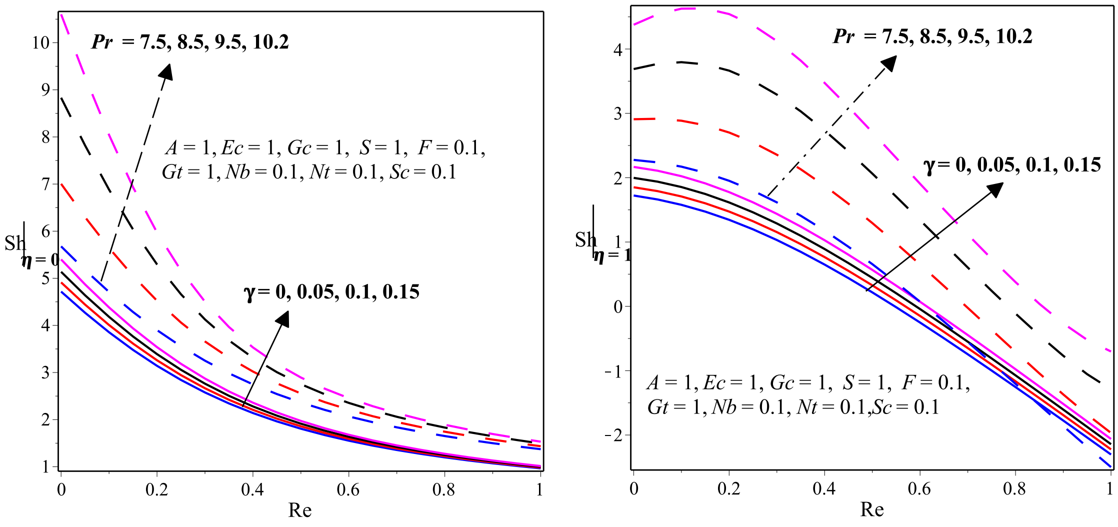

(b) **(b)**

Figure 4.29: **(a)** Sherwood number at $\eta = 0$ and **(b)** Sherwood number at $\eta = 1$ with varying λ, Pr and Re

CHAPTER 5

MODELING HEAT TRANSFER ENHANCEMENT OF FERROFLUID FLOW IN A MICROCHANNEL FILLED WITH A POROUS MEDIUM

The heat transfer characteristics and the hydrodynamical properties of ferrofluid in microchannels in the presence of porous media with non-uniform permeable walls temperature plays an important role in modern microfluidic applications, such as solar collectors, nuclear reactors, micro-electro-chemical cell transport, micro heat exchanging, microchip cooling, and electronic equipment. Therefore, this chapter aims to present the investigation of forced convection flow and heat transfer characteristics of ferrofluid ($Fe_3O_4 - H_2O$) through a microchannel with non-uniform permeable walls in the presence of a porous medium. The Tewari and Das single phase nanofluids flow model was used to study the hydrodynamic and thermal behaviors of ferrofluid.

5.1 Mathematical Model Formulation

Assume that the flow is viscous and unsteady as well as the fluid is Newtonian ferrofluid ($Fe_3O_4 - H_2O$) passing through the microchannel in the presence of a saturated porous medium. Also assume that the walls of the microchannel are permeable and located at $y = 0$ and $y = a$ as indicated in figure 5.1, where a designates the walls separation length.

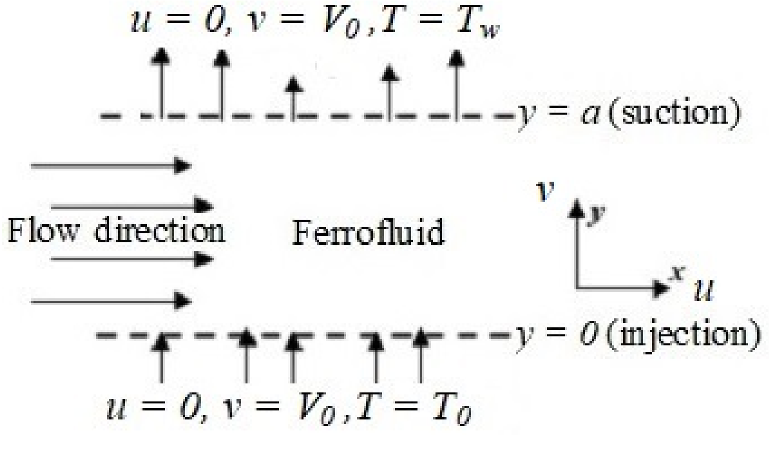

Figure 5.1: Flow Geometry and the Coordinate System

The flow is assumed to be driven by the Darcy-Forchheimer inertial resistivity force and the pressure gradient. Moreover, injection of the ferrofluid into the microchannel occurs at the cold wall ($y = 0$) while the suction of the ferrofluid out of the microchannel takes place through the hot wall ($y = a$). When the time $t = 0$, the temperature of the ferrofluid is kept at T_0 and the ferrofluid is in the stationary point. When the time is large ($t > 0$), the flow process happens only after the ferrofluid begins to travel with the time inside the flow regime of the microchannel. It is also assumed that there are no-slip conditions at the walls for the ferrofluid velocity, and the temperature of the walls is considered to be not uniform so that the cold wall of the microchannel is positioned at temperature T_0 whereas the hot wall is positioned at temperature T_0 where $T_0 < T_w$. The initial temperature is zero within the ferrofluid flow regime but the temperature at the walls is kept to be constant. The temperature-dependent dynamic viscosity of the ferrofluid is considered as an exponentially retarding function of temperature T and thus written as $\mu_{nf}(T) = \mu_f\, e^{-\gamma_1(T-T_0)}$, where γ_1 is a viscosity variation parameter and μ_f is the base fluid (water) dynamic viscosity. Furthermore, in the model equations, it it also assumed that convection terms in the axial direction are very small and are ignored as compared to the convection terms in the normal direction and hence we have, $\frac{\partial T}{\partial x} \ll \frac{\partial T}{\partial y}$, $\frac{\partial u}{\partial x} \ll \frac{\partial u}{\partial y}$.

Indeed, the flow model in this chapter is similar to the one in the previous chapter except the effect of gravitational acceleration is assumed to be negligible. Thus, by taking all the aforementioned assumptions into account as well as employing the Darcy-Forchheimer porous medium flow model, the equations of continuity, linear momentum and energy that govern the flow of the ferrofluid are given as follows:

$$\frac{\partial u}{\partial x} = 0 \tag{5.1}$$

$$\frac{\partial u}{\partial t} + V_0\frac{\partial u}{\partial y} = \frac{1}{\rho_{nf}}\frac{\partial P}{\partial x} + \frac{1}{\rho_{nf}}\frac{\partial}{\partial y}\left[\mu_{nf}(T)\frac{\partial u}{\partial y}\right] - \frac{\mu_{nf}(T)u}{\rho_{nf}K} - \frac{bu^2}{\sqrt{K}} \tag{5.2}$$

$$\frac{\partial T}{\partial t} + V_0\frac{\partial T}{\partial y} = \frac{k_{nf}}{(\rho C_p)_{nf}}\frac{\partial^2 T}{\partial y^2} + \frac{\mu_{nf}(T)}{(\rho C_p)_{nf}}(\frac{\partial u}{\partial y})^2 + \frac{\mu_{nf}(T)u^2}{(\rho C_p)_{nf}K} + \frac{\rho_{nf}bu^3}{(\rho C_p)_{nf}\sqrt{K}} \tag{5.3}$$

with the initial and boundary conditions:

$$u(y,0) = 0, T(y,0) = T_0 \ \text{ and } \ \left.\begin{array}{l} u(0,t) = 0, \ \ T(0,t) = T_0, \\ u(a,t) = 0, \ \ T(a,t) = T_w, \end{array}\right\} \text{for } t > 0 \tag{5.4}$$

where t is time, u is ferrofluid velocity in the axial direction, V_0 is a constant suction/injection velocity at the walls, a is width of the microchannel, ρ_{nf} is density of the ferrofluid, $\mu_{nf}(T)$ is the temperature-dependent ferrofluid dynamic viscosity, P is ferrofluid pressure, T is the ferrofluid temperature, $(\rho C_P)_{nf}$ is the ferrofluid specific heat capacitance at constant pressure, k_{nf} is thermal conductivity of the ferrofluid, K is permeability of the porous medium, and b denotes coefficient of the porous inertia resistance also called the dimensionless Forchheimer constant where $b = 0$ represents the Darcy law.

Following (Tarafdar et al., 2018; Hamid et al., 2018), the effective thermophysical properties of the ferrofluid in terms of that of the base fluid and nanoparticles are presented by the following formulae.

$$\begin{aligned} &\rho_{nf} = (1-\varphi)\rho_f + \varphi\rho_s, \quad (\rho C_P)_{nf} = (1-\varphi)(\rho C_P)_f + \varphi(\rho C_P)_s \\ &\mu_{nf} = \frac{\mu_f e^{-\gamma(T-T_0)}}{(1-\varphi)^{2.5}}, \quad \frac{k_{nf}}{k_f} = \frac{k_s + 2k_f - 2\varphi(k_f - k_s)}{k_s + 2k_f + \varphi(k_f - k_s)} \end{aligned} \tag{5.5}$$

where ρ_f is the base fluid density, ρ_s is the nanoparticles density, k_f is thermal conductivity of the base fluid, k_s is thermal conductivity of the nanoparticles, φ is volume fraction of the nanoparticles, μ_s is dynamic viscosity of the base fluid, $(\rho C_P)_f$ is specific heat capacitance of the base fluid at constant pressure and $(\rho C_P)_s$ is specific heat capacitance of the nanoparticles at constant pressure.

Table 5.1: Thermophysical Properties of the Base Fluid and Nanoparticles (Tarafdar et al., 2018; Hamid et al., 2018)

Physical Properties	$\rho(kg/m^3)$	$C_P(J/kg\cdot K)$	$k(W/m\cdot K)$	
H_2O	997.1	4179	0.613	
Fe_3O_4	5180	670	9.7	

5.2 Non-Dimensional Formulation

Define the following non-dimensional variables to convert the governing equations (5.1)–(5.4) into dimensionless forms.

$$\eta = \frac{y}{a}, \; X = \frac{x}{a}, \; W = \frac{\rho_f a u}{\mu_f}, \; \tau = \frac{\mu_f t}{\rho_f a^2}, \; \theta = \frac{T - T_0}{T_w - T_0}, \; P^* = \frac{\rho_f a^2 P}{\mu_f^2} \tag{5.6}$$

From the dimensionless variables defined in (5.6), one can have the following.

$$\frac{\partial u}{\partial t} = \frac{\partial u}{\partial \tau}\frac{\partial \tau}{\partial t} = \frac{\mu_f}{\rho_f a^2}\frac{\mu_f}{\rho a}\frac{\partial W}{\partial \tau} = (\frac{\mu_f}{\rho_f})^2 \frac{1}{a^3}\frac{\partial W}{\partial \tau} \tag{5.7}$$

$$\frac{\partial u}{\partial x} = \frac{\partial u}{\partial X}\frac{\partial X}{\partial x} = \frac{1}{a}\frac{\partial u}{\partial X} = \frac{\mu_f}{\rho_f a^2}\frac{\partial W}{\partial X} \tag{5.8}$$

$$\frac{\partial u}{\partial y} = \frac{\partial u}{\partial \eta}\frac{\partial \eta}{\partial y} = \frac{1}{a}\frac{\partial u}{\partial \eta} = \frac{\mu_f}{\rho_f a^2}\frac{\partial W}{\partial \eta} \tag{5.9}$$

$$\frac{\partial^2 u}{\partial y^2} = \frac{\partial}{\partial y}(\frac{\partial u}{\partial y}) = \frac{\partial}{\partial y}(\frac{\mu_f}{\rho_f a^2}\frac{\partial W}{\partial \eta}) = \frac{\partial}{\partial \eta}(\frac{\partial}{\partial y})\frac{\partial \eta}{\partial y} = \frac{\mu_f}{\rho_f a^3}\frac{\partial^2 W}{\partial \eta^2} \tag{5.10}$$

$$\frac{1}{\rho_{nf}}\frac{\partial P}{\partial x} = \frac{1}{\rho_{nf}}\frac{\partial P}{\partial X}\frac{\partial X}{\partial x} = \frac{1}{\rho_{nf} a}\frac{\partial P}{\partial X} = \frac{\mu_f^2}{\rho_{nf}\rho_f}\frac{1}{a^3}\frac{\partial P*}{\partial X} \tag{5.11}$$

$$\frac{\partial T}{\partial t} = \frac{\partial T}{\partial \tau}\frac{\partial \tau}{\partial t} = \frac{\mu_f}{\rho_f a^2}\frac{\partial T}{\partial \tau} = \frac{\mu_f}{\rho_f a^2}(T_w - T_0)\frac{\partial \theta}{\partial \tau} \tag{5.12}$$

$$\frac{\partial T}{\partial y} = \frac{\partial T}{\partial \eta}\frac{\partial \eta}{\partial y} = \frac{1}{a}\frac{\partial T}{\partial \eta} = \frac{(T_w - T_0)}{a}\frac{\partial \theta}{\partial \eta} \tag{5.13}$$

$$\frac{\partial^2 T}{\partial y^2} = \frac{\partial}{\partial y}(\frac{\partial T}{\partial y}) = \frac{\partial}{\partial y}\left(\frac{(T_w - T_0)}{a}\frac{\partial \theta}{\partial \eta}\right) = \frac{(T_w - T_0)}{a^2}\frac{\partial^2 \theta}{\partial \eta^2} \tag{5.14}$$

$$\begin{aligned}
\frac{\partial}{\partial y}\left(\mu_{nf}(T)\frac{\partial u}{\partial y}\right) &= \frac{\partial}{\partial y}(\mu_{nf}(T))\frac{\partial u}{\partial y} + \mu_{nf}(T)\frac{\partial^2 u}{\partial y^2} \\
&= \frac{\partial}{\partial \eta}(\mu_{nf}(T))\frac{\partial \eta}{\partial y}\frac{\partial u}{\partial \eta}\frac{\partial \eta}{\partial y} + \mu_{nf}(T)\frac{\partial^2 u}{\partial y^2} \\
&= \frac{1}{a^2}\frac{\partial}{\partial \eta}(\mu_{nf}(T)\frac{\partial u}{\partial \eta} + \frac{\mu_f^2}{\rho_f a^3(1-\varphi)^{2.5}}e^{-\gamma_1\theta(T_w-T_0)}\frac{\partial^2 W}{\partial \eta^2} \\
&= \frac{\mu_f}{a^2(1-\varphi)^{2.5}}\frac{\partial}{\partial \eta}[e^{-\gamma_1\theta(T_w-T_0)}]\frac{\mu_f}{\rho_f a}\frac{\partial W}{\partial \eta} + \frac{\mu_f^2}{\rho_f a^3(1-\varphi)^{2.5}}e^{-\gamma_1\theta(T_w-T_0)}\frac{\partial^2 W}{\partial \eta^2} \\
&= \frac{\mu_f^2}{\rho_f a^3(1-\varphi)^{2.5}}\frac{\partial}{\partial \theta}(e^{-\gamma_1\theta(T_w-T_0)}\frac{\partial \theta}{\partial \eta}\frac{\partial W}{\eta} + \frac{\mu_f^2}{\rho_f a^3(1-\varphi)^{2.5}}e^{-\gamma_1\theta(T_w-T_0)}\frac{\partial^2 W}{\partial \eta^2} \\
&= \frac{-\gamma_1(T_w-T_0)\mu_f^2}{\rho_f a^3(1-\varphi)^{2.5}}e^{-\gamma_1\theta(T_w-T_0)}\frac{\partial \theta}{\partial \eta}\frac{\partial W}{\partial \eta} + \frac{\mu_f^2}{\rho_f a^3(1-\varphi)^{2.5}}e^{-\gamma_1\theta(T_w-T_0)}\frac{\partial^2 W}{\partial \eta^2} \\
&= \frac{\mu_f^2}{\rho_f a^3(1-\varphi)^{2.5}}e^{-\gamma_1\theta(T_w-T_0)}\left(\frac{\partial^2 W}{\partial \eta^2} - \gamma_1(T_w-T_0)\frac{\partial \theta}{\partial \eta}\frac{\partial W}{\partial \eta}\right)
\end{aligned}$$

Hence,

$$\frac{1}{\rho_{nf}}\frac{\partial}{\partial y}\left(\mu_{nf}(T)\frac{\partial u}{\partial y}\right) = \frac{1}{\rho_{nf}}\frac{\mu_f^2}{\rho_f a^3(1-\varphi)^{2.5}}e^{-\gamma\theta}\left(\frac{\partial^2 W}{\partial \eta^2} - \gamma\frac{\partial \theta}{\partial \eta}\frac{\partial W}{\partial \eta}\right) \tag{5.15}$$

where $\gamma = \gamma_1(T_w - T_0)$.

Then by using (5.7)–(5.15), the dimensionless forms of the governing equations were derived as follows.

Continuity Equation

$\frac{\partial u}{\partial x} = 0$. But from (5.8), it is possible to have $\frac{\partial u}{\partial x} = \frac{\mu_f}{\rho_f a^2}\frac{\partial W}{\partial X}$. This implies that $\frac{\mu_f}{\rho_f a^2}\frac{\partial W}{\partial X} = 0$. Since $\frac{\mu_f}{\rho_f a^2} \neq 0$, one must have that $\frac{\partial W}{\partial X} = 0$. Thus, the dimensionless equation of continuity takes the form:

$$\frac{\partial W}{\partial X} = 0 \tag{5.16}$$

Momentum Equation

$$\frac{\partial u}{\partial t} + V_0\frac{\partial u}{\partial y} = -\frac{1}{\rho_{nf}}\frac{\partial P}{\partial x} + \frac{1}{\rho_{nf}}\frac{\partial}{\partial y}\left[\mu_{nf}(T)\frac{\partial u}{\partial y}\right] - \frac{\mu_{nf}(T)u}{\rho_{nf}K} - \frac{bu^2}{\sqrt{K}}$$

$$\begin{aligned}\Rightarrow (\frac{\mu_f}{\rho_f})^2\frac{1}{a^3}\frac{\partial W}{\partial \tau}+V_0\frac{\mu_f}{\rho_f a^2}\frac{\partial W}{\partial \eta} &= -\frac{\mu_f^2}{\rho_{nf}\rho_f}\frac{1}{a^3}\frac{\partial P*}{\partial X}+\frac{1}{\rho_{nf}}\frac{\mu_f^2}{\rho_f a^3(1-\varphi)^{2.5}}e^{-\gamma\theta}\left(\frac{\partial^2 W}{\partial \eta^2}-\gamma\frac{\partial \theta}{\partial \eta}\frac{\partial W}{\partial \eta}\right)\\ &\quad -\frac{\mu_f^2 e^{-\gamma\theta}}{\rho_{nf}\rho_f aK(1-\varphi)^{2.5}}W-\frac{b\mu_f^2}{\sqrt{K}\rho_f^2 a^2}W^2\end{aligned}$$

$$\begin{aligned}\Rightarrow \frac{\partial W}{\partial \tau}+\frac{V_0 a\rho_f}{\mu_f}\frac{\partial W}{\partial \eta} &= -\frac{\rho_f}{\rho_{nf}}\frac{\partial P*}{\partial X}+\frac{\rho_f}{\rho_{nf}}\frac{e^{-\gamma\theta}}{(1-\varphi)^{2.5}}\left(\frac{\partial^2 W}{\partial \eta^2}-\gamma\frac{\partial \theta}{\partial \eta}\frac{\partial W}{\partial \eta}\right)-\frac{\rho_f}{\rho_{nf}}\frac{a^2}{K}\frac{e^{-\gamma\theta}}{(1-\varphi)^{2.5}}W\\ &\quad -\frac{ba}{\sqrt{K}}W^2\end{aligned}$$

$$\Rightarrow \frac{\partial W}{\partial \tau}+Re\frac{\partial W}{\partial \eta}=\frac{\rho_f}{\rho_{nf}}G+\frac{\rho_f}{\rho_{nf}}\frac{e^{-\gamma\theta}}{(1-\varphi)^{2.5}}\left(\frac{\partial^2 W}{\partial \eta^2}-\gamma\frac{\partial \theta}{\partial \eta}\frac{\partial W}{\partial \eta}\right)-\frac{\rho_f}{\rho_{nf}}\frac{e^{-\gamma\theta}}{Da(1-\varphi)^{2.5}}W-\frac{b}{\sqrt{Da}}W^2$$

$$\Rightarrow \frac{\rho_{nf}}{\rho_f}\left[\frac{\partial W}{\partial \tau}+Re\frac{\partial W}{\partial \eta}\right]=G+\frac{e^{-\gamma\theta}}{(1-\varphi)^{2.5}}\left(\frac{\partial^2 W}{\partial \eta^2}-\gamma\frac{\partial \theta}{\partial \eta}\frac{\partial W}{\partial \eta}\right)-\frac{e^{-\gamma\theta}}{Da(1-\varphi)^{2.5}}W-\frac{\rho_{nf}}{\rho_f}\frac{b}{\sqrt{Da}}W^2$$

$$\begin{aligned}\Rightarrow \left[1-\varphi+\varphi\frac{\rho_s}{\rho_f}\right]\left[\frac{\partial W}{\partial \tau}+Re\frac{\partial W}{\partial \eta}\right] &= G+\frac{e^{-\gamma\theta}}{(1-\varphi)^{2.5}}\left(\frac{\partial^2 W}{\partial \eta^2}-\gamma\frac{\partial \theta}{\partial \eta}\frac{\partial W}{\partial \eta}\right)-\frac{e^{-\gamma\theta}}{Da(1-\varphi)^{2.5}}W\\ &\quad -\left[1-\varphi+\varphi\frac{\rho_s}{\rho_f}\right]\frac{b}{\sqrt{Da}}W^2, \text{ since } \rho_{nf}=(1-\varphi)\rho_f+\varphi\rho_s\end{aligned}$$

Therefore, the dimensionless form of the momentum equation takes the form:

$$\begin{aligned}\left[1-\varphi+\varphi\frac{\rho_s}{\rho_f}\right]\left[\frac{\partial W}{\partial \tau}+Re\frac{\partial W}{\partial \eta}\right] &= G+\frac{e^{-\gamma\theta}}{(1-\varphi)^{2.5}}\left[\frac{\partial^2 W}{\partial \eta^2}-\gamma\frac{\partial \theta}{\partial \eta}\frac{\partial W}{\partial \eta}\right]\\ &\quad -\frac{e^{-\gamma\theta}W}{(1-\varphi)^{2.5}Da}-\left[1-\varphi+\varphi\frac{\rho_s}{\rho_f}\right]\frac{bW^2}{\sqrt{Da}}\end{aligned} \tag{5.17}$$

where $G=\frac{\partial P^*}{\partial X}, Re=\frac{\rho_f V_0 a}{\mu_f}, Da=\frac{K}{a^2}$.

Energy Equation

$$\frac{\partial T}{\partial t}+V_0\frac{\partial T}{\partial y}=\frac{k_{nf}}{(\rho C_p)_{nf}}\frac{\partial^2 T}{\partial y^2}+\frac{\mu_{nf}(T)}{(\rho C_p)_{nf}}(\frac{\partial u}{\partial y})^2+\frac{\mu_{nf}(T)u^2}{(\rho C_p)_{nf}K}+\frac{\rho_{nf}bu^3}{(\rho C_p)_{nf}\sqrt{K}}$$

$$\begin{aligned}\Rightarrow \frac{\mu_f}{\rho_f a^2}(T_w-T_0)\frac{\partial \theta}{\partial \tau}+V_0\frac{(T_w-T_0)}{a}\frac{\partial \theta}{\partial \eta} &= \frac{k_{nf}}{(\rho C_p)_{nf}}\frac{(T_w-T_0)}{a^2}\frac{\partial^2 \theta}{\partial \eta^2}+\frac{\mu_{nf}(T)}{(\rho C_p)_{nf}}\frac{\mu_f^2}{\rho_f^2 a^4}(\frac{\partial W}{\partial \eta})^2\\ &\quad +\frac{\mu_{nf}(T)}{(\rho C_p)_{nf}K}\frac{\mu_f^2}{\rho_f^2 a^2}W^2+\frac{\rho_{nf}b}{(\rho C_p)_{nf}\sqrt{K}}\frac{\mu_f^3}{\rho_f^3 a^3}W^3\end{aligned}$$

$$\begin{aligned}\Rightarrow \frac{\mu_f}{\rho_f a^2}(T_w-T_0)\frac{\partial \theta}{\partial \tau}+V_0\frac{(T_w-T_0)}{a}\frac{\partial \theta}{\partial \eta} &= \frac{k_{nf}}{(\rho C_p)_{nf}}\frac{(T_w-T_0)}{a^2}\frac{\partial^2 \theta}{\partial \eta^2}+\frac{e^{-\gamma\theta}}{(\rho C_p)_{nf}(1-\varphi)^{2.5}}\frac{\mu_f^3}{\rho_f^2 a^4}(\frac{\partial W}{\partial \eta})^2\\ &\quad +\frac{e^{-\gamma\theta}}{(\rho C_p)_{nf}K(1-\varphi)^{2.5}}\frac{\mu_f^3}{\rho_f^2 a^2}W^2+\frac{\rho_{nf}b}{(\rho C_p)_{nf}\sqrt{K}}\frac{\mu_f^3}{\rho_f^3 a^3}W^3\end{aligned}$$

$$\begin{aligned}\Rightarrow \frac{\partial \theta}{\partial \tau}+\frac{V_0\rho_f a}{\mu_f}\frac{\partial \theta}{\partial \eta} &= \frac{k_{nf}}{(\rho C_p)_{nf}}\frac{\rho_f}{\mu_f}\frac{\partial^2 \theta}{\partial \eta^2}+\frac{e^{-\gamma\theta}}{(\rho C_p)_{nf}(1-\varphi)^{2.5}}\frac{\mu_f^2}{\rho_f a^2(T_w-T_0)}(\frac{\partial W}{\partial \eta})^2\\ &\quad +\frac{e^{-\gamma\theta}}{(\rho C_p)_{nf}K(1-\varphi)^{2.5}}\frac{\mu_f^2}{\rho_f(T_w-T_0)}W^2+\frac{\rho_{nf}b}{(\rho C_p)_{nf}(T_w-T_0)a\sqrt{K}}\frac{\mu_f^2}{\rho_f^2}W^3\end{aligned}$$

$$\begin{aligned}\Rightarrow \frac{(\rho C_p)_{nf}}{(\rho C_p)_f}\left[\frac{\partial \theta}{\partial \tau}+Re\frac{\partial \theta}{\partial \eta}\right] &= k_{nf}\frac{\rho_f}{\mu_f(\rho C_p)_f}\frac{\partial^2 \theta}{\partial \eta^2}+\frac{e^{-\gamma\theta}}{(1-\varphi)^{2.5}}\frac{\mu_f^2}{\rho_f a^2(T_w-T_0)(\rho C_p)_f}(\frac{\partial W}{\partial \eta})^2\\ &\quad +\frac{e^{-\gamma\theta}}{K(1-\varphi)^{2.5}}\frac{\mu_f^2}{\rho_f(T_w-T_0)(\rho C_p)_f}W^2+\frac{\rho_{nf}b}{a\sqrt{K}(T_w-T_0)(\rho C_p)_f}\frac{\mu_f^2}{\rho_f^2}W^3\end{aligned}$$

$$\begin{aligned}\Rightarrow \frac{(\rho C_p)_{nf}}{(\rho C_p)_f}\left[\frac{\partial \theta}{\partial \tau}+Re\frac{\partial \theta}{\partial \eta}\right] &= k_f\left[\frac{k_s+2k_f-2\varphi(k_f-k_s)}{k_s+2k_f+\varphi(k_f-k_s)}\right]\frac{\rho_f}{\mu_f(\rho C_p)_f}\frac{\partial^2 \theta}{\partial \eta^2}\\ &\quad +Ec\frac{e^{-\gamma\theta}}{(1-\varphi)^{2.5}}(\frac{\partial W}{\partial \eta})^2+\frac{Ec}{Da}\frac{e^{-\gamma\theta}}{(1-\varphi)^{2.5}}W^2+\frac{bEc}{\sqrt{Da}}\frac{\rho_{nf}}{\rho_f}W^3\end{aligned}$$

$$\begin{aligned}\Rightarrow \left[1-\varphi+\varphi\frac{(\rho C_p)_s}{(\rho C_p)_f}\right]\left[\frac{\partial \theta}{\partial \tau}+Re\frac{\partial \theta}{\partial \eta}\right] &= \frac{1}{Pr}\left[\frac{k_s+2k_f-2\varphi(k_f-k_s)}{k_s+2k_f+\varphi(k_f-k_s)}\right]\frac{\partial^2 \theta}{\partial \eta^2}\\ &\quad +Ec\frac{e^{-\gamma\theta}}{(1-\varphi)^{2.5}}(\frac{\partial W}{\partial \eta})^2+\frac{Ec}{Da}\frac{e^{-\gamma\theta}}{(1-\varphi)^{2.5}}W^2\\ &\quad +\frac{bEc}{\sqrt{Da}}\left[1-\varphi+\varphi\frac{\rho_s}{\rho_f}\right]W^3\end{aligned}$$

Thus, the dimensionless form of the energy equation resembles the following.

$$\begin{aligned}\Rightarrow \left[1-\varphi+\varphi\frac{(\rho C_p)_s}{(\rho C_p)_f}\right]\left[\frac{\partial \theta}{\partial \tau}+Re\frac{\partial \theta}{\partial \eta}\right] &= \frac{1}{Pr}\left[\frac{k_s+2k_f-2\varphi(k_f-k_s)}{k_s+2k_f+\varphi(k_f-k_s)}\right]\frac{\partial^2 \theta}{\partial \eta^2}\\ &\quad +Ec\frac{e^{-\gamma\theta}}{(1-\varphi)^{2.5}}(\frac{\partial W}{\partial \eta})^2+\frac{Ec}{Da}\frac{e^{-\gamma\theta}}{(1-\varphi)^{2.5}}W^2 \qquad (5.18)\\ &\quad +\frac{bEc}{\sqrt{Da}}\left[1-\varphi+\varphi\frac{\rho_s}{\rho_f}\right]W^3\end{aligned}$$

where $Ec=\frac{\mu_f^2}{\rho_f^2 a^2 (C_p)_f(T_w-T_0)}$, $Pr=\frac{\mu_f(C_P)_f}{k_f}$.

Initial and Boundary Conditions

The corresponding dimensionless initial and boundary conditions are:

$$W(\eta,0)=0,\theta(\eta,0)=0,\text{ and}\quad \left.\begin{aligned}W(0,\tau)=0,\theta(0,\tau)=0,\\ W(1,\tau)=0,\theta(1,\tau)=1,\end{aligned}\right\}\text{for } \tau>0 \qquad (5.19)$$

Consequently, the non-dimensional forms of the governing equations are summarized as follows:

$$\frac{\partial W}{\partial X}=0 \qquad (5.20)$$

$$\left[1-\varphi+\varphi\frac{\rho_s}{\rho_f}\right]\left[\frac{\partial W}{\partial \tau}+Re\frac{\partial W}{\partial \eta}\right]=G+\frac{e^{-\gamma\theta}}{(1-\varphi)^{2.5}}\left[\frac{\partial^2 W}{\partial \eta^2}-\gamma\frac{\partial \theta}{\partial \eta}\frac{\partial W}{\partial \eta}\right] -\frac{e^{-\gamma\theta}W}{(1-\varphi)^{2.5}Da}-\left[1-\varphi+\varphi\frac{\rho_s}{\rho_f}\right]\frac{bW^2}{\sqrt{Da}} \tag{5.21}$$

$$\left[1-\varphi+\varphi\frac{(\rho C_P)_s}{(\rho C_P)_f}\right]\left[\frac{\partial \theta}{\partial \tau}+Re\frac{\partial \theta}{\partial \eta}\right]=\frac{1}{Pr}\left[\frac{k_s+2k_f-2\varphi(k_f-k_s)}{k_s+2k_f+\varphi(k_f-k_s)}\right]\frac{\partial^2 \theta}{\partial \eta^2} +\frac{Ece^{-\gamma\theta}}{(1-\varphi)^{2.5}}(\frac{\partial W}{\partial \eta})^2+\frac{Ec}{Da}\frac{e^{-\gamma\theta}}{(1-\varphi)^{2.5}}W^2+\frac{bEc}{\sqrt{Da}}\left[1-\varphi+\varphi\frac{\rho_s}{\rho_f}\right]W^3 \tag{5.22}$$

The corresponding dimensionless initial and boundary conditions are:

$$W(\eta,0)=0,\theta(\eta,0)=0,\ \text{and}\quad \left.\begin{array}{l} W(0,\tau)=0,\theta(0,\tau)=0,\\ W(1,\tau)=0,\theta(1,\tau)=1, \end{array}\right\}\text{for } \tau>0 \tag{5.23}$$

where τ is non-dimensional time, Re is dimensionless Reynolds number or suction/injection parameter, Ec denotes Eckert number of the base fluid, Pr is Prandtl number of the base fluid, G is non-dimensional pressure gradient parameter, γ is non-dimensional dynamic viscosity variation parameter, and Da designates the Darcy number.

5.3 Physical Quantities of Engineering Interests

The coefficient of skin friction C_f and the wall heat transfer rate (local Nusselt number) Nu are among other physical variables with great concern in engineering. Hence, the dimensionless coefficient of skin friction C_f and local Nusselt number Nu take the following forms.

The wall shear stress: Coefficient of skin friction (C_f)

$$C_f=\frac{\rho_f a^2}{\mu_f^2}\tau_w,\ \text{where}\ \tau_w=\mu_{nf}(T)\frac{\partial u}{\partial y}\Bigg|_{y=0,a}=\frac{\mu_f}{(1-\varphi)^{2.5}}e^{-\gamma\theta}\frac{\mu_f}{\rho a^2}\frac{\partial W}{\partial \eta}\Bigg|_{\eta=0,1}$$

$$\Rightarrow C_f=\frac{\rho_f a^2}{\mu_f^2}\frac{\mu_f}{(1-\varphi)^{2.5}}e^{-\gamma\theta}\frac{\mu_f}{\rho_f a^2}\frac{\partial W}{\partial \eta}\Bigg|_{\eta=0,1}=\frac{e^{-\gamma\theta}}{(1-\varphi)^{2.5}}\frac{dW}{d\eta}\Bigg|_{\eta=0,1}$$

Hence, the dimensionless skin friction coefficient is given by:

$$C_f=\frac{e^{-\gamma\theta}}{(1-\varphi)^{2.5}}\frac{dW}{d\eta}\Bigg|_{\eta=0,1} \tag{5.24}$$

The wall heat transfer rate: Nusselt number (Nu)

$$
\begin{aligned}
Nu &= \frac{aq_w}{k_f(T_w - T_0)} \quad \text{where } q_w = -k_{nf}\frac{\partial T}{\partial y}\bigg|_{y=0,a} = -\frac{k_{nf}(T_w - T_0)}{a}\frac{\partial \theta}{\partial \eta}\bigg|_{\eta=0,1} \\
\Rightarrow Nu &= \frac{aq_w}{k_f(T_w - T_0)} = \frac{-a}{k_f(T_w - T_0)}\frac{k_{nf}(T_w - T_0)}{a}\frac{\partial \theta}{\partial \eta}\bigg|_{\eta=0,1} = -\frac{k_{nf}}{k_f}\frac{\partial \theta}{\partial \eta}\bigg|_{\eta=0,1} \\
\Rightarrow Nu &= -\frac{k_{nf}}{k_f}\frac{\partial \theta}{\partial \eta}\bigg|_{\eta=0,1} = -\left[\frac{k_s + 2k_f - 2\varphi(k_f - k_s)}{k_s + 2k_f + \varphi(k_f - k_s)}\right]\frac{d\theta}{d\eta}\bigg|_{\eta=0,1}
\end{aligned}
$$

Therefore, the dimensionless Nusselt number is given by:

$$
Nu = -\left[\frac{k_s + 2k_f - 2\varphi(k_f - k_s)}{k_s + 2k_f + \varphi(k_f - k_s)}\right]\frac{d\theta}{d\eta}\bigg|_{\eta=0,1} \tag{5.25}
$$

5.4 Numerical Solutions

The system of governing equations (5.21)–(5.22) along with the initial and boundary conditions (5.23) were solved by using the semi-discretization finite difference method. The method is also called the method of lines which comprises two steps namely time integration and space discretization. Firstly, the spatial derivatives were approximated by the central finite difference method so that the governing partial differential equations (PDEs) were converted into a system of ordinary differential equations (ODEs) as a function of time that corresponds to the solution at some grid points. Secondly, the resulting nonlinear system of the initial value problem of ODEs is iteratively solved by employing the fourth order Runge-Kutaa integrator using the Maple software. As a consequence, the semi-discretization finite difference scheme for equations (5.21)–(5.23) resembles the following form:

$$
\begin{aligned}
\left[1 - \varphi + \varphi\frac{\rho_s}{\rho_f}\right]\frac{dW_i}{d\tau} = G - \left[1 - \varphi + \varphi\frac{\rho_s}{\rho_f}\right]Re\frac{W_{i+1} - W_{i-1}}{2\Delta\eta} \\
+ \frac{e^{-\gamma\theta_i}}{(1-\varphi)^{2.5}}\left[\frac{W_{i-1} - 2W_i + W_{i+1}}{(\Delta\eta)^2} - \gamma\frac{\theta_{i+1} - \theta_{i-1}}{2\Delta\eta}\cdot\frac{W_{i+1} - W_{i-1}}{2\Delta\eta}\right] \\
- \frac{e^{-\gamma\theta_i}W_i}{(1-\varphi)^{2.5}Da} - \left[1 - \varphi + \varphi\frac{\rho_s}{\rho_f}\right]\frac{bW_i^2}{\sqrt{Da}}
\end{aligned}
\tag{5.26}
$$

$$\left[1-\varphi+\varphi\frac{(\rho C_P)_s}{(\rho C_P)_f}\right]\frac{d\theta_i}{d\tau} = -\left[1-\varphi+\varphi\frac{(\rho C_P)_s}{(\rho C_P)_f}\right]Re\frac{\theta_{i+1}-\theta_{i-1}}{2\Delta\eta} + \frac{1}{Pr}\left[\frac{k_s+2k_f-2\varphi(k_f-k_s)}{k_s+2k_f+\varphi(k_f-k_s)}\right]\frac{\theta_{i-1}-2\theta_i+\theta_{i+1}}{(\Delta\eta)^2} + \frac{Ece^{-\gamma\theta_i}}{(1-\varphi)^{2.5}}\left[\frac{W_{i+1}-W_{i-1}}{2\Delta\eta}\right]^2 + \frac{Ec}{Da}\frac{e^{-\gamma\theta_i}}{(1-\varphi)^{2.5}}W_i^2 + \frac{bEc}{\sqrt{Da}}\left[1-\varphi+\varphi\frac{\rho_s}{\rho_f}\right]W_i^3 \tag{5.27}$$

with initial conditions:

$$W_i(0)=0,\ \ \theta_i(0)=0 \tag{5.28}$$

where, $W_i(\tau) = W(\eta_i,\tau)$, $\theta_i(\tau) = \theta(\eta_i,\tau)$ and the interval for spatial which is $[0,1]$ was subdivided into N sub-intervals of equal length. The size of the grid is defined as $\Delta\eta = \frac{1}{N}$ and the grid points are defined as $\eta_i = \frac{i-1}{\Delta\eta}$ for $1 \le i \le N+1$.

Moreover, the values for $\rho_f, \rho_s, (C_P)_f, (C_P)_s, k_f, k_s$ that are appearing in the semi-discretized equations (5.26)–(5.27) are taken from Table 5.1 during the numerical computation.

5.5 Results and Discussion

5.5.1 The Transient and Steady State profiles

Figures 5.2(a) and 5.2(b) portray the steady state and the transient solutions for velocity and temperature of the ferrofluid. These figures display that both velocity and temperature profiles show a parabolic transient surge and attain the states of steadiness nearly at $\tau \ge 2.0$. In addition, the no-slip boundary conditions at the walls leads the ferrofluid velocity to reach its peak value at about the center and then decrease to zero as depicted in figure 5.2(a). The ferrofluid temperature gradually increasing towards the cold wall of the microchannel where it obtained its maximum value as demonstrated in figure 5.2(b).

5.5.2 Parameters Dependent Solutions

The effects of the suction/injection Reynolds number *Re* and the dimensionless pressure gradient parameter *G* on the ferrofluid velocity and temperature are portrayed in figures 5.3(a) and 5.3(b) respectively. The present study has taken into account that a uniform injection of ferrofluid into the flow regime through the cold wall (vertical line $\eta = 0$) whereas ferrofluid suction out occurs through the hot wall (vertical line $\eta = 1$). From figure 5.3(a), it can be noticed that the ferrofluid velocity decreases with increasing values of *Re* where it also shows a slight skewing pattern towards the microchannel hot wall. Physically speaking, an increment in the suction at the wall of the microchannel decreases the rate of flow inside the core region. However, figure 5.3(b) indicates that the ferrofluid temperature increases as

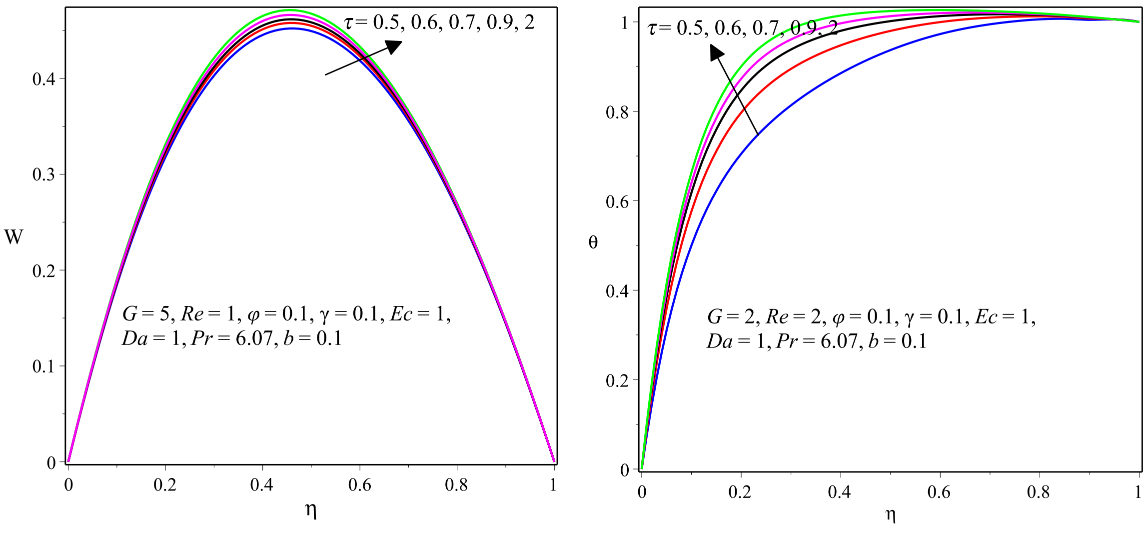

(a) **(b)**

Figure 5.2: **(a)** Velocity and **(b)** Temperature of ferrofluid for transient and steady state solutions

Re increase. The reason behind this result may be because an increase in *Re* implies a rise in ferrofluid suction at the permeable wall with convective heat loss, leading to an increase in the ferrofluid temperature within the core region. Moreover, figures 5.3(a) and 5.3(b) illustrate that both ferrofluid velocity and temperature rise with increasing values of *G*. The reason for this result is, the ferrofluid motion is driven by the axial pressure gradient. That is, increasing values of *G* implies that the ferrofluid flows faster which leads to the ferrofluid velocity and temperature increment.

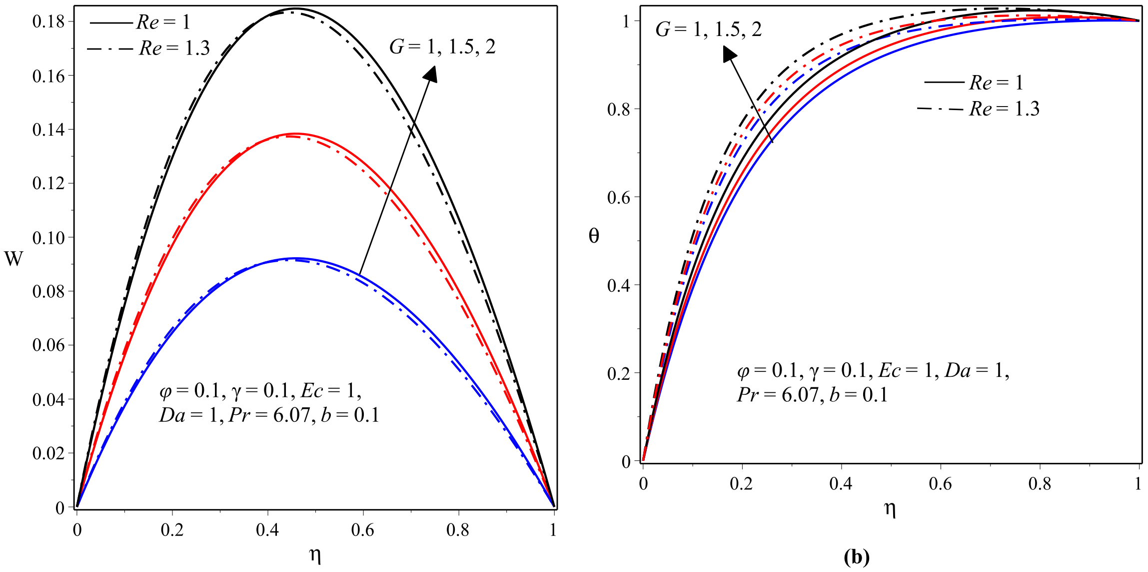

Figure 5.3: **(a)** Velocity and **(b)** Temperature of ferrofluid for increasing values of *G* and *Re*

Figures 5.4(a) and 5.4(b) portray the influence of volume fraction of nanoparticles on the ferrofluid velocity and temperature. Both the ferrofluid velocity and temperature decline as the value of φ increases. The argument for this result can be when φ increases the ferrofluid dynamic viscosity rises that results in the decrement of ferrofluid velocity which also, in turn, decreases its temperature.

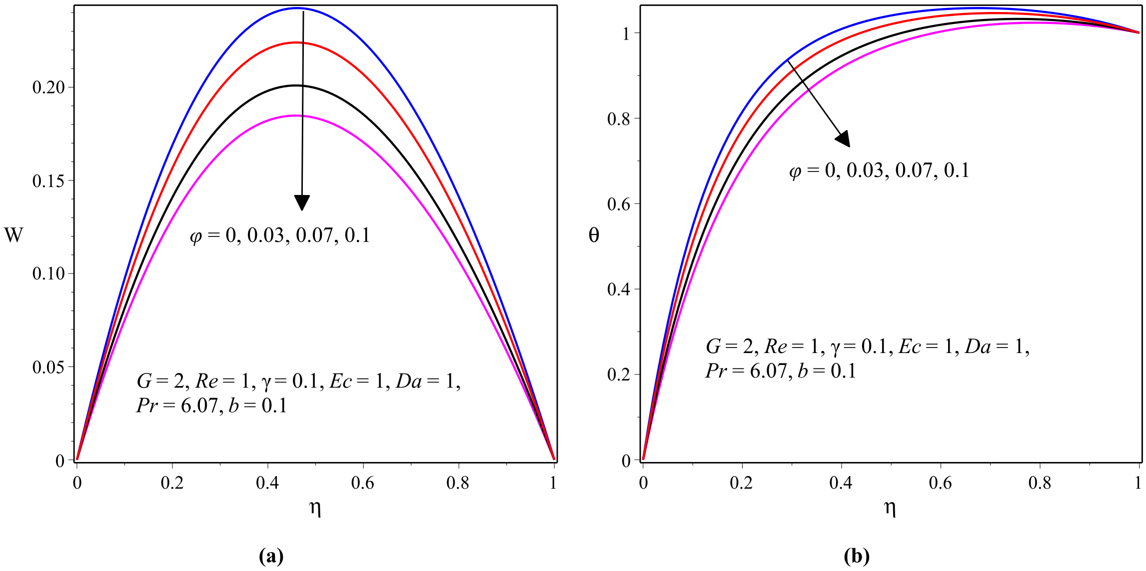

(a)

(b)

Figure 5.4: **(a)** Velocity and **(b)** Temperature of ferrofluid for increasing values of φ

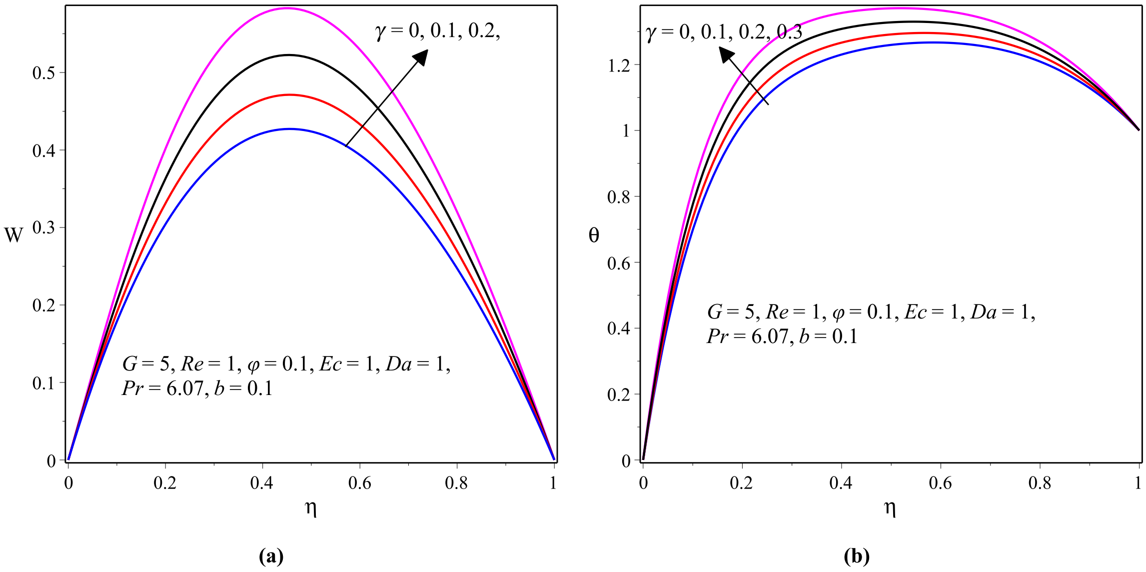

(a)

(b)

Figure 5.5: **(a)** Velocity and **(b)** Temperature of ferrofluid for increasing values of γ

Figures 5.5(a) and 5.5(b) exhibit that the velocity and temperature of the ferrofluid rise significantly with the dimensionless variable viscosity parameter. This result may be attributed to the fact that as γ increases, the viscosity of the ferrofluid decreases because $\mu(T) = \mu_0 e^{-\gamma\theta}$. Therefore, the friction within the ferrofluid particles reduces which in turn increases the ferrofluid velocity.

Figures 5.6(a) and 5.6(b) present the influences of the Darcy number *Da* and the Forchheimer constant *b* on the ferrofluid velocity and temperature. Both the ferrofluid velocity

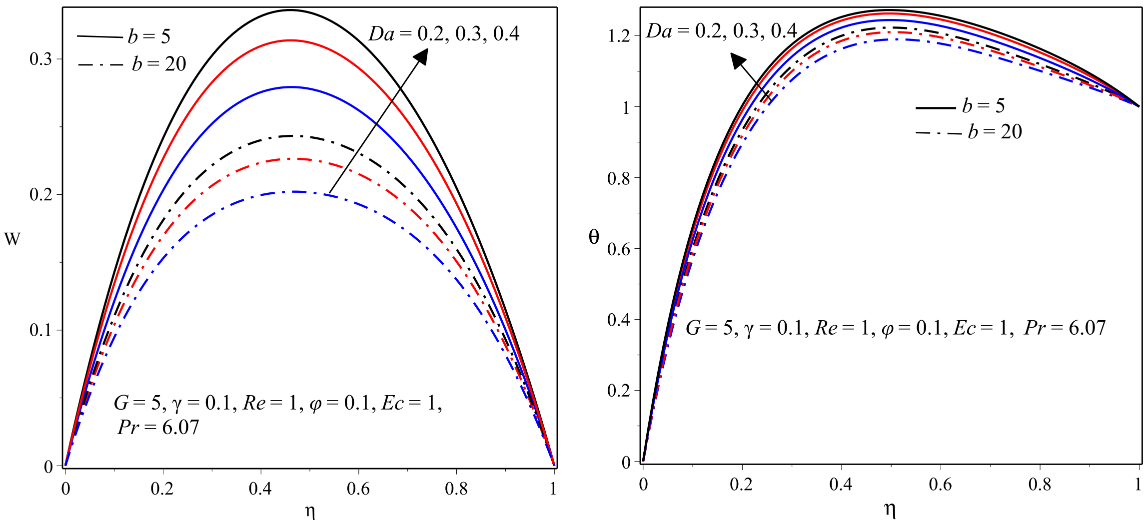

(a) **(b)**

Figure 5.6: **(a)** Velocity and **(b)** Temperature of ferrofluid for increasing values of *Da* and *b*

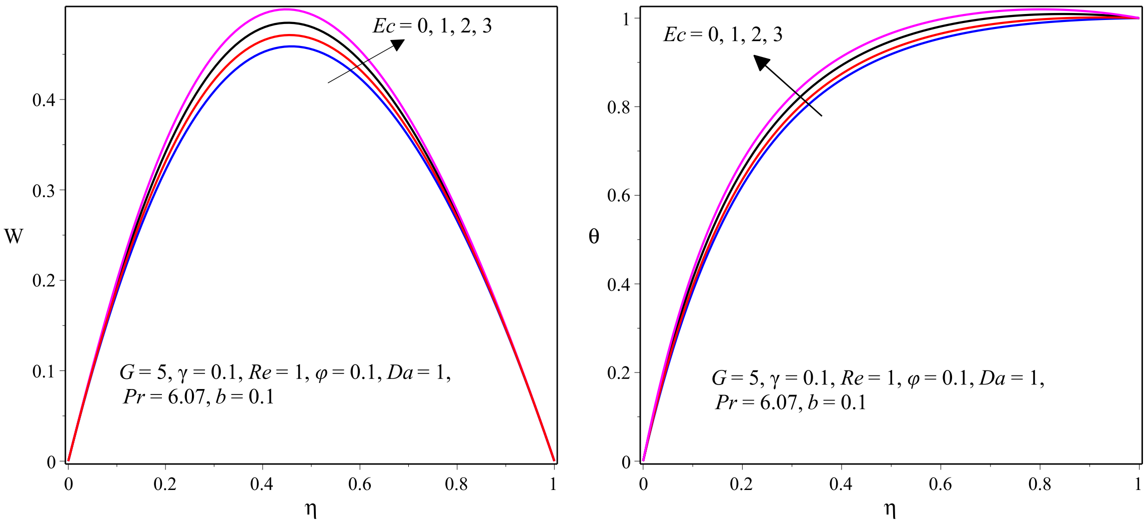

(a) **(b)**

Figure 5.7: **(a)** Velocity and **(b)** Temperature of ferrofluid for increasing values of *Ec*

and temperature show a significant increase with increasing values of *Da* as portrayed in Figures 5.6(a) and 5.6(b). This result is attributed to the fact that when the value of *Da* increases, the permeability of the porous medium increases that indeed support the flow of the ferrofluid and, hence the noticed increase of ferrofluid velocity that in turn increases the ferrofluid temperature. In contrast, the same figures reveal that both velocity and temperature of the ferrofluid decline as the Forchheimer constant *b* that is also called the inertial resistance parameter increases. A bigger value of *b* implies that there is a stronger inertial resistivity force acting in the normal direction to the flow of the ferrofluid. For a large magnitude of *b* stronger inertial resistivity force is in effect inside the flow region of the ferrofluid as a consequence of which the ferrofluid velocity turns out to be lessening which also results in the decline of the ferrofluid temperature.

The effect of the Eckert number Ec on the velocity and temperature profiles of the ferrofluid is depicted in Figures 5.7(a) and 5.7(b) respectively. From these figures, it can be noticed that as the magnitudes of Ec increase, both velocity and temperature of the ferrofluid rise. Indeed, Ec indicates the relation between the enthalpy difference of flow boundary layer and its kinetic energy that leads to the generation of an extra heat and thus describes the viscous heating inside the region of flow. Consequently, when the magnitude of Ec increases the amount of viscous heating also increases inside the region of flow leading to the increment of the ferrofluid temperature that also results in the rise of the ferrofluid velocity.

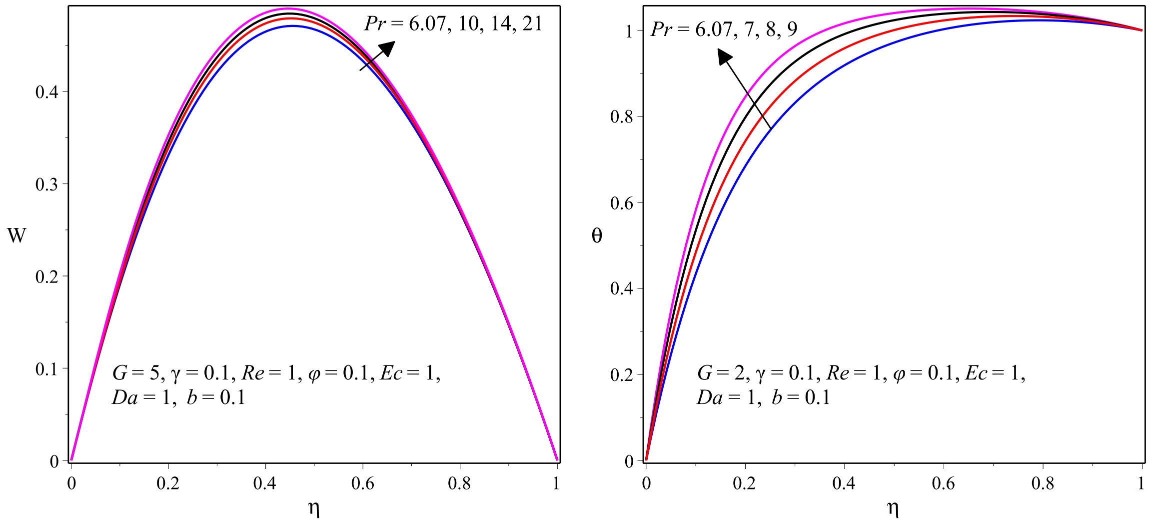

(a) **(b)**

Figure 5.8: **(a)** Velocity and **(b)** Temperature of ferrofluid for increasing values of Pr

Figures 5.8(a) and 5.8(b) display the effects of the Prandtl number Pr on the ferrofluid velocity and temperature profiles. Accordingly, a rise in values of Pr results in an increment of the ferrofluid velocity and temperature profiles. The argument behind this result is the fact that physically Pr is defined as $Pr = \frac{\text{momentum diffusivity}}{\text{thermal diffusivity}}$ and therefore, the elevated value of Pr enhances the momentum diffusivity that results in the enhancement of velocity and temperature profiles of the ferrofluid.

5.5.3 The Wall Shear Stress and Wall Heat Transfer Rate

This subsection encompasses the influences of the embedded flow parameters on the wall shear stress (coefficient of the skin friction) and wall heat transfer rate (local Nusselt number). Actually, all plotted graphs elaborated under this subsection for the coefficient of the skin friction C_f and the Nusselt number Nu are sketched for larger time, $\tau \geq 2$ (steady state) and therefore the results found may not be disturbed by an increment in values of the time for every value of the parameters as a consequence of the result found under subsection 5.6.1.

The Shear Stress at the Wall: Coefficient of the Skin Friction

The effects of the nanoparticles volume fraction φ and Ec on the cofficient of skin friction are indicated in figures 5.9(a) and 5.9(b). Figure 5.9(a) indicated that the coefficient of skin friction at the cold wall of the microchannel was increased with φ and Ec. Physically, the coefficient of skin friction is a decreasing function of ferrofluid temperature as presented in equation (5.24). Besides, as indicated in figure 5.4(b), higher values of φ imply lower ferrofluid temperature. Therefore, as φ increases the coefficient of skin friction at the cold wall ($\eta = 0$) of the microchannel increases as shown in figure 5.9(a). The reverse scenario was noticed at the hot wall ($\eta = 1$) of the microchannel as displayed in figure 5.9(b).

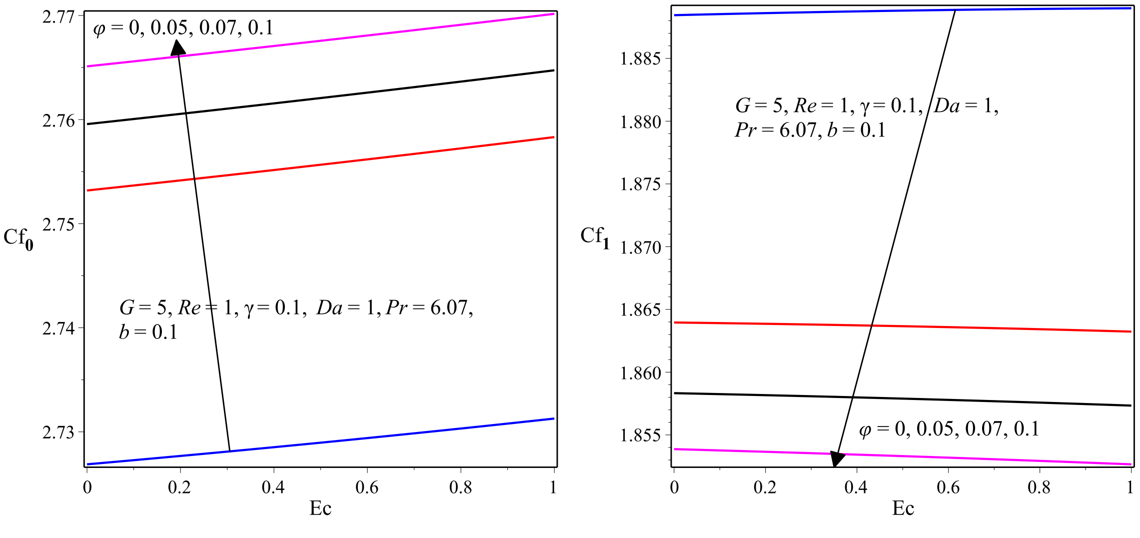

(a) **(b)**

Figure 5.9: **(a)** Skin friction at $\eta = 0$ and **(b)** Skin friction at $\eta = 0$ with increasing values of φ and Ec

Figure 4.10(a) showed that the coefficient of skin friction at the cold wall of the microchannel increases as the dimensionless variable viscosity parameter γ and Ec increase whereas the coefficient of skin friction at the hot wall decreases (see figure 5.10(b)). This may be justified as the hot wall gets more heat than the cold wall for higher values of γ.

Figures 5.11(a) and 5.11(b) described that the skin friction coefficient for both cold and hot walls of the microchannel increases as the Darcy number Da and Ec increases. This may be the case because the ferrofluid velocity increases with Da as shown in figure 5.6(a) and as a consequence, C_f at both walls increases with increasing values of Da.

Figures 5.12(a) and 5.12(b) showed that the coefficient of skin friction for both cold as well as hot walls of the microchannel decreases as the Forchheimer constant b and Ec increase. This may be the case because the ferrofluid temperature decreases with b as shown in figure 5.6(b) and as a result both walls may acquire heat equally.

Figures 5.13(a) indicated that the skin friction coefficient for the cold wall of the microchannel decreases as the Prandtl number Pr and Ec increase. The opposite is observed

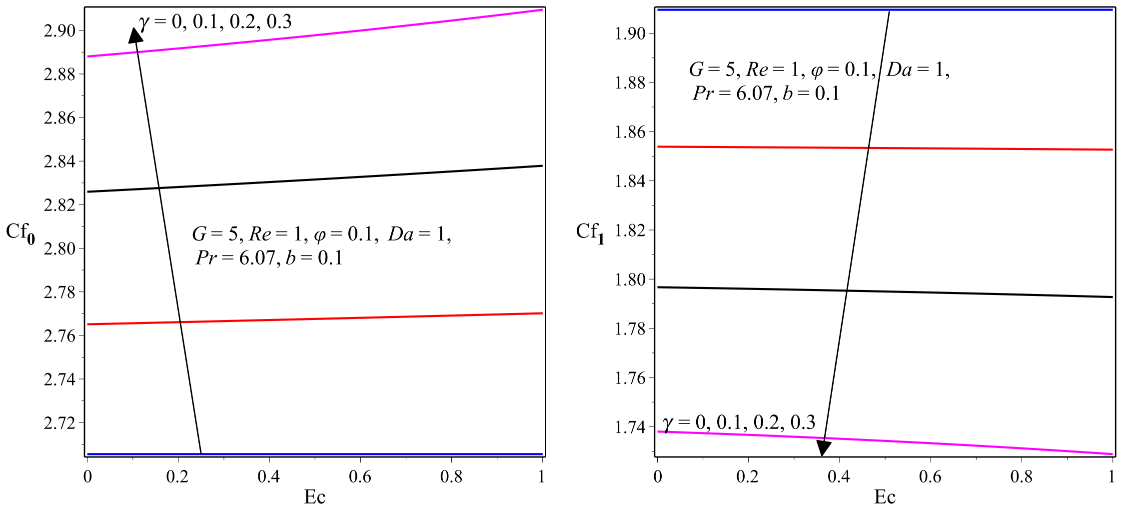

(a) **(b)**

Figure 5.10: **(a)** Skin friction at $\eta = 0$ and **(b)** Skin friction at $\eta = 1$ with increasing values of γ and Ec

for the hot wall as displayed in fig 5.13(b). These results may be justified as when Pr increases the cold wall of the microchannel gets more heat than the hot wall.

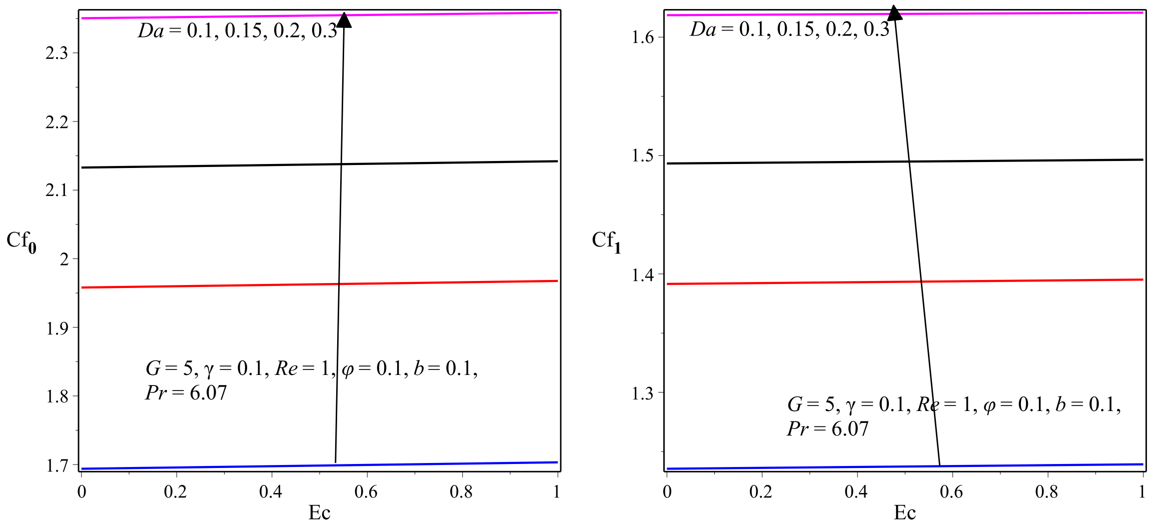

(a) **(b)**

Figure 5.11: **(a)** Skin friction at $\eta = 0$ and **(b)** Skin friction at $\eta = 1$ with increasing values of Da and Ec

Rate of Heat Transfer at the Wall: The Nusselt Number

Figures 5.14(a) and 5.14(b) indicated that the heat transfer rate at both hot and cold walls of the microchannel decreases as the value of the nanoparticles volume fraction φ and Ec increase. The argument behind this result may be, as φ increases the ferrofluid temperature decreases as shown in figure 5.4(b) which results in a decline in the rate of heat transfer at

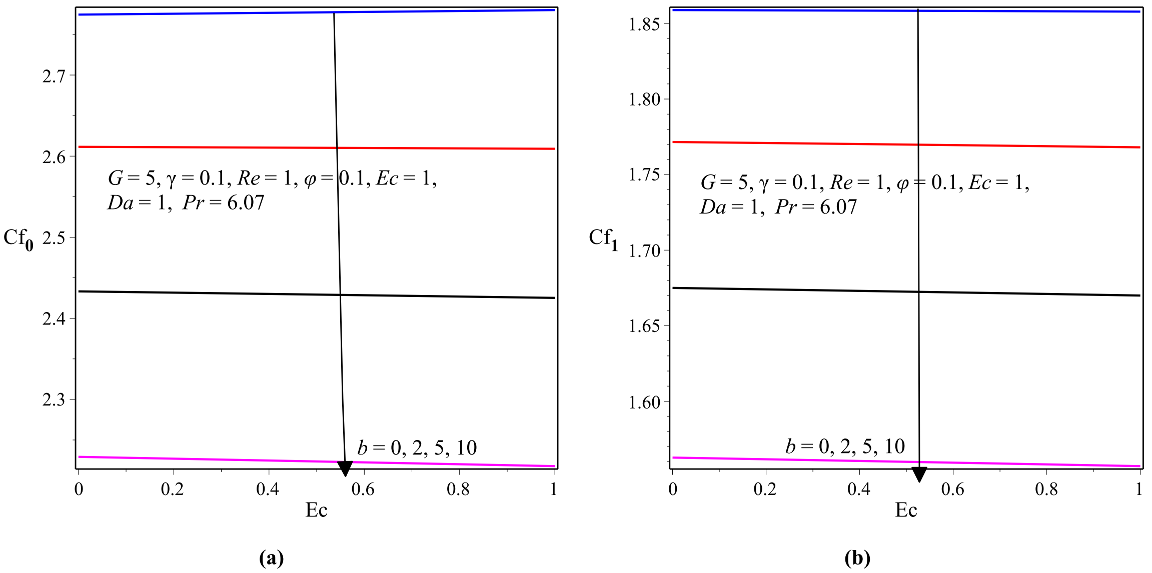

Figure 5.12: **(a)** Skin friction at $\eta = 0$ and **(b)** Skin friction at $\eta = 1$ with increasing values of b and Ec

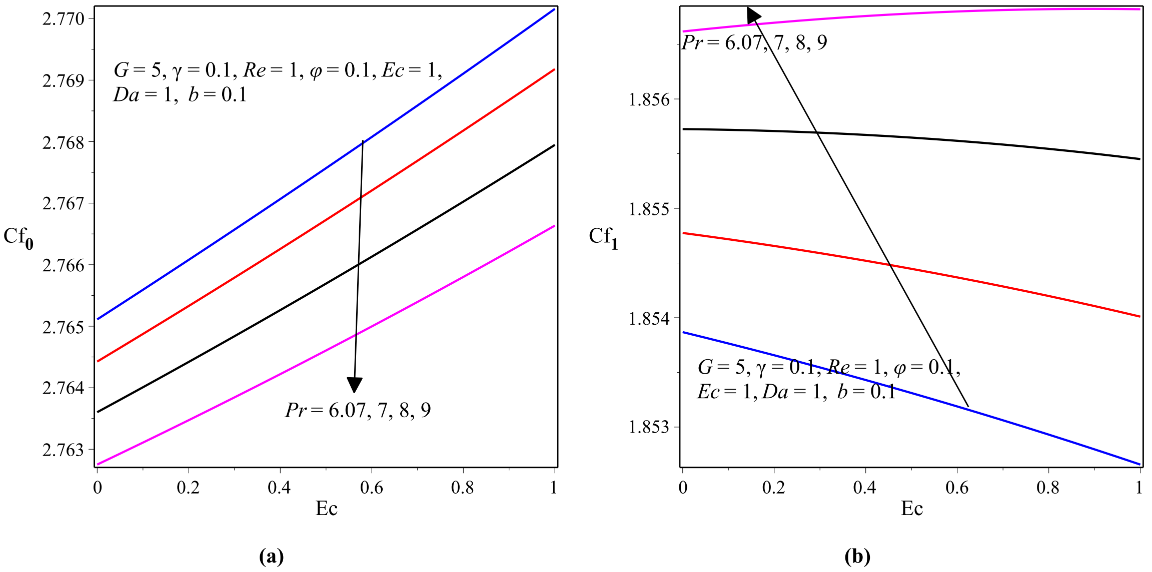

Figure 5.13: **(a)** Skin friction at $\eta = 0$ and **(b)** Skin friction at $\eta = 1$ with increasing values of Pr and Ec

both walls of the microchannel.

Figures 5.15(a) and 5.15(b) described that the heat transfer rate at both cold and hot walls of the microchannel rises with the dimensionless variable viscosity parameter γ and Ec. The reason behind this result may be, as γ increases the ferrofluid temperature increases as shown in figure 5.5(b) which in turn enhances the heat transfer rate at both walls of the microchannel.

Figures 5.16(a) and 5.16(b) illustrated that the heat transfer rate at both hot and cold walls of the microchannel increases as the values of the Darcy number Da and Ec increase. The justification for this result may be, as Da increase the ferrofluid temperature increases

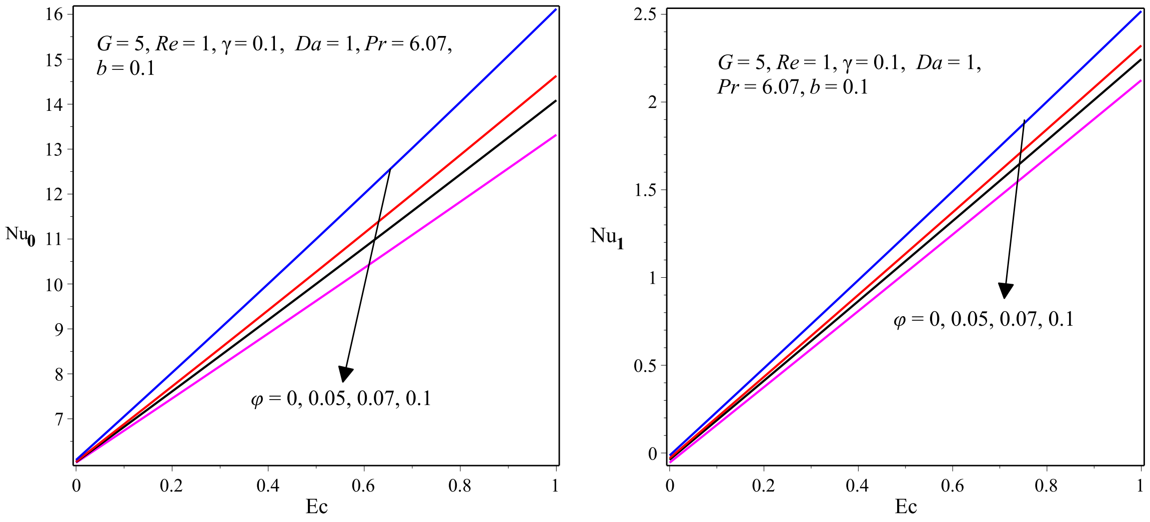

(a) **(b)**

Figure 5.14: **(a)** Nusselt number at $\eta = 0$ and **(b)** Nusselt number at $\eta = 1$ with varying φ and Ec

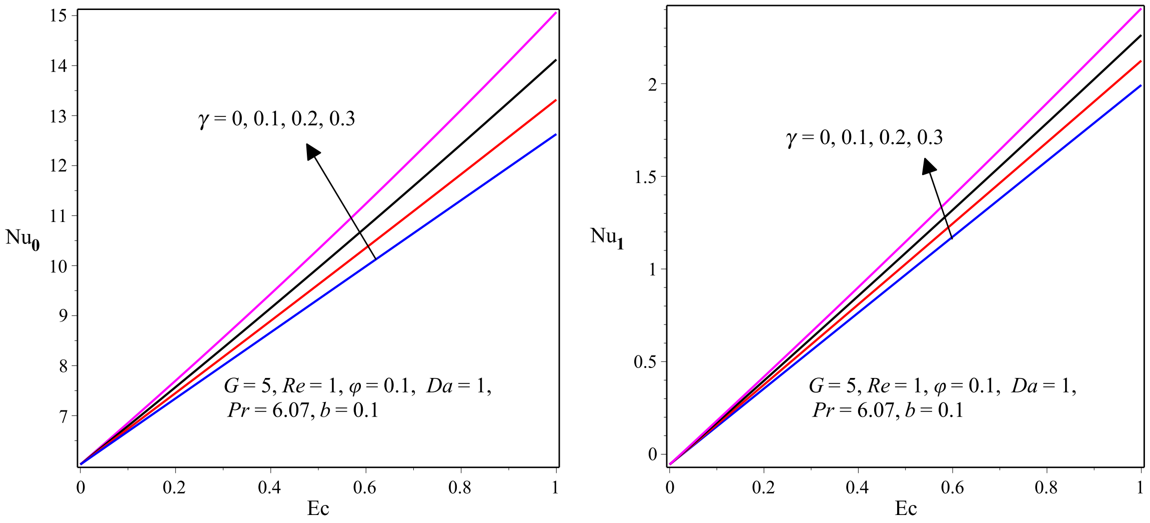

(a) **(b)**

Figure 5.15: **(a)** Nusselt number at $\eta = 0$ and **(b)** Nusselt number at $\eta = 1$ with varying γ and Ec

as illustrated by figure 5.6(b). Consequently, the rate of heat transfer at both walls of the microchannel increases.

Figures 5.17(a) and 5.17(b) demonstrated that the rate of heat transfer for both hot and cold walls of the microchannel decreases as the values of the Forchheimer constant b and Ec increase. This is the case because as b increases the ferrofluid temperature decreases as shown in figure 5.6(b) as a result of which the rate of heat transfer at both walls of the microchannel decreases.

Figures 5.18(a) and 5.18(b) revealed that the rate of heat transfer for cold and hot walls of the microchannel increases with the Prandtl number Pr and Ec. The argument behind this result may be, as *Pr* increases the ferrofluid temperature increases as shown in figure 5.8(b) as a result of which the rate of heat transfer for both walls of the microchannel increases.

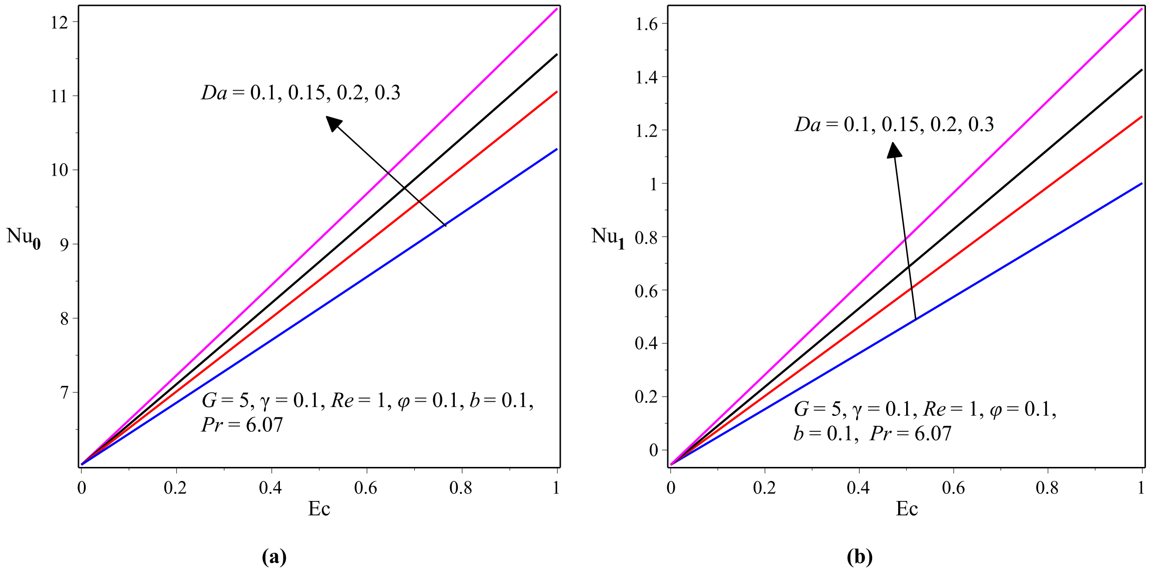

(a) **(b)**

Figure 5.16: **(a)** Nusselt number at $\eta = 0$ and **(b)** Nusselt number at $\eta = 1$ with varying Da and Ec

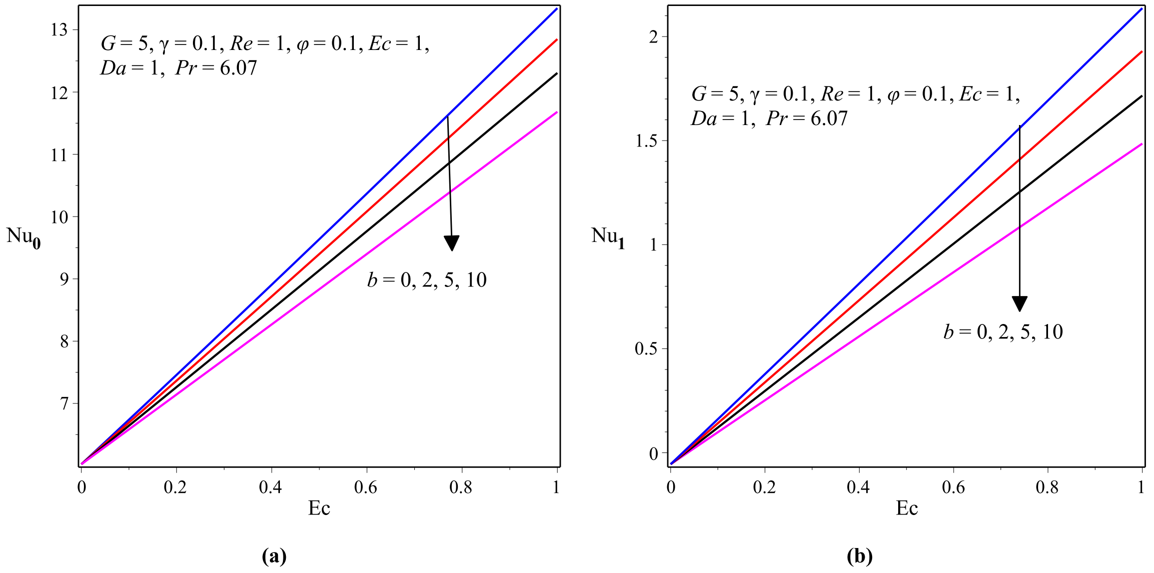

(a) **(b)**

Figure 5.17: **(a)** Nusselt number at $\eta = 0$ and **(b)** Nusselt number at $\eta = 1$ with varying b and Ec

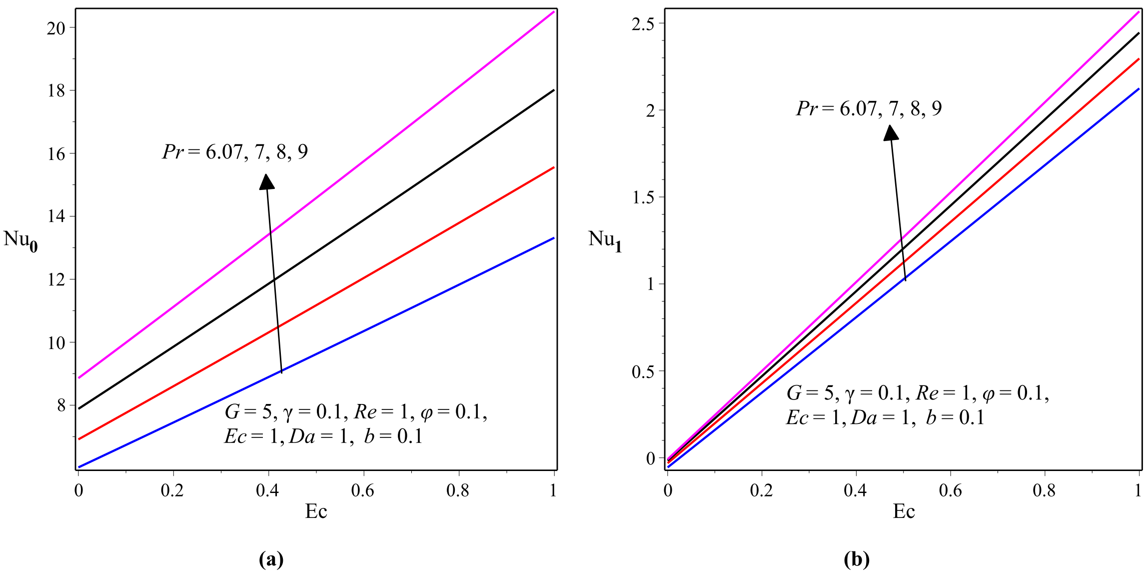

Figure 5.18: **(a)** Nusselt number at $\eta = 0$ and **(b)** Nusselt number at $\eta = 1$ with varying Pr and Ec

CHAPTER 6

UNSTEADY MIXED CONVECTION OF A RADIATING AND REACTING NANOFLUID WITH VARIABLE PROPERTIES IN A POROUS MEDIUM MICROCHANNEL

Radiating and reacting nanofluids flow in microchannels with non-uniform permeable walls temperature and filled with porous media plays an important role in the modern industrial and engineering applications. Therefore, this chapter presents the investigation of hydrodynamical characteristics and thermal properties of radiating and reacting nanofluid with variable transport properties in a microchannel filled with a porous medium. The Buongiorno nanofluid model is employed and the convective boundary condition is also taken into consideration. Indeed, the work in this chapter is an extension of the model problem studied in chapter 4.

6.1 Mathematical Model Formulation

Consider unsteady mixed convective flow of Newtonian incompressible nanofluid in a microchannel filled with a saturated porous medium having permeable walls placed at $y = 0$ and $y = a$ as shown in figure 6.1, where a denotes the distance between two permeable walls of the microchannel. It is assumed that the flow is driven by the combined actions of axial pressure gradient together with fluid body forces due to solutal and thermal buoyancy variations. Furthermore, a nanofluid injection into the microchannel takes place through the left wall ($y = 0$) while a nanofluid suction out of the microchannel occurs at the right wall ($y = a$). At time $t = 0$, the fluid temperature is maintained at T_0 and the fluid is in the static position. For large time ($t > 0$), the flow occurs only when the nanofluid starts to move with the time within the microchannel flow regime and is subject to a convective heat exchange with the surrounding boundaries.

For the axial velocity at the walls, no-slip conditions were imposed and the wall temperature is taken to be non-uniform where the left microchannel wall is placed at temperature T_0 while the right wall is placed at temperature T_w such that $T_0 < T_w$. Both the temperature and concentration are initially zero within the fluid except at the walls where the constant values are maintained.

The nanofluid dynamic viscosity is assumed to be an exponential decreasing function of temperature and hence given as $\mu(T) = \mu_0\, e^{-\gamma_1 (T - T_w)}$, where γ_1 is a viscosity variation parameter and μ_0 is the initial nanofluid dynamic viscosity at temperature T_0. Be-

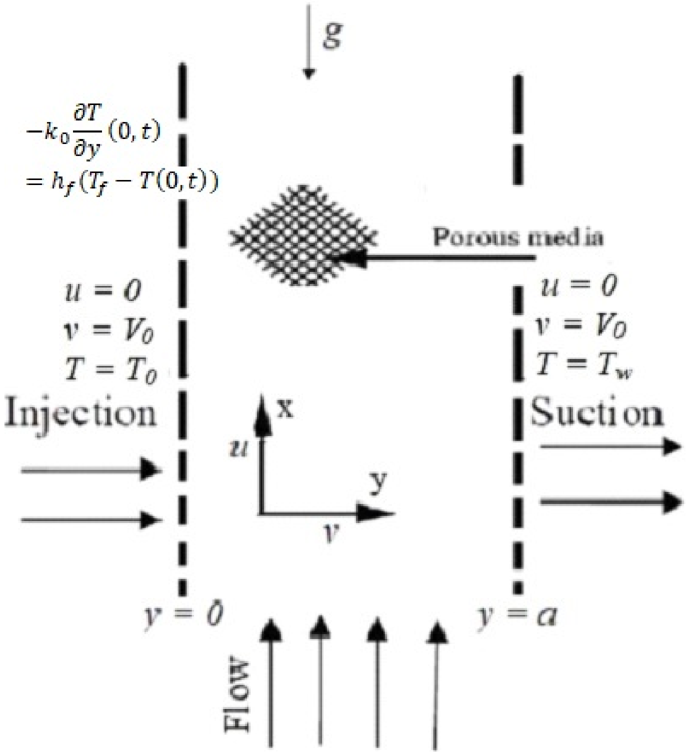

Figure 6.1: Physical Flow Model with Coordinate System

sides, the thermal conductivity of the nanofluid is also assumed to be an exponential increasing function of temperature and hence given as $k(T) = k_0\, e^{\gamma_2(T-T_w)}$ where γ_2 is the thermal conductivity variation parameter and k_0 is the initial nanofluid thermal conductivity at temperature T_0. The axial convection terms are also assumed to be very small in the model equations and are neglected as compared to the normal convection terms and thus, $\frac{\partial T}{\partial x} \ll \frac{\partial T}{\partial y}$, $\frac{\partial C}{\partial x} \ll \frac{\partial C}{\partial y}$, $\frac{\partial u}{\partial x} \ll \frac{\partial u}{\partial y}$.

Actually, the continuity, momentum equations are the same as that of the problem studied in chapter four. However, the energy equation is modified to incorporate temperature-dependent thermal conductivity, heat radiation and convective boundary condition. The concentration equation incorporated the chemical reaction term. Therefore, by considering the above assumptions and using the Darcy-Forchheimer flow model, the governing equations of continuity, linear momentum, energy and concentration under the usual Oberbeck-Boussinesq approximation are presented in the following form.

$$\frac{\partial u}{\partial x} = 0 \tag{6.1}$$

$$\frac{\partial u}{\partial t} + V_0\frac{\partial u}{\partial y} = -\frac{1}{\rho}\frac{\partial P}{\partial x} + \frac{1}{\rho}\frac{\partial}{\partial y}\left[\mu(T)\frac{\partial u}{\partial y}\right] - \frac{\mu(T)u}{\rho K} - \frac{bu^2}{\sqrt{K}} + \beta_1 g(T-T_w) + \beta_2 g(C-C_0) \tag{6.2}$$

$$\begin{aligned}\frac{\partial T}{\partial t}+V_0\frac{\partial T}{\partial y}=\frac{1}{\rho C_p}\frac{\partial}{\partial y}\left[k(T)\frac{\partial T}{\partial y}\right]+\Gamma\left[D_B\frac{\partial C}{\partial y}\frac{\partial T}{\partial y}+\frac{D_T}{T_w}(\frac{\partial T}{\partial y})^2\right]+\frac{\mu(T)}{\rho C_p}(\frac{\partial u}{\partial y})^2\\+\frac{\mu(T)u^2}{\rho C_p K}+\frac{bu^3}{C_p\sqrt{K}}-\frac{1}{\rho Cp}\frac{\partial q_r}{\partial y}\end{aligned}\tag{6.3}$$

$$\frac{\partial C}{\partial t}+V_0\frac{\partial C}{\partial y}=D_B\frac{\partial^2 C}{\partial y^2}+\frac{D_T}{T_w}\frac{\partial^2 T}{\partial y^2}-\varepsilon(C-C_0)\tag{6.4}$$

with the initial and boundary conditions:

$$\begin{aligned}&u(y,0)=0,T(y,0)=T_0,C(y,0)=C_0,\\ \text{and}\quad&\left.\begin{aligned}&u(0,t)=0,-k_0\tfrac{\partial T}{\partial y}(0,t)=h_f(T_f-T(0,t)),\\&D_B\tfrac{\partial C(0,t)}{\partial y}=\tfrac{-D_T}{T_w}\tfrac{\partial T(0,t)}{\partial y},\\&u(a,t)=0,T(a,t)=T_w,\\&C(a,t)=C_1\end{aligned}\right\}\text{for } t>0\end{aligned}\tag{6.5}$$

where u is the axial velocity, V_0 is constant wall suction/injection velocity, ρ is the nanofluid density, P is nanofluid pressure, T is the nanofluid temperature, C is the nanoparticles concentration, C_P is specific heat at constant pressure, Γ is the heat capacity ratio which is the ratio of heat capacity of the nanoparticle and heat capacity of base fluid, K is the porous medium permeability, g is gravitational acceleration, D_B is the Brownian diffusion coefficient, D_T is thermal diffusion coefficient, h_f is convective heat transfer coefficient, T_f is the temperature of the nanofluid heating the surface of the microchannel, ε is the reaction rate, q_r is the thermal radiative heat flux vector and b is the second order dimensionless (porous inertia) resistance coefficient also known as the dimensionless Forchheimer constant such that $b=0$ corresponds to the Darcy law.

Radiation is a process which involves energy transfer by electromagnetic wave propagation which can occur in vacuum as well as in a medium. Experimental evidence indicates that radiant heat transfer is proportional to the fourth power of the absolute temperature, whereas conduction and convection are proportional to a linear temperature difference. From the Rosseland approximation of equation (1.3), the radiative heat flux q_r in the energy equation (6.3) is given by

$$q_r=-\frac{4\sigma^*}{3k^*}\frac{\partial T^4}{\partial y}\tag{6.6}$$

where σ^* and k^* represent the Stefan Boltzmann constant and the Rosseland mean absorption coefficient, respectively. The temperature difference within the flow is also assumed to be sufficiently small so that T^4 in equation (6.6) can be easily linearized about T_0 by using the Taylor series expansion as $T^4=T_0^4+4T_0^3(T-T_0)+6T_0^2(T-T_0)^2+\ldots$ Then neglecting the second and higher order terms, we have $T^4\approxeq 4T_0^3T-3T_0^4$. So, $\frac{\partial T^4}{\partial y}=4T_0^3\frac{\partial T}{\partial y}$. Now using this in equation (6.6) we get $q_r = -\frac{16\sigma^* T_0^3}{3k^*}\frac{\partial T}{\partial y}$. Therefore,

$$\frac{\partial q_r}{\partial y} = -\frac{16\sigma^* T_0^3}{3k^*}\frac{\partial^2 T}{\partial y^2} \tag{6.7}$$

Substituting equation (6.7) into the energy equation (6.3) yields,

$$\begin{aligned} \frac{\partial T}{\partial t} + V_0\frac{\partial T}{\partial y} &= \frac{1}{\rho C_p}\frac{\partial}{\partial y}\left[k(T)\frac{\partial T}{\partial y}\right] + \Gamma\left[D_B\frac{\partial C}{\partial y}\frac{\partial T}{\partial y} + \frac{D_T}{T_w}(\frac{\partial T}{\partial y})^2\right] \\ &+ \frac{\mu(T)}{\rho C_p}(\frac{\partial u}{\partial y})^2 + \frac{\mu(T)u^2}{\rho C_p K} + \frac{bu^3}{C_p\sqrt{K}} + \frac{1}{\rho Cp}\frac{16\sigma^* T_0^3}{3k^*}\frac{\partial^2 T}{\partial y^2} \end{aligned} \tag{6.8}$$

6.2 Non-Dimensional Formulation

The steps of non-dimensionalization procedure is similar to that of the one followed in chapter four. Hence, in order to non-dimensionalize the governing equations, the following dimensionless variables were introduced.

$$\begin{aligned} &\eta = \frac{y}{a}, X = \frac{x}{a}, W = \frac{\rho a u}{\mu_0}, \tau = \frac{\mu_0 t}{\rho a^2}, \theta = \frac{T - T_0}{T_w - T_0}, \phi = \frac{C - C_0}{C_1 - C_0}, P^* = \frac{\rho a^2 P}{\mu_0^2}, A = -\frac{\partial P^*}{\partial X}, \\ &Re = \frac{\rho V_0 a}{\mu_0}, \gamma = \gamma_1(T_w - T_0), \lambda = \gamma_2(T_w - T_0), S = \frac{a^2}{K}, F = \frac{ba}{\sqrt{K}}, Bi = \frac{ah_f}{k_0}, \alpha = \frac{\varepsilon\rho a^2}{\mu_0}, \\ &Gt = \frac{\beta_1 g\rho^2 a^3(T_w - T_0)}{\mu_0^2}, Gc = \frac{\beta_2 g\rho^2 a^3(C_1 - C_0)}{\mu_0^2}, Nt = \Gamma\frac{D_T}{T_w}(T_w - T_0)\frac{\rho}{\mu_0}, R = \frac{16\sigma^* T_0^3}{3k^* k_0}, \\ &Nb = \Gamma_B(C_1 - C_0)\frac{\rho}{\mu_0}, Ec = \frac{\mu_0^2}{\rho^2 a^2 C_p(T_w - T_0)}, Pr = \frac{\mu_0 C_p}{k_0}, Sc = \frac{\mu_0}{\rho D_B} \end{aligned} \tag{6.9}$$

Using the dimensionless variables defined in (6.9) into (6.1)–(6.2), (6.4)–(6.5) and (6.8) yields, the following dimensionless governing equations.

$$\frac{\partial W}{\partial X} = 0 \tag{6.10}$$

$$\frac{\partial W}{\partial \tau} + Re\frac{\partial W}{\partial \eta} = A + e^{-\gamma\theta}\left[\frac{\partial^2 W}{\partial \eta^2} - \gamma\frac{\partial \theta}{\partial \eta}\frac{\partial W}{\partial \eta}\right] - Se^{-\gamma\theta}W - FW^2 + Gt\theta + Gc\phi \tag{6.11}$$

$$\begin{aligned} \frac{\partial \theta}{\partial \tau} + Re\frac{\partial \theta}{\partial \eta} = \frac{1}{Pr}\left[e^{\lambda\theta} + R\right]\frac{\partial^2 \theta}{\partial \eta^2} + Nb\frac{\partial \phi}{\partial \eta}\frac{\partial \theta}{\partial \eta} + \left[Nt + \frac{1}{Pr}\lambda e^{\lambda\theta}\right](\frac{\partial \theta}{\partial \eta})^2 \\ + Ece^{-\gamma\theta}(\frac{\partial W}{\partial \eta})^2 + SEce^{-\gamma\theta}W^2 + FEcW^3 \end{aligned} \tag{6.12}$$

$$\frac{\partial \phi}{\partial \tau} + Re\frac{\partial \phi}{\partial \eta} = \frac{1}{Sc}\left[\frac{\partial^2 \phi}{\partial \eta^2} + \frac{Nt}{Nb}\frac{\partial^2 \theta}{\partial \eta^2}\right] - \alpha\phi \tag{6.13}$$

However, it is important to show the steps followed to non-dimensionalize the convective boundary condition: $-k_0\frac{\partial T}{\partial y}(0,t) = h_f(T_f - T(0,t))$, where T_f is convective surface temperature and h_f is convective heat transfer coefficient.

$$\begin{aligned}
&-k_0\frac{\partial T}{\partial y}(0,t) = h_f(T_f - T(0,t)) \\
&\Rightarrow -k_0\frac{(T_w - T_0)}{a}\frac{\partial \theta}{\partial \eta}(0,\tau) = h_f(T_w - T(0,\tau)), \text{ since } T_f = T_w
\end{aligned}$$

$$\begin{aligned}
&\Rightarrow -k_0\frac{(T_w - T_0)}{a}\frac{\partial \theta}{\partial \eta}(0,\tau) = h_f(T_w - T_0 + T_0 - T(0,\tau)) \\
&\Rightarrow \frac{\partial \theta}{\partial \eta}(0,\tau) = -\frac{ah_f}{k_0}\frac{(T_w - T_0 + T_0 - T(0,\tau))}{T_w - T_0} = -Bi(1-\theta(0,\tau)), \text{ since } \theta = \frac{T - T_w}{T_w - T_0}
\end{aligned}$$

Therefore,

$$\frac{\partial \theta}{\partial \eta}(0,\tau) = -Bi(1-\theta(0,\tau)) \tag{6.14}$$

where, $Bi = \frac{ah_f}{k_0}$ is the Biot number of the microchannel.

Therefore, the corresponding dimensionless initial and boundary conditions are:

$$\begin{aligned}
&W(\eta,0) = 0, \theta(\eta,0) = 0, \phi(\eta,0) = 0, \\
&\text{and} \quad \left.\begin{array}{l}
W(0,\tau) = 0, \frac{\partial \theta(0,\tau)}{\partial \eta} = -Bi[1-\theta(0,\tau)], \\
Nb\frac{\partial \phi(0,\tau)}{\partial \eta} + Nt\frac{\partial \theta(0,\tau)}{\partial \eta} = 0, \\
W(1,\tau) = 0, \theta(1,\tau) = 1, \\
\phi(1,\tau) = 1
\end{array}\right\} \text{for } \tau > 0
\end{aligned} \tag{6.15}$$

where, τ is dimensionless time, *Re* is the suction/injection Reynolds number, *Gt* is the Grashof number due to thermal buoyancy effect, *Gc* is the Grashof number due to solutal buoyancy effect, *Ec* is the Eckert number, *Pr* is the Prandtl number, *A* is dimensionless axial pressure gradient parameter, γ is the dimensionless viscosity variation parameter, λ is the dimensionless thermal conductivity variation parameter, *S* is the porous media shape factor parameter and *F* is the Forchheimer number also called the Forchheimer inertial resistance which is the second order porous media resistance parameter, *R* is radiation parameter, *Sc* is the Schmidt number, *Nb* is the Brownian motion parameter, *Nt* is the thermophoresis parameter, α is dimensionless reaction rate parameter and *Bi* is the Biot number of the microchannel.

6.3 Physical Quantities of Engineering Interests

Other physical quantities of practical significance in this study are the skin friction coefficient C_f, the local Nusselt number *Nu* and the local Sherwood number *Sh*. Indeed, the derivation of the skin friction coefficient, Nusselt number and Sherwood number follow the same steps to that of the problem in chapter four and thus C_f, Nu, Sh at the microchannel walls take the following dimensionless forms.

$$C_f = e^{-\gamma\theta}\frac{dW}{d\eta}\bigg|_{\eta=0,1}, \quad Nu = -\frac{d\theta}{d\eta}\bigg|_{\eta=0,1}, \quad Sh = -\frac{d\phi}{d\eta}\bigg|_{\eta=0,1} \tag{6.16}$$

6.4 Numerical Solutions

The finite difference numerical method adopted to tackle the obtained model initial boundary value problem (IBVP) (6.11)–(6.13) and (6.15) is the semi-discretization method (method of lines). The method is numerically stable with a high level of accuracy based on the well known Fourth Order Runge-Kutta integration scheme (Hamid et al., 2019). The numerical approach includes transforming the obtained IBVP into Initial Value Problem (IVP) by discretizing centrally in space only. Thereafter, the obtained IVP is numerically solved using the fourth order Runge-Kutta integration scheme. Thus, the semi-discretization scheme for the velocity, temperature and concentration fields are recorded as follows:

$$\begin{aligned}\frac{dW_i}{d\tau} &= A - Re\frac{W_{i+1}-W_{i-1}}{2\Delta\eta} - e^{-\gamma\theta_i}S^2W_i - FW_i^2 + Gt\theta_i + Gc\phi_i \\ &+ e^{-\gamma\theta_i}\left[\frac{W_{i-1}-2W_i+W_{i+1}}{(\Delta\eta)^2} - \gamma\frac{\theta_{i+1}-\theta_{i-1}}{2\Delta\eta}\cdot\frac{W_{i+1}-W_{i-1}}{2\Delta\eta}\right]\end{aligned} \tag{6.17}$$

$$\begin{aligned}\frac{d\theta_i}{d\tau} &= -Re\frac{\theta_{i+1}-\theta_{i-1}}{2\Delta\eta} + \frac{1}{Pr}\left[e^{-\lambda\theta_i}+R\right]\left[\frac{\theta_{i-1}-2\theta_i+\theta_{i+1}}{(\Delta\eta)^2}\right] + Nb\frac{\phi_{i+1}-\phi_{i-1}}{2\Delta\eta}\cdot\frac{\theta_{i+1}-\theta_{i-1}}{2\Delta\eta} \\ &+ \left[Nt + \frac{1}{Pr}\lambda e^{\lambda\theta_i}\right]\left[\frac{\theta_{i+1}-\theta_{i-1}}{2\Delta\eta}\right]^2 + Ece^{-\gamma\theta_i}\left[\frac{W_{i+1}-W_{i-1}}{2\Delta\eta}\right]^2 + S^2Ece^{-\gamma\theta_i}W_i^2 + FEcW_i^3\end{aligned} \tag{6.18}$$

$$\frac{d\phi_i}{d\tau} = -Re\frac{\phi_{i+1}-\phi_{i-1}}{2\Delta\eta} + \frac{1}{Sc}\left[\frac{\phi_{i-1}-2\phi_i+\phi_{i+1}}{(\Delta\eta)^2} + \frac{Nt}{Nb}\cdot\frac{\theta_{i-1}-2\theta_i+\theta_{i+1}}{(\Delta\eta)^2}\right] - \alpha\phi_i \tag{6.19}$$

The initial conditions are

$$W_i(0) = 0, \;\; \theta_i(0) = 0, \;\; \phi_i(0) = 0 \tag{6.20}$$

where, $W_i(\tau) = W(\eta_i,\tau), \theta_i(\tau) = \theta(\eta_i,\tau), \phi_i(\tau) = \phi(\eta_i,\tau)$ and the spatial interval $[0,1]$ partitioned into N equal sub-intervals. The grid size and the grid points are defined as $\Delta\eta = \frac{1}{N}$ and $\eta_i = \frac{i-1}{\Delta\eta}$ for $1 \leq i \leq N+1$.

6.5 Results and Discussion

This subsection presents the detailed overview of numerical outcomes and physical interpretation of the effects of various embedded parameters such as A, Re, Ec, Gt, Gc, S, F, γ,

λ, Nt, Nb, Pr, Sc, α, Bi, R on the flow field variables (W, θ, ϕ) as well as on the physical quantities of engineering interests (C_f, Nu, Sh).

6.5.1 Transient and Steady State Profiles

The transient and steady state profiles for the fluid velocity, temperature and concentration are portrayed in figure 6.2(a), figure 6.2(b) and figure 6.3 respectively. From these figures it can be observed that the velocity, temperature and concentration profiles show a parabolic shape with transient increase and attains the steady states at about $\tau \geq 1.9$. In addition, figure 6.2(a) shows that the velocity profile attains its maximum value around the microchannel center line region and then reduces to zero because of the no-slip boundary conditions. Figure 6.2(b) demonstrates that the temperature profile attained its lowest value at the cold wall and gradually increasing towards the hot wall where it attained its maximum value whereas figure 6.3 indicates that the concentration profile attained its maximum value at the cold wall and starts declining gradually towards the hot wall where it attains its lowest value.

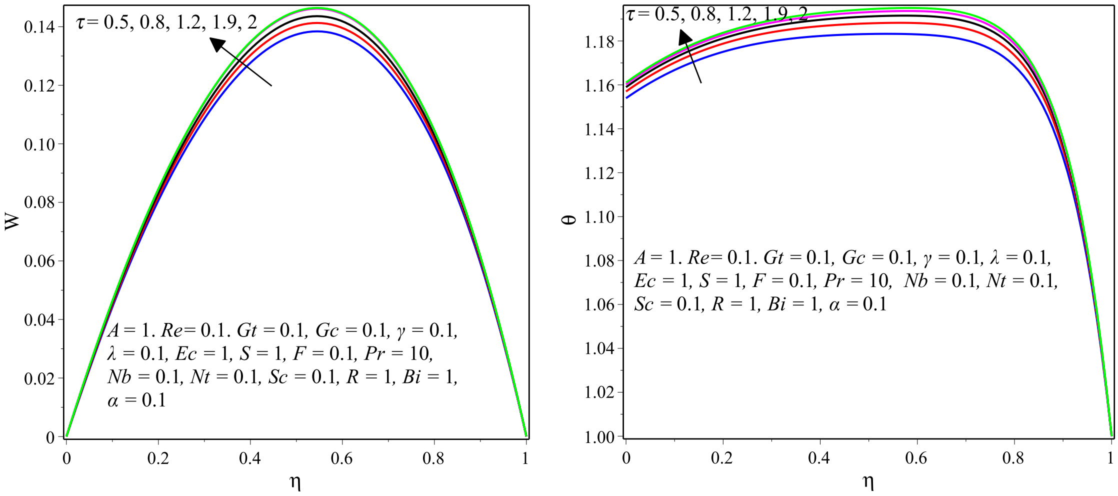

(a) **(b)**

Figure 6.2: **(a)** Velocity and **(b)** Temperature profiles with transient and steady state solutions

6.5.2 Parameter Dependent Solutions

From figures 6.4(a) and 6.4(b) it is observed that as the magnitude of the Eckert number Ec increases both the nanofluid velocity and temperature profiles increase. From the literature, the studies in (Makinde et al., 2019; Monaledi and Makinde, 2018) reported similar results. However, the concentration profile shows a retarding trend with increasing values of the Eckert number Ec as presented in figure 6.5(a). This result is similar to the one obtained in (Bhandari, 2019). Figures 6.4(a) and 6.4(b) also display that both the nanofluid velocity and temperature profiles increase with the chemical reaction parameter α. References

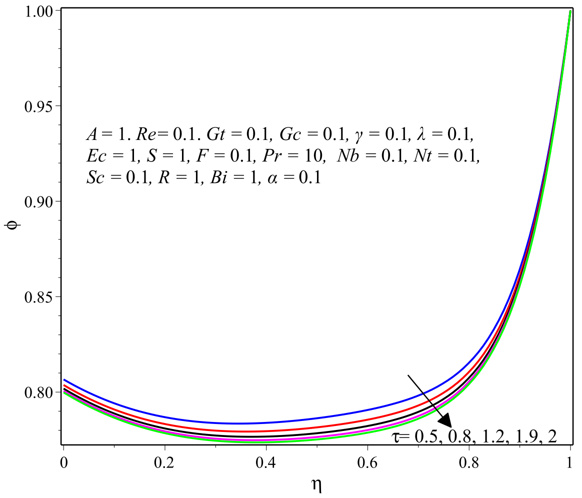

Figure 6.3: Concentration profile with transient and steady state solution

Venkateswarlu et al. (2019) and Bhandari (2019) reported similar findings. Unlike, from figure 6.5(a) it is observed that an increment in α shows a retarding effect on the concentration profile. This is because of the fact that the reactants are consumed during the homogeneous reaction and thus a decrease in the concentration is observed.

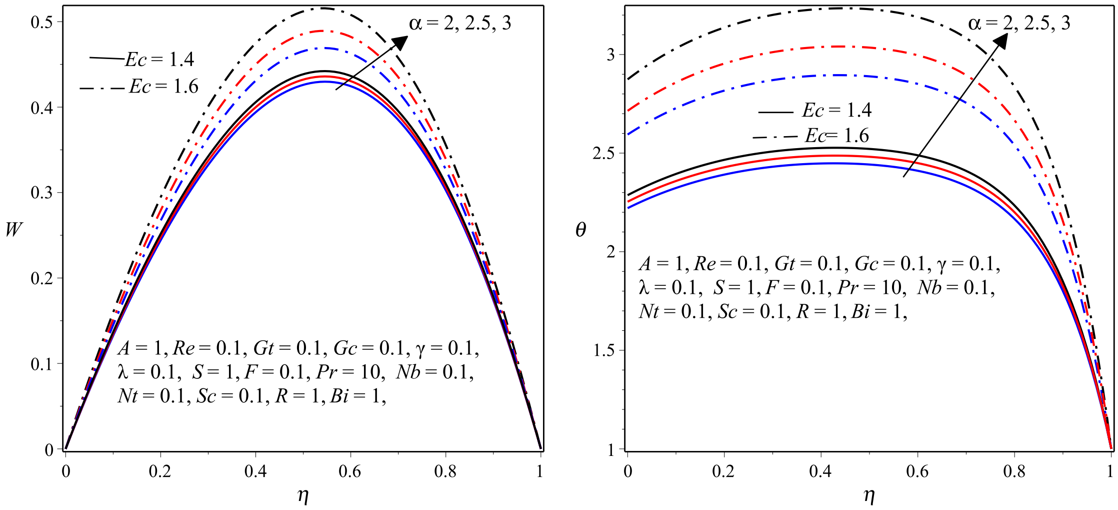

(a) **(b)**

Figure 6.4: **(a)** Velocity and **(b)** Temperature profiles with varying Ec and α

Figures 6.6(a) and 6.6(b) pictures that as the dimensionless variable viscosity parameter γ increases a significant rise in the fluid velocity and temperature profiles is observed. This is the case because an increase in γ reduces the fluid viscosity since $\mu(T) = \mu_0 e^{-\gamma\theta}$. So, the fluid becomes less viscous and hence friction between fluid layers decrease due to which fluid velocity remains at higher levels for higher values of γ. The research works in (Monaledi and Makinde, 2018; Venkateswarlu et al., 2019) indicated similar results. However, increasing the values of the variable thermal conductivity parameter λ decreases the nanofluid velocity

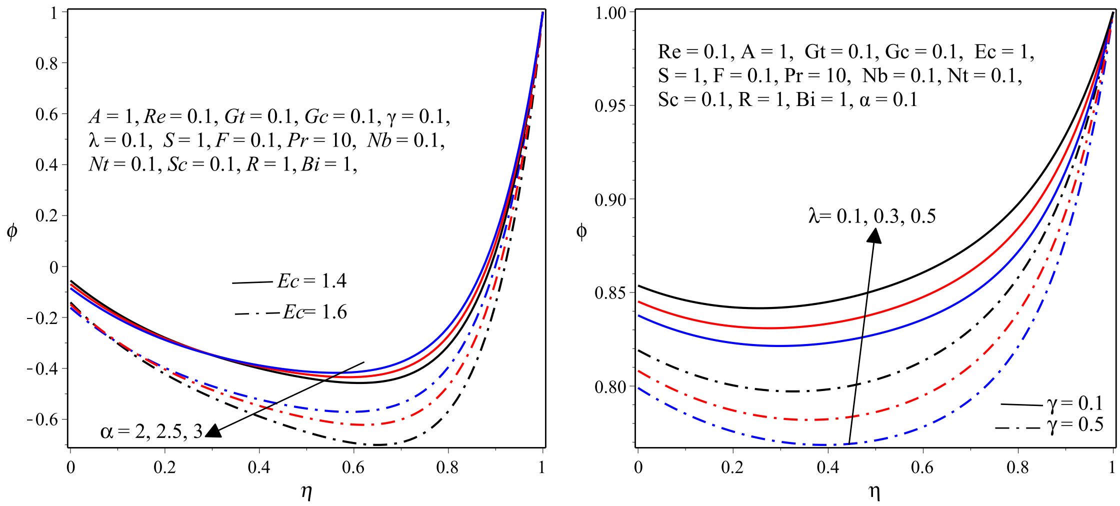

(a) **(b)**

Figure 6.5: **(a)** Effects of Ec and α and **(b)** γ and λ on the concentration profile

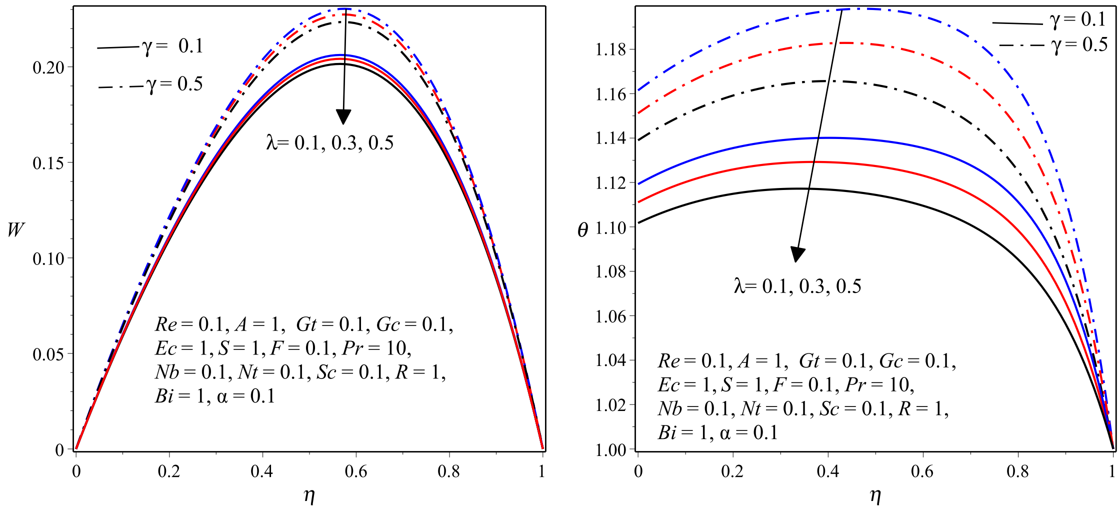

(a) **(b)**

Figure 6.6: **(a)** Velocity and **(b)** Temperature profiles with varying γ and λ

and temperature. A similar outcome was reported in (Venkateswarlu et al., 2019). Figure 6.5(b) shows the opposite trend for the concentration profile.

Figures 6.7(a) and 6.7(b) display the effects of the thermal Grashof number Gt and the solutal Grashof number Gc on velocity and temperature profiles. The velocity and temperature profiles increase with Gt and Gc as shown in figures 6.7(a) and 6.7(b). This is the case because as the values of Gt and Gc enhanced, the body forces acting on the fluid (thermal and solutal buoyancy forces) also get enhanced which also enhance the velocity that in turn increase the viscous heating and hence increasing the fluid temperature. The study in (Monaledi and Makinde, 2018; Bhandari, 2019) revealed similar results. The opposite scenario is demonstrated in figure 6.8(a) for the concentration profile.

Figures 6.9(a) and 6.9(b) depict the effects of the porous medium parameters S and F on

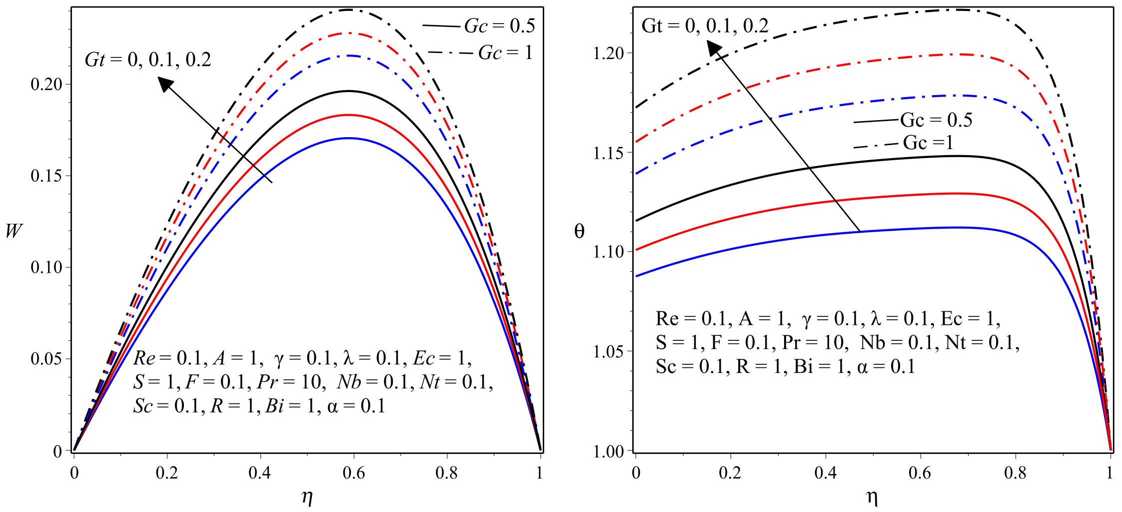

(a) **(b)**

Figure 6.7: **(a)** Velocity and **(b)** Temperature profiles with varying *Gt* and *Gc*

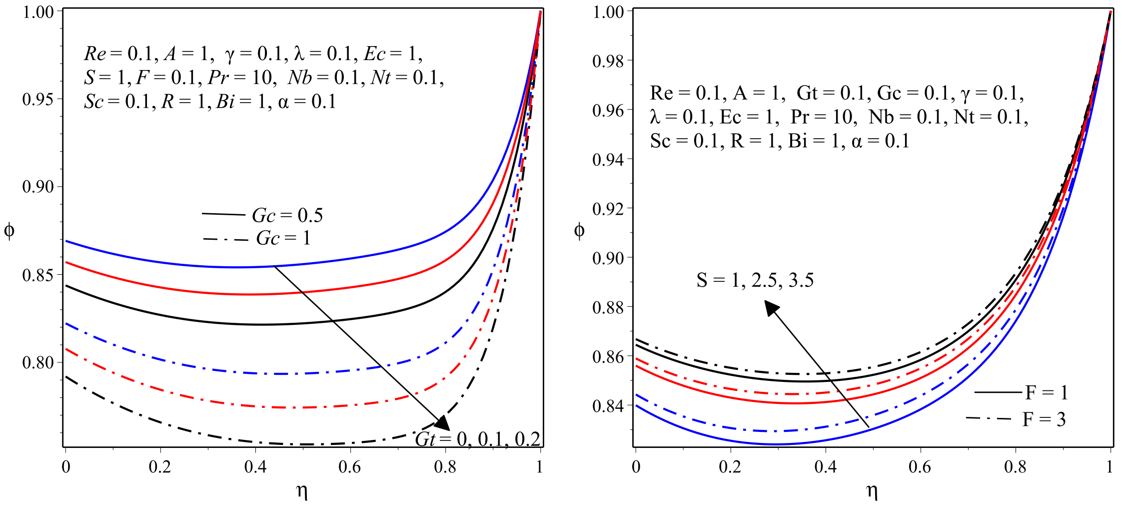

(a) **(b)**

Figure 6.8: **(a)** Effects of *Gt* and *Gc* and **(b)** Effects of *S* and *F* on the concentration profile

the velocity and temperature profiles. Figures 6.9(a) and 6.9(b) portray that both the velocity and temperature profiles decrease significantly as the porous medium shape parameter S increases. The reason behind this result is the fact that as the value of S increase, the porous medium permeability decreases which should naturally dampens the fluid flow and thus the observed decline in the magnitude of fluid velocity which also results in the decrement of viscous heating which in turn decreases the magnitude of fluid temperature. Besides, from the same figures it is observed that the fluid velocity and temperature profiles decreases with increasing values of the Forchheimer number F which is also known as inertial resistance parameter. Physically, large values of F implies the stronger resistant inertial force in the direction normal to the fluid flow which is due to the intensive dimensionless drag force coefficient b since $F = \frac{ba}{\sqrt{K}}$. For higher values of b stronger resistivity inertial force is ef-

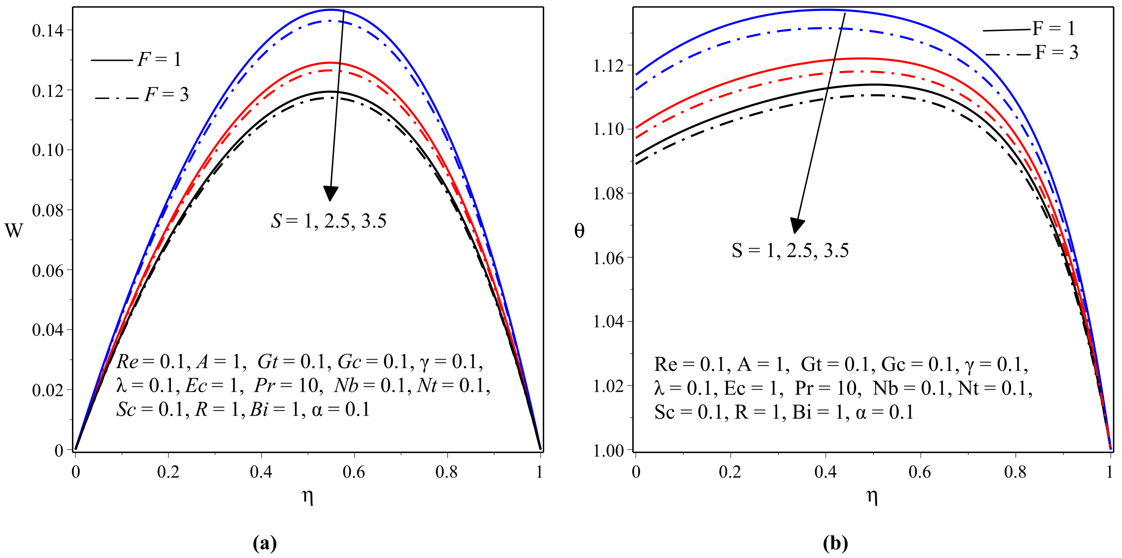

Figure 6.9: **(a)** Velocity and **(b)** Temperature profiles with varying S and F

fective within the fluid flow so that the velocity becomes lessen and consequently the fluid temperature decreases. These results are similar to the findings in the works of (Makinde and Rundora, 2018). On the contrary, figure 6.8(b) reveals that as both S and F increase the concentration profile decreases.

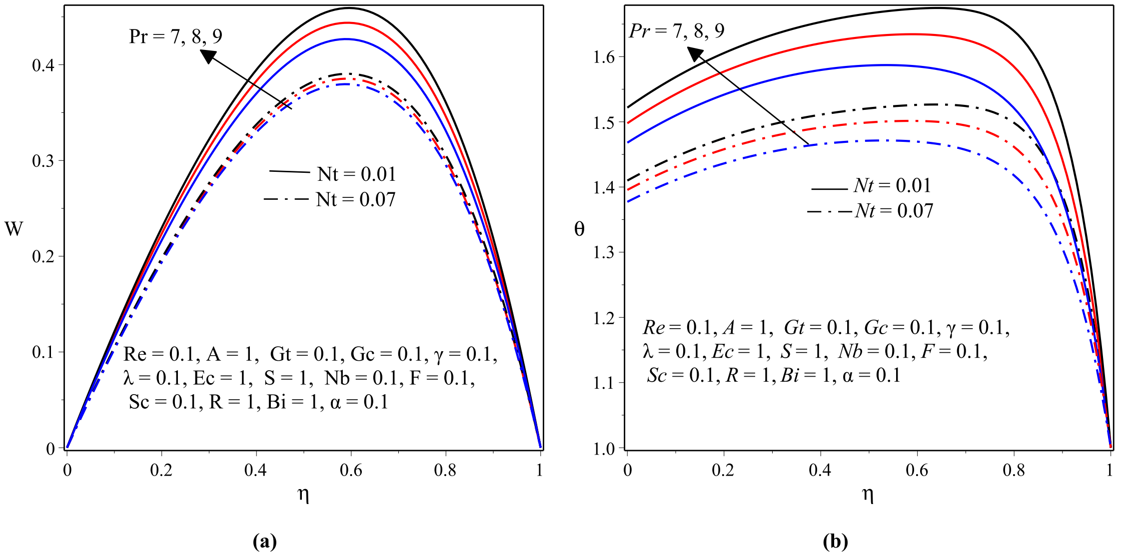

Figure 6.10: **(a)** Velocity and **(b)** Temperature profiles with varying Pr and Nt

Figures 6.10(a) and 6.10(b) are double graphs that display the effects of the Prandtl number Pr and the thermophoresis parameter Nt on the velocity and temperature profiles. According to figures 6.10(a) the larger values of Pr leads to a significant increase in the velocity and temperature profiles since Pr is the ratio of momentum diffusivity to thermal diffusivity, therefore, the elevated values of Pr enhance the momentum diffusivity that results in enhancement of the velocity and temperature profiles. From the literature, (Venkateswarlu

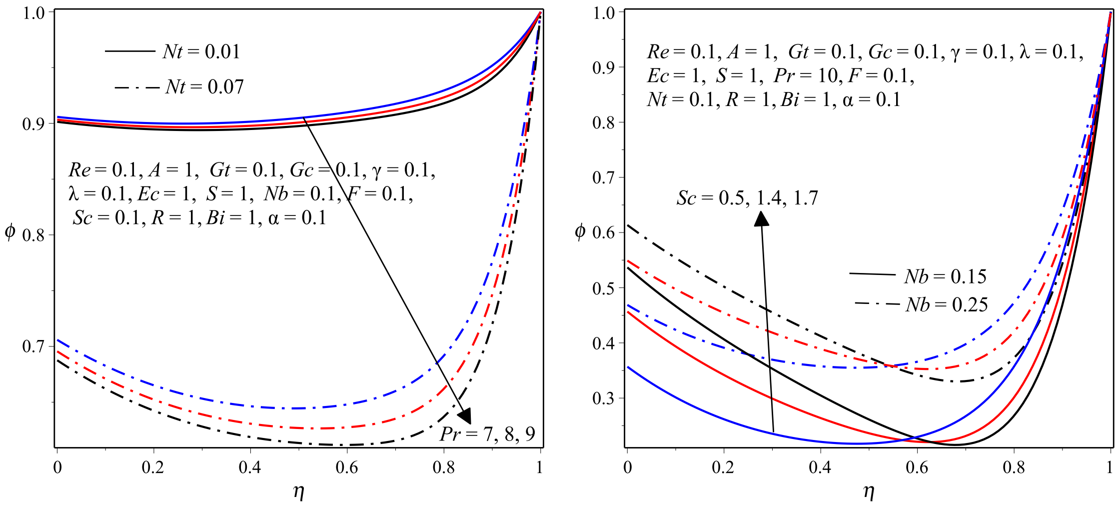

(a) **(b)**

Figure 6.11: **(a)** Effects of *Pr* and *Nt* and **(b)** Effects of *Sc* and *Nb* on the concentration profile

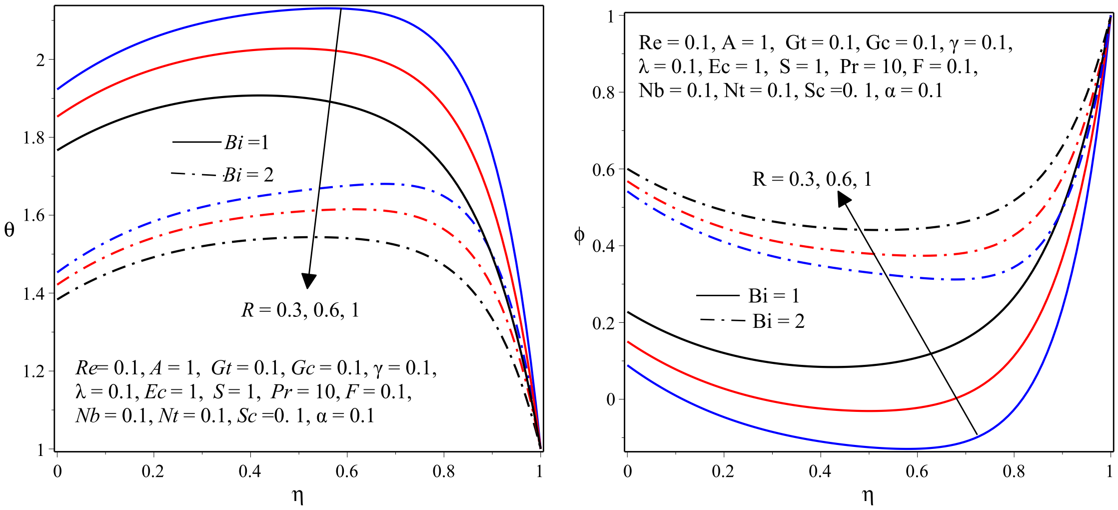

(a) **(b)**

Figure 6.12: **(a)** Temperature and **(b)** Concentration profiles with varying *Bi* and *R*

et al., 2019; Sujatha et al., 2019) indicated similar findings. On the other hand, thermophoresis is a mechanism in which small particles are pulled away from hot region to cold one and thus figure 6.10(a) and 6.10(b) declare that as the value of *Nt* enhances the velocity and temperature profiles decline. The reason behind this argument is that an enhancement in *Nt* yields a stronger thermophoretic force which allows deeper migration of nanoparticles from hot nanofluid to the cold surface resulting in lower fluid temperature. Figure 6.11(a) shows that the concentration profile decreases with both the Prandtl number *Pr* and the thermophoresis parameter *Nt*. Actually, these outcomes confirm the results reported in (Venkateswarlu et al., 2019; Bhandari, 2019; Sujatha et al., 2019).

Figure 6.11(b) is also a double graph that portrays the effects of *Sc* and *Nb* on the concentration profile. This figure displays that the concentration profile increases with the the Schmidt number Sc. Physically, larger values of Schmidt number Sc indicate less mass diffusion which causes the concentration of nanoparticles to remain larger in the fluid. The same results were obtained in the references (Venkateswarlu et al., 2019; Ramzan et al., 2020; Sujatha et al., 2019). The concentration profile also shows an increasing behavior for larger values of the Brownian motion parameter Nb as shown in figure 6.11(b). The argument behind this result may be when the magnitudes of Nb increases, arbitrary disorganized motion and also collision of the nanoparticles in the fluid increase which may enhance the concentration of the nanoparticles in the fluid. The same result was presented by (Bhandari, 2019).

The effects of the radiation parameter R and the Biot number Bi on the nanofluid temperature and concentration profiles are are displayed through figures 6.12(a) and 6.12(b) respectively. Consequently, from figure 6.12(a) it is observed that the temperature profile decreases as R increases due to fact that when a large value of radiative heat is absorbed by the nanofluid the buoyancy force decreases which retards the flow rate and thereby retarding the temperature profiles. Thus, R quite effectively controls the microchannel temperature distribution and flow transport which plays a significant role in cooling the system. These types of applications can be used in pseudoscientific alternative medicine to control blood pressure through the process of magnetoelectric machine therapy. The results obtained in this work is similar to the one obtained in (Venkateswarlu et al., 2019; Ramzan et al., 2020; Sujatha et al., 2019). From the same figure, it is also noticed that the temperature distribution declines with increased values of the Biot number Bi. This is the case because increment in Bi results in enhanced convective heat transport that results in the lowering of the temperature field. In the contrary, the Radiation parameter R and the Biot number Bi indicates rising effects on the concentration profile as displayed in figure 6.12(b). These results are the same as the result reported in the work of (Monaledi and Makinde, 2018).

6.5.3 The Wall Shear Stress, Wall Heat Transfer and Mass Transfer Rates

This subsection comprises the effects of flow parameters on the wall shear stress, wall heat and mass transfer rates. In deed, the graphical results that are illustrated in this subsection for the skin friction coefficient C_f, the Nusselt number Nu and the Sherwood number Sh are plotted for large time, say $\tau \geq 1.9$ (steady state) and thus the results obtained may not be affected by time increasing for all parameters values as a consequence of the results obtained in subsection 6.6.1.

The Wall Shear Stress: Skin Friction Coefficient

The effects of pertinent parameters on the wall shear stress at the cold wall $\eta = 0$ and at the hot wall $\eta = 1$ are illustrated in figures 6.13(a)–6.16(b). Consequently, from these graphs it is observed that the coefficient of skin friction C_f at both cold and hot walls shows an increasing behavior with increasing values of the thermal Grashof number Gt, the Schmidt number Sc, the Brownian motion parameter Nb and the porous medium shape parameter S for varying scaled values of the suction/injection Reynolds number Re. However, the Eckert number Ec, the thermophoresis parameter Nt, the radiation parameter R and the Biot number Bi indicate a decreasing effect on C_f at both walls of the microchannel.

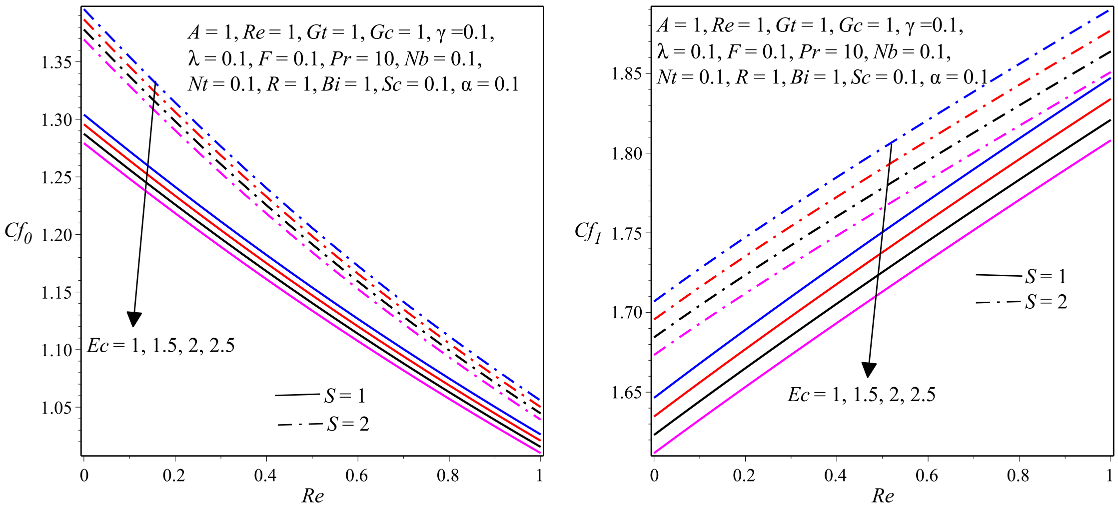

(a) **(b)**

Figure 6.13: **(a)** Skin friction at $\eta = 0$ and **(b)** Skin friction at $\eta = 1$ with varying S, Ec and Re

The Wall Heat Transfer Rate: Nusselt Number

The effects of pertinent governing flow parameters on the wall heat transfer rate at the cold wall $\eta = 0$ and at the hot wall $\eta = 1$ are portrayed in figures 6.17(a)–6.21(b). Consequently, from these graphs it can be seen that the wall heat transfer rate, the Nusselt number Nu at both cold and hot walls shows an increasing behavior with increasing the values of the variable viscosity parameter γ, the Brownian motion parameter Nb and the porous medium shape parameter S for varying scaled values of the suction/injection Reynolds number Re. Nevertheless, the variable thermal conductivity parameter λ, the thermophoresis parameter Nt, the radiation parameter R and the Eckert number Ec show a decreasing effect on Nu at both walls of the microchannel. As presented in figures 6.20(a), 6.20(b), 6.21(a) and 6.21(b), the Nusselt number Nu increases with increasing values of the the Schmidt number Sc, the Grashof number Gt and the Biot number Bi respectively at the cold wall of the microchannel $\eta = 0$ but the reverse trend is observed at the hot wall $\eta = 1$ of the microchannel.

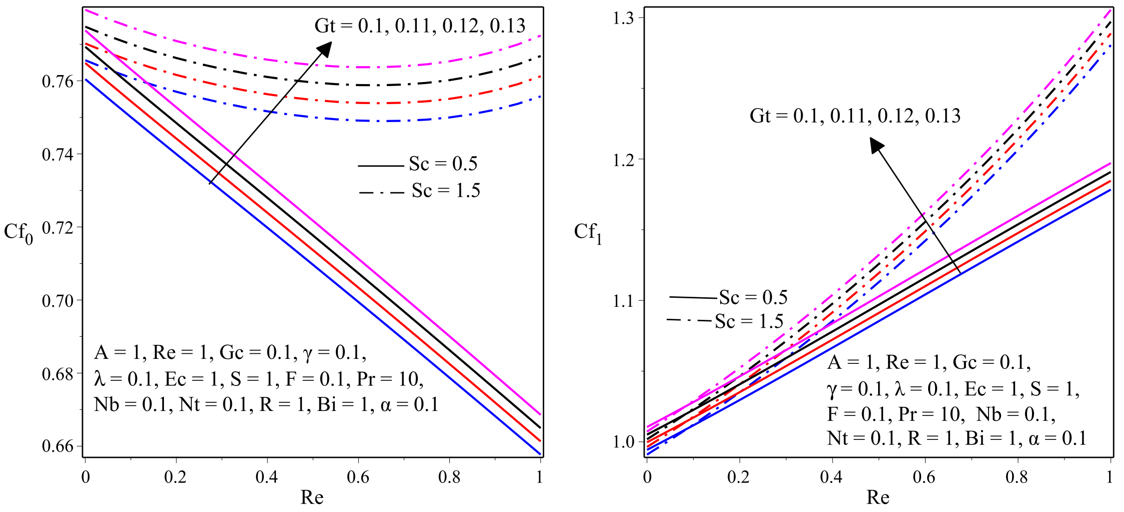

(a) **(b)**

Figure 6.14: **(a)** Skin friction at $\eta = 0$ and **(b)** Skin friction at $\eta = 1$ with varying Sc, Gt and Re

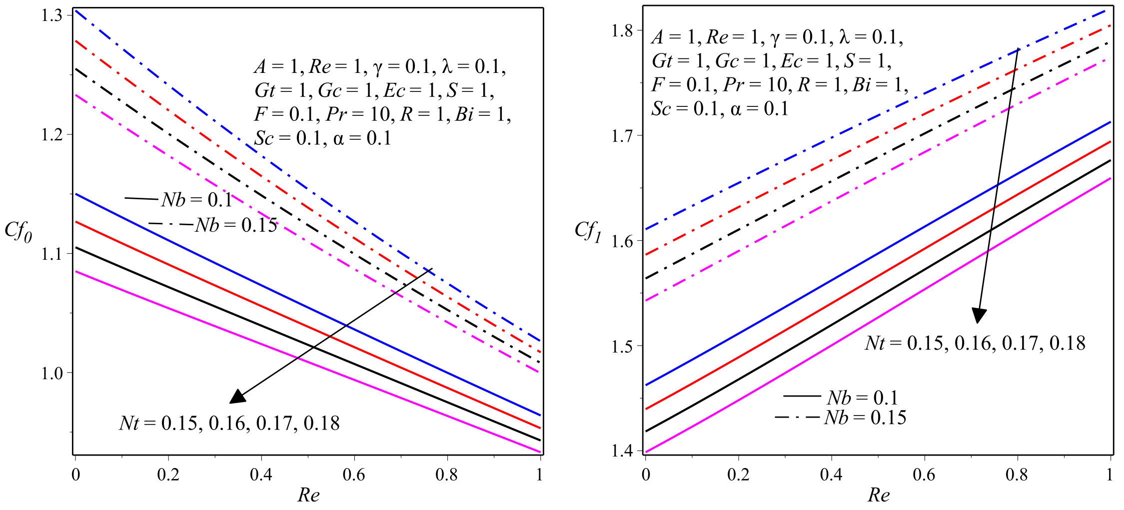

(a) **(b)**

Figure 6.15: **(a)** Skin friction at $\eta = 0$ and **(b)** Skin friction at $\eta = 1$ with varying Nt, Nb and Re

The Wall Mass Transfer Rate: Sherwood Number

The effects of embedded governing flow parameters on the wall mass transfer rate at the cold wall $\eta = 0$ and at the hot wall $\eta = 1$ are displayed in figures 6.22(a)–6.26(b). As a result, these graphs indicate that the wall mass transfer rate, the Sherwood number Sh at both cold and hot walls shows an increasing behavior with increasing values of the porous medium shape parameter S, the variable viscosity parameter γ,and the thermophoresis parameter Nt for varying scaled values of the suction/injection Reynolds number Re. However, the Eckert number Ec, the variable thermal conductivity parameter λ, the Brownian motion parameter Nb and the radiation parameter R show a decreasing effect on Sh at both walls of

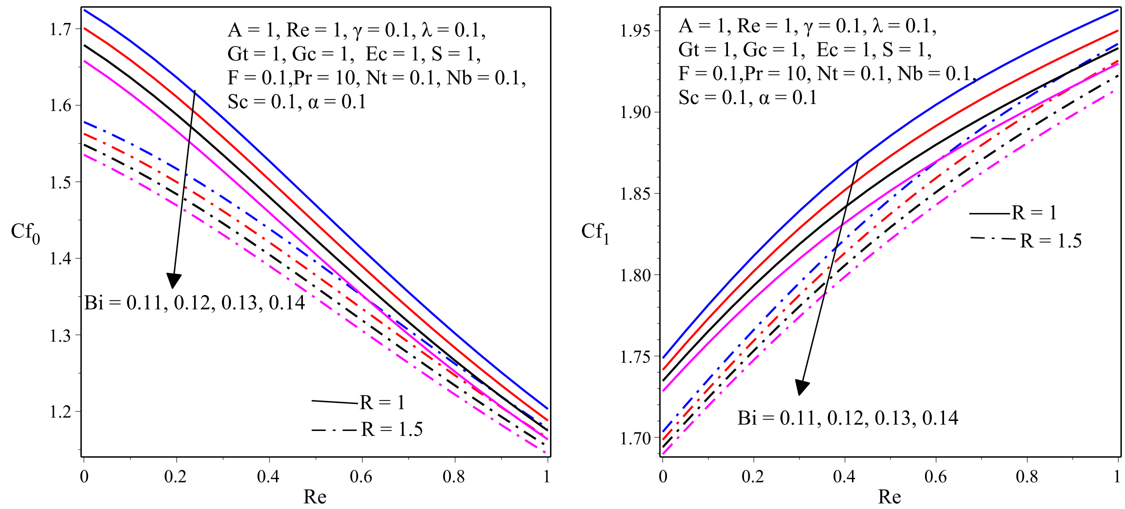

(a) **(b)**

Figure 6.16: **(a)** Skin friction at $\eta = 0$ and **(b)** Skin friction at $\eta = 1$ with varying *Bi*, *R* and *Re*

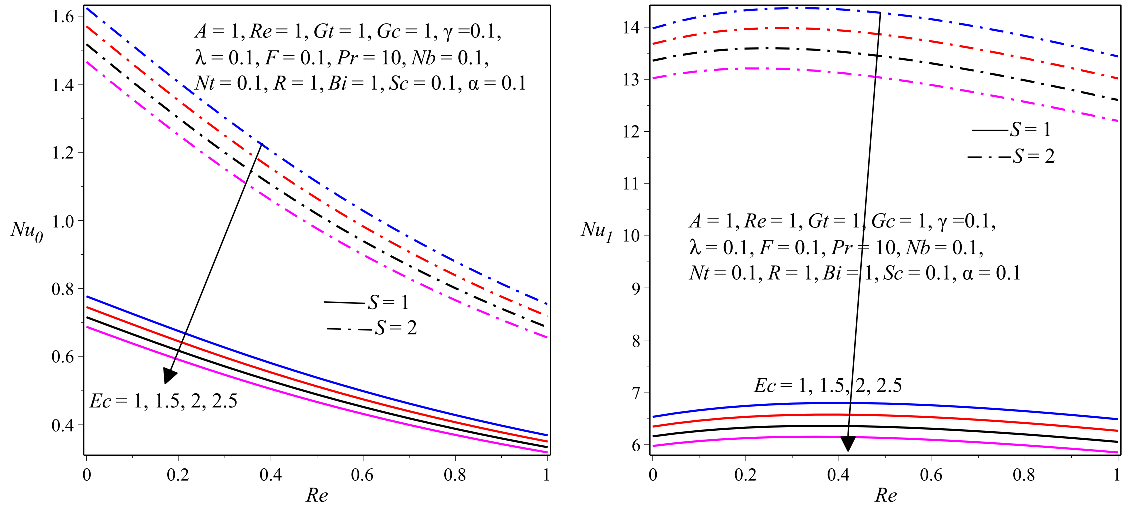

(a) **(b)**

Figure 6.17: **(a)** Nusselt number at $\eta = 0$ and **(b)** Nusselt number at $\eta = 1$ with varying *Ec*, *S* and *Re*

the microchannel. Figures 6.25(a), 6.25(b), 6.26(a) and 6.26(b) presented that the Sherwood number *Sh* rises with rising values of the the Schmidt number *Sc*, the Grashof number *Gt* and the Biot number *Bi* respectively at the cold wall of the microchannel $\eta = 0$ but the opposite is observed at the hot wall $\eta = 1$ of the microchannel.

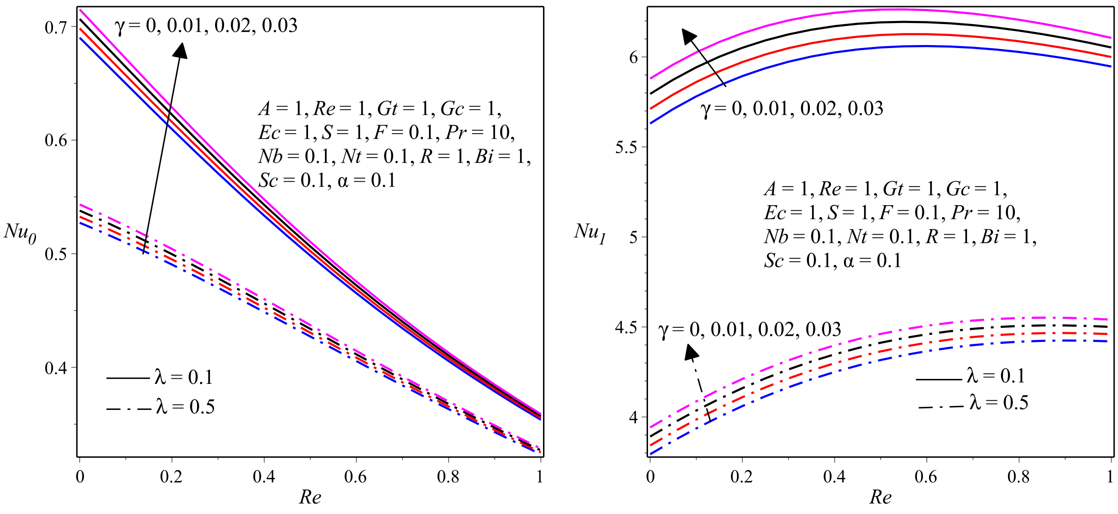

(a) **(b)**

Figure 6.18: **(a)** Nusselt number at $\eta = 0$ and **(b)** Nusselt number at $\eta = 1$ with varying γ, λ and Re

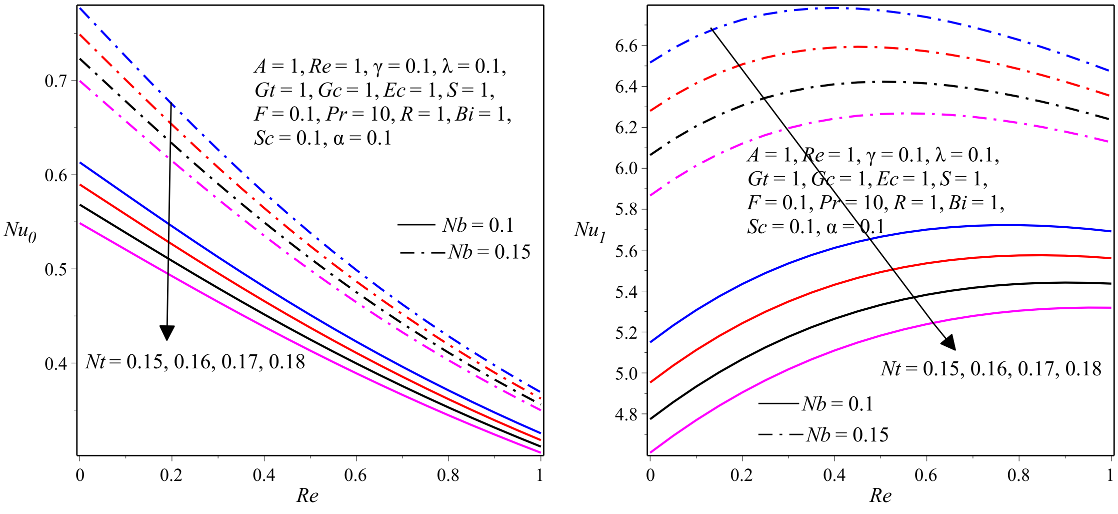

(a) **(b)**

Figure 6.19: **(a)** Nusselt number at $\eta = 0$ and **(b)** Nusselt number at $\eta = 1$ with varying Nt, Nb and Re

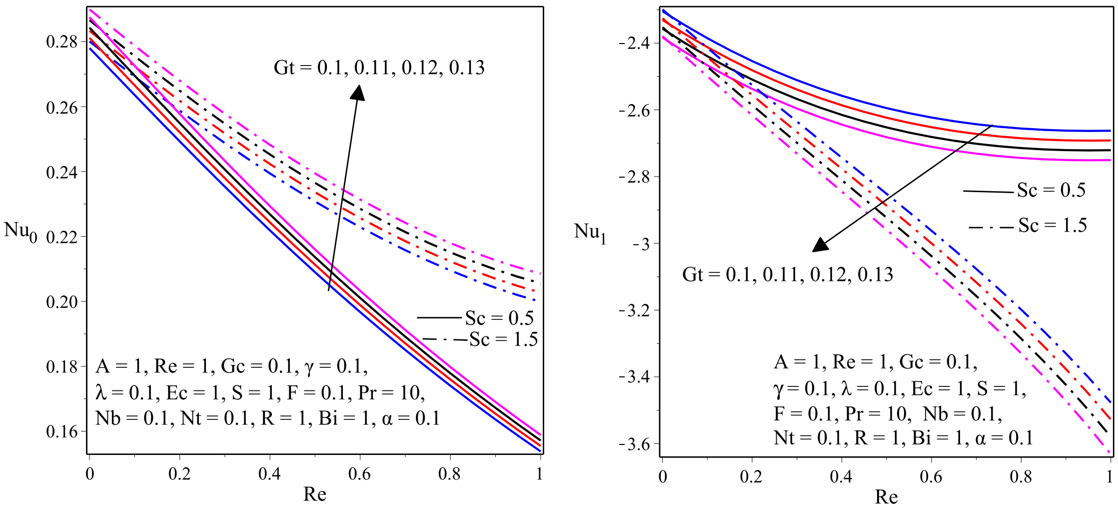

(a) **(b)**

Figure 6.20: **(a)** Nusselt number at $\eta = 0$ and **(b)** Nusselt number at $\eta = 1$ with varying *Sc*, *Gt* and *Re*

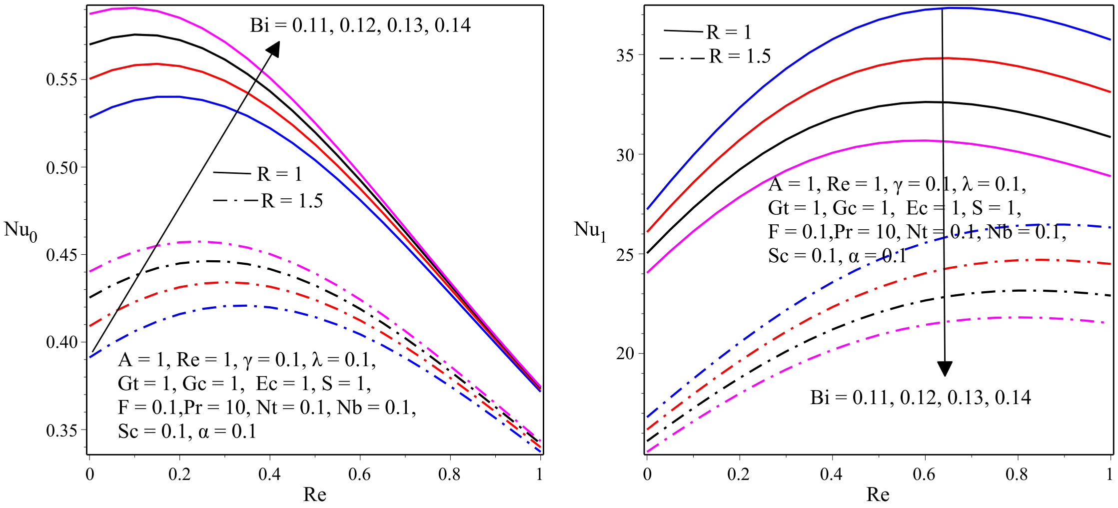

(a) **(b)**

Figure 6.21: **(a)** Nusselt number at $\eta = 0$ and **(b)** Nusselt number at $\eta = 1$ with varying *Bi*, *R* and *Re*

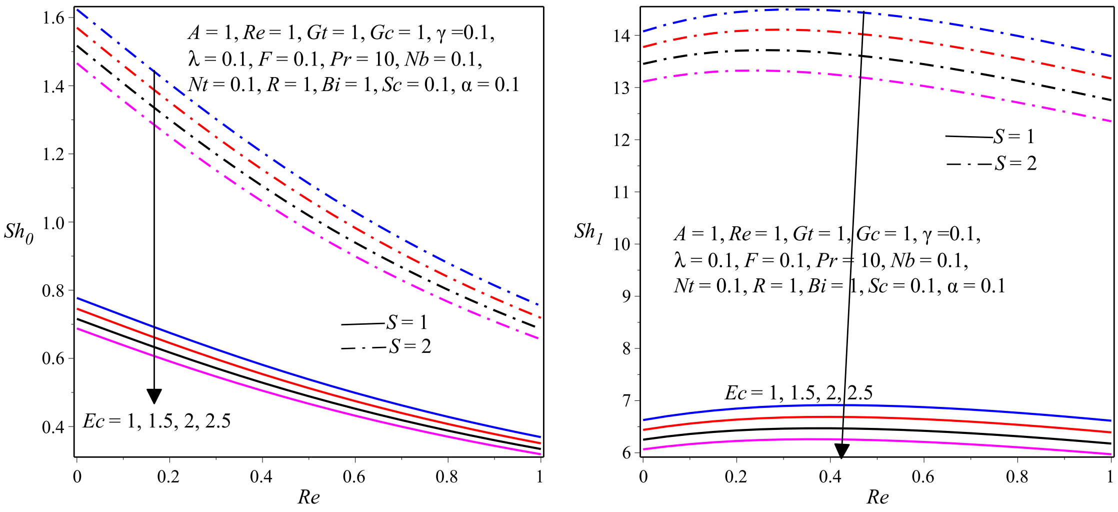

(a)

(b)

Figure 6.22: **(a)** Sherwood number at $\eta = 0$ and **(b)** Sherwood number at $\eta = 1$ with varying Ec, S and Re

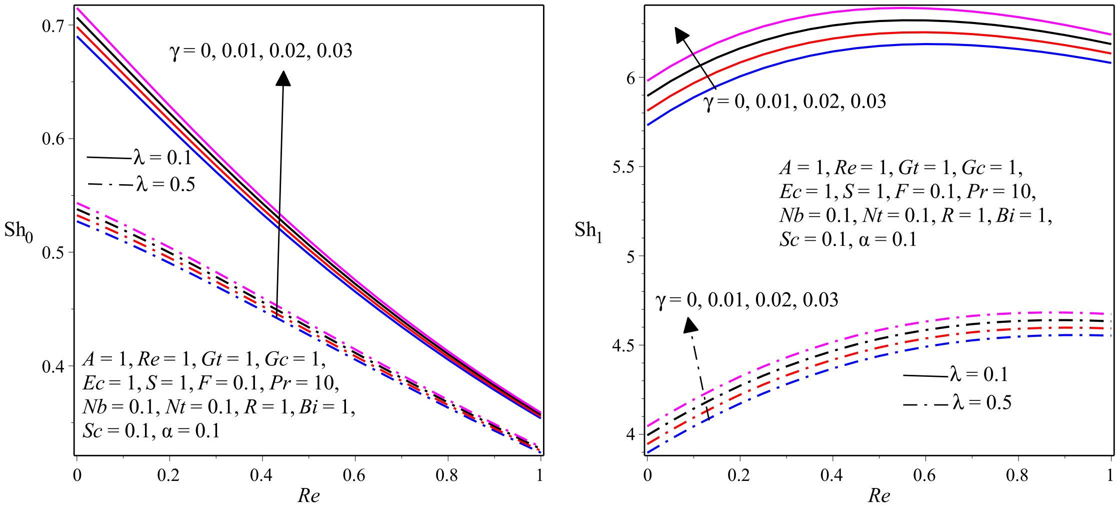

(a)

(b)

Figure 6.23: **(a)** Sherwood number at $\eta = 0$ and **(b)** Sherwood number at $\eta = 1$ with varying γ, λ and Re

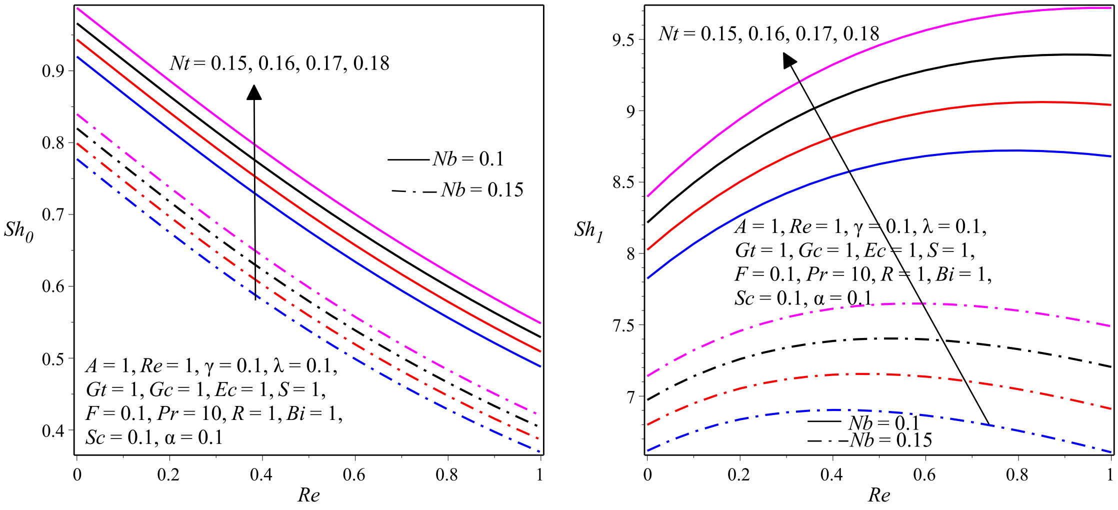

(a) **(b)**

Figure 6.24: **(a)** Sherwood number at $\eta = 0$ and **(b)** Sherwood number at $\eta = 1$ with varying Nt, Nb and Re

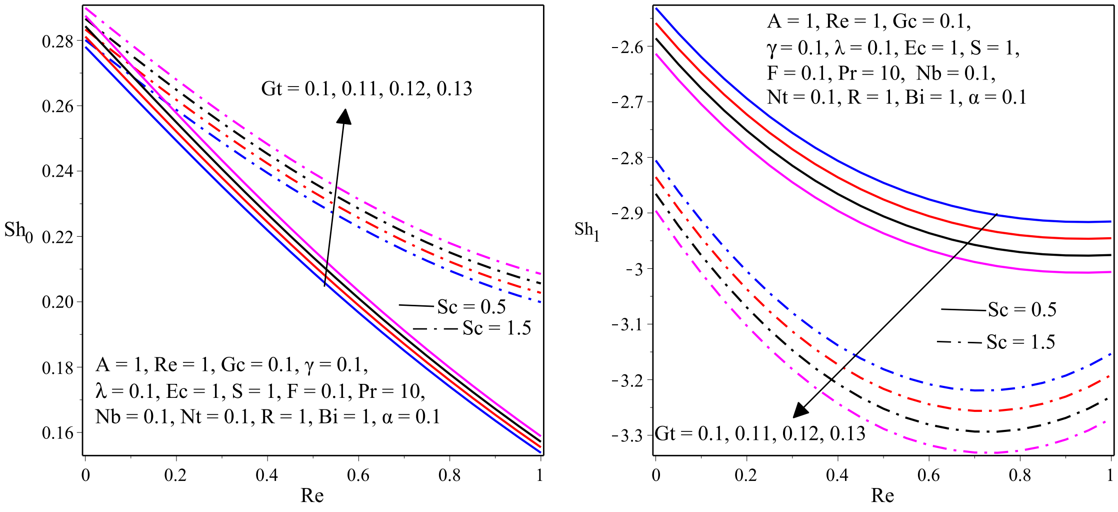

(a) **(b)**

Figure 6.25: **(a)** Sherwood number at $\eta = 0$ and **(b)** Sherwood number at $\eta = 1$ with varying Sc, Gt and Re

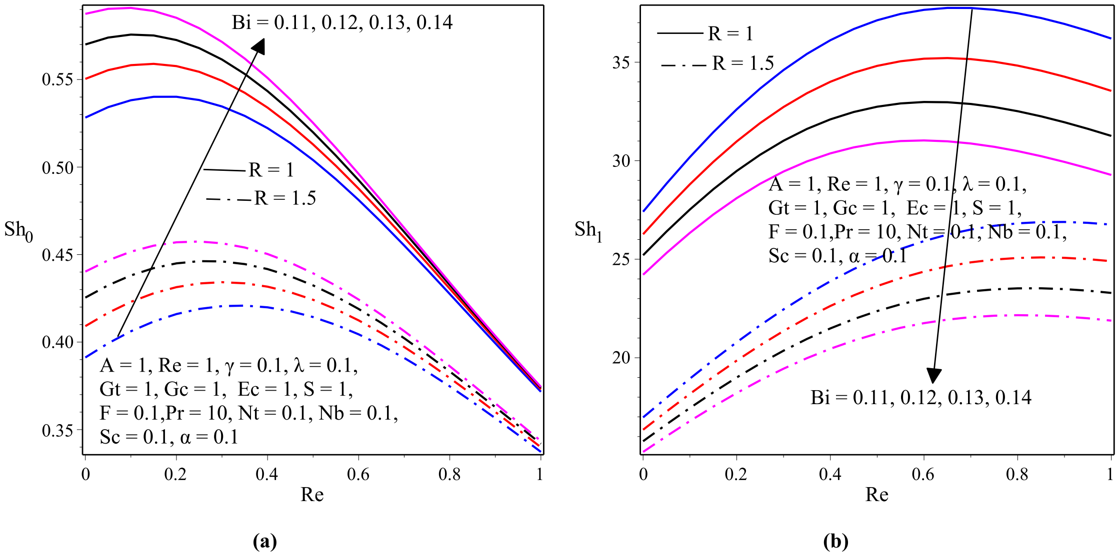

Figure 6.26: **(a)** Sherwood number at $\eta = 0$ and **(b)** Sherwood number at $\eta = 1$ with varying *Bi*, *R* and *Re*

CHAPTER 7

SUMMARY, CONCLUSIONS AND RECOMMENDATIONS

7.1 Summary

The heat and mass transfer characteristics as well as the hydrodynamical properties of nanofluids through microchannels in the presence of porous media with non-uniform permeable walls temperature have large scale utilization in industrial and technological processes such as electronics cooling, engine cooling/vehicle thermal management, aerospace technology, nuclear system cooling, defense applications (cooling military devices and systems), cooling in chillers and refrigerators, laser equipment, geothermal extraction, crude oil extraction, underground water movement, environmental control, and pharmaceutical and biotechnological applications including DNA hybridization, cancer therapy and drug delivery. Therefore, this study considered the analysis of unsteady laminar flow of Newtonian nanofluids with some variable properties through microchannels with non-uniform permeable walls temperature and filled with porous media. The flows were generated due to the axial pressure gradient, suction/injection and buoyancy forces. The Darcy-Forchheimer model was considered to study the interaction between the nanofluid and the porous media. Specific problems were studied under various scenarios including variable transport properties, thermal radiation, chemical reaction, no slip and convective boundary conditions.

In chapter 4, unsteady mixed convection flow of variable viscosity nanofluid in a microchannel filled with porous medium was analyzed. The Buongiorno's nanofluids flow model (two-phase model) was used to examine the effects of the Brownian diffusion and the thermophoresis diffusion of nanoparticles.

In chapter 5, the mathematical modeling and heat transfer enhancement of ferrofluid $(Fe_3O_4 - H_2O)$ flow in a microchannel filled with a porous medium was presented. The Tiwari and Das nanofluids flow model (single-phase model) was used to examine the flow and heat transfer characteristics.

In chapter 6, unsteady mixed convection of a radiating and reacting nanofluid with variable properties in a porous medium microchannel was examined. Indeed, this chapter is an extension of the works in chapter 4 to include the effects of variable thermal conductivity, radiation, chemical reaction and convective boundary condition.

For the aforementioned specific flow model problems, the highly non-linear partial differential equations (initial boundary value problems) for continuity, momentum, energy and concentration were formulated. Thereafter, the non-linear PDEs (IBVPs) governing the nanofluids flow were non-dimensionalized and transformed into ordinary differential equations (ODEs) of initial value problems (IVPs) using the semi-discretization finite difference method also known as method of lines (MOL). Finally, the IVPs were solved by using the well known fourth order Runge-Kutta integration scheme in MAPLE software. The numerical solutions were displayed via graphs to indicate effects of the pertinent parameters on the velocity, temperature, species concentration, skin-friction coefficient, heat transfer rate (Nusselt number) and mass transfer rate (Sherwood number). Furthermore, comparisons of results were done for some parameters with prior published results where a very sound agreement has been attained.

7.2 Conclusions

This dissertation presented the investigation of hydrodynamic and thermal behaviours of nanofluids flow in microchannels filled with porous media. Therefore, depending on the results obtained from the models and analysis presented in this dissertation, the following key conclusions are worth-mentioning.

- Both the velocity and temperature profiles for the variable viscosity nanofluid show an increasing behavior with increasing values of the pressure gradient parameter A, the variable viscosity parameter γ, the Eckert number Ec, the thermal Grashof number Gt, the solutal Grashof number Gc and the thermophoresis parameter Nt.

- The concentration profile for the variable viscosity nanofluid indicates an increasing trend with increasing values of the suction injection Reynolds number Re, the porous medium shape parameter S, the Forchheimer number F, the Prandtl number Pr, the Schmidt number Sc and the thermophoresis parameter Nt.

- The skin friction coefficient C_f for the variable viscosity nanofluid is large for higher vales of the pressure gradient parameter A, the Eckert number Ec, the thermal Grashof number Gt, the Schmidt number Sc and the Prandtl number Pr on both sides of the microchannel walls.

- Both the Nusselt number Nu and the Sherwood number Sh for the variable viscosity nanofluid show an increasing pattern with an increasing values of the pressure gradient parameter A, the variable viscosity parameter γ, the thermal Grashof number Gt, the Schmidt number Sc and the Prandtl number Pr on both sides of the microchannel walls.

- The ferrofluid velocity and temperature reveal a rising pattern with pressure gradient parameter G, variable viscosity parameter γ, Darcy number Da, Eckert number Ec and Prandtl number Pr.

- The Reynolds number Re also called the suction/injection parameter shows a decreasing effect on velocity of the ferrofluid whereas it indicates an increasing effect on temperature.

- The nanoparticles volume fraction φ and the Forchheimer constant b show a decreasing effect on both the ferrofluid velocity and temperature.

- The coefficient of skin friction for the ferrofluid at the cold wall of the microchannel is larger for higher values of nanoparticles volume fraction φ, variable viscosity parameter γ, Darcy number Da and Eckert number Ec.

- The coefficient of skin friction for the ferrofluid at the hot wall of the microchannel increases with Darcy number Da and Prandtl number Pr.

- The heat transfer rate for the ferrofluid at both cold and hot walls of the microchannel reveals a rising pattern for a rising value of variable viscosity parameter γ, Darcy number Da, Eckert number Ec and Prandtl number Pr.

- The nanoparticles volume fraction φ and the Darcy number Da show retarding effects on the rate of heat transfer for the ferrofluid at both hot and cold microchannel walls.

- Both the velocity and temperature profiles of the radiating and reacting nanofluid show an increasing behavior with increasing values of variable viscosity parameter γ, Eckert number Ec, thermal Grashof number Gt, solutal Grashof number Gc, Prandtl number Pr and chemical reaction parameter α.

- The concentration profile of the radiating and reacting nanofluid indicates an increasing trend with increasing values of variable thermal conductivity parameter $lambda$, porous medium shape parameter S, Forchheimer number F, Schmidt number Sc, Brownian motion parameter Nb, radiation parameter R and Biot number Bi.

- The skin friction coefficient C_f of the radiating and reacting nanofluid is large for higher vales of suction/injection Reynolds number Re, porous medium shape parameter S, thermal Grashof number Gt, Schmidt number Sc and Brownian motion parameter Nb on both sides of the microchannel walls.

- The heat transfer and mass transfer rates of the radiating and reacting nanofluid on both sides of the microchannel walls indicate an increasing behaviour for increasing values of suction/injection Reynolds number Re, porous medium shape parameter S, variable viscosity parameter γ but a decreasing behaviour for increasing values of Eckert number Ec, variable thermal conductivity parameter λ and radiation parameter R.

- Grashof number Gt, Schmidt number Sc and Biot number Bi indicate an increasing effect on both the heat transfer and mass transfer rates of the radiating and reacting nanofluid at the cold wall of the microchannel.
- The Brownian motion parameter Nb and the thermophoresis parameter Nt show an opposite effect on the heat transfer and mass transfer rates of the radiating and reacting nanofluid on both sides of the microchannel walls.

7.3 Recommendation and Suggestions for Future Research

7.3.1 Recommendation

The findings of this dissertation are useful for engineering and industrial processes specifically in heat transfer systems design. Thus, integrating the findings of the present theoretical models with experimental investigations may improve the existing design in cooling systems by making use of variable viscosity nanofluids, radiating and reacting nanofluids, and ferrofluid trough permeable microchannels filled with porous media.

7.3.2 Suggestions for Future Research

The works presented in this dissertation can be extended to different problems in the following ways. That is, this dissertation suggests the following future areas of research.

- One can include the effects of the body forces such as Lorentz and Coriolis forces by considering rotating MHD nanofluid flow.
- The same geometry of microchannels flow can also be considered for non-Newtonian fluids with non-Fourier heat conduction law.
- The Soret and Dufour effects (thermal-diffusion and diffusion-thermo) with slip and hall current can also be considered.
- One can consider the entropy generation analysis with heat source.
- Radiating and reacting nanofluid flow (or the problem in chapter 6) can be studied by considering particular nanofluids such as $Cu - H_2O$, $Ag - H_2O$, $Al_2O_3 - H_2O$.

REFERENCES

Aghamiri, H., Niknejadi, M., and Toghraie, D. (2021). Analysis of the forced convection of two-phase ferro-nanofluid flow in a completely porous microchannel containing rotating cylinders. *Scientific Reports*, 11:1–18.

Agoor, B. (2018). Slip flow in porous medium of micropolar fluid in a rectangular microchannel under the effect of a magnetic field. *Journal of Applied Mechanics and Engineering*, 7(1):1–14.

Ahadi, A., Antoun, S., Saghir, M., and Swift, J. (2019). Computational fluid dynamic evaluation of heat transfer enhancement in microchannel solar collectors sustained by alumina nanofluid. *Energy Storage*, 1(2):e37.

Aina, B. and Malgwi, P. (2019). MHD convection fluid and heat transfer in an inclined micro-porouschannel. *Nonlinear Engineering*, pages 755–763.

Akinshilo, A., Ilegbusi, A., Ali, H., and Surajo, A. (2020). Heat transfer analysis of nanofluid flow with porous medium through Jeffery Hamel diverging/converging channel. *J. Appl. Comput. Mech.*, 6(3).

Al-Rashed, A., Sheikhzadeh, G., Aghaei, A., Monfared, F., Shahsavar, A., and Afrand, M. (2020). Effect of a porous medium on flow and mixed convection heat transfer of nanofluids with variable properties in a trapezoidal enclosure. *Journal of Thermal Analysis and Calorimetry*, 139(1):741–754.

Ali, M. (2021). The method of lines analysis of heat transfer of Ostwald-de Waele fluid generated by a non-uniform rotating disk with a variable thickness. *J. Appl. Comput. Mech.*, 7(2):432441.

Ali, M., Khan, W., Sultan, F., and Shahzad, M. (2020). Numerical investigation on thermally radiative time-dependent sisko nanofluid flow for curved surface. *Physica*, A(550):1–13.

Alkasasbeh, H., Swalmeh, M., Hussanan, A., and Mamat, M. (2019). Effects of mixed convection on methanol and kerosene oil based micropolar nanofluid containing oxide nanoparticles. *Akademia baru. CFD Letters*, 11(1):55–68.

Alzgool, H., Alkasasbeh, H., Abu-ghurra, S., Al-houri, Z., and Swalmeh, M. (2019). Numerical solution of heat transfer in MHD mixed convection flow micropolar Casson fluid about solid sphere with radiation effect. *International Journal of Engineering Research and Technology*, 12(4):519–529.

Amhalhel, G. and Furmanski, P. (1997). *Problems of modeling flow and heat transfer in porous media*. Biuletyn Instytutu Techniki Cieplnej Politechniki Warsza Wskiej. Nr 85.

Anwar, M., Rafique, K., Misiran, M., and Khan, I. (2019). Keller-Box scheme for Casson nanofluid flow over nonlinear inclined surface with Soret and Dufour effects. *Front.Phys.*, 7(139).

Anwar, T., Kumam, P., Shah, Z., and Thounthong, P. (2020). Unsteady radiative natural convective mhd nanofluid flow past a porous moving vertical plate with heat source/sink. *Molecules*, 25(854):1–21.

Bergman, T., Incropera, F., DeWitt, D., and Lavine, A. (2011). *Fundamentals of Heat and Mass Transfer*. Wiley & Sons.

Bhandari, A. (2019). Radiation and chemical reaction effects on nanofluid flow over a stretching sheet. *Fluid Dynamics & Materials Processing, FDMP*, 15(5):557–582.

Buongiorno, J. (2006). Convective transport in nanofluids. *ASME J. Heat Transfer*, 128(3):240–250.

Chamkha, A., Ameur, H., and Menni, Y. (2020). Nanofluids advances through heat exchangers. *Heat Transfer*, pages 1–29.

Chaudhary, M. and Merkin, J. (1995). A simple isothermal model for homogeneous-heterogenous reactions in boundary-layer flow II. unequal diffusivities. *Fluid Dyn. Res.*, 16:335–359.

Choi, S. (1995). Enhancing thermal conductivity of fluids with nanoparticles. *ASME Int Mech Eng.*, 66:99–105.

Cortés-Molina, M., Reyes, J., and García-Alonso, F. (2018). The G-functions series method adapted to the numerical integration of parabolic PDE. *ournal of Applied Mathematics and Physics*, 6:161–173.

Das, K., Kundu, P., and Acharya, N. (2019). Computational investigation on the mechanism of heat transport and entropy generation through a nozzle of liquid rocket engine using ferrofluid. *Journal of Computational Design and Engineering*, 6:739–750.

Das, S., Choi, S., Yu, W., and Pradeep, T. (2008). *Nanofluids*. John Wiley & Sons.

Delisle, C., Welsford, C., and Saghir, M. (2019). Forced convection study with microporous channels and nanofluid: experimental and numerical. *Journal of Thermal Analysis and Calorimetry*, 140(6):1205–1214.

Dewan, A. and Srivastava, P. (2015). A review of heat transfer enhancement through flow disruption in a microchannel. *Journal of Thermal Science*, 24(3):203–214.

Dhlamini, M., Kameswaran, P., Sibanda, P., Motsa, S., and Monda, H. (2019). Activation energy and binary chemical reaction effects in mixed convective nanofluid flow with convective boundary conditions. *Journal of Computational Design and Engineering*, 6:149–158.

Dogonchi, A., Asghar, Z., and Waqas, M. (2020). CVFEM simulation for $Fe_3O_4-H_2O$ nanofluid in an annulus between two triangular enclosures subjected to magnetic field and thermal radiation. *International Communications in Heat and Mass Transfer*, (112):1–9.

Dong, S., Geng, P., Dong, D., and Li, C. (2020). Mixing enhancement of electroos-motic flow in microchannels under DC and Ac electric field. *Journal of Applied Fluid Mechanics*, 13(1):79–88.

Eegunjobi, A. and Makinde, O. (2019). Irreversibility analysis of MHD buoyancy-driven variable viscosity liquid film along an inclined heated plate convective cooling. *J. Appl. Comput. Mech.*, 5(5):840–848.

El-dawy, H. and Gorla, R. (2019). Effects of nanoparticles on non-Darcy mixed convective heat transfer in nanofluids over a shrinking and stretching wedge. *Applied and Computational Mathematics*, 8(4):70–74.

Endalew, M., Sarkar, S., Seth, G, S., and Makinde, O. (2018). Dual-phase-lag heat transfer model in hydromagnetic second grade flow through a microchannelfilled with porous material: A time-bound analysis. *Revue des composites et des matériaux avancés*, 28:173–194.

Farzad, P., Ali, A., Abbasian, A., Mohammad, R., Hoang, M., and Amin, A. (2019). On the thermal characteristics of a manifold microchannel heat sink subjected to nanofluid using two-phase flow simulation. *International Journal of Heat and Mass Transfer*, 143:118518–118530.

Ganji, D. and Malvandi, A. (2016). *Heat Transfer Enhancement Using Nanofluid Flow in Microchannels* 1^{st} *Edition*. Elsevier.

Geridonmez, B. (2020). Effects of non-Darcy and Kelvin forces on convection flow of ferrofluid: a numerical study. *AIMS Mathematics*, 3(1):195–210.

Gireesha, B., Srinivasa, C., Shashikumar, N., Macha, M., Singh, J., and Mahanthesh, B. (2019). Entropy generation and heat transport analysis of Casson fluid flow with viscous and Joule heating in an inclined porous microchannel. *Proc I Mech E Part E: J Process Mechanical Engineering*, 0(0):1–12.

Hamdi, S., S. W. and Griffiths, G. (2009). *Method of Lines*, volume 2. Scholarpedia.

Hamid, M., Usman, M., Waheed, A., Mohyud-Din, S., and Wang, W. (2018). Comparative investigation of uniform heat flux on the flow and heat transportation of ferrofluids through smooth plate. *International Journal of Bio-mathematics*, 11(2):1–19.

Hamid, M., Zubair, T., Usman, M., and Haq, R. (2019). Numerical investigation of fractional-order unsteady natural convective radiating flow of nanofluid in a vertical channel. *AIMS Math.*, 4(5):1413–1429.

Hayat, T., H. F. and Alsaedi, A. (2020). Darcy-Forchheimer flow with nonlinear mixed convection. *Applied Mathematics and Mechanics (English Edition)*, 41(11):1–12.

Henniche, R. and Ziane, A. (2018). Mixed convection heat transfer in a channel in presence of baffles. *CRND-Draria, Alger. CFD & Tech.*

Holman, J. (2010). *Heat Transfer: Tenth Edition*. McGraw-Hill Education.

Ilias, M., Ismail, N., Ab Raji, N., Rawi, N., and Shafie, S. (2020). Unsteady aligned MHD boundary layer flow and heat transfer of a magnetic nanofluids past an inclined plate. *International Journal of Mechanical Engineering and Robotics Research*, 9(2):1–9.

Irfan, M., Farooq, M., and Iqra, T. (2019). Magnetohydrodynamic free stream and heat transfer of nanofluid flow over an exponentially radiating stretching sheet with variable fluid properties. *Front. Phys.*, 7(186).

Jahangiri, M., Farsani, R., and Shamsabadi, A. (2018). Numerical investigation of the water/alumina nanofluid within a microchannelwith baffeles. *Journal of Mechanical Engineering and Technology*, 10(2):67–76.

Jamaludin, A., Naganthran, K., Nazar, R., and Pop, I. (2020). Thermal radiation and MHD effects in the mixed convection flow of Fe_3O_4-water ferrofluid towards a nonlinearly moving surface. *Processes*, 8(95):3283–3305.

Jedi, A., Shamsudeen, A., Razali, N., Othman, H., Zainuri, N., Zulkarnain, N., Abu Bakar, N., Pati, K., and Thanoon, T. (2020). Statistical modeling for nanofluid flow: A stretching sheet with thermophysical property data. *Colloids Interfaces*, 4(3).

Joshi, V., Ram, P., Kumar, A., and Makinde, O. (2018). Boundary layer convective flow of magnetic nanofluids in the presence of geothermal viscosity. *Defect and Diffusion Forum*, 387:296–307.

Jothimani, S. and Vidhya, T. (2015). Mixed convection of non-Newtonian fluid flow and heat transfer over a non-linearly stretching surface. *Int. J. Adv. Appl. Math. and Mech.*, 3(1):28–35.

Kandlikar, S., Garimella, S., Li, D., Colin, S., and King, M. (2006). *Heat Transfer and Fluid Flow in Minichannels and Microchannels*. Elsevier.

Kasaeian, A., Daneshazarian, R., Mahian, O., Kolsi, L., Chamkha, A., Wongwises, S., and Pop, I. (2017). Nanofluid flow and heat transfer in porous media: A review of the latest developments. *International Journal of Heat and Mass Transfer*, 107:778–791.

Khan, A., Kumam, W., Khan, I., Saeed, A., Gul, T., and Kumam, P. (2021). Chemically reactive nanofluid flow past a thin moving needle with viscous dissipation, magnetic effects and hallcurrent. *PLoS ONE*, 16(4).

Khan, Z., Makinde, O., Ahmad, R., and Khan, W. (2018). Numerical study of unsteady MHD flow and entropy generation in a rotating permeable channel with slip and hall effects. *Communications in Theoretical Physics*, 70(5):641–650.

Khan, Z., Makinde, O., Hamid, M., Haq, R., and Khan, W. (2019). Hydromagnetic flow of ferrofluid in an enclosed partially heated trapezoidal cavity filled with a porous medium. *Journal of Magnetism and Magnetic Materials*, 499:166–241.

Khodabandeh, E., Bahiraei, M., Mashayekhi, R., Talebjedi, B., and Toghraie, D. (2018). Thermal performance of Ag–water nanofluid in tube equipped with novel conical strip inserts using two-phase method: Geometry effects and particle migration considerations. *Powder Technology.*, pages 87–100.

Kmiotek, M. and Kucab-Pietal, A. (2018). Influence of slim obstacle geometry on the flow and heat transfer in microchannels. *Bulletin of the Polish Academy of Technical Sciences*, 66(2):111–118.

Kumar, R., Islam, M., and Hasan, M. (2014). A review of experimental investigations on heat transfer characteristics of single phase liquid flow in microchannels. *International Journal of Advanced Mechanical Engineering*, 4(1):115–120.

Lakshmi, S., Purbarun, D., Sundararajan, T., and Sarit, K. (2017). Heat spreader with parallel microchannel configurations employing nanofluids for near-active cooling of MEMS. *International Journal of Heat and Mass Transfer*, 111:570–581.

Li, Z., Zhang, H., Liu, Y., and McDonough, J. (2020). Implementation of compressible porous-fluid coupling method in an aerodynamics and aeroacoustics code part I: Laminar flow. *Applied Mathematics and Computation*, 364:124682–124702.

Mabood, F., Makinde, O., and Ibrahim, M. (2018). Chemically reacting on MHD boundary-layer flow of nanofluids over a nonlinear stretching sheet with heat source/sink and thermal radiation. *Thermal Science*, 22(18):495–506.

Madhura, K. R., Kalpana, B., and Makinde, O. (2020). Thermal performance of straight porous fin with variable thermal conductivity under magnetic field and radiation effects. *Heat Transfer*, 49(8):5002–5019.

Maghsoudi, P. and Siavashi, M. (2018). Application of nanofluid and optimization of pore size arrangement of heterogeneous porous media to enhance mixed convection inside a two-sided lid-driven cavity. *J. Therm. Anal. Calorim.*

Mahanthesh, B., Shashikumar, N., Gireesha, B., and Animasaun, I. (2019). Effectiveness of Hall current and exponential heat source on unsteady heat transport of dusty TiO_2-EO nanoliquid with nonlinear radiative heat. *Journal of Computational Design and Engineering*, 6:551–561.

Mahdy, A. and Hoshoudy, G. (2019). Two-phase mixed convection nanofluid flow of a dusty tangent hyperbolic past a nonlinearly stretching sheet. *Journal of the Egyptian Mathematical Society*.

Mahmoudi, Y., Hooman, K., and Vafai, K. (2020). *Convective Heat Transfer in Porous Media*. Taylor & Francis Group. CRC Press.

Makinde, O. (2018). Heat transfer in variable viscosity microchannelflow of EG-water/Ag nanofluids with convective cooling. *Defect and Diffusion Forum*, 387:510–522.

Makinde, O., Khan, Z., Ahmad, R., Haq, R., and Khan, W. (2019). Unsteady MHD flow in a porous channel with thermal radiation and heat source/sink. *Int. J. Appl. Comput. Math.*, 559:1–21.

Makinde, O. and Rundora, L. (2017). Unsteady mixed convection flow of a reactive Casson fluid in a permeable wall channel filled with a porous medium. *Defect and Diffusion Forum*, 377:166–179.

Makinde, O. and Rundora, L. (2018). Unsteady MHD flow of non-Newtonian fluid in a channel filled with a saturated porous medium with asymmetric Navier slip and convective heating. *Applied Mathematics & Information Sciences*, 12(3):483–493.

Manjunatha, S., Kuttan, B., Jayanthi, S., Chamkha, A., and Gireesha, B. (2019). Heat transfer enhancement in the boundary layer flow of hybrid nanofluids due to variable viscosity and natural convection. *Heliyon*, 5(e01469).

Matao, P., Reddy, B., Sunzu, J., and Makinde, O. (2020). Finite element numerical investigation into unsteady MHD radiating and reacting mixed convection past an impulsively started oscillating plate. *International Journal of Engineering, Science and Technology*, 12(1):38–53.

Mehendale, S., Jacobi, A., and Shah, R. (2000). Fluid flow and heat transfer at micro- and meso-scales with applications to heat exchanger design,. *Appl. Mech. Rev.,*, 53:175–193.

Menni, Y., Chamkha, A., and Azzi, A. (2018). Nanofluid transport in porous media: a review. special topics & reviews in porous media. *An International Journal*, 9(4):1–16.

Mohsan, H., Rahmat, E., Ahmed, Z., and Muhammad, M. B. (2019). Analysis of natural convective flow of non-Newtonian fluid under the effects of nanoparticles of different materials. *Proceedings of the Institution of Mechanical Engineers, Part E: Journal of Process Mechanical Engineering*, 233(3):643–652.

Monaledi, R. and Makinde, O. (2018). Entropy analysis of a radiating variable viscosity EG/Ag nanofluid flow in microchannels with buoyancy force and convective cooling. *Defect Diffusion Forum*, 387:273–285.

Mondal, H., Mishra, S., Kundu, P., and Sibanda, P. (2020). Entropy generation of variable viscosity and thermal radiation on magneto nanofluid flow with dusty fluid. *J. Appl. Comput. Mech.*, 6(1):171–182.

Moon, J., Pacheco, J., and Pacheco-Vega, A. (2019). Heat transfer enhancement in wavy microchannels: Effect of block material. *Proceedings of the 4th World Congress on Momentum, Heat and Mass Transfer*, MHMT'19(ENFHT120):1–11.

Muthamilselvan, M. and Ureshkumar, S. (2018). A tilted lorentz force effect on porous media filled with nanofluid. *Journal of Theoretical and Applied Mechanics*, 48(2):50–71.

Nabway, H., Chamkha, A., Rashad, A., and Abdelrahman, Z. (2019). Mixed bioconvective flow of a nanofluid past a wedge with porous media. *Journal of Nanofluids*, 8(8):1692–1703.

Nayak, M., Mabood, F., and Makinde, O. (2019). Heat transfer and buoyancy-driven convective MHD flow of nanofluids impinging over a thin needle moving in a parallel stream influenced by prandtl number. *Heat Transfer-Asian Res.*, pages 1–18.

Nayak, M., Shaw, S., and Makinde, O. (2018). Chemically reacting and radiating nanofluid flow past an exponentially stretching sheet in a porous medium. *Indian Journal of Pure & Applied Physics*, 56:773–786.

Niazi, M. and Xu, H. (2020). Modelling two-layer nanofluid flow in a microchannelwith electro-osmotic effects by means of the Buongiorno's model. *Applied Mathematics and Mechanics (English Edition). Shanghai University and Springer-Verlag GmbH Germany*, 41(1):83–104.

Nilankush, A. (2019). On the flow patterns and thermal behaviour of hybrid nanofluid flow inside a microchannel in presence of radiative solar energy. *Journal of Thermal Analysis and Calorimetry*, 141:1425–1442.

Noreen, S., Waheed, S., and Hussanan, A. (2019). Peristaltic motion of MHD nanofluid in an asymmetric microchannelwith joule heating, wall flexibility and different zeta potential. *Boundary Value Problems*.

Nwaigwe, C., Weli, A., and Makinde, O. (2019). Computational analysis of porous channel flow with cross-diffusion. *American Journal of Computational and Applied Mathematics*, 9(5):119–132.

Okari, S., Rifin, N., Nuar-Mohamed, M., Kasim, A., Mohammad, N., and Zukisalleh, M. (2018). Mathematical model of mixed convection boundary layer flow over a horizontal circular cylinder filled in a Jeffrey fluid with viscous dissipation effect. *Sains Malaysiana*, 47(7):607–1615.

Patel, A., Bhuvad, S., and Rajput, S. (2019). Effects of nanofluid flow in microchannel heat sink for forced convection cooling of electronics device: A numerical simulation. *International Journal of Innovative Technology and Exploring Engineering (IJITEE)*, 9(2).

Pence, D. (2010). The simplicity of fractal-like flow networks for effective heat and mass transport. *Experimental Thermal and Fluid Science*, 34(4):474–486.

Prameela, M., Venkateswarlu, M., and Makinde, O. (2019). Influence of heat generation and viscous dissipation on hydromagnetic fully developed natural convection flow in a vertical microchannel. *J. Nanofluids*, 8(7):1506–1516.

Rai, S., Sharma, R., Saifi, M., Tyagi, R., Singh, D., and Gupta, H. (2018). Review of recent applications of microchannel in MEMS devices. *International Journal of Applied Engineering Research*, 13(9):64–69.

Raizah, Z. and Aly, A. (2021). Natural convection in an H-shaped porous enclosure filled with a nanofluid. *Computers, Materials & Continua*, 66(3):3233–3251.

Ram, P., Makinde, O., and Mahajan, A. (2020). Flow of magnetic fluids with penetrative internally heated convection. *Defect and Diffusion Forum*, 387:373–384.

Ramzan, M., Rafiq, A., Chung, J., Kadry, S., and Chu, Y. (2020). Nanofluid flow with autocatalytic chemical reaction over a curved surface with nonlinear thermal radiation and slip condition. *Scientific Reports*, 10(18339):1–13.

Rashad, A., Chamkha, A., Abdelrahman, Z., Nabwey, H., and Alsabery, A. (2020). Mixed convection flow of magneto-ferrofluids through enclosure with partial slip impacts. *ASME Journal of Thermal Science and Engineering Application*, 12(5):1–13.

Rashad, A., Chamkha, A., EL-Mky, H., and EL-Zahar, E. (2019). Flow of Fe_3O_4-water nanofluid past a moveable plane in a parallel stream with the presence of high suction: Analytical and numerical study. *Energies*, 12(1):198.

Rashad, A., Chamkha, A., Mansour, M., and Armaghani, T. (2018). MHD combined convection flow of cu-water nanofluid through a lid-driven saturated porous enclosure with entropy generation and partial slip effects. *Journal of Thermal Analysis & Calorimetry*, 132:1291–1306.

Rasool, G., Shafiq, A., and Baleanu, D. (2020). Consequences of Soret-Dufour effects, thermal radiation, and binary chemical reaction on Darcy-Forchheimer flow of nanofluids. *Symmetry*, 12(1421):1–19.

Rasool, G., Zhang, T., Shafiq, A., and Durur, H. (2019). Influence of chemical reaction on marangoni convective flow of nanoliquid in the pres- ence of Lorentz forces and thermal radiation: A numerical investigation. *Journal of advances in nanotechnology*, 1(1):32–49.

Reddy, K., Makinde, O., and Reddy, M. (2018). Thermal analysis of mhd electro-osmotic peristaltic pumping of casson fluid through a rotating asymmetric microchannel. *Indian J Phys.*, 92(11):1439–1448.

Reddy, K., Reddy, M., and Makinde, O. (2019). Thermophoresis and Brownian motion effects on MHD electro-osmotic jeffrey nanofluid peristaltic flow in asymmetric rotating microchannel. *J. Nanofluids*, 8(2).

Risto, C. and Zahid, H. (2009). New technologies in ammonia refrigerating and air-conditioning systems. *Heat Transfer Engineering*, 30(4):324–329.

Roja, A., GIireesha, B., and Nagaraja, B. (2021). Irreversibility investigation of Casson fluid flow in an inclined channel subject to a Darcy-Forchheimer porous medium: a numerical study. *Appl. Math. Mech. Engl. Ed.*, 42(1):95–108.

Roknujjaman, M. and Asaduzzaman, M. (2018). On the solution procedure of partial differential equation (PDE) with the method of lines (MOL) using Crank-Nicholson method (CNM). *American Journal of Applied Mathematics*, 6(1):1–7.

Roy, K., Giri, A., and Das, B. (2020). Laminar entry region mixed convection heat transfer from an inclined rectangular fin array. *International Journal of numerical Methods for Heat & Fluid Flow*, 30(6).

Rundora, L. and Makinde, O. (2018). Buoyance effects on unsteady reactive variable properties fluid flow in a channel filled with a porous medium. *Journal of Porous Media*, 21(8):721–737.

Sajid, T., Sagheer, M., Hussain, S., and M. Bilal, M. (2018). Darcy-Forchheimer flow of Maxwell nanofluid flow with nonlinear thermal radiation and activation energy. *AIP Advances*, 8(035102):1–20.

Saleel, C., Algahtani, A., Badruddin, I., Khan, T., Kamangar, S., and Abdelmohimen, M. (2019). Pressure-driven electro-osmotic flow and mass transport in constricted mixing microchannels. *Journal of Applied Fluid Mechanics*, 13(2):429–441.

Sarkar, S., Endalew, M., and Makinde, O. (2019). Study of MHD second grade flow through a porous microchannel under the dual-phase-lag heat and mass transfer model. *J. Appl. Comput. Mech.*, 5(4).

Schiesser, W. (2016). *Method of Lines PDE Analysis in Biomedical Science and Engineering*. John Wiley & Sons.

Schiesser, W. (2017). *Method of Lines Analysis of Turing Models*. World Scientific Publishing Company.

Sedighi, A., Esmailpour, M., and Abdollahzadeh, M. (2018). Effects of heat generation on the stagnation point flow of nanofluids in stretching sheet with a porous medium. *Journal of Nanofluids*, 7(1):149–155.

Shahrestani, M., Maleki, A., Shadloo, M., and Tlili, I. (2020). Numerical investigation of forced convective heat transfer and performance evaluation criterion of Al_2O_3/water nanofluid flow inside an axisymmetric microchannel. *Symmetry*, 120.

Sharaf, O., Al-Khateeb, A., Kyritsis, D., and Abu-Nada, E. (2019). Numerical investigation of nanofluid particle migration and convective heat transfer in microchannels using an Eulerian-Lagrangian approach. *J. Fluid Mech.*, 878:62–97.

Sharma, M., Manjeet, and Makinde, O. (2018). Flow and heat transfer in nanofluid flow through a cylinder filled with foam porous medium under radial injection. *Defect and Diffusion Forum*, 387:166–181.

Shashikumar, N., Prasannakumara, B., Gireesha, B., and Makinde, O. (2018). Thermodynamics analysis of MHD Casson fluid slip flow in a porous microchannel with thermal radiation. *Diffusion Foundations*, 16:120–139.

Shaw, S., Makinde, O., and Nayak, M. (2018). Rotational flow of nanofluids with radiative and variable properties past impermeable riga plate with transient effects. *Defect and Diffusion Forum*, 387:640–652.

Sheikholeslami, M., Jafaryar, M., Abohamzeh, E., Shafee, A., and Babazadeh, H. (2020). Energy and entropy evaluation and two-phase simulation of nanoparticles within a solar unit with impose of new turbulator. *Sustainable Energy Technologies and Assessments*, 39(100727):1–18.

Sindhu, S. and Gireesha, B. (2021). Irreversibility analysis of nanofluid flow in a vertical microchannel with the influence of particle shape. *Proceedings of the Institution of Mechanical Engineers, Part E: Journal of Process Mechanical Engineering*, 235(2):312–320.

Subramanian, K., Rao, T., and Balakrishnan, A. (2020). *Nanofluids and Their Engineering Applications*. Taylor & Francis Group. CRC Press.

Sujatha, T., Reddy, J., and Kumar, J. G. (2019). Chemical reaction effect on nonlinear radiative MHD nanofluid flow over cone and wedge. *Defect and Diffusion Forum*, 393:83–102.

Suniland, A. and Kumar, R. (2019). CFD analysis of thermal performance of microchannel nanofluid flow at different reynolds numbers. *J. Sci. Technol.*, pages 109–116.

Suresh, B., Kumar, B. R., and Makinde, O. D. (2018). Chemical reaction and thermal radiation effects on MHD mixed convection over a vertical plate with variable fluid properties. *Defect and Diffusion Forum*, 387:332–342.

Tadrist, L., Miscevic, M., Rahli, O., and Topin, F. (2004). About the use of fibrous materials in compact heat exchangers. *Experimental Thermal and Fluid Science*, 28:193–199.

Tamayol, A., Gray, B., Khosla, A., and Bahrami, M. (2010). Pressure drop in microchannels filled with porous media. *Proceedings of ASME 2010 3rd Joint US-European Fluids Engineering Summer Meeting and 8th International Conference on Nanochan- nels, Microchannels, and Minichannels. FEDSM2010-ICNMM. Montreal.*

Tarafdar, B., Das, S., Makinde, O., and Jana, R. (2018). Fully developed mixed convection flow of nanofluids through vertical channel with influences of MHD and wall conductivities. *Journal of Engineering Physics and Thermophysics*, 91(3):784–796.

Tarakaramu, N. and Narayana, P. (2019). Chemical reaction effects on bio-convection nanofluid flow between two parallel plates in rotating system with variable viscosity: A numerical study. *J. Appl. Comput. Mech.*, 5(4):791–803.

Tiwari, R. and Das, M. (2007). Heat transfer augmentation in a two-sided lid-driven differentially heated square cavity utilizing nanofluids. *Int. J. Heat Mass Transf*, 50:2002–2018.

Tuckerman, D. and Pease, R. (1981). High-performance heat sinking for VLSI. *IEEE Electron device letters*, 2(5):126–129.

Vafai, K. (2005). *Handbook of Porous Media. 2nd ed.* Taylor & Francis.

Vaidya, H., Prasad, K., Tlili, B., Makinde, O., Rajashekhar, C., Khan, S., Kumar, R., and Mahendra, D. (2021). Mixed convective nanofluid flow over a nonlinearly stretched riga plate. *Case Studies in Thermal Engineering*, 24:1–19.

Vaidya, H., Rajashekhar, C., Manjunatha, G., Prasad, K., Makinde, O., and Vajravelu, K. (2020). Heat and mass transfer analysis of MHD peristaltic flow through a complaint porous channel with variable thermal conductivity. *Physica Scripta*, 95(4):045219.

Venkateswarlu, M., Makinde, O., and Lakshmi, D. (2019). Influence of thermal radiation and heat generation on steady hydromagnetic flow in a vertical micro-porous-channel in presence of suction/injection. *Journal of Nanofluids*, 8(5):1010–1019.

Verwer, J. and Sanz-Serna, J. (1984). Convergence of method of lines approximations to partial differential equations. *Computing*, 33:297–313.

Vinod, S., Philip, J., and Felicia, L. (2016). A critical review of recent advances in magnetorheology of magnetic nanofluids (ferrofluids). *Journal of Nanofluids*, 5:1–22.

Waghmare, P., Mithra, S., Mather, A., and McLaughlin, J. (2008). Modeling, fabrication and simulation of microfilters. *ECI International Conference on Heat Transfer and Fluid Flow in Microscale*, pages 260–277.

Waqas, W., Jabeen, S., Hayat, T., Shehzad, S., and Alsaedi, A. (2020). Numerical simulation for nonlinear radiated Eyring-Powell nanofluid considering magnetic dipole and activation energy. *International Communications in Heat and Mass Transfer*.

Whitaker, S. (1986). Flow in porous media I: A theoretical derivation of Darcy's law. *Transport in Porous Media*, 1:3–25.

Xu, H., Huang, H., Xu, X., and Sun, Q. (2019). Modeling heat transfer of nanofluid flow in microchannels with electrokinetic and slippery effects using Buongiorno's model. *International Journal of Numerical Methods for Heat & Fluid Flow*, 29(8):2566–2587.

Yadav, D. (2020). Numerical solution of the onset of buoyancy driven nanofluid convective motion in an isotropic porous medium layer with variable gravity and internal heating. *Heat Transfer-Asian Res. Wiley Periodicals, Inc.*, pages 1–22.

Yashkun, U., Zaimi, K., Abu Bakar, N., Ishak, A., and Pop, I. (2020). MHD hybrid nanofluid flow over a permeable stretching/shrinking sheet with thermal radiation effect. *International Journal of Numerical Methods for Heat & Fluid Flow*, pages 1–18.

Yusuf, T., Mabood, F., KhanW, W., and Gbadeyan, J. (2020). Irreversibility analysis of $Cu-TiO2-H2O$ hybrid-nanofluid impinging on a $3-D$ stretching sheet in a porous medium with nonlinear radiation: Darcy-Forchhiemer's model. *Alexandria Engineering Journal*, 59(6):5247–5261.

Zafarullah, A. (1970). Application of the method of lines to parabolic partial differential equations with error estimates. *Journal of the Association for Computing Machinery*, 17(2):294–302.

Zigita, B. (2020). Effect of thermal radiation and chemical reaction on MHD flow of blood in stretching permeable vessel. *Int. J. of Applied Mechanics and Engineering*, 25(3):198–211.

Zuhra, S., Khan, N., Alam, M., Islam, S., and Khan, A. (2020). Buoyancy effects on nanoliquids film flow through a porous medium with gyrotactic microorganisms and cubic autocatalysis chemical reaction. *Advances in Mechanical Engineering*, 12(1):1–17.

APPENDIX A

MATHEMATICAL PRELIMINARIES AND DEFINITIONS OF KEY TERMS

In this Appendix, essential hypothesis and theorem as well as definitions of some key terms were given.

A.1 Mathematical Preliminaries

Continuum Hypothesis: In continuum Mechanics, a fluid is approximated as a continuum (aggregate or macroscopic) rather than as a discontinuous molecular medium or a fluid is at the macroscopic scale of the flow. That is, fluid properties such as mass, density, volume, viscosity, linear or angular momentum, body and surface forces, pressure etc. are considered to be with continuum characteristics and thus these quantities are considered to be (piece-wise) continuous functions in space and time. As a consequence of the continuum hypothesis, the following theorems are utilized in formulating the flow governing equations.
Reynolds Transport Theorem: Let Φ be any smooth vector (or scalar) field, and suppose $R(t)$ is a fluid element with surface $S(t)$ traveling at the flow velocity U. Then

$$\frac{d}{dt}\int_{R(t)} \Phi \ dV = \int_{R(t)} \frac{\partial \Phi}{\partial t} \ dV + \int_{S(t)} \Phi(U \cdot \vec{n}) \ dA$$

Gauss, or divergence Theorem: For any smooth vector field F over a region $R \subset R^3$ with a smooth boundary S. Then

$$\int_R \nabla \cdot F \ dV = \int_S F \cdot \vec{n} \ dA$$

A.2 Definitions of Key Terms

A.2.1 Classification of Fluids

Fluid is any substance that deforms continuously when subjected to a shear stress regardless of magnitude of the shear stress.
Shear stress is a force per unit area that act tangentially to the surface.
Microchannel is a medium through which fluid is used to dissipate heat from a hot surface by forcing the fluid through a passage of hydraulic diameter ranges from 1μm-100μm.
Porous medium is a solid matrix which is characterized by the presence of void spaces called pores which are interconnected by a network of channels where a fluid can move.

Compressible and Incompressible Fluids: A fluid is said to be compressible if its density changes with pressure but if the density of the fluid is constant or has no significant change with pressure, it is called incompressible fluid.

Viscous and Inviscid Fluids: A fluid is said to be viscous when both the normal stress (pressure) and the shearing stress exist but it is said to be inviscid fluid when only the normal stress (pressure) acts between the adjoining layers.

Newtonian and Non-Newtonian Fluids: Newton's law of viscosity is given by $\tau_{ij} = \mu \frac{du}{dy}$. It sates that the shear stress is linearly related to the rate of strain or velocity gradient (rate of deformation) where dynamic viscosity (μ) is a constant of proportionality. Thus, fluids that obey the Newton's law of viscosity are called Newtonian fluids but that do not are called non-Newtonian fluids.

A.2.2 Types of Flows

Internal and External flow: The flow of an unbounded fluid over a surface is called external flow and if the fluid is completely bounded by the surface, then it is called internal flow. For example, flow over a flat plate is considered as external flow and flow through a channel or pipe/duct is internal flow.

Steady and Unsteady Flows: If a fluid flows in such a way that all its properties at every point in the flow depend upon time then it is called unsteady flow; otherwise, it is called steady flow.

Rotational and Irrotational Flows: A flow is said to be irrotational if the fluid particles along their path translate without rotation about the particles center. If along their path the fluid particles translate and rotate about the particles center, the flow is rotational.

Laminar and Turbulent Flows: A flow is said to be a laminar flow if the fluid particles move in a definite path or streamlines. In contrary, turbulent flow is characterized by the irregular movement of particles of the fluid. That is, the particles travel in irregular paths with no observable pattern and no definite layers.

APPENDIX B

MAPLE CODE FOR MODEL PROBLEM IN CHAPTER 4

```
% This code solves the transient and steady state solution for the velocity profile.
with(plots);
A := 1; R := 1; Gt := .1; Gc := .1; lam := .1; Ec := 1; S := 1; Pr := 10; Nt := .1; Nb := .1; Sc
:= .1;F := .1;
fcns := [w(y, t), T(y, t), C(y, t)]; IBC := [w(y, 0) = 0, w(0, t) = 0, w(1, t) = 0, T(y, 0) = 0, T(0,
t) = 0,T(1, t) = 1, C(y, 0) = 0, Nt*(D[1](T))(0,t)+Nb*(D[1](C))(0, t) = 0, C(1, t) = 1];
sys := [diff(w(y, t), t) = -R*(diff(w(y, t), y))+A+exp(-lam*T(y, t))*(diff(w(y, t),(y,2))) −
lam ∗ exp(−lam ∗ T(y,t)) ∗ (diff(w(y,t),y)) ∗ (diff(T(y,t),y)) − S ∗ exp(−lam ∗ T(y,t)) ∗
w(y,t) − F ∗ w(y,t) ∗ w(y,t) + Gt ∗ T(y,t) + Gc ∗ C(y,t),
diff(T(y,t),t) = −R∗(diff(T(y,t),y)) + (diff(T(y,t),(y, 2))+Nb*(diff(C(y, t), y))*(diff(T(y,
t), y)))/Pr+Nt*(diff(T(y, t), y))*(diff(T(y, t), y))+Ec*exp(-lam*T(y, t))*(diff(w(y, t), y))*(diff(w(y,
t), y))+S*Ec*w(y, t)*w(y, t)
+(S*Ec*w(y, t)*w(y, t))*w(y, t),
Sc*(diff(C(y, t), t)) = -Sc*R*(diff(C(y, t), y))+diff(C(y, t), ‘‘(y,2)) + Nt ∗ (diff(T(y,t), ‘‘(y,
2)))/Nb]
pds := pdsolve(sys, IBC, fcns, numeric);
p1w := pds:-plot(w(y, t), t = .1, y = 0 .. 1, numpoints = 100, labeldirections = ["horizontal",
"vertical"], labels = ["y", "velocity"], style = line, color = blue);
p2w := pds:-plot(w(y, t), t = .2, y = 0 .. 1, numpoints = 100, labeldirections = ["horizontal",
"vertical"], labels = ["y", "velocity"], style = line, color = red);
p3w := pds:-plot(w(y, t), t = .4, y = 0 .. 1, numpoints = 100, labeldirections = ["horizontal",
"vertical"], labels = ["y", "velocity"], style = line, color = black);
p4w := pds:-plot(w(y, t), t = .9, y = 0 .. 1, numpoints = 100, labeldirections = ["horizontal",
"vertical"], labels = ["y", "velocity"], style = line, color = magenta);
p5w := pds:-plot(w(y, t), t = 2, y = 0 .. 1, numpoints = 100, labeldirections = ["horizontal",
"vertical"], labels = ["y", "velocity"], style = line, color = green);
plots[display](p1w, p2w, p3w, p4w, p5w);
% % %%%% % % %%%%% % %%%%% % %%%%% % %%%%
% This code solves the parameters dependant solution for the velocity profile.
with(plots);
A := .1; R := 1; Gt := 1; Gc := 1; lam := .1; Ec := 1; S := 1; Pr := 10; Nt := .1; Nb := .1; Sc
:= .1; F := .1;
fcns := C(y), T(y), w(y); sys := -R*(diff(w(y), y))+A+exp(-lam*T(y))*(diff(w(y), ‘‘(y,2)) −
```

```
lam∗exp(−lam∗T(y))∗(diff(w(y),y))∗(diff(T(y),y)))−S∗exp(−lam∗T(y))∗w(y)−
F^w(y)∗w(y)+Gt∗T(y)+Gc∗C(y) = 0,
−R∗(diff(T(y),y))+(diff(T(y),(y, 2))+Nb*(diff(C(y), y))*(diff(T(y), y)))/Pr+Nt*(diff(T(y),
y))*(diff(T(y), y))+Ec*exp(-lam*T(y))*(diff(w(y), y))*(diff(w(y), y))+S*Ec*w(y)*w(y)
+(S*Ec*w(y)*w(y))*w(y) = 0,
-Sc*R*(diff(C(y), y))+diff(C(y), ‘‘(y,2))+Nt∗(diff(T(y),‘‘(y, 2)))/Nb = 0;
p1 := dsolve(sys, Nt*(D(T))(0)+Nb*(D(C))(0) = 0, C(1) = 1, T(0) = 0, T(1) = 1, w(0) = 0,
w(1) = 0, fcns, type = numeric, method = bvp[midrich], abserr = 0.1e-7);
p1w := odeplot(p1, [y, w(y)], 0 .. 1, numpoints = 100, labels = ["y", "u"], style = line, color
= blue);
p1t := odeplot(p1, [y, T(y)], 0 .. 1, numpoints = 100, labels = ["y", "T"], style = line, color =
blue);
p1c := odeplot(p1, [y, C(y)], 0 .. 1, numpoints = 100, labels = ["y", "C"], style = line, color
= blue);
with(plots);
A := .3; R := 1; Gt := 1; Gc := 1; lam := .1; Ec := 1; S := 1; Pr := 10; Nt := .1; Nb := .1; Sc
:= .1; F := .1;
fcns := C(y), T(y), w(y); sys := -R*(diff(w(y), y))+A+exp(-lam*T(y))*(diff(w(y), ‘‘(y,2))−
lam∗exp(−lam∗T(y))∗(diff(w(y),y))∗(diff(T(y),y)))−S∗exp(−lam∗T(y))∗w(y)−
F^w(y)∗w(y)+Gt∗T(y)+Gc∗C(y) = 0,
−R∗(diff(T(y),y))+(diff(T(y),‘‘(y, 2))+Nb*(diff(C(y), y))*(diff(T(y), y)))/Pr+Nt*(diff(T(y),
y))*(diff(T(y), y))+Ec*exp(-lam*T(y))*(diff(w(y), y))*(diff(w(y), y))+S*Ec*w(y)*w(y)
+(S*Ec*w(y)*w(y))*w(y) = 0,
-Sc*R*(diff(C(y), y))+diff(C(y), ‘‘(y,2))+Nt∗(diff(T(y),‘‘(y, 2)))/Nb = 0;
p2 := dsolve(sys, Nt*(D(T))(0)+Nb*(D(C))(0) = 0, C(1) = 1, T(0) = 0, T(1) = 1, w(0) = 0,
w(1) = 0, fcns, type = numeric, method = bvp[midrich], abserr = 0.1e-7);
p2w := odeplot(p2, [y, w(y)], 0 .. 1, numpoints = 100, labels = ["y", "u"], style = line, color
= red);
p2t := odeplot(p2, [y, T(y)], 0 .. 1, numpoints = 100, labels = ["y", "T"], style = line, color =
red);
p2c := odeplot(p2, [y, C(y)], 0 .. 1, numpoints = 100, labels = ["y", "C"], style = line, color
= red);
with(plots);
A := .5; R := 1; Gt := 1; Gc := 1; lam := .1; Ec := 1; S := 1; Pr := 10; Nt := .1; Nb := .1; Sc
:= .1; F := .1;
fcns := C(y), T(y), w(y); sys := -R*(diff(w(y), y))+A+exp(-lam*T(y))*(diff(w(y), ‘‘(y,2))−
lam∗exp(−lam∗T(y))∗(diff(w(y),y))∗(diff(T(y),y)))−S∗exp(−lam∗T(y))∗w(y)−
F^w(y)∗w(y)+Gt∗T(y)+Gc∗C(y) = 0,
−R∗(diff(T(y),y))+(diff(T(y),‘‘(y, 2))+Nb*(diff(C(y), y))*(diff(T(y), y)))/Pr+Nt*(diff(T(y),
```

```
y))*(diff(T(y), y))+Ec*exp(-lam*T(y))*(diff(w(y), y))*(diff(w(y), y))+S*Ec*w(y)*w(y)
+(S*Ec*w(y)*w(y))*w(y) = 0,
-Sc*R*(diff(C(y), y))+diff(C(y), ‘‘(y,2)) + Nt ∗ (diff(T(y), ‘‘(y, 2)))/Nb = 0;
p3 := dsolve(sys, Nt*(D(T))(0)+Nb*(D(C))(0) = 0, C(1) = 1, T(0) = 0, T(1) = 1, w(0) = 0,
w(1) = 0, fcns, type = numeric, method = bvp[midrich], abserr = 0.1e-7);
p3w := odeplot(p3, [y, w(y)], 0 .. 1, numpoints = 100, labels = ["y", "u"], style = line, color
= black);
p3t := odeplot(p3, [y, T(y)], 0 .. 1, numpoints = 100, labels = ["y", "T"], style = line, color =
black);
p3c := odeplot(p3, [y, C(y)], 0 .. 1, numpoints = 100, labels = ["y", "C"], style = line, color
= black);
with(plots);
A := .1; R := 1.5; Gt := 1; Gc := 1; lam := .1; Ec := 1; S := 1; Pr := 10; Nt := .1; Nb := .1; Sc
:= .1; F := .1;
fcns := C(y), T(y), w(y); sys := -R*(diff(w(y), y))+A+exp(-lam*T(y))*(diff(w(y), ‘‘(y,2)) −
lam∗exp(−lam∗T(y))∗(diff(w(y),y))∗(diff(T(y),y))) − S∗exp(−lam∗T(y))∗w(y) −
F^w(y)∗w(y) + Gt∗T(y) + Gc∗C(y) = 0, −R∗(diff(T(y),y)) + (diff(T(y), ‘‘(y, 2))+Nb*(diff(C(y),
y))*(diff(T(y), y)))/Pr+Nt*(diff(T(y), y))*(diff(T(y), y))+Ec*exp(-lam*T(y))*(diff(w(y), y))*(diff(w(y),
y))+S*Ec*w(y)*w(y)
+(S*Ec*w(y)*w(y))*w(y) = 0, -Sc*R*(diff(C(y), y))+diff(C(y), ‘‘(y,2)) + Nt∗(diff(T(y), ‘‘(y,
2)))/Nb = 0;
p6 := dsolve(sys, Nt*(D(T))(0)+Nb*(D(C))(0) = 0, C(1) = 1, T(0) = 0, T(1) = 1, w(0) = 0,
w(1) = 0, fcns, type = numeric, method = bvp[midrich], abserr = 0.1e-7);
p6w := odeplot(p6, [y, w(y)], 0 .. 1, numpoints = 100, labels = ["y", "u"], style = line, color
= blue);
p6t := odeplot(p6, [y, T(y)], 0 .. 1, numpoints = 100, labels = ["y", "T"], style = line, color =
blue);
p6c := odeplot(p6, [y, C(y)], 0 .. 1, numpoints = 100, labels = ["y", "C"], style = line, color
= blue);
with(plots);
A := .3; R := 1.5; Gt := 1; Gc := 1; lam := .1; Ec := 1; S := 1; Pr := 10; Nt := .1; Nb := .1; Sc
:= .1; F := .1;
fcns := C(y), T(y), w(y); sys := -R*(diff(w(y), y))+A+exp(-lam*T(y))*(diff(w(y), ‘‘(y,2)) −
lam∗exp(−lam∗T(y))∗(diff(w(y),y))∗(diff(T(y),y))) − S∗exp(−lam∗T(y))∗w(y) −
F^w(y)∗w(y) + Gt∗T(y) + Gc∗C(y) = 0, −R∗(diff(T(y),y)) + (diff(T(y), ‘‘(y, 2))+Nb*(diff(C(y),
y))*(diff(T(y), y)))/Pr+Nt*(diff(T(y), y))*(diff(T(y), y))+Ec*exp(-lam*T(y))*(diff(w(y), y))*(diff(w(y),
y))+S*Ec*w(y)*w(y)
+(S*Ec*w(y)*w(y))*w(y) = 0, -Sc*R*(diff(C(y), y))+diff(C(y), ‘‘(y,2)) + Nt∗(diff(T(y), ‘‘(y,
2)))/Nb = 0;
```

```
p7 := dsolve(sys, Nt*(D(T))(0)+Nb*(D(C))(0) = 0, C(1) = 1, T(0) = 0, T(1) = 1, w(0) = 0,
w(1) = 0, fcns, type = numeric, method = bvp[midrich], abserr = 0.1e-7);
p7w := odeplot(p7, [y, w(y)], 0 .. 1, numpoints = 100, labels = ["y", "u"], style = line, color
= red);
p7t := odeplot(p7, [y, T(y)], 0 .. 1, numpoints = 100, labels = ["y", "T"], style = line, color =
red);
p7c := odeplot(p7, [y, C(y)], 0 .. 1, numpoints = 100, labels = ["y", "C"], style = line, color
= red);
with(plots);
A := .5; R := 1.5; Gt := 1; Gc := 1; lam := .1; Ec := 1; S := 1; Pr := 10; Nt := .1; Nb := .1; Sc
:= .1; F := .1;
fcns := C(y), T(y), w(y); sys := -R*(diff(w(y), y))+A+exp(-lam*T(y))*(diff(w(y), ‘‘(y,2)) −
lam∗exp(−lam∗T(y))∗(diff(w(y),y))∗(diff(T(y),y))) − S∗exp(−lam∗T(y))∗w(y) −
F^w(y)∗w(y) + Gt∗T(y) + Gc∗C(y) = 0, −R∗(diff(T(y),y)) + (diff(T(y),‘‘(y, 2))+Nb*(diff(C(y),
y))*(diff(T(y), y)))/Pr+Nt*(diff(T(y), y))*(diff(T(y), y))+Ec*exp(-lam*T(y))*(diff(w(y), y))*(diff(w(y),
y))+S*Ec*w(y)*w(y)
+(S*Ec*w(y)*w(y))*w(y) = 0, -Sc*R*(diff(C(y), y))+diff(C(y), ‘‘(y,2)) + Nt∗(diff(T(y),‘‘(y,
2)))/Nb = 0;
p8 := dsolve(sys, Nt*(D(T))(0)+Nb*(D(C))(0) = 0, C(1) = 1, T(0) = 0, T(1) = 1, w(0) = 0,
w(1) = 0, fcns, type = numeric, method = bvp[midrich], abserr = 0.1e-7);
p8w := odeplot(p8, [y, w(y)], 0 .. 1, numpoints = 100, labels = ["y", "u"], style = line, color
= black);
p8t := odeplot(p8, [y, T(y)], 0 .. 1, numpoints = 100, labels = ["y", "T"], style = line, color =
black);
p8c := odeplot(p8, [y, C(y)], 0 .. 1, numpoints = 100, labels = ["y", "C"], style = line, color
= black);
plots[display](p1w, p2w, p3w, p6w, p7w, p8w); % % %%%% % % %%%%% % %%%%%
% %%%%% % %%%%
% This code solves the cf, Nu, and Sh .
% Maple program written by Prof-O D Makinde
% Skin friction, Nusselt number and Sherwood numbers
with(plots);
R := array(1 .. 352); T11 := array(1 .. 352); T12 := array(1 .. 352); T13 := array(1 ..
352); i := 1; A := 0; Gt := 1; Gc := 1; lam := .1; Ec := 1; S := 1; Pr := 10; Nt := .1;
Nb := .1; Sc := .1; F := .1; for RI from 0 by 0.5e-1 to 1 do fcns := C(y), T(y), w(y); sys
:= -RI*(diff(w(y), y))+A+exp(-lam*T(y))*(diff(w(y), ‘‘(y,2)) − lam ∗ exp(−lam ∗ T(y)) ∗
(diff(w(y),y)) ∗ (diff(T(y),y))) − S ∗ exp(−lam ∗ T(y)) ∗ w(y) − F ∗ w(y) ∗ w(y) + Gt ∗
T(y) + Gc∗C(y) = 0, −RI∗(diff(T(y),y)) + (diff(T(y),‘‘(y, 2))+Nb*(diff(C(y), y))*(diff(T(y),
y)))/Pr+Nt*(diff(T(y), y))*(diff(T(y), y))+Ec*exp(-lam*T(y))*(diff(w(y), y))*(diff(w(y), y))
```

```
+S*Ec*w(y)*w(y)+(S*Ec*w(y)*w(y))*w(y) = 0,
-Sc*RI*(diff(C(y), y))+diff(C(y), ‘‘(y,2)) + Nt * (diff(T(y), ‘‘(y, 2)))/Nb = 0;
p1 := dsolve(sys, Nt*(D(T))(0)+Nb*(D(C))(0) = 0, C(1) = 1, T(0) = 0, T(1) = 1, w(0) = 0,
w(1) = 0, fcns, type = numeric, method = bvp[midrich], abserr = 0.1e-7); R[i] := RI; T11[i]
:= rhs(p1(0)[7]); T12[i] := rhs(p1(0)[5]); T13[i] := -rhs(p1(0)[3]); i := i+1 end do;
A := 'A'; RI := 'RI'; Gt := 'Gt'; Gc := 'Gc'; Nt := 'Nt'; Nb := 'Nb'; Sc := 'Sc'; Ec := 'Ec';
Pr := 'Pr'; lam := 'lam'; S := 'S'; F := 'F'; points1 := seq([R[j], T11[j]], j = 1 .. 21); points2
:= seq([R[j], T12[j]], j = 1 .. 21); points3 := seq([R[j], T13[j]], j = 1 .. 21);
pCf1 := pointplot(points1, labels = ["Nt", "Cf"], style = line, color = blue);
pNu1 := pointplot(points2, labels = ["Nt", "Nu"], style = line, color = blue);
pSh1 := pointplot(points3, labels = ["lam", "Sh"], style = line, color = blue);
with(plots);
R := array(1 .. 352); T11 := array(1 .. 352); T12 := array(1 .. 352); T13 := array(1 ..
352); i := 1; A := .1; Gt := 1; Gc := 1; lam := .1; Ec := 1; S := 1; Pr := 10; Nt := .1;
Nb := .1; Sc := .1; F := .1; for RI from 0 by 0.5e-1 to 1 do fcns := C(y), T(y), w(y); sys
:= -RI*(diff(w(y), y))+A+exp(-lam*T(y))*(diff(w(y), ‘‘(y,2)) - lam * exp(-lam * T(y)) *
(diff(w(y),y)) * (diff(T(y),y))) - S * exp(-lam * T(y)) * w(y) - F * w(y) * w(y) + Gt *
T(y) + Gc*C(y) = 0, -RI*(diff(T(y),y)) + (diff(T(y), ‘‘(y, 2))+Nb*(diff(C(y), y))*(diff(T(y),
y)))/Pr+Nt*(diff(T(y), y))*(diff(T(y), y))+Ec*exp(-lam*T(y))*(diff(w(y), y))*(diff(w(y), y))
+S*Ec*w(y)*w(y)+(S*Ec*w(y)*w(y))*w(y) = 0,
-Sc*RI*(diff(C(y), y))+diff(C(y), ‘‘(y,2)) + Nt * (diff(T(y), ‘‘(y, 2)))/Nb = 0;
p1 := dsolve(sys, Nt*(D(T))(0)+Nb*(D(C))(0) = 0, C(1) = 1, T(0) = 0, T(1) = 1, w(0) = 0,
w(1) = 0, fcns, type = numeric, method = bvp[midrich], abserr = 0.1e-7); R[i] := RI; T11[i]
:= rhs(p1(0)[7]); T12[i] := rhs(p1(0)[5]); T13[i] := -rhs(p1(0)[3]); i := i+1 end do;
A := 'A'; RI := 'RI'; Gt := 'Gt'; Gc := 'Gc'; Nt := 'Nt'; Nb := 'Nb'; Sc := 'Sc'; Ec := 'Ec'; Pr
:= 'Pr'; lam := 'lam'; S := 'S'; F := 'F'; points11 := seq([R[j], T11[j]], j = 1 .. 21); points21
:= seq([R[j], T12[j]], j = 1 .. 21); points31 := seq([R[j], T13[j]], j = 1 .. 21);
pCf2 := pointplot(points11, labels = ["Nt", "Cf"], style = line, color = red);
pNu2 := pointplot(points21, labels = ["Nt", "Nu"], style = line, color = red);
pSh2 := pointplot(points31, labels = ["lam", "Sh"], style = line, color = red);
with(plots);
R := array(1 .. 352); T11 := array(1 .. 352); T12 := array(1 .. 352); T13 := array(1 ..
352); i := 1; A := .2; Gt := 1; Gc := 1; lam := .1; Ec := 1; S := 1; Pr := 10; Nt := .1;
Nb := .1; Sc := .1; F := .1; for RI from 0 by 0.5e-1 to 1 do fcns := C(y), T(y), w(y); sys
:= -RI*(diff(w(y), y))+A+exp(-lam*T(y))*(diff(w(y), ‘‘(y,2)) - lam * exp(-lam * T(y)) *
(diff(w(y),y)) * (diff(T(y),y))) - S * exp(-lam * T(y)) * w(y) - F * w(y) * w(y) + Gt *
T(y) + Gc*C(y) = 0, -RI*(diff(T(y),y)) + (diff(T(y), ‘‘(y, 2))+Nb*(diff(C(y), y))*(diff(T(y),
y)))/Pr+Nt*(diff(T(y), y))*(diff(T(y), y))+Ec*exp(-lam*T(y))*(diff(w(y), y))*(diff(w(y), y))
+S*Ec*w(y)*w(y)+(S*Ec*w(y)*w(y))*w(y) = 0,
```

```
-Sc*RI*(diff(C(y), y))+diff(C(y), ‘‘(y,2)) + Nt * (diff(T(y), ‘‘(y, 2)))/Nb = 0;
p1 := dsolve(sys, Nt*(D(T))(0)+Nb*(D(C))(0) = 0, C(1) = 1, T(0) = 0, T(1) = 1, w(0) = 0,
w(1) = 0, fcns, type = numeric, method = bvp[midrich], abserr = 0.1e-7); R[i] := RI; T11[i]
:= rhs(p1(0)[7]); T12[i] := rhs(p1(0)[5]); T13[i] := -rhs(p1(0)[3]); i := i+1 end do;
A := ’A’; RI := ’RI’; Gt := ’Gt’; Gc := ’Gc’; Nt := ’Nt’; Nb := ’Nb’; Sc := ’Sc’; Ec := ’Ec’; Pr
:= ’Pr’; lam := ’lam’; S := ’S’; F := ’F’; points12 := seq([R[j], T11[j]], j = 1 .. 21); points22
:= seq([R[j], T12[j]], j = 1 .. 21); points32 := seq([R[j], T13[j]], j = 1 .. 21);
pCf3 := pointplot(points12, labels = ["Nt", "Cf"], style = line, color = black);
pNu3 := pointplot(points22, labels = ["Nt", "Nu"], style = line, color = black);
pSh3 := pointplot(points32, labels = ["lam", "Sh"], style = line, color = black);
with(plots);
R := array(1 .. 352); T11 := array(1 .. 352); T12 := array(1 .. 352); T13 := array(1 ..
352); i := 1; A := .3; Gt := 1; Gc := 1; lam := .1; Ec := 1; S := 1; Pr := 10; Nt := .1;
Nb := .1; Sc := .1; F := .1; for RI from 0 by 0.5e-1 to 1 do fcns := C(y), T(y), w(y); sys
:= -RI*(diff(w(y), y))+A+exp(-lam*T(y))*(diff(w(y), ‘‘(y,2)) - lam * exp(-lam * T(y)) *
(diff(w(y),y)) * (diff(T(y),y))) - S * exp(-lam * T(y)) * w(y) - F * w(y) * w(y) + Gt *
T(y) + Gc*C(y) = 0, -RI*(diff(T(y),y)) + (diff(T(y), ‘‘(y, 2))+Nb*(diff(C(y), y))*(diff(T(y),
y)))/Pr+Nt*(diff(T(y), y))*(diff(T(y), y))+Ec*exp(-lam*T(y))*(diff(w(y), y))*(diff(w(y), y))
+S*Ec*w(y)*w(y)+(S*Ec*w(y)*w(y))*w(y) = 0,
-Sc*RI*(diff(C(y), y))+diff(C(y), ‘‘(y,2)) + Nt*(diff(T(y), ‘‘(y, 2)))/Nb = 0; p1 := dsolve(sys,
Nt*(D(T))(0)+Nb*(D(C))(0) = 0, C(1) = 1, T(0) = 0, T(1) = 1, w(0) = 0, w(1) = 0, fcns, type
= numeric, method = bvp[midrich], abserr = 0.1e-7); R[i] := RI; T11[i] := rhs(p1(0)[7]);
T12[i] := rhs(p1(0)[5]); T13[i] := -rhs(p1(0)[3]); i := i+1 end do;
A := ’A’; RI := ’RI’; Gt := ’Gt’; Gc := ’Gc’; Nt := ’Nt’; Nb := ’Nb’; Sc := ’Sc’; Ec := ’Ec’; Pr
:= ’Pr’; lam := ’lam’; S := ’S’; F := ’F’; points12 := seq([R[j], T11[j]], j = 1 .. 21); points22
:= seq([R[j], T12[j]], j = 1 .. 21); points32 := seq([R[j], T13[j]], j = 1 .. 21);
pCf4 := pointplot(points12, labels = ["lam", "Cf"], style = line, color = magenta);
pNu4 := pointplot(points22, labels = ["lam", "Nu"], style = line, color = magenta);
pSh4 := pointplot(points32, labels = ["lam", "Sh"], style = line, color = magenta);
with(plots);
R := array(1 .. 352); T11 := array(1 .. 352); T12 := array(1 .. 352); T13 := array(1 ..
352); i := 1; A := 1; Gt := 1; Gc := 1; lam := .1; Ec := 1; S := 1; Pr := 10; Nt := .1;
Nb := .1; Sc := .1; F := 0; for RI from 0 by 0.5e-1 to 1 do fcns := C(y), T(y), w(y); sys
:= -RI*(diff(w(y), y))+A+exp(-lam*T(y))*(diff(w(y), ‘‘(y,2)) - lam * exp(-lam * T(y)) *
(diff(w(y),y)) * (diff(T(y),y))) - S * exp(-lam * T(y)) * w(y) - F * w(y) * w(y) + Gt *
T(y) + Gc*C(y) = 0, -RI*(diff(T(y),y)) + (diff(T(y), ‘‘(y, 2))+Nb*(diff(C(y), y))*(diff(T(y),
y)))/Pr+Nt*(diff(T(y), y))*(diff(T(y), y))+Ec*exp(-lam*T(y))*(diff(w(y), y))*(diff(w(y), y))
+S*Ec*w(y)*w(y)+(S*Ec*w(y)*w(y))*w(y) = 0,
-Sc*RI*(diff(C(y), y))+diff(C(y), ‘‘(y,2)) + Nt * (diff(T(y), ‘‘(y, 2)))/Nb = 0;
```

```
p1 := dsolve(sys, Nt*(D(T))(0)+Nb*(D(C))(0) = 0, C(1) = 1, T(0) = 0, T(1) = 1, w(0) = 0,
w(1) = 0, fcns, type = numeric, method = bvp[midrich], abserr = 0.1e-7); R[i] := RI; T11[i]
:= rhs(p1(0)[7]); T12[i] := rhs(p1(0)[5]); T13[i] := -rhs(p1(0)[3]); i := i+1 end do;
A := ’A’; RI := ’RI’; Gt := ’Gt’; Gc := ’Gc’; Nt := ’Nt’; Nb := ’Nb’; Sc := ’Sc’; Ec := ’Ec’;
Pr := ’Pr’; lam := ’lam’; S := ’S’; F := ’F’; points1 := seq([R[j], T11[j]], j = 1 .. 21); points2
:= seq([R[j], T12[j]], j = 1 .. 21); points3 := seq([R[j], T13[j]], j = 1 .. 21);
pCf5 := pointplot(points1, labels = ["RI", "Cf"], style = line, color = blue);
pNu5 := pointplot(points2, labels = ["RI", "Nu"], style = line, color = blue);
pSh5 := pointplot(points3, labels = ["RI", "Sh"], style = line, color = blue);
with(plots); R := array(1 .. 352); T11 := array(1 .. 352); T12 := array(1 .. 352); T13 :=
array(1 .. 352); i := 1; A := 1; Gt := 1; Gc := 1; lam := .1; Ec := 1; S := 1; Pr := 10; Nt :=
.1; Nb := .1; Sc := .1; F := 1; for RI from 0 by 0.5e-1 to 1 do fcns := C(y), T(y), w(y); sys
:= -RI*(diff(w(y), y))+A+exp(-lam*T(y))*(diff(w(y), ‘‘(y,2)) − lam ∗ exp(−lam ∗ T(y)) ∗
(diff(w(y),y)) ∗ (diff(T(y),y))) − S ∗ exp(−lam ∗ T(y)) ∗ w(y) − F ∗ w(y) ∗ w(y) + Gt ∗
T(y) + Gc∗C(y) = 0, −RI∗(diff(T(y),y)) + (diff(T(y), ‘‘(y, 2))+Nb*(diff(C(y), y))*(diff(T(y),
y)))/Pr+Nt*(diff(T(y), y))*(diff(T(y), y))+Ec*exp(-lam*T(y))*(diff(w(y), y))*(diff(w(y), y))
+S*Ec*w(y)*w(y)+(S*Ec*w(y)*w(y))*w(y) = 0,
-Sc*RI*(diff(C(y), y))+diff(C(y), ‘‘(y,2)) + Nt ∗ (diff(T(y), ‘‘(y, 2)))/Nb = 0; p1 := dsolve(sys,
Nt*(D(T))(0)+Nb*(D(C))(0) = 0, C(1) = 1, T(0) = 0, T(1) = 1, w(0) = 0, w(1) = 0, fcns, type
= numeric, method = bvp[midrich], abserr = 0.1e-7); R[i] := RI; T11[i] := rhs(p1(0)[7]);
T12[i] := rhs(p1(0)[5]); T13[i] := -rhs(p1(0)[3]); i := i+1 end do;
A := ’A’; RI := ’RI’; Gt := ’Gt’; Gc := ’Gc’; Nt := ’Nt’; Nb := ’Nb’; Sc := ’Sc’; Ec := ’Ec’; Pr
:= ’Pr’; lam := ’lam’; S := ’S’; F := ’F’; points11 := seq([R[j], T11[j]], j = 1 .. 21); points21
:= seq([R[j], T12[j]], j = 1 .. 21); points31 := seq([R[j], T13[j]], j = 1 .. 21);
pCf6 := pointplot(points11, labels = ["RI", "Cf"], style = line, color = red);
pNu6 := pointplot(points21, labels = ["RI", "Nu"], style = line, color = red);
pSh6 := pointplot(points31, labels = ["RI", "Sh"], style = line, color = red);
with(plots);
R := array(1 .. 352); T11 := array(1 .. 352); T12 := array(1 .. 352); T13 := array(1 ..
352); i := 1; A := 1; Gt := 1; Gc := 1; lam := .1; Ec := 1; S := 1; Pr := 10; Nt := .1;
Nb := .1; Sc := .1; F := 2; for RI from 0 by 0.5e-1 to 1 do fcns := C(y), T(y), w(y); sys
:= -RI*(diff(w(y), y))+A+exp(-lam*T(y))*(diff(w(y), ‘‘(y,2)) − lam ∗ exp(−lam ∗ T(y)) ∗
(diff(w(y),y)) ∗ (diff(T(y),y))) − S ∗ exp(−lam ∗ T(y)) ∗ w(y) − F ∗ w(y) ∗ w(y) + Gt ∗
T(y) + Gc∗C(y) = 0, −RI∗(diff(T(y),y)) + (diff(T(y), ‘‘(y, 2))+Nb*(diff(C(y), y))*(diff(T(y),
y)))/Pr+Nt*(diff(T(y), y))*(diff(T(y), y))+Ec*exp(-lam*T(y))*(diff(w(y), y))*(diff(w(y), y))
+S*Ec*w(y)*w(y)+(S*Ec*w(y)*w(y))*w(y) = 0,
-Sc*RI*(diff(C(y), y))+diff(C(y), ‘‘(y,2)) + Nt ∗ (diff(T(y), ‘‘(y, 2)))/Nb = 0; p1 := dsolve(sys,
Nt*(D(T))(0)+Nb*(D(C))(0) = 0, C(1) = 1, T(0) = 0, T(1) = 1, w(0) = 0, w(1) = 0, fcns, type
= numeric, method = bvp[midrich], abserr = 0.1e-7); R[i] := RI; T11[i] := rhs(p1(0)[7]);
```

```
T12[i] := rhs(p1(0)[5]); T13[i] := -rhs(p1(0)[3]); i := i+1 end do;
A := ’A’; RI := ’RI’; Gt := ’Gt’; Gc := ’Gc’; Nt := ’Nt’; Nb := ’Nb’; Sc := ’Sc’; Ec := ’Ec’; Pr
:= ’Pr’; lam := ’lam’; S := ’S’; F := ’F’; points12 := seq([R[j], T11[j]], j = 1 .. 21); points22
:= seq([R[j], T12[j]], j = 1 .. 21); points32 := seq([R[j], T13[j]], j = 1 .. 21);
pCf7 := pointplot(points12, labels = ["RI", "Cf"], style = line, color = black);
pNu7 := pointplot(points22, labels = ["RI", "Nu"], style = line, color = black);
pSh7 := pointplot(points32, labels = ["RI", "Sh"], style = line, color = black);
with(plots);
R := array(1 .. 352); T11 := array(1 .. 352); T12 := array(1 .. 352); T13 := array(1 ..
352); i := 1; A := 1; Gt := 1; Gc := 1; lam := .1; Ec := 1; S := 1; Pr := 10; Nt := .1;
Nb := .1; Sc := .1; F := 3; for RI from 0 by 0.5e-1 to 1 do fcns := C(y), T(y), w(y); sys
:= -RI*(diff(w(y), y))+A+exp(-lam*T(y))*(diff(w(y), ‘‘(y,2)) − lam ∗ exp(−lam ∗ T(y)) ∗
(diff(w(y),y)) ∗ (diff(T(y),y))) − S ∗ exp(−lam ∗ T(y)) ∗ w(y) − F ∗ w(y) ∗ w(y) + Gt ∗
T(y) + Gc∗C(y) = 0, −RI∗(diff(T(y),y)) + (diff(T(y), ‘‘(y, 2))+Nb*(diff(C(y), y))*(diff(T(y),
y)))/Pr+Nt*(diff(T(y), y))*(diff(T(y), y))+Ec*exp(-lam*T(y))*(diff(w(y), y))*(diff(w(y), y))
+S*Ec*w(y)*w(y)+(S*Ec*w(y)*w(y))*w(y) = 0,
-Sc*RI*(diff(C(y), y))+diff(C(y), ‘‘(y,2)) + Nt∗(diff(T(y), ‘‘(y, 2)))/Nb = 0; p1 := dsolve(sys,
Nt*(D(T))(0)+Nb*(D(C))(0) = 0, C(1) = 1, T(0) = 0, T(1) = 1, w(0) = 0, w(1) = 0, fcns, type
= numeric, method = bvp[midrich], abserr = 0.1e-7); R[i] := RI; T11[i] := rhs(p1(0)[7]);
T12[i] := rhs(p1(0)[5]); T13[i] := -rhs(p1(0)[3]); i := i+1 end do;
A := ’A’; RI := ’RI’; Gt := ’Gt’; Gc := ’Gc’; Nt := ’Nt’; Nb := ’Nb’; Sc := ’Sc’; Ec := ’Ec’; Pr
:= ’Pr’; lam := ’lam’; S := ’S’; F := ’F’; points12 := seq([R[j], T11[j]], j = 1 .. 21); points22
:= seq([R[j], T12[j]], j = 1 .. 21); points32 := seq([R[j], T13[j]], j = 1 .. 21);
pCf8 := pointplot(points12, labels = ["RI", "Cf"], style = line, color = magenta);
pNu8 := pointplot(points22, labels = ["RI", "Nu"], style = line, color = magenta);
pSh8 := pointplot(points32, labels = ["RI", "Sh"], style = line, color = magenta);
plots[display](pCf1, pCf2, pCf3, pCf4, pCf5, pCf6, pCf7, pCf8);
plots[display](pNu1, pNu2, pNu3, pNu4, pNu5, pNu6, pNu7, pNu8);
plots[display](pSh1, pSh2, pSh3, pSh4, pSh5, pSh6, pSh7, pSh8);
```